

# Detailed mathematical modelling of transient combustion processes

(Detaillierte mathematische Modellierung  
von transienten Verbrennungsprozessen)

Zur Erlangung des akademischen Grades eines  
DOKTORS DER INGENIEURWISSENSCHAFTEN  
(Dr.-Ing.)

bei der KIT-Fakultät für Maschinenbau des  
Karlsruher Instituts für Technologie (KIT)  
genehmigte

DISSERTATION

von

M.Sc. Andrey Koksharov

Hauptreferent: Prof. Dr. rer. nat. habil. U. Maas  
Korreferent: apl.-Prof. Dr.-Ing. A. Class

Tag der mündlichen Prüfung: 31.01.2019



# Zusammenfassung

Die Flamme ist ein komplexes Phänomen, die mehrere physikalische Prozesse aufgreift. Nach der Zündung passieren schnelle Änderungen, nicht nur im physikalischen Raum, sondern auch im thermodynamischen und chemischen Zustandsraum. Je nach Anfangs- und Randbedingungen kann eine komplexe Flammendynamik beobachtet werden, wie beispielsweise Turbulenz, Flammenbeschleunigung, Umkehrung der Flammenspitze, Flammenlöschung und der Übergang zur Detonation. Ein Modell von Verbrennungsprozessen muss die thermodynamischen Eigenschaften, die chemischen Reaktionen und die Gasdynamik berücksichtigen. Starke Kopplung der gasdynamischen und thermochemischen Prozessen führt zur besonders geprägten Sensitivität der Zündprozesse bezüglich der Systemparameter. Die Vielzahl der beteiligten hydrodynamischen und thermochemischen Prozesse überdecken eine sehr große Breite der Zeit- und Raumskalen, von Mikrometern bis zu einigen Metern. Dies macht die genaue Modellierung von Systemparametern besonders wichtig. In den meisten Fällen ist die Lösung der Navier-Stokes-Gleichungen, die mit der Energieerhaltung und chemischen Komponenten erweitert werden, erforderlich.

Die Spektrale Methode (SM) bietet eine vielversprechende Alternative zu den klassischen Verfahren, wie z.B. die Methode der Finiten Differenzen oder Finiten Volumen. Die SM benötigt für die gleiche Genauigkeit im Vergleich zu den Verfahren mit geringen Ordnungen weniger Diskretisierungspunkte. Außerdem enthält diese Methode keine numerische Viskosität. Allerdings wird die SM mit einer nichtausreichenden Auflösung instabil. Um diesen Nachteil zu umgehen, wird im Rahmen dieser Arbeit die Adaptive Pseudo-Spektrale Methode (APSM) angewendet. Die APSM erlaubt eine dynamische strukturelle Anpassung des funktionellen Raums zu den schnell veränderten Verbrennungszuständen, sodass die benutzerdefinierten Toleranzen erfüllt werden. Die strukturelle Adaption erlaubt eine effiziente Lösung des resultierenden linearen Systems, die nur lokalisierte Aktualisierungen der Jacobimatrix benötigt.

Die in der Arbeit entwickelte APSM wurde zunächst auf die Lösung der Master-Gleichung (MG) der chemischen Kinetik angewendet. Die MG ist eine steife integro-differentielle Gleichung, die Berechnungen von Reaktionskonstanten aus quantenmechanischen Überlegungen erlaubt. Die damit berechneten Konstanten für den unimolekularen Zerfall von „2,3-Dihydro-2,5-Dimethylfuran-3-yl“ (25DMF2H) und für die Isomerisierung zwischen Allene und Propin stimmen mit den experimentellen und theoretischen Daten überein. Im Vergleich zu den klassischen Verfahren ist die Berechnungszeit um den Faktor 100 schneller.

Danach wurde das Verfahren auf die Untersuchung von transienten Verbrennungsprozessen in engen Kanälen während und direkt nach der Zündung eingesetzt. Es wurde gezeigt, wie unter bestimmten Verhältnissen zwischen Kanallänge und -breite in den

geschlossenen Systemen eine Umkehrung der Flammenspitze erfolgt. Dabei wurden vier kritische Stadien der Flammenentwicklung identifiziert. In einem halboffenen Kanal wurde eine starke Flammenbeschleunigung und eine Turbulenz beobachtet. Im Folgenden wurde eine Verbrennung im Mikro-Durchfluss-Reaktor modelliert, welche die Rolle der Modellierung der Grenzschicht und der Chemilumineszenz hervorhebt, um einen besseren Vergleich mit experimentellen Beobachtungen zu ermöglichen. Anschließend wurde eine Flammenbeschleunigung im unbeschränkten Raum untersucht. Die Untersuchung zeigt, dass ein kritischer Wert der Flammenfaltung existiert, bei der direkt nach der Zündung eine starke Flammenbeschleunigung mit anschließendem Übergang zur Detonation beobachtet wird. Die Analyse des thermochemischen Zustandsraums hat die Wichtigkeit der chemischen Kinetik auf den Übergang gezeigt. Die letzte Anwendung zeigt eine extreme Kopplung zwischen hydrodynamischen und thermochemischen Prozessen, wobei die teilnehmenden Prozesse einen Unterschied von 9 Größenordnungen erreichen.

# Contents

<b>1. Introduction</b>	<b>1</b>
<b>2. Mathematical model of transient reacting flows</b>	<b>5</b>
2.1. Conservation laws . . . . .	5
2.1.1. Mass and momentum conservation . . . . .	5
2.1.2. Species conservation . . . . .	7
2.1.3. Energy conservation . . . . .	9
2.2. Thermodynamic gas properties . . . . .	10
2.2.1. Thermodynamic properties of monomolecular gas . . . . .	10
2.2.2. Viscosity of monomolecular gas . . . . .	10
2.2.3. Heat conductivity of monomolecular gas . . . . .	11
2.2.4. Binary diffusion coefficients . . . . .	13
2.2.5. Collision integrals . . . . .	14
2.2.6. Multi-component gas properties . . . . .	14
2.3. Chemical reactions . . . . .	19
2.3.1. Forward elementary reactions . . . . .	19
2.3.2. Reverse elementary reactions . . . . .	20
2.3.3. Pressure dependent reactions . . . . .	20
<b>3. Methodology</b>	<b>23</b>
3.1. Motivation . . . . .	23
3.2. Spectral methods . . . . .	24
3.3. Incremental method for time integration . . . . .	27
3.3.1. Modified Newton Method . . . . .	29
3.3.2. Error estimation . . . . .	32
3.3.3. Interval adaptation . . . . .	33
3.4. Adaptive pseudo spectral method . . . . .	35
3.4.1. Solution of linear system in binary tree . . . . .	37
3.4.2. Error estimation and optimal collocation points . . . . .	38
3.4.3. Grid adaptation . . . . .	40
3.4.4. Antialiasing and Filter . . . . .	47
<b>4. Computation of reaction rates for isomerisation and decomposition reactions</b>	<b>49</b>
4.1. Solution of integro-differential equations . . . . .	50
4.2. Single-well Master Equation . . . . .	53
4.2.1. Unimolecular decomposition of 25DMF2H . . . . .	56
4.3. Multi-well Master Equation . . . . .	62
4.3.1. Isomerisation of Allene to Propyne . . . . .	64

<b>5. Applications to combustion systems</b>	<b>71</b>
5.1. Benchmarking and code validation . . . . .	71
5.1.1. Ignition delay of Hydrogen-Oxygen mixtures . . . . .	71
5.1.1.1. Mathematical model for homogeneous systems . . . . .	72
5.1.2. Unconfined hydrogen-air flame . . . . .	75
5.1.3. Laminar flame speed of hydrogen-air mixtures . . . . .	78
5.2. Ignition and flame propagation in narrow channels . . . . .	82
5.2.1. Flame development in narrow ducts . . . . .	82
5.2.1.1. Flame tip inversion in closed channel . . . . .	85
5.2.1.2. Flame acceleration in open channel . . . . .	95
5.2.2. Combustion in micro flow reactor . . . . .	101
<b>6. Modelling of flame acceleration in unconfined settings</b>	<b>111</b>
6.1. Flame acceleration near wall . . . . .	112
6.2. Acceleration of a free flame . . . . .	118
<b>7. Conclusions</b>	<b>127</b>
<b>Appendix</b>	<b>131</b>
A. Conservation laws in general orthogonal coordinates . . . . .	131
A.1. 1D symmetry . . . . .	133
A.2. 2D symmetry . . . . .	134
A.3. Standard geometric symmetry relations . . . . .	136
B. General coordinate transformations . . . . .	137
B.1. 1D transformation . . . . .	137
B.2. 2D transformation . . . . .	139
B.3. 3D transformation . . . . .	141
C. Benchmarking of time integration scheme . . . . .	146
C.1. Semenov's explosion model . . . . .	146
C.2. The reaction of Robertson . . . . .	147
C.3. HIRES . . . . .	148
D. Adaptive pseudo spectral method . . . . .	150
D.1. Domain matching and boundary conditions . . . . .	152
D.2. Solution of the linear system for spectral elements . . . . .	153
D.3. Implementation of adaptive pseudo spectral method . . . . .	158
D.4. Grid adaptation . . . . .	170
<b>List of Figures</b>	<b>179</b>
<b>List of Tables</b>	<b>185</b>
<b>Bibliography</b>	<b>187</b>

# Nomenclature

## Physics Constants

$k_B$	Boltzmann constant	$1.38064853 \times 10^{-23}$ J/K
$N_A$	Avogadro's number	$6.022140858 \times 10^{23}$ 1/mol
$R$	Gas constant	8.3144598 J/mol/K

## Mathematical symbols

$e$	Relative error
$f$	Scalar function (zero order tensor)
$\mathbf{f}$	Vector function (first order tensor)
$g_i$	Orthogonal transformation parameter for coordinate $i$
$h$	Time step increment
$\tilde{u}$	Approximation of function $u$
$\hat{u}_i$	Spectral coefficient of function $u$
$E$	Normalised relative error
$\mathbf{F}$	Tensor function (second order tensor)
$\mathbf{J}$	Jacobi matrix
$R$	Residual function
$\mathbf{R}$	Residual at collocation points
$\tilde{\mathbf{U}}$	Approximation of function $u$ on collocation points
$\lambda_i$	Wave length or Eigenvalue
$\phi_i$	Basis function
$\psi_i$	Test function

$\Phi$	Matrix of values of basis functions on collocation points	
$\nabla$	Gradient operator	
$\nabla \cdot$	Divergence operator	
$ATOL$	Absolute tolerance	
$RTOL$	Relative tolerance	

### Physical Symbols

$c$	Concentration	mol/m <sup>3</sup>
$c_P$	Isobaric mass heat capacity	J/kg/K
$\bar{c}_P$	Isobaric molar heat capacity	J/mol/K
$h$	Mass enthalpy	J/kg
$\bar{h}$	Molar enthalpy	J/mol
$\mathbf{j}_i$	Mass diffusion flux	kg/m <sup>2</sup> /s
$\bar{\mathbf{j}}_i$	Molar diffusion flux	mol/m <sup>2</sup> /s
$k$	Rate of elementary reaction	
$n(E)$	Normalised reactant population	
$s$	Mass entropy	J/kg/K
$\bar{s}$	Molar entropy	J/mol/K
$\mathbf{v}$	Velocity vector	m/s
$\mathcal{D}_{ij}$	Binary diffusion coefficient	m <sup>2</sup> /s
$D_{ij}$	Diffusion coefficient	m <sup>2</sup> /s
$K^c$	Equilibrium constant	
$\mathcal{M}$	Mach number	
$M$	Molar mass	g/mol
$P$	Pressure	Pa
$P(E, E')$	Transition probability function	
$T$	Temperature	K
$V$	Volume	m <sup>3</sup>

$\mathbf{V}_i$	Diffusion velocity	mol/m <sup>2</sup> /s
$X_i$	Mole fraction	
$Y_i$	Mass fraction	
$\gamma$	Adiabatic index	
$\lambda$	Heat conductivity	W/m/K
$\mu$	Dynamic viscosity	Pa · s
$\rho$	Density	kg/m <sup>3</sup>
$\sigma$	Scalar component of stress tensor	Pa
$\tau_{ij}$	Component of shear stress tensor $\mathbf{T}$	Pa
$\phi_i$	Specific mole number	mol/kg
$\omega$	Collision efficiency	
$\omega$	Vorticity	1/s
$\dot{\omega}_i$	Chemical source	mol/m <sup>3</sup> /s
$\mathbf{T}$	Shear stress tensor	Pa
$\Phi$	Equivalence ratio	



# 1. Introduction

Flame is a complex phenomenon incorporating multiple physical processes. After ignition it undergoes a rapid development not only in physical space but also in the thermodynamical and chemical state spaces. Depending on particular conditions, after the ignition, one may observe very complicated dynamics including flame turbulisation, flame acceleration, flame tip inversion, flame quenching, transition to detonation etc. In many cases ignition has a pivotal influence on the flame front development. An accurate assessment of conditions determining the flame initiation and its transient behaviour belong to one of the most important challenges facing the contemporary combustion theory.

Many technical applications, e.g. internal combustion engines, rely on ignition and transient combustion processes. An optimisation of these processes can lead to a reduced pollutant emission and an increased efficiency. With modern trend for downsizing of combustion facilities, it becomes a very complicated task to sustain combustion, due to the heat losses, flame-wall interaction and heterogeneous chemical effects at the boundary. On one side, an unexpected ignition or a spontaneous flame acceleration may lead to a damage of facilities [WMD06]. On the other side, even the hazardous detonation itself offers a new perspective in propulsion, such as pulse detonation and rotation detonation engines, which promise higher thermal and exergetic efficiency [Kai03].

In order to address these difficult issues, a model of a combustion process has to include thermodynamic properties, chemical reaction and gas dynamics. Thermodynamic models involve heat capacity, heat conductivity, equation of state and energy transport. Chemical models describe multiple chemical reactions taking place simultaneously, with corresponding chemical transformation rules and heat release. The strong coupling of gas dynamics and thermo-chemical processes leads to particular sensitivity of ignition process to thermodynamic, chemical and flow parameters. The multitude of participating hydrodynamical and thermo-chemical processes cover a very large range of time and space scales. These range from several micrometers to the integral scales of several meters [WMD06]. Thus, it makes the accurate modelling of these parameters particularly important. In most cases, the solution of Navier-Stokes equations, extended by conservation of energy and of individual chemical components [Wil88, KCG03, WMD06], is required. The strong coupling of gas dynamics and thermo-chemical processes makes the modelling of ignition a particular challenging task.

Analytical solutions of Navier-Stokes equations for thermo-chemical reacting flows

are limited to a very small scope of simplified problems [Wil88, WMD06]. Thus development of a numerical technique that provides both accurate and stable numerical solution of considered governing equations is a difficult problem of modern computational physics and numerical analysis. Prevailing number of works in computational combustion science rely on lower order numerical schemes like finite differences and finite volumes [KCG03, OB05]. These schemes produce very sparse linear systems of equations, which can be treated efficiently with modern algorithms for linear algebra (see e.g. [QSS00]). The low order schemes however tend to introduce a relatively high numerical viscosity in the solution, which could be slightly reduced only by utilising extremely fine numerical grids. Note, that this numerical viscosity can affect significantly the outcome of the computation of ignition and transient regimes [BKKY].

An alternative numerical approach is based on the ideas of Fourier and Galerkin (see e.g. [Boy89, YS07, LI14]), when the solution of the system of partial differential equations is represented as a series representation using eigenfunctions in an appropriate functional space. These so-called spectral methods are extremely powerful when a basis (of eigenfunctions) of a functional space is constructed. However, up to now there are only limited attempts to adopt them to the problems of reacting flows, mainly due to difficulties to construct a basis in a functional space. Current successful applications are either limited to relatively “smooth” problems [BM87, PFM<sup>+</sup>08] or add a small amount of artificial viscosity to stabilise the solution when the system becomes stiff [YS07, WZSN12]. Nevertheless, as the current study shows, the spectral method can be still very efficient for stiff problems of the ignition, without artificial viscosity, when supplied by adaptation and matching algorithms. However, the method has to overcome the following problems:

- Resolve all time and space scales of participating processes, varying from several micrometers of ignition kernel and shock waves, to integral scales of several meters;
- Avoid usage of numerical dissipation (viscosity), which may lead to physically incorrect results, e.g. faster ignition and flame propagation, or missing flame instabilities.;
- Minimise number of discretisation parameters, e.g. collocation points. Large number of state variables prohibits simulation of large computational domains on modern CPUs;
- Define a variable functional basis, that depends significantly on initial and boundary conditions, as well as on problem formulation.

Accordingly, in the chapter 2, the state of the art for mathematical description of combustion processes is outlined.

In the following chapter 3 the computational and numerical methods are presented. Firstly, the incremental algorithm for time integration is discussed. Then, a method for solution of stiff parabolic space-time equations, required for the study of ignition problems, is further elaborated. Here a structured functional space refinement in binary tree is introduced, which makes application of spectral methods for stiff

problems possible. Additionally, an algorithm for quasi Gauss elimination presented. This algorithm allows efficient solution of the linear systems for the coefficients of basis functions with only localised updates of the matrix inverse. Finally, the explicit quasi spectral method, which can be seen as high order extension of finite differences method with variable functional basis, is given.

The chapter 4 demonstrates, that the developed method can be applied to other problems without significant efforts. It is shown, that the method can be applied efficiently to the solution of Master Equation of chemical gas kinetics, which is a stiff integro-differential equation. The study of decomposition of 2,3-dihydro-2,5-dimethylfuran-3-yl (25DMF2H) and of mutual isomerisation between allene and propyne allowed to derive corresponding rate constants with high accuracy and significant performance improvement, compared to standard numerical approach.

The chapter 5 is devoted to application of the proposed method to ignition and transient combustion problems. The first step is concerned with an extensive validation of mathematical description of ignition processes and with the validation of proposed integration schemes. Ignition delay times, stationary profiles and flame burning velocities of various hydrogen-air flames are compared with results of other well established codes and with experimental measurements. The hydrogen-air system exhibits extremely high sensitivity to initial parameters, such as temperature and mixture composition. Moreover, grouping of results of physical experiments, according to the method, lead to different estimations of flame burning velocity. A more accurate transient modelling of these experiments, may improve the accuracy.

The main application is focused on ignition and on flame propagation in narrow channels, which is accompanied by versatile effects. On one side, in closed ducts with particular width to length ratios, a counterintuitive flame tip inversion may occur [Ell28, DR09]. On the other side, in open ducts, the flame may accelerate and become turbulent. It is found the hydrodynamic plays the leading role in these phenomena. Particularly interesting, that thermo-chemical state spaces before the flame tip inversion and before onset of the turbulence are identical. Additionally, the flame imposition in micro channels, where the combustion is complicated by the small channel cross-section with radius well below quenching radius, is studied [MPO<sup>+</sup>04]. The numerical results emphasise the importance of multidimensional transport processes, which lead to a significantly better agreement with physical experiments, compared to the previously used simplified model.

Additionally, in chapter 6, the method is applied to ignition and flame acceleration in unconfined settings, which can be modelled, with high reliability, using 1D models. It was reported, that under particular conditions an unconfined premixed flame can undergo spontaneous acceleration after a period of laminar flame propagation [GIS88, KS17b]. The importance of chemical kinetic on flame acceleration from the wall and in “free” propagating regime is thoroughly investigated and a value of critical flame folding ratio is estimated. At this ratio, the flame begins spontaneously accelerating, after a relatively long deflagration regime. The importance of chemical kinetic becomes here obvious, after analysing of the thermo-chemical state space.



## 2. Mathematical model of transient reacting flows

### 2.1. Conservation laws

The continuum conservation equations for mass, momentum, energy and gas components are well known, see e.g. [CM00, Wil88, KCG03, WMD06] for derivation. The idea is based on several coexisting continua (multicomponent), which obey laws of hydrodynamic and thermodynamic. In general the continuum assumption leads to Navier-Stokes equations (NSE), extended by the conservation of energy and gas components. There is a large number of studies supporting correctness of NSE. However, the proof of existence of a general solution is still missing. Moreover, in some extreme case, e.g. intensive turbulence or detonation, the continuum assumption is questioned: the thickness of flame structures may become in the range of several molecules [HCB54, Wil88]. In order to overcome this difficulty, multicomponent flows can be described from the standpoint of dynamic of elementary particles. The direct modelling of such processes is yet possible for micro-scales only and a more realistic application require the knowledge of distribution functions. Applying this functions for averaging the motion of molecules, it has been shown that classical NSE can be derived [Wil88].

Baring in mind limitations of continuum assumption, the Navier-Stockes equations can still provide the most accurate mathematical description of gas dynamics. In the following the conservation equation for general multicomponent reaction flows are presented. The equations are given in the form they implemented in the proposed code.

#### 2.1.1. Mass and momentum conservation

Imagine a particle moving in Euclidean space at time: it can be defined then  $\mathbf{r} = (t, x, y, z)$  as space-time coordinate vector and  $\mathbf{v} = (1, v_x, v_y, v_z)$  as velocity vector of this point. Let  $\Omega$  be a subregion in space at an instance of time  $t$  filled with fluid. For any extensive quantity

$$F(\mathbf{r}) = \int_{\Omega} f_t(\mathbf{r}) dV \quad (2.1)$$

its total change is then described by space-time derivative:

$$\frac{\partial}{\partial t} f_t + \frac{\partial}{\partial x} f_x + \frac{\partial}{\partial y} f_y + \frac{\partial}{\partial z} f_z = q \quad (2.2)$$

or in vector notation:

$$\nabla \cdot \mathbf{f} = q \quad (2.3)$$

where  $\mathbf{f} = (f_t, f_x, f_y, f_z)$  is a vector, describing flux through surface of the control volume  $\Omega$  and  $q = q(\mathbf{r})$  is a source term (s. Fig. 2.1).

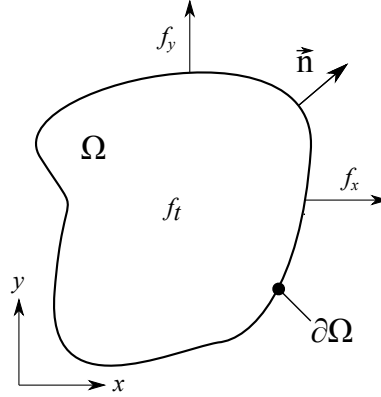


**Figure 2.1.:** Change of an extensive quantity in control volume (in 2D)

For the conservation of mass, it is assumed that there exists mass density  $\rho$  such that:

$$m(\mathbf{r}) = \int_{\Omega} \rho(\mathbf{r}) dV. \quad (2.4)$$

and this function is smooth enough (continuity assumption). Considering the molecular structure of gases, it is obviously not true, but on macroscopic scale it appears to be very accurate.

An additional assumption is that the mass is neither created or destroyed. Mass conservation in general form Eq. (2.2) can be now written as (see e.g. [CM00]):

$$\frac{\partial}{\partial t} \rho + \frac{\partial}{\partial x} v_x \rho + \frac{\partial}{\partial y} v_y \rho + \frac{\partial}{\partial z} v_z \rho = 0 \quad (2.5)$$

By the construction of the conservation equation for momentum, the following has to be considered:

- the pressure  $P$  on the surface  $\partial\Omega$  of the control volume in space,
- dissipative (viscous) forces  $\mathbf{T}$ ,
- potential forces (gravity)  $\rho \mathbf{g} = \rho(0, g_x, g_y, g_z)$ .

The general conservation equation (2.2) for momentum takes the following form (see e.g. [CM00]):

$$\frac{\partial}{\partial t} (\rho v_x) + \frac{\partial}{\partial x} (\rho v_x^2 + \sigma + \tau_{xx}) + \frac{\partial}{\partial y} (\rho v_x v_y + \tau_{xy}) + \frac{\partial}{\partial z} (\rho v_x v_z + \tau_{xz}) = \rho g_x \quad (2.6)$$

$$\frac{\partial}{\partial t}(\rho v_y) + \frac{\partial}{\partial x}(\rho v_y v_x + \tau_{yx}) + \frac{\partial}{\partial y}(\rho v_y^2 + \sigma + \tau_{yy}) + \frac{\partial}{\partial z}(\rho v_y v_z + \tau_{yz}) = \rho g_y \quad (2.7)$$

$$\frac{\partial}{\partial t}(\rho v_z) + \frac{\partial}{\partial x}(\rho v_z v_x + \tau_{zx}) + \frac{\partial}{\partial y}(\rho v_z v_y + \tau_{zy}) + \frac{\partial}{\partial z}(\rho v_z^2 + \sigma + \tau_{zz}) = \rho g_z \quad (2.8)$$

where

$$\sigma = P + \frac{2}{3}\mu \left( \frac{\partial v_x}{\partial x} + \frac{\partial v_y}{\partial y} + \frac{\partial v_z}{\partial z} \right) \quad (2.9)$$

is scalar component of the stress tensor.  $P$  is thermodynamic pressure and  $\mu$  is coefficient of dynamic viscosity. The non-scalar components of the shear-stress tensor are defined as:

$$\begin{aligned} \tau_{xx} &= -2\mu \frac{\partial v_x}{\partial x}, \\ \tau_{yy} &= -2\mu \frac{\partial v_y}{\partial y}, \\ \tau_{zz} &= -2\mu \frac{\partial v_z}{\partial z}, \\ \tau_{xy} = \tau_{yx} &= -\mu \left( \frac{\partial v_x}{\partial y} + \frac{\partial v_y}{\partial x} \right), \\ \tau_{yz} = \tau_{zy} &= -\mu \left( \frac{\partial v_y}{\partial z} + \frac{\partial v_z}{\partial y} \right), \\ \tau_{zx} = \tau_{xz} &= -\mu \left( \frac{\partial v_z}{\partial x} + \frac{\partial v_x}{\partial z} \right). \end{aligned} \quad (2.10)$$

Let us define space-time stress tensor as

$$\mathbf{T} = \begin{pmatrix} 0 & 0 & 0 & 0 \\ 0 & \sigma + \tau_{xx} & \tau_{xy} & \tau_{xz} \\ 0 & \tau_{yx} & \sigma + \tau_{yy} & \tau_{yz} \\ 0 & \tau_{zx} & \tau_{zy} & \sigma + \tau_{zz} \end{pmatrix}. \quad (2.11)$$

Then mass conservation Eq. (2.5) and momentum conservation eq. (2.6 - 2.8) can be rewritten in a joined vector form:

$$\nabla \cdot (\rho \mathbf{v} \otimes \mathbf{v} + \mathbf{T}) = \rho \mathbf{g}, \quad (2.12)$$

where

$$\nabla = \left( \frac{\partial}{\partial t}, \frac{\partial}{\partial x}, \frac{\partial}{\partial y}, \frac{\partial}{\partial z} \right) \quad (2.13)$$

is space-time gradient operator.

### 2.1.2. Species conservation

Typical reacting flow consists of several components, i.e. fuel, oxidiser, products and intermediates. The total mass of mixture is thus the sum of over all components  $m = \sum m_i$ , where  $m_i$  is the mass of component  $i$ . The same can be applied for the mole number:  $n = \sum n_i$ , where  $n_i$  mole number of the component  $i$ . The it is not difficult to show that the following expressions hold (see e.g. [WMD06]):

- density

$$\rho = \sum_i \rho_i = \sum_i M_i c_i, \quad (2.14)$$

- concentration

$$c = \sum_i c_i = \sum_i \frac{\rho_i}{M_i}, \quad (2.15)$$

- mass fraction

$$Y_i = \frac{\rho_i}{\rho} = \frac{X_i M_i}{M}, \quad (2.16)$$

- mole fraction

$$X_i = \frac{c_i}{c} = \frac{Y_i M}{M_i}, \quad (2.17)$$

- mean molar mass

$$M = \frac{\rho}{c} = \sum_i X_i M_i = \frac{1}{\sum_i Y_i / M_i}, \quad (2.18)$$

- specific mole number

$$\phi_i = \frac{c_i}{\rho} = \frac{Y_i}{M_i}. \quad (2.19)$$

If each component  $i$  moves its own velocity  $\mathbf{v}_i$  and has a molar production/destruction rate  $\omega_i$  then holds the following expression (see e.g. [WMD06]):

$$\frac{\partial}{\partial t} (c_i) + \frac{\partial}{\partial x} (v_{i,x} c_i) + \frac{\partial}{\partial y} (v_{i,y} c_i) + \frac{\partial}{\partial z} (v_{i,z} c_i) = \omega_i. \quad (2.20)$$

For practical consideration it is common to define species velocity relative to the velocity of the mass centre  $\mathbf{v}$ :

$$\mathbf{v}_i = \mathbf{v} + \mathbf{V}_i, \quad (2.21)$$

where  $\mathbf{V}_i = (0, V_{i,x}, V_{i,y}, V_{i,z})$  is diffusion velocity of the component  $i$ . Combining Eq. (2.20) and (2.21), the conservation equation of a component  $i$  is derived:

$$\frac{\partial}{\partial t} (c_i) + \frac{\partial}{\partial x} (v_x c_i + \bar{\mathbf{j}}_{i,x}) + \frac{\partial}{\partial y} (v_y c_i + \bar{\mathbf{j}}_{i,y}) + \frac{\partial}{\partial z} (v_z c_i + \bar{\mathbf{j}}_{i,z}) = \omega_i, \quad (2.22)$$

or in vector notation

$$\nabla \cdot (c_i \mathbf{v} + \bar{\mathbf{j}}_i) = \dot{\omega}_i, \quad (2.23)$$

where  $\bar{\mathbf{j}}_i = c_i \mathbf{V}_i$  is known as diffusive mole flux of species  $i$ . It is instructive to construct an alternative formulation of the conservation equation (2.22) and (2.23) for mass fraction, which is commonly used (see e.g. [Wil88, WMD06]):

$$\nabla \cdot (\rho Y_i \mathbf{v} + \mathbf{j}_i) = M_i \dot{\omega}_i, \quad (2.24)$$

where  $\mathbf{j}_i = M_i \bar{\mathbf{j}}_i$  is diffusive mass flux of species  $i$ . Following the definition of diffusion velocity, the mass transport of some species in one direction must be balanced by transport of other species in the other direction. For this reason it is generally true that [WMD06]:

$$\sum_i \mathbf{j}_i = 0. \quad (2.25)$$

### 2.1.3. Energy conservation

The conservation of energy can be derived using the following considerations and the continuity assumption:

- total energy consists of internal, kinetic and potential energy,  $E = U + K + \Pi$ ,
- there exists function  $e$  and  $u$  such that  $E = \int_{\Omega} \rho (e - \mathbf{g} \cdot \mathbf{r}) dV = \int_{\Omega} \rho (u + \frac{1}{2} \mathbf{v} \cdot \mathbf{v} - \mathbf{g} \cdot \mathbf{r}) dV$
- first law of thermodynamic, stating that the rate of change of stored energy is equal to the heat transferred to the system minus the rate of work done by the system on the surroundings, is valid:  $\frac{dE}{dt} = \frac{dQ}{dt} - \frac{dW}{dt}$  [WMD06],
- the work of pressure and friction forces on the surface of the control volume  $\dot{W}_f = \int_{\partial\Omega} \mathbf{T} \cdot \mathbf{v} dS$ ,
- the heat flux across the surface of the control volume  $\dot{Q} = - \int_{\partial\Omega} \mathbf{q} \cdot \mathbf{n} dS$ .

Here  $\dot{W} = dW/dt$  and  $\dot{Q} = dQ/dt$ . These lead to the general conservation equation for energy:

$$\begin{aligned} \frac{\partial}{\partial t} (\rho e) + \frac{\partial}{\partial x} (v_x (\rho e + \sigma + \tau_{xx}) + v_y \tau_{xy} + v_z \tau_{xz} + q_x) \\ + \frac{\partial}{\partial y} (v_x \tau_{yx} + v_y (\rho e + \sigma + \tau_{yy}) + v_z \tau_{yz} + q_y) \\ + \frac{\partial}{\partial z} (v_x \tau_{zx} + v_y \tau_{zy} + v_z (\rho e + \sigma + \tau_{zz}) + q_z) \\ = \rho (g_x v_x + g_y v_y + g_z v_z). \end{aligned} \quad (2.26)$$

In vector notation the Eq. (2.26) takes form:

$$\nabla \cdot (\rho e \mathbf{v} + \mathbf{T} \cdot \mathbf{v} + \mathbf{q}) = \rho \mathbf{g} \cdot \mathbf{v}. \quad (2.27)$$

The specific energy is usually computed by introducing a function called enthalpy,  $\rho h = \rho u + P$ :

$$\rho e = \rho \left( h + \frac{1}{2} \mathbf{v} \cdot \mathbf{v} \right) - P, \quad (2.28)$$

with

$$\rho h = \sum_i \rho_i h_i = \sum_i c_i \bar{h}_i, \quad (2.29)$$

where  $h_i$  is specific enthalpy and  $\bar{h}_i$  is the molar enthalpy of species  $i$ . The use of eq. (2.28) is particularly motivated for low speed flows, where pressure variations are small and can be neglected [KCG03].

The heat flux  $\mathbf{q} = (0, q_x, q_y, q_z) = \mathbf{q}^c + \mathbf{q}^r + \mathbf{q}^s + \mathbf{q}^d$  is commonly attributed to:

- heat conductivity (Fourier's law),  $\mathbf{q}^c = -\lambda (\partial T / \partial x, \partial T / \partial y, \partial T / \partial z)$ ,
- heat flux with species diffusion. Each species carries energy as it diffuses across the control surface  $\mathbf{q}^s = \sum h_i \mathbf{j}_i = \sum \bar{h}_i \bar{\mathbf{j}}_i$ ,

- heat radiation  $\mathbf{q}^r$  and Dufour effect  $\mathbf{q}^d$  and are commonly neglected [KCG03, Wil88]. There are a number of problems where the heat radiation cannot be neglected, particularly when absorption and scattering is large.

## 2.2. Thermodynamic gas properties

### 2.2.1. Thermodynamic properties of monomolecular gas

In the conservation equation (2.27) and in following section on gas kinetics important thermodynamic properties are specific molar enthalpy, entropy and heat capacity. There are large experimental data available for these properties, i.e. the NIST-JANAF Thermochemical Tables<sup>1</sup> are a good starting point. Typically the data are stored in form of NASA polynomials [nasa93] which simplifies the calculation:

specific molar heat capacity:

$$\bar{c}_p(T) = R \sum_{i=0}^4 a_i T^i, \quad (2.30)$$

specific molar enthalpy:

$$\bar{h}(T) = \bar{h}(T_0) + \int_{T_0}^T \bar{c}_p(T) dT = R \left( b_0 + \sum_{i=0}^4 \frac{1}{i+1} a_i T^{i+1} \right) \quad (2.31)$$

specific molar entropy:

$$\bar{s}(T) = \bar{s}(T_0) + \int_{T_0}^T \frac{\bar{c}_p(T)}{T} dT = R \left( b_1 + a_0 \ln(T) + \sum_{i=1}^4 \frac{1}{i} a_i T^i \right) \quad (2.32)$$

here  $T_0$  is standard temperature at 298.15 K.

With units for ideal gas constant  $R$  (J/mol/K), the units of specific molar heat capacity  $\bar{c}_p$  are also (J/mol/K), of specific molar enthalpy  $\bar{h}$  are (J/mol) and of specific molar entropy  $\bar{s}$  are (J/mol/K)

For moderate pressures (below 10 bar), the ideal gas equation of state provides a good approximation of real gas behaviour (deviation is below 5%) [ADP06]:

$$P = cRT. \quad (2.33)$$

### 2.2.2. Viscosity of monomolecular gas

The dynamic viscosity of pure monomolecular gas is derived from kinetic theory [HCB54, KCG03]:

$$\mu_i = \frac{5\sqrt{\pi m_i k_B T}}{16\pi \sigma_i^2 \Omega_{ii}^{(2,2)*}} = \frac{5\sqrt{\pi M_i R_0 T}}{16\pi N_A \sigma_i^2 \Omega_{ii}^{(2,2)*}}, \quad (2.34)$$

<sup>1</sup><http://kinetics.nist.gov/janaf/>

where  $\sigma_i$  is the collision diameter,  $m_i$  is the mass of the molecule  $i$ ,  $k_B$  is Boltzmann constant,  $N_A$  is Avogadro's number,  $M_i$  is molar mass,  $T$  is temperature and  $\Omega_{ii}^{(2,2)*} = \Omega_{ii}^{(2,2)*}(T^*, \tilde{\delta}_{ij}^*)$  is collision integral, which is a function of reduced temperature:

$$T_{ii}^* = \frac{T}{\epsilon_i/k_B} \quad (2.35)$$

and reduced dipole moment [KCG03]:

$$\tilde{\delta}_i^* = \frac{(\bar{\mu}_i)^2}{2\epsilon_i\sigma_i^3}. \quad (2.36)$$

Using units for molar mass  $M_i$  (g/mol), for collision diameter  $\sigma_i$  (Å), a simplified expression for dynamic viscosity of a pure gas can be derived:

$$\mu_i \left[ \frac{\text{kg}}{\text{m} \cdot \text{s}} \right] = 2.6696 \times 10^{-6} \frac{\sqrt{M_i T}}{\sigma_i^2 \Omega_{ii}^{(2,2)*}} \quad (2.37)$$

The depth of the well of LJ potential is normally provided weighted with inverse Boltzmann's constant  $\epsilon_i/k_B$  (K) and dipole moment has typically units  $\bar{\mu}$  (Debye). In the given units the expression for the reduced dipole moment eq. (2.55) takes form:

$$\tilde{\delta}_i^* = 3621.5 \frac{\bar{\mu}_i^2}{(\epsilon/k_B)\sigma_i^3} \quad (2.38)$$

The depth of the well of LJ potential  $\epsilon$  and collision diameter  $\sigma$  are constant gas properties, which can be found e.g in [sve].

### 2.2.3. Heat conductivity of monomolecular gas

Heat conductivity is assumed to consist of translational, rotational and vibrational contributions [Warnatz82, Kee, §12.5.2]. It is computed traditionally in form of Eucken factor for viscosity:

$$\lambda_i = \frac{\mu_i}{M} (f_{tra} c_{v,tra} + f_{rot} c_{c,rot} + f_{vib} c_{c,vib}), \quad (2.39)$$

where

$$f_{tra} = \frac{5}{2} \left( 1 - \frac{2c_{c,rot}A}{\pi c_{v,tra}B} \right), \quad (2.40)$$

$$f_{rot} = \frac{\rho \mathcal{D}_{ii}}{\mu_i} \left( 1 + \frac{2A}{\pi B} \right), \quad (2.41)$$

$$f_{vib} = \frac{\rho \mathcal{D}_{ii}}{\mu_i}, \quad (2.42)$$

with

$$A = \frac{5}{2} - \frac{\rho \mathcal{D}_{ii}}{\mu_i}, \quad (2.43)$$

$$B = Z_{rot} + \frac{2}{\pi} \left( \frac{5c_{v,rot}}{R} + \frac{\rho \mathcal{D}_{ii}}{\mu_i} \right), \quad (2.44)$$

The rotational relaxation number is assumed to be known at  $T = 298K$ ,  $Z_{rot}(298) = Z_{rot}^0$  and its temperature dependance is computed from [Kee, §12.5.2]:

$$Z_{rot} = Z_{rot}^0 \frac{F(298)}{F(T)}, \quad (2.45)$$

with

$$F(T) = 1 + \frac{\pi^{3/2}}{2} \left( \frac{\epsilon/k_B}{T} \right)^{1/2} + \left( \frac{\pi^2}{4} + 2 \right) \left( \frac{\epsilon/k_B}{T} \right) + \pi^{3/2} \left( \frac{\epsilon/k_B}{T} \right)^{3/2}. \quad (2.46)$$

The required self-diffusion coefficient is derived from [HCB54]:

$$\mathcal{D}_{ii} = \frac{3\sqrt{\pi k_B^3 T^3 / m_i}}{8P\pi\sigma_i^2\Omega_{ii}^{(1,1)*}} \quad (2.47)$$

or in units for molar mass  $M_i$  (g/mol), Temperature  $T$  (K), collision diameter  $\sigma_i$  (Å) and pressure  $P$  (Pa) <sup>2</sup>:

$$\mathcal{D}_{ii} \left[ \frac{\text{m}^2}{\text{s}} \right] = 26.635 \times 10^{-3} \frac{\sqrt{T^3/M_i}}{P\sigma_i^2\Omega_{ii}^{(1,1)*}}. \quad (2.48)$$

The rotational  $c_{v,rot}$  and translational  $c_{v,tra}$  are assumed to be constant species properties, which are defined as:

$$c_{v,rot} = \begin{cases} 0, & \text{if single atom} \\ R_0, & \text{if linear molecule} \\ \frac{3}{2}R_0, & \text{if nonlinear or polyatomic molecule} \end{cases} \quad (2.49)$$

$$c_{v,tra} = \frac{3}{2}R_0. \quad (2.50)$$

The vibrational heat capacity  $c_{v,vib}$  is calculated from total heat capacity  $c_v$ :

$$c_{v,vib} = c_v - c_{v,tra} - c_{v,rot}. \quad (2.51)$$

With units for specific heat capacity  $c$  (J/mol), viscosity  $\mu$  (m<sup>2</sup>/s) and molar mass  $M$  (g/mol) the heat conductivity equals:

$$\lambda_i \left[ \frac{\text{W}}{\text{m} \cdot \text{K}} \right] = 1000 \frac{\mu_i}{M} (f_{tra}c_{v,tra} + f_{rot}c_{v,rot} + f_{vib}c_{v,vib}). \quad (2.52)$$

<sup>2</sup>Expression  $\rho\mathcal{D}_{ii}$  in (2.42) can be further simplified using ideal gas law  $P = \rho R_0 T / M_i$

### 2.2.4. Binary diffusion coefficients

In a low-density limit the binary diffusion coefficient between two gaseous species may be determined from kinetic theory as [HCB54]:

$$\mathcal{D}_{ij} = \frac{3\sqrt{2\pi k_B^3 T^3/m_{ij}}}{16\pi P \sigma_{ij}^2 \Omega_{ij}^{(1,1)*}} \quad (2.53)$$

here  $\Omega_{ij}^{(1,1)*} = \Omega_{ij}^{(1,1)*}(T_{ij}^*, \tilde{\delta}_{ij}^*)$  is collision integral as a function of reduced temperature

$$T_{ij}^* = \frac{T}{\epsilon_{ij}/k_B}, \quad (2.54)$$

and reduced dipole moment

$$\tilde{\delta}_{ij}^* = \frac{\bar{\mu}_i \bar{\mu}_j}{2\epsilon_{ij} \sigma_{ij}^3}. \quad (2.55)$$

The reduced mass is defined as:

$$m_{ij} = \frac{m_i m_j}{m_i + m_j} \quad (2.56)$$

The combined collision diameter  $\sigma_{ij}$  and the depth of potential well  $\epsilon_{ij}$  depend on the type of interacting molecules:

$$\sigma_{ij} = \frac{1}{2}(\sigma_i + \sigma_j)\xi^{-1/6}, \quad (2.57)$$

$$\epsilon_{ij} = \xi^2 \sqrt{\epsilon_i \epsilon_j} \quad (2.58)$$

where  $\xi$  is a parameter describing interaction type [HCB54]:

$$\xi = \begin{cases} 1, & \text{if both polar or both nonpolar} \\ 1 + \frac{\alpha_i}{4\sigma_i^3} \frac{\bar{\mu}_j^2}{\epsilon_j \sigma_j^3} \sqrt{\frac{\epsilon_j}{\epsilon_i}}, & \text{if } i \text{ nonpolar and } j \text{ polar} \\ 1 + \frac{\alpha_j}{4\sigma_j^3} \frac{\bar{\mu}_i^2}{\epsilon_i \sigma_i^3} \sqrt{\frac{\epsilon_i}{\epsilon_j}}, & \text{if } i \text{ polar and } j \text{ nonpolar} \end{cases} \quad (2.59)$$

With typical units for temperature  $T$  (K), molar mass  $M_i$  (g/mol), pressure  $P$  (Pa) and collision diameter  $\sigma_i$  (Å), polarizability  $\alpha_i$  (Å<sup>3</sup>), dipole moment  $\bar{\mu}_i$  (Debye), also taking into account that depth of the potential well is provided normed with Boltzmann's constant  $\epsilon_i/k_B$  (K) and that  $\xi$  is dimensionless parameter, one can get a more practical expressions:

$$\mathcal{D}_{ij} \left[ \frac{\text{m}^2}{\text{s}} \right] = 18.834^{-3} \frac{\sqrt{T^3/M_{ij}}}{P \sigma_{ij}^2 \Omega_{ij}^{(1,1)*}}, \quad (2.60)$$

$$\tilde{\delta}_{ij}^* = 3621.5 \frac{\bar{\mu}_i \bar{\mu}_j}{(\epsilon_{ij}/k_B) \sigma_{ij}^3}, \quad (2.61)$$

$$\xi = \begin{cases} 1, & \text{if both polar or both nonpolar} \\ 1 + 1810.74 \frac{\alpha_i}{\sigma_i^3} \frac{\bar{\mu}_j^2}{(\epsilon_j/k_B) \sigma_j^3} \sqrt{\frac{(\epsilon_j/k_B)}{\epsilon_i/k_B}}, & \text{if } i \text{ nonpolar and } j \text{ polar} \\ 1 + 1810.74 \frac{\alpha_j}{\sigma_j^3} \frac{\bar{\mu}_i^2}{(\epsilon_i/k_B) \sigma_i^3} \sqrt{\frac{(\epsilon_i/k_B)}{\epsilon_j/k_B}}, & \text{if } i \text{ polar and } j \text{ nonpolar} \end{cases} \quad (2.62)$$

here  $M_{ij} = M_i M_j / (M_i + M_j)$  is reduced molar mass.

### 2.2.5. Collision integrals

Collision integrals  $\Omega_{ij}^{(1,1)*}$  and  $\Omega_{ij}^{(2,2)*}$  are typically given as a function of reduced temperature  $T_{ij}^*$  and reduced dipole moment  $\tilde{\delta}_{ij}^*$ . Tabulated values can be found in [MM61] or for nonpolar interactions  $\tilde{\delta}_{ij}^* = 0$  in [HCB54]. Expressions below provide a reasonable approximation of these tables [KCG03]:

$$\Omega_{ij}^{(1,1)*} \approx \left( a_1 T^{*-a_2} + (T^* + a_3)^{-a_4} \right) f^{(1,1)}, \quad (2.63)$$

where the adjustment factor  $f^{(1,1)}$  represents the approximation of Stockmayer potential between polar molecules and is given as:

$$f^{(1,1)} = 1 + \frac{\left( \exp(a_5/T^*) - \exp(-a_6/T^*) \right) \left( \tilde{\delta}_{ij}^* \right)^2}{2 + 2.5\tilde{\delta}_{ij}^*} \quad (2.64)$$

and similarly for the second integral:

$$\Omega_{ij}^{(2,2)*} \approx \left( b_1 T^{*-b_2} + (T^* + b_3)^{-b_4} \right) f^{(2,2)}, \quad (2.65)$$

with the adjustment factor for Stockmayer potential between polar molecules given as:

$$f^{(2,2)} = 1 + \frac{\left( \exp(b_5/T^*) - \exp(-b_6/T^*) \right) \left( \tilde{\delta}_{ij}^* \right)^2}{2 + 2.5\tilde{\delta}_{ij}^*}. \quad (2.66)$$

The coefficients in expressions (2.63) through (2.66) are given in Table 2.1.

$j$	1	2	3	4	5	6
$a_j$	1.0548	0.15504	0.55909	2.1705	0.093193	1.5
$b_j$	1.0413	0.11930	0.43628	1.6041	0.095661	2.0

**Table 2.1.:** Coefficients for fits of  $\Omega^{(1,1)*}$  and  $\Omega^{(2,2)*}$

### 2.2.6. Multi-component gas properties

Accurate first order approximation of integral transport properties of a mixture from Chapman-Enskog theory requires an inverse of  $3n_S \times 3n_S$  matrix [HCB54, ADP06] for each computational point, where  $n_S$  is number of species. This procedure is computationally prohibitive for real combustion systems. Semiempirical mixture-average formulæ provide a reasonable accuracy with significantly lower computational expenses compared to the approach from Chapman-Enskog theory.

Dynamic viscosity of gas mixture [BSL07]

$$\mu = \sum_i \frac{X_i \mu_i}{\sum_j X_j \Phi_{ij}}, \quad (2.67)$$



where

$$L_{ij}^{00,00} = \frac{16T}{25P} \sum_{k=1}^{n_S} \frac{X_k}{M_i \mathcal{D}_{ik} \left( M_j X_j (1 - \delta_{ik}) - M_i X_i (\delta_{ij} - \delta_{jk}) \right)}. \quad (2.76)$$

the exact expression for other  $L^{xx,xx}$  is quite cumbersome and is not required for current work. They can be still found in [HCB54, KCG03]. The solution of the  $L$ -Matrix equation (2.75) leads to the complete set of multicomponent gas properties:

- Multicomponent diffusion coefficients, according to eq. (2.74):

$$D_{ij} = \frac{16T}{25P} (A_{ii} - A_{ij}), \quad (2.77)$$

where  $A = (L^{00,00})^{-1}$ ;

- Heat conductivity

$$\lambda_i = -4 \sum_{j=1}^{n_S} X_j (a_{i,10}^1 + a_{i,01}^1); \quad (2.78)$$

- Thermal diffusion coefficients

$$D_i^T = \frac{8M_i X_i}{5R} a_{i,00}^1. \quad (2.79)$$

Both Stefan-Maxwell and  $L$ -Matrix equations are computationally demanding. A faster approach (mixture-average) with a reasonable loss of accuracy can be derived from Stefan-Maxwell equation using a number of simplifications [WMD06, KCG03]:

$$\mathbf{j}_{x,j}^* = -\rho Y_i D_i^* \frac{\partial X_i}{\partial x}, \quad (2.80)$$

with diffusion coefficient:

$$D_i^* = \frac{1}{X_i} \frac{1 - Y_i}{\sum_{j \neq i} X_j / \mathcal{D}_{ij}} = \frac{M_i}{Y_i M} \frac{1 - Y_i}{\sum_{j \neq i} X_j / \mathcal{D}_{ij}}. \quad (2.81)$$

Unfortunately, the expression (2.80) cannot guarantee the mass conservation Eq. (2.25). For this reason two correction schemes can be applied [WMD06]:

- Fix flux of a species in excess (assume it is the last species), e.g. nitrogen, with

$$\mathbf{j}_{x,N} = - \sum_{j=1}^{N-1} \mathbf{j}_{x,j} \quad (2.82)$$

- Adjust all fluxes with

$$\mathbf{j}_{x,i} = \mathbf{j}_{x,i}^* - Y_i \sum_{j=1}^N \mathbf{j}_{x,j}. \quad (2.83)$$

If the computation is performed with concentrations (see eq. (2.23)), with the molar flux defined as:

$$\bar{j}_{x,i} = -D_{ij}^c \frac{\partial c_j}{\partial x} \quad (2.84)$$

it is easy to show that the diffusion coefficients  $D_i^*$  in equations (2.25) and (2.81) are related to  $D_{ij}^c$  through the following expressions

- Fixing flux for a species in excess (last species), eq. (2.82):

$$D_{ij}^c = X_i \left[ (1 - \delta_{iN}) (\delta_{ij} - X_i) D_i^* - \frac{\delta_{iN}}{Y_i} \left( Y_N D_N^* - \sum_k Y_k D_k X_k \right) \right] \quad (2.85)$$

- Adjusting all fluxes with mass fractions eq. (2.83):

$$D_{ij}^c = X_i \left[ (\delta_{ij} - X_i - Y_i) D_i^* + \sum_k Y_k D_k^* X_k \right], \quad (2.86)$$

where  $\delta_{ij}$  is Dirac-function, which is equal zero for  $i \neq j$  and is equal one for  $i = j$ .

In the same manner, if the computation concerns the mass fractions (s. eq. (2.24)), where the mass diffusion flux is defined as:

$$j_{x,i} = -D_{ij}^m \frac{\partial Y_j}{\partial x} \quad (2.87)$$

it is also straightforward to show the relation between mixture average diffusion coefficients  $D_{ij}^*$  and mass diffusion coefficients  $D_{ij}^m$ ,

- Fixing flux for a species in excess (last species):

$$D_{ij}^m = M \rho Y_i \left[ \frac{1 - \delta_{iN}}{M_i} \left( \delta_{ij} - Y_i \frac{M}{M_j} \right) D_i^* - \frac{\delta_{iN}}{Y_i M_N} \left( Y_N D_N^* - M \sum_{k=1}^{N-1} Y_k D_k^* \frac{Y_k}{M_k} \right) \right] \quad (2.88)$$

- Adjusting all fluxes with mass fractions eq. (2.83):

$$D_{ij}^m = M \rho Y_i \left[ \frac{1}{M_i} \left( \delta_{ij} - \frac{Y_i}{M_j} (M + M_i) \right) D_i^* + \frac{M}{M_j} \sum_k Y_k D_k^* \frac{Y_k}{M_k} \right]. \quad (2.89)$$

Chemical mechanism are normally equipped with the transport data, which provide information for each reactant  $i$  on:

- Type of molecule: atom, linear or non-linear molecule;
- Depth of the potential well  $\epsilon_i/k_B$ , K;
- Collision diameter  $\sigma_i$ , Å;
- Dipole moment,  $\bar{\mu}_i$ , Debye;
- Polarisability,  $\alpha_i$ , Å<sup>3</sup>;

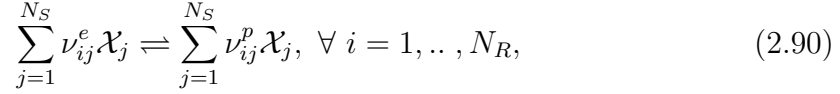
- Rotation relaxation number at standard temperature,  $Z_{rot}(298)$ .

In computation for each system state  $(T, c_0, \dots, c_N)$ , pure gas properties are computed: viscosity  $\mu_i$ , heat conductivity  $\lambda_i$  and binary diffusion coefficients  $D_{ij}$ . Then these properties are combined, using either simplified mixture average rules or using detailed approach through the solution of Stefan-Maxwell equation or  $L$ -Matrix equation.

## 2.3. Chemical reactions

### 2.3.1. Forward elementary reactions

From the view of chemical kinetics a global chemical reaction is viewed as an ensemble of elementary reactions. In general, a typical elementary reaction can be written in the following form [WMD06, KCG03]:



here stoichiometric coefficients  $\nu_{ij}$  are integral numbers and  $\mathcal{X}_j$  is chemical symbol of species  $j$ ,  $N_S$  is the number of species and  $N_R$  is the total number of elementary reactions. The superscript of stoichiometric coefficients:  $e$  is for educts and  $p$  – for products.

Assuming that the reaction rate is proportional to the collision rate between reactants and taking into account that the collision rate is proportional to reactant concentrations, the phenomenological mass action law is formulated. This law states that the rate of production/consumption is proportional to the product of concentrations of reactants [Wil88]:

$$\dot{\omega}_l = \sum_{j=1}^{N_R} \nu_{jl} \left( k_j^f \prod_{i=1}^{N_S} c_i^{\nu_{ji}^e} - k_j^b \prod_{i=1}^{N_S} c_i^{\nu_{ji}^p} \right), \quad (2.91)$$

where  $c_i$  is the concentration of species  $i$ ,  $k_j$  is the rate constant of the reaction  $j$ , with superscript  $f$  – for forwards and  $b$  – for backwards, and

$$\nu_{jl} = \nu_{jl}^p - \nu_{jl}^e. \quad (2.92)$$

It has been found experimentally that forward rate constants  $k^f$  follow for the most elementary reactions the Arrhenius temperature dependence [ADP06]:

$$k_i^f \left[ \frac{1}{\text{s}} \cdot \left( \frac{\text{m}^3}{\text{mol}} \right)^{n-1} \right] = A_i T^{\beta_i} \exp \left( -\frac{E_i}{RT} \right) \quad (2.93)$$

where the pre-exponential factor  $A_i$ , with units  $(\text{m}^3/\text{mol})^{n-1}/\text{s}/\text{K}^\beta$ , the temperature exponent  $\beta_i$  and the activation energy  $E_i$ , in Joule, are specified. Rate constant and pre-exponential factor have different units depending on reaction order  $n = \sum_j \nu_{ij}^e$ .

If in third-bodies are involved in reaction  $i$  the production rate for this reaction is multiplied by an efficient third-body concentration:

$$[M]_i = \sum_{j=1}^{N_S} \alpha_{ij} c_j, \quad (2.94)$$

where  $\alpha_{ij}$  is enhanced third-body collision efficiency of reactant  $j$  in reaction  $i$ . If not specified, the collision efficiency is assumed unity  $\alpha_{ij} = 1$ .

### 2.3.2. Reverse elementary reactions

Assuming that the equilibrium between forward and reverse reactions is reached faster than other processes in the system, it is common to give the parameters of forward rate constants  $k_i^f$  for eq. (2.93) and to compute the rate of the reverse reaction  $k_i^b$  from thermodynamic equilibrium [WMD06, KCG03]. Taking into account that uncertainties in estimation of rate constants often exceeding a factor of 10, and the equilibrium constant can be computed very accurately from thermodynamic properties (as outlined below), the equilibrium assumption is believed to be appropriate [Wil88].

The equilibrium constant in concentration units is defined as:

$$K_i^c = \frac{k_i^f}{k_i^b}, \quad (2.95)$$

which is related to equilibrium constant in pressure units  $K_i^p$  via:

$$K_i^c = K_i^p \left( \frac{P^0}{RT} \right)^{\nu_i}, \quad (2.96)$$

where  $P^0 = 10^5$  Pa is standard-state pressure,  $R = 8.3144598$  J/K/mol – ideal gas constant,  $T$  – temperature and

$$\nu_i = \sum_{j=1}^{N_s} \nu_{ij}. \quad (2.97)$$

The equilibrium constant  $K_i^P$  is derived from the change in Gibbs free energy during the reaction at standard pressure:

$$-RT \ln K_i^P = \Delta G_i^0 = T\Delta S_i^0 - \Delta H_i^0, \quad (2.98)$$

with change of entropy during the reaction:

$$\Delta S_i^0 = \sum_{j=0}^{N_s} \nu_{ij} \bar{s}_i, \quad (2.99)$$

and change of enthalpy during the reaction:

$$\Delta H_i^0 = \sum_{j=0}^{N_s} \nu_{ij} \bar{h}_i, \quad (2.100)$$

here  $\nu_{ij}$  are defined by eq. (2.92), the molar entropy of species  $\bar{s}_i$  is computed with eq. (2.32) and the molar enthalpy  $\bar{h}_i$  of species is calculated with eq. (2.31).

### 2.3.3. Pressure dependent reactions

Many unimolecular reactions show not only temperature but also pressure dependence [GS90]. Here two limits are considered. In the high pressure limit the reaction follows the unimolecular path, e.g.:



and shows only temperature dependence:

$$k_i^\infty \left[ \frac{1}{\text{s}} \right] = A_i^\infty T^{\beta_i^\infty} \exp \left( -\frac{E_i^\infty}{RT} \right), \quad (2.102)$$

with production rate of reactants A and B:

$$\frac{d[A]}{dt} = \frac{d[B]}{dt} = k_i^\infty [C]. \quad (2.103)$$

In the low pressure limit the reaction requires an addition energy from a collision partner, e.g.:



and has also Arrhenius temperature dependence:

$$k_i^0 \left[ \frac{\text{m}^3}{\text{mol} \cdot \text{s}} \right] = A_i^0 T^{\beta_i^0} \exp \left( -\frac{E_i^0}{RT} \right), \quad (2.105)$$

with the production rates:

$$\frac{d[A]}{dt} = \frac{d[B]}{dt} = k_i^0 [C] [M]. \quad (2.106)$$

The reaction rate for the pressure between the limits (fall-off region) is seen as unimolecular (eq. (2.101)) and is approximated as a combination of both limits [KCG03]:

$$k_i^f = k_i^\infty \left( \frac{P_r}{1 + P_r} \right) F, \quad (2.107)$$

with unimolecular production rate for reactant A and B:

$$\frac{d[A]}{dt} = \frac{d[B]}{dt} = k_i^f [C]. \quad (2.108)$$

Here the reduced pressure  $P_r$  is defined as:

$$P_r = \frac{k_i^0 [M]}{k_i^\infty}. \quad (2.109)$$

The concentration of the mixture  $[M]$  is enhanced, where appropriate, with collision efficiencies.

The broadening factor  $F$  has two different forms. In Lindemann approach it is unity  $F = 1$  and in Troe-Formalismus it is defined as [GLT83]:

$$\lg F = \left[ 1 + \left( \frac{\lg P_r + c}{n - d(\lg P_r + c)} \right)^2 \right]^{-1} \lg F_c, \quad (2.110)$$

with constants defined as [GLT83]:

$$c = -0.4 - 0.67 \lg F_c, \quad (2.111)$$

$$n = 0.75 - 1.27 \lg F_c, \quad (2.112)$$

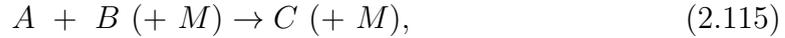
$$d = 0.14 \quad (2.113)$$

and

$$F_c = (1 - \alpha) \exp\left(-\frac{T}{T^{***}}\right) + \alpha \exp\left(-\frac{T}{T^*}\right) + \exp\left(-\frac{T^{**}}{T}\right). \quad (2.114)$$

The type of the model (Lindemann or Troe) and the constant parameters  $\alpha$ ,  $T^{***}$ ,  $T^*$  and  $T^{**}$  must be provided for each reaction.

The same approach applies for reactions of recombination:



with production rate for reactant C:

$$\frac{d[C]}{dt} = k_i^f [A][B]. \quad (2.116)$$

Compare eq. (2.101) and eq. (2.104). In this case the units of  $k_\infty$  are  $\text{m}^3/\text{mol}/\text{s}$  and for  $k_0$  –  $\text{m}^6/\text{mol}^2/\text{s}$ . The reaction rate in the fall-off region is computed also with eq. (2.107).

The computation requires a reaction mechanism, equipped with data for forward and eventually for reverse reactions, which includes:

- Stoichiometric coefficients,  $\nu_{ij}$ ;
- Arrhenius parameters  $A_i$ ,  $\beta_i$ ,  $E_i$ , if no pressure dependency considered;
- Arrhenius parameters for low and high pressure limits  $A_i^0$ ,  $\beta_i^0$ ,  $E_i^0$  and  $A_i^\infty$ ,  $\beta_i^\infty$ ,  $E_i^\infty$ , if reaction is pressure dependent;
- Broadening type and parameters, if pressure dependent: Lindemann-model – no parameters, Troe-Formalismus –  $\alpha$ ,  $T^{***}$ ,  $T^*$  and  $T^{**}$ ;
- Enhanced collision efficiencies  $\alpha_{ij}$  (optional);
- Each reaction must be marked, if the reverse reaction is computed from thermodynamical equilibrium.

# 3. Methodology

## 3.1. Motivation

Analytical solutions for thermo-chemical systems are known only for a few special cases [Wil88, WMD06]. A more general application requires a numerical treatment. However, a numerical approximation of the required governing equations (see §2.1) is still a challenging task. The computation is complicated by [Wil88, OG07]:

- Large time and space scale differences of underlying processes (stiffness), varying from Kolmogorov micrometers to integral scales of several meters;
- Strong dependency of results on system parameters, e.g. rate constants, diffusion coefficients, heat conductivity, etc;
- Large number of state variables and of corresponding participating partial differential equations (PDEs), coming from complex description of reacting systems;
- Strong coupling of hydrodynamical and thermo-chemical processes, leading to a large number of phenomena, e.g. tulip flame, turbulisation, flame instabilities, flame quenching, flame acceleration, etc.

On one side, the stiffness of the problem dictates a large number of discretisation parameters (points) to be used. On the other side, already a large number of state variables, and the capacities of modern computers, enforce a strong limitation on the discretisation [OG07]. Additionally, a complex description of thermo-chemical and of transport processes, impedes the computation considerably. Moreover, very fine spatial discretisation limits the time increment, which make implicit time integration almost indispensable [QSS00]. This in turn leads to the solution of very large linear systems within each time step, which is very time consuming, within standard numerical schemes.

For these reasons, the prevailing number of works, rely on lower order numerical schemes like finite differences and finite volumes [KCG03, OB05, Maa88]. These schemes results in very sparse linear systems, which can be solved efficiently with modern linear algebra algorithms (see e.g. [QSS00]). They tend however, to introduce a relatively high numerical viscosity in the solution, which could be slightly reduced only by utilising extremely fine numerical grids. There are a number of efficient grid adaptation algorithms, which increase grid density locally (see e.g. [OG07]).

However, lower order schemes are still limited to linear growth of accuracy and the numerical viscosity can be only slightly decreased.

The spectral methods provide an alternative numerical approach, based on the ideas of Fourier and Galerkin (see e.g., [Boy89, YS07, LI14]). Here, solution of the system of partial differential equations is represented as a series representation using eigenfunctions in an appropriate functional space. The spectral methods are well known to scientific community but their application is yet rather limited to special problems. In [BM87] a global spectral method was applied to treat 1D reaction-diffusion combustion system. The method rely on a global grid adaptation. There are also reported applications to hydrogen combustion in micro-channel using spectral element method [PFM<sup>+</sup>08, PFM<sup>+</sup>10]. Typically, the projection method is used in order to treat the pressure in the momentum equation avoiding resolution of sound/pressure waves. There is a significant progress made in application of discontinuous Galerkin (DG) for gaseous detonations with the one-step kinetic and Euler equations system [WZSN12]. In [LI14] a shock capturing DG scheme with detailed mechanism of chemical kinetics was presented.

In contrast to the lower order counterparts, the spectral methods have a very low numerical viscosity and require significantly less number of points for the same accuracy [Boy89]. The accuracy of spectral methods grows faster than of any other methods but they become increasingly unstable when under-resolved or used on irregular meshes [MB97]. In order to overcome this difficulty, most schemes use either spectral approximation and low order (e.g. finite differences) for stiff solution behaviour [PCT95], or add a small amount of artificial viscosity to the solution, when the system becomes stiff [YS07].

An alternative approach is to use an adaptive pseudo spectral method suggested in [KYB<sup>+</sup>18, KBKS18]. The main idea of the proposed method is to apply pseudo-spectral method within a particular computational cell with dynamically adaptive mesh generation via a priori user specified error control and by employing matching procedure [Boy89]. The computational domain is automatically split up into a number of sub-domains, while matching the solution  $\mathbf{u}$  and its first derivative, e.g.  $\partial(\mathbf{u})/\partial x$ , at the boundaries. For instance, if the order of polynomial approximation, within each interval, is equal 3, then the method becomes similar to B-Spline collocation method [Joh05].

Such an approach provides the accuracy of spectral methods, required for the study of ignition. The variable polynomial order and adaptive grid of subdomain lead to a very limited number of discretisation parameters even for large physical domains. Using error estimations from the theory of orthogonal polynomial, makes the adaption process generically applicable. A structured localised refinement of the functional space allows not only efficient solution of the resulting linear system but allows also local solution updates.

## 3.2. Spectral methods

The basic idea underlying spectral methods is that a function  $\mathbf{u}(x)$  can be approximated by a weighted, eventually infinite, sum of so-called basis functions  $\varphi_i(x)$

[Boy89]:

$$\mathbf{u}(x) \approx \tilde{\mathbf{u}}(x) = \sum_{i=0}^N \hat{\mathbf{u}}_i \varphi_i(x), \quad (3.1)$$

where  $\tilde{\mathbf{u}}$  is the function approximation and  $\hat{\mathbf{u}}_i$  are scalar weights. As  $N$  approaches infinity the function approximation becomes the function itself:

$$\mathbf{u}(x) = \lim_{N \rightarrow \infty} \sum_{i=0}^N \hat{\mathbf{u}}_i \varphi_i(x). \quad (3.2)$$

When the expression (3.1) is introduced into equation:

$$\mathbf{L}\mathbf{u} = \mathbf{f}(x), \quad (3.3)$$

where  $\mathbf{L}$  is a differential or an integral operator, the purpose of the SM is to find such weights  $\hat{\mathbf{u}}_i$  that the residual

$$R(x, \hat{\mathbf{u}}_0, \hat{\mathbf{u}}_1, \dots) = \mathbf{L}\tilde{\mathbf{u}} - \mathbf{f}(x), \quad (3.4)$$

vanishes.

On one side, if the solution of the PDEs system is relatively smooth with finite curvature, then global spectral methods show geometric convergence rate in solution approximation. On the other side, an insufficient resolution causes aliasing and spectral blocking.

If there are waves  $\hat{u}$  with wave length  $\lambda$  twice of the interval spacing  $\Delta x$

$$\lambda \leq 2\Delta x \quad (3.5)$$

the solution can create aliasing instability (Nyquist–Shannon sampling theorem, [Sha49]). The example of sampling is shown in fig. 3.1. In this case the original signal (black line) with  $\lambda = \frac{1}{5}$  is sampled on  $\Delta\xi = \frac{1}{3}$  (4 collocation points, shown in blue) which leads to a completely wrong approximation (red line). Taking the sampling period to  $\Delta\xi = \frac{1}{5}$  (6 collocation points) would lead to even greater catastrophe, as the signal at this points is zero. Only starting from 11 collocation points, an accurate approximation of the signal can be insured.

If a solution encounters discontinuities, e.g. shock waves. The approximation of discontinuity requires almost unlimited number of spectral coefficients. Consider for example fig. 3.2 (left). The jump in the solution (black line, left) is approximated with Chebyshev polynomials of order  $O(100)$  (red line, left). In this case even the 100th frequency cannot be neglected, fig. 3.2(right). The shock creates waves distributed over a large spectrum, with the smallest wave length smaller than the shock width. According to Nyquist–Shannon theorem (3.5), even a finer grid is required, in order to capture the smallest frequency created by the shock.

If there are dissipation processes in the system with wave length  $\lambda_{dis}$ , then all wave lengths  $\lambda_i > \lambda_{dis}$  will be damped exponentially fast. If the truncated wave length is greater than the dissipation wave length  $\lambda_N < \lambda_{dis}$ , then it will result in high frequency noise accumulation and eventually to “blow-up” of the solution (spectral blocking) [Boy89].

There are two general approaches in order to overcome aliasing and spectral blocking.

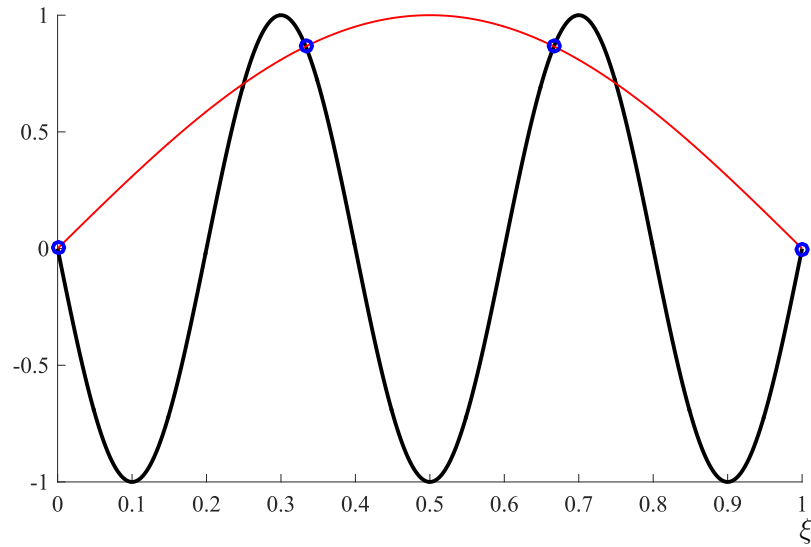


**Figure 3.1.:** Aliasing effect. Black line - original signal, red line - bad sampled signal on 4 collocation points.

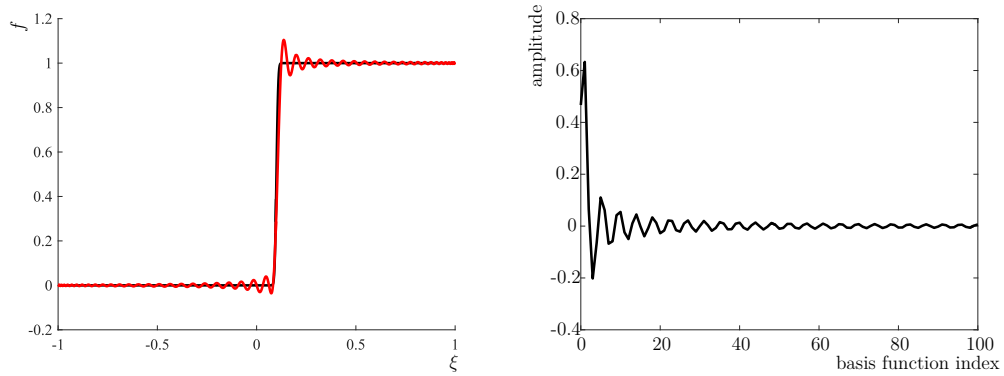


**Figure 3.2.:** Spectral approximation of discontinuity (left) and the corresponding spectral coefficients (right)

- Increase resolution, e.g. locally through grid adaptation;
- Frequencies damping, e.g. introduce filters to equation system.

The first approach assumes that a stiff solution becomes smooth, iff a sufficiently small scale (zoom in) is chosen. In this case a fixed order polynomial (a priori fixed number of basis functions) will be enough to describe the solution with prescribed accuracy. Within such a scale, the series of spectral coefficients for the approximation will rapidly vanish.

Some equations do not have intrinsic dissipation processes, e.g. Euler equation, and in some cases the resolution of the lowest scales is not required, e.g. acoustic waves during laminar flame propagation. In this case the second approach becomes advantageous. However, a simple addition of artificial viscosity to conservation equations leads to rapid accuracy reduction. A better strategy considers only high frequency modes, which makes an underresolved system stable but keep the order of the accuracy nonetheless high.

The time integration of homogeneous system provides a relatively simple illustration of the suggested approach. The application to numerical solution of ordinary differential equations (ODE) is covered by “incremental” method. The approach is then further elaborated to the solution of parabolic partial differential equations (PDE), using adaptive pseudo spectral method and quasi spectral method.

### 3.3. Incremental method for time integration

Spectral approximation of ODEs was, to author’s best knowledge, first introduced by B. Hulme [Hul72]. M. Delfour [DHT81] developed an approach to reduce the error at the discontinuity between polynomial spaces. A. Logg studied a multi-variate method with different polynomial spaces for each variable [Log98, Log03, Log04a, Log04b], which is also capable of solving stiff problems [EJL04].

In this work a study of the applicability of the spectral approximation for the solution of stiff system of ODE is presented. The main component of the proposed approach is the Galerkin weighted residual method which is covered in variety of textbooks like [Boy89]. Only the aspects that are important for the understanding of the suggested approach are summarised. Starting point here is a system of ODEs with suitable initial conditions  $\mathbf{u}_0$ :

$$\begin{cases} \frac{d}{dt} \mathbf{f}(t, \mathbf{u}) = \mathbf{q}(t, \mathbf{u}), & t \in [t_0, T] \\ \mathbf{u}(0) = \mathbf{u}_0 \end{cases}, \quad (3.6)$$

where  $\mathbf{f}, \mathbf{q} : \mathbb{R} \times \mathbb{R}^{n_v} \rightarrow \mathbb{R}^{n_v}$  are given vector functions and  $\mathbf{u} \in \mathbb{R}^{n_v}$  is the solution vector. The approximation of the solution  $\tilde{\mathbf{u}}$  on an interval  $t \in [t_a, t_b]$  is being sought as a weighted sum of  $N$  basis functions:

$$\tilde{\mathbf{u}}(t) = \sum_i^N \hat{\mathbf{u}}_i \varphi_i(t) \quad (3.7)$$

where  $\hat{\mathbf{u}}_i$  are weights of corresponding basis functions  $\varphi_i(t)$ . It is also required that  $\mathbf{u}$  is Lipschitz continuous on the interval  $t \in [t_a, t_b]$ . It is also assumed that the

approximation of functions  $\mathbf{f}$  and  $\mathbf{q}$  belong to the same functional space as the solution  $\mathbf{u}$ .

Both pseudo-spectral and Gauss-Galerkin methods rely on a set of predefined collocation points, which are theoretically determined (see §3.4.2), in this case the projection of approximation in functional space  $\hat{\mathbf{U}}$  to physical space on the collocation points  $\tilde{\mathbf{U}}$  is defined as:

$$\tilde{\mathbf{U}} = \hat{\mathbf{U}} \Phi, \quad (3.8)$$

where  $\Phi_{ij} = \varphi_i(t_j)$ .

Conducting a dot product with  $N$  test functions  $\psi_i(t)$  and applying integration by parts, a weak form of the equation (3.6) is derived<sup>1</sup>:

$$\int_{t_a}^{t_b} \dot{\mathbf{f}} \psi_i dt - \int_{t_a}^{t_b} \mathbf{q} \psi_i dt = \mathbf{R}_i, \quad \forall i = 1, \dots, N \quad (3.9)$$

where  $\dot{(\cdot)} = d(\cdot)/dt$ .

The main idea is to minimise the residual  $\mathbf{R} \rightarrow 0$ . There are two common spectral approaches to solve the system eq. (3.9):

- Collocation method, i.e. test functions are chosen from the space of Dirac functions  $\psi_i = \delta(t - t_i)$ ,
- Gauss-Galerkin method, i.e. test functions are chosen from the space of basis functions  $\psi_i = \varphi_i$ . In some cases an appropriate weight function may also be required.

Note, that by using other types of test and basis functions, finite volumes and finite element methods can be also derived from the eq. (3.9).

In both cases it leads to the following semi-linear system on control points:

$$\mathbf{F}(\mathbf{U}) \mathbf{B} - \mathbf{Q}(\mathbf{U}) \mathbf{A} = \mathbf{R} \quad (3.10)$$

where  $\mathbf{F} = (\mathbf{f}(t_1, \tilde{\mathbf{u}}_1), \mathbf{f}(t_2, \tilde{\mathbf{u}}_2), \dots, \mathbf{f}(t_N, \tilde{\mathbf{u}}_N))$ ,  $\mathbf{Q} = (\mathbf{q}(t_1, \tilde{\mathbf{u}}_1), \mathbf{q}(t_2, \tilde{\mathbf{u}}_2), \dots, \mathbf{q}(t_N, \tilde{\mathbf{u}}_N))$  and  $\mathbf{U} = (\tilde{\mathbf{u}}_1, \tilde{\mathbf{u}}_2, \dots, \tilde{\mathbf{u}}_N)$ .

The structure of projection matrices  $\mathbf{A}$  and  $\mathbf{B}$  depend on the method. For collocation method  $\mathbf{A} = \mathbf{I}$ , where  $\mathbf{I}$  is identity matrix  $N \times N$ ;  $\mathbf{B} = \Phi^{-1} \dot{\Phi}$ . Here  $\Phi_{ij} = \varphi_i(t_j)$ .

<sup>1</sup> In case of Galerkin method, eq. (3.9) can be also modified by using integration by parts:

$$\int_{t_a}^{t_b} \mathbf{f} \dot{\psi}_i dt - [\mathbf{f} \psi_i]_{t_a}^{t_b} + \int_{t_a}^{t_b} \mathbf{q} \psi_i dt = \mathbf{R}_i, \quad \forall i = 1, \dots, N$$

or use a weight function  $w$ , such that:

$$\int_{t_a}^{t_b} \mathbf{f} \dot{\psi}_i w dt - \int_{t_a}^{t_b} \mathbf{q} \psi_i w dt = \mathbf{R}_i, \quad \forall i = 1, \dots, N$$

The projection matrices for Galerkin method, using Gauss quadrature, are  $A = \Phi^{-1} A^*$  and  $B = \Phi^{-1} B^*$ . Where  $A_{ij}^* = \int_{t_a}^{t_b} \varphi_i \varphi_j dt$  and  $B_{ij}^* = \int_{t_a}^{t_b} \dot{\varphi}_i \varphi_j dt$

Basis functions are normally defined on a finite interval, e.g.  $[-1, 1]$  for Chebyshev polynomials, for this reason a coordinate transformation must be taken into account by the computation of matrices A and B (see Appendix B for more details).

The notion of incremental method is to split the main interval in  $n_t$  subintervals, such that:

$$t_0 < \dots < t_k < \dots < T, \quad k = 1, 2, \dots, (n_t - 1) \quad (3.11)$$

Then the solution is being sought one interval after the other: the initial condition  $\tilde{\mathbf{u}}(t_k)$  on the interval  $t \in [t_k, t_{k+1}]$  is provided from the solution of the previous interval  $t \in [t_{k-1}, t_k]$ :

$$\tilde{\mathbf{u}}_k(t_k) = \begin{cases} \tilde{\mathbf{u}}_{k-1}(t_k), & k > 0, \\ \mathbf{u}_0, & k = 0. \end{cases} \quad (3.12)$$

The algorithm of the incremental method for time integration is illustrated in fig. 3.3.

The resulted approach belongs to implicit Runge-Kutta methods [Hul72] However, the corresponding Butchers tableau depends on functional approximation (Power Series, Chebyshev, Legendre, etc) and whether collocation or Gauss-Galerkin method is used. The accuracy for Gauss-Galerkin approach is of order  $O((\Delta t)^{N+1})$  and the accuracy of collocation method is of order  $O((\Delta t)^{N-1})$ . Although Chebyshev and Legendre polynomials tend to provide faster convergency of Newton iterations (see below) compared to power series, the optimal choice of basis functions depend on the studied problem.

### 3.3.1. Modified Newton Method

In order to find a solution approximation  $\tilde{\mathbf{u}}$  on each time step, the residual for semi-linear approximation of differential equation is minimised

$$R(\tilde{\mathbf{u}}) \approx 0. \quad (3.13)$$

The starting point is linearisation around current solution approximation  $\tilde{\mathbf{u}}_0$ :

$$R_0 + J\Delta\tilde{\mathbf{u}} = 0, \quad (3.14)$$

where  $R_0 = R(\tilde{\mathbf{u}}_0)$  and  $J = \partial R / \partial \mathbf{u}$ . Then the increment in solution approximation is computed with:

$$\Delta\tilde{\mathbf{u}} = -J^{-1} R_0 \quad (3.15)$$

and the improved approximation is

$$\tilde{\mathbf{u}}_1 = \tilde{\mathbf{u}}_0 + a\Delta\tilde{\mathbf{u}}, \quad (3.16)$$

where  $0 < a \leq 1$  is a damping factor. The classical Newton method correspond to  $a = 1$  (see e.g. [QSS00]), which is increasingly unstable for stiff non-linear systems.

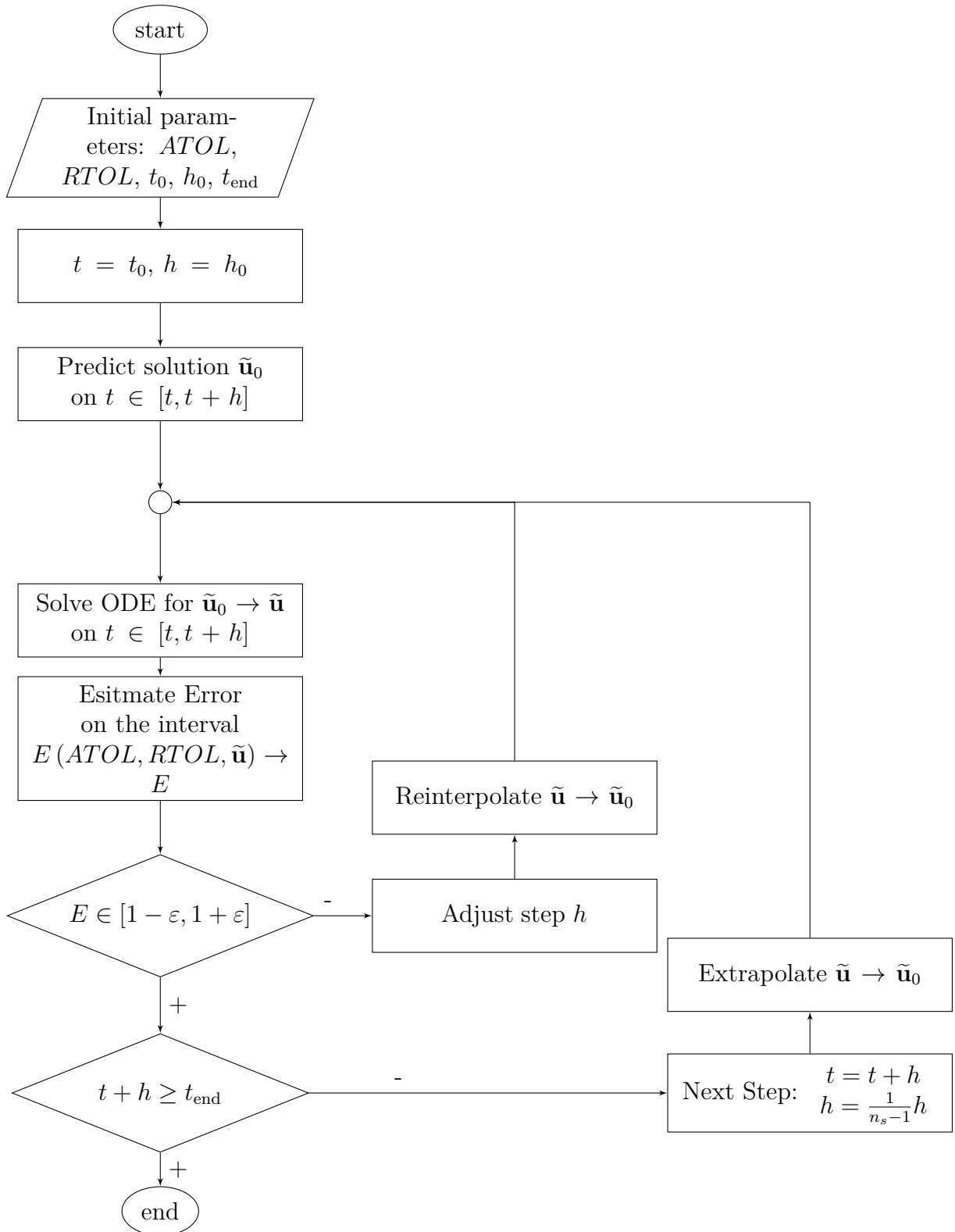


**Figure 3.3.:** Algorithm of incremental method

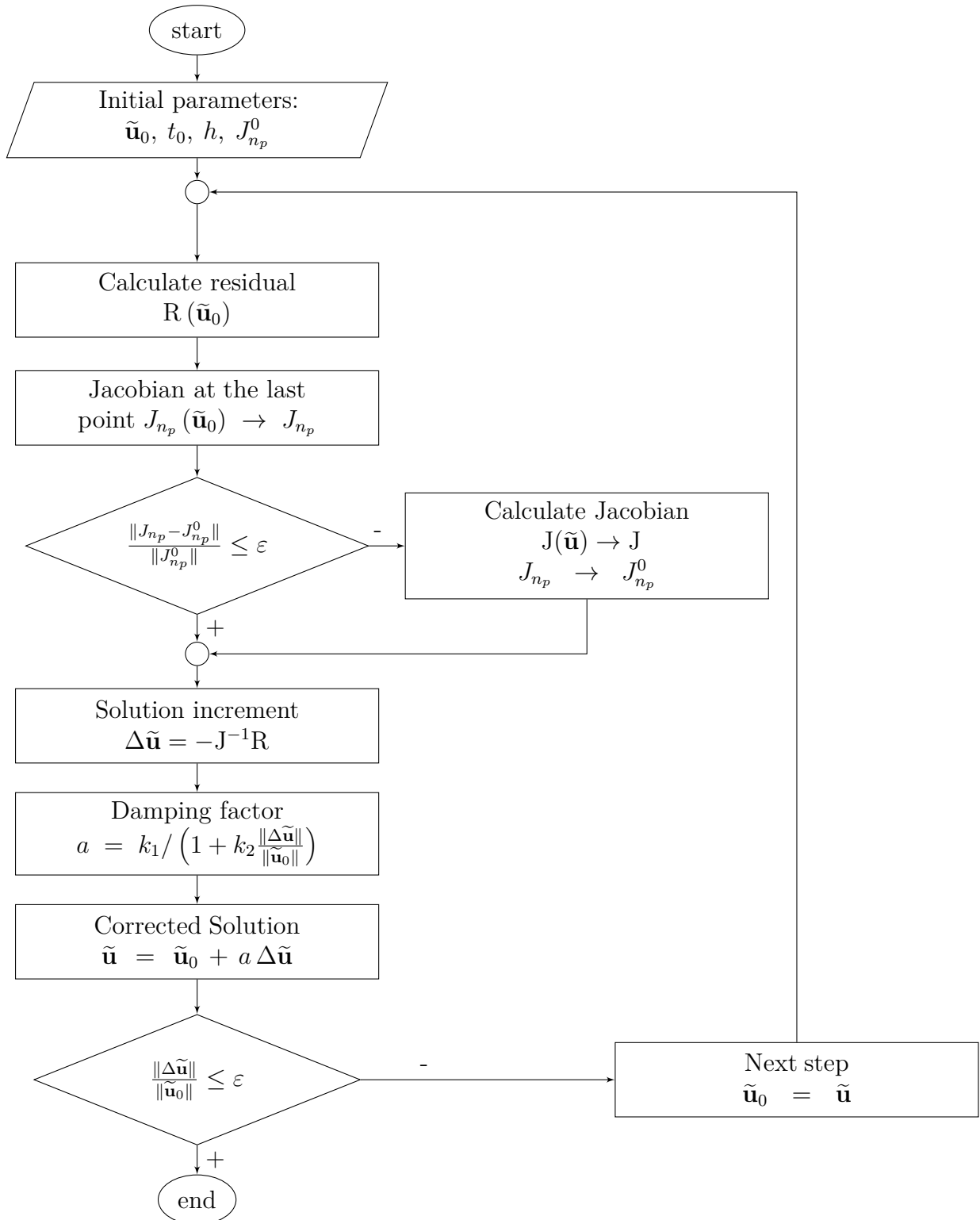


Figure 3.4.: Algorithm of modified Newton method

The common approach for finding of damping factor is to perform a line search such that [DM77, Sha70]:

$$|\mathbf{R}(\tilde{\mathbf{u}}_0 + a\Delta\tilde{\mathbf{u}}) - (\mathbf{R}_0 - a\mathbf{J}\Delta\tilde{\mathbf{u}})| < \varepsilon \quad (3.17)$$

However, this approach is connected with extra calculation overheads for residual evaluation. The proposed algorithm is constructed in such a way that for each time step, a good approximation is already available, either from the last step or from the step size adaptation (see fig. 3.3). Then the increment  $a\Delta\tilde{\mathbf{u}}$  should be small relative to  $\tilde{\mathbf{u}}$ . Thus, an empirical formula is introduced:

$$a = \frac{k_1}{1 + k_2 \frac{\|\Delta\tilde{\mathbf{u}}\|}{\|\tilde{\mathbf{u}}\|}}, \quad (3.18)$$

where  $k_1 \leq 1$  and  $k_2 \geq 1$  are the empirical factors. With a sufficiently good initial approximation the factors  $k_1 = 1$  and  $k_2 = 2$  the iterative showed a stable convergency, with less than 10 iterations, for studied problems.

The resulted modified Newton algorithm is illustrated in fig. 3.4.

The biggest disadvantage of this method comes from its implicit nature: for each iteration a Jacobian is required, which can be computationally expensive. However, it appears that the knowledge of the exact Jacobian is not required [QSS00]. Common methods are to use either inexact form of the Jacobian [Bro67, DES82] or to compute the Jacobian sporadic [Bro67, BBH89, RH93]. In fact, the last method comes from the observation that Jacobian near the exact solution changes only a little. Considering that for each step a good initial solution is provided (see §3.3.3), the sporadic Jacobian updates are chosen.

A simple strategy to check the update necessity is applied here. The Jacobian  $\mathbf{J}$  of the residual  $\mathbf{R}$  is constructed from Jacobians  $J_k$  at  $N_p$  collocation points. The Jacobian  $J$  is checked only at one (the last) time point within time segment and if it has changed more than a specified value:

$$\frac{\|J_{N_p} - J_{N_p}^0\|}{\|J_{N_p}^0\|} > \varepsilon_J \quad (3.19)$$

a full Jacobian update is performed. Here  $J_{N_p}$  is the current value of the Jacobian at the collocation point  $N_p$  and  $J_{N_p}^0$  is previous value of the Jacobian at the same point.

### 3.3.2. Error estimation

As showed by B. Hulme the method is equivalent to implicit Runge-Kutta method which is A-Stable [Hul72]. It can be also shown that maximal error is bounded [Hul72, DHT81]:

$$\max_{t_0 \leq t \leq T} |\mathbf{u}(t) - \tilde{\mathbf{u}}(t)| \leq C h^{N+1}, \quad (3.20)$$

where  $\mathbf{u}$  is the exact solution,  $\mathbf{x}$  - solution approximation,  $h$  - time step size and  $N$  - number of basis functions in the polynomial expansion. However, the constant  $C$

can be arbitrary large. For this reason after the modified Newton iterations found a solution approximation on an interval  $h_k$ , the actual error is estimated for each equation using  $L_1$  metric:

$$e_k^i = \frac{\int_{t_k}^{t_{k+1}} |f_i(t, \tilde{\mathbf{u}}) - q_i(t, \tilde{\mathbf{u}})| dt}{ATOL_i + f_i(t_0, \tilde{\mathbf{u}})}, \quad \forall i = 1, 2, \dots, n_v, \quad (3.21)$$

where  $e_k^i$  is a relative error of the equation  $i$  on the interval (element)  $k$  and  $n_v$  - number of equations in the linear system (3.6). The equation (3.21) is calculated using numerical integration.

The formula eq. (3.21) gives an error approximation of one (conservation) equation. There are 2 common approaches to derive a single error representation needed for interval adaptation (§3.3.3) [BBH89, RH93, Log04a]:

$$E_k = \max_{i=1, \dots, n_v} \left( \frac{e_k^i}{RTOL_i} \right), \quad (3.22)$$

or

$$E_k = \frac{1}{\sqrt{n_v}} \sqrt{\sum_{i=1}^{n_v} \left( \frac{e_k^i}{RTOL_i} \right)^2}, \quad (3.23)$$

where  $ATOL_i$  is the absolute tolerance and  $RTOL_i$  is the relative error of the equation  $i$  in the system of ODEs eq. (3.6). On one side, the tests showed that both formulae provide equivalent component error and the number of time segments. On the other side, the interval adaptation works more efficient with the second formula due to its smooth character.

Here it is important to note that the tolerances required by the algorithm are provided per equation basis and, in general case, do not direct represent the tolerances of variables. Iff the mass matrix is equal to identity matrix  $M \equiv I$ , then the error estimate corresponds to the error of state variables.

The error estimation is presented for general functional basis. If an orthogonal polynomial basis within a Banach space is used, the error can be more efficiently approximated using the approach described in §3.4.2.

### 3.3.3. Interval adaptation

The main idea is to find such intervals  $t \in [t_k, t_{k+1}]$ , that the relative error estimation lays within given limits  $E_k \in [1 - \varepsilon, 1 + \varepsilon]$ . The classical approach to determine the step size  $h_k = t_{k+1} - t_k$  based on the correction from the previous step (see e.g. [Gri10]):

$$h_{k+1} = h_k \left( \frac{1}{E_k} \right)^{\frac{1}{p}}, \quad (3.24)$$

where  $p = N - 1$  is the method order.

An alternative approach comes from the control theory, using a PID<sup>2</sup> controller,

<sup>2</sup>proportional-integral-derivative controller

where the next step size is estimated from 2 or 3 previous steps [Gus88, BHB04]:

$$h_{k+1} = h_k \left( \frac{1}{E_k} \right)^{k_I} \left( \frac{E_{k-1}}{E_k} \right)^{k_P} \left( \frac{E_{k-1}^2}{E_k E_{k-2}} \right)^{k_D}, \quad (3.25)$$

here  $k_P$ ,  $k_I$  and  $k_D$  are the proportional, integration and derivative gains respectively, which are determined experimentally.

If the solution on the predicted interval  $h_{k+1}$  is not satisfy the error criteria (i.e.  $E_{k+1} > 1$ ), then the standard procedure is to reduce the interval. However, the strategy is to find an interval with an estimated error close to the desired tolerance, thus intervals, which have to small an error, are also rejected. This is particularly challenging to find an appropriate first step size, because no previous information is available. In order to find an optimal step size  $h_k$ , one could solve a minimisation problem:

$$|E_k(h_k) - 1|^2 < \varepsilon. \quad (3.26)$$

However, the explicit dependency of error  $E_k$  from the step size  $h_k$  is not known. Thus, different geometric approaches for root finding [QSS00] were evaluated. The secant method (i.e. Regula Falsi) worked fine for smooth functions, allowing to find an optimal  $h_k$  within a few iterations. However, in the case of stiff problems this method fails because the function  $E_k(h_k)$  is not strictly continuous: small increment in  $h_k$  (around minimal numeric meaningful number) may result in a very large jump of the error.

An additional problem arises from the method himself. If a solution is being sought with polynomials of the higher order (e.g.  $p > 6$ ), the time segments (elements)  $h_k$  are getting very large and their size can be hardly determined from the size of the previous segments. Additionally, the super-convergency of the Newton method can be guaranteed only in the vicinity of the solution. However, to author's best knowledge, there exists no method to predict a solution for a large interval. Even if the size of the interval is predicted correctly, a sufficiently good initial approximation, which insures fast convergency of the polynomial fitting on the interval, cannot be accurately extrapolated from the previous step.

In order to overcome the above outlined problems, small sub-steps (segments)  $h_k^* < h_k$  are generated. The segment  $h_k$  grows with  $h_k^*$  till the error criteria are satisfied. The semi-empirical method works then as follows (see fig. 3.3):

#### **New interval $h_k$**

1. Set  $h_k = h_{k-1}/p$
2. Make prediction  $\tilde{\mathbf{u}}_k^0$  through extrapolation from the previous interval  $\tilde{\mathbf{u}}_{k-1}$ .
3. Do modified Newton iterations to find  $\tilde{\mathbf{u}}_k^1$

#### **Growing interval $h_k$**

1. Increase  $h_k$  with PID controller (3.24).
2. Extrapolate solution  $\tilde{\mathbf{u}}_k^i$  to the new increased interval.

3. Do modified Newton iterations to find  $\tilde{\mathbf{u}}_k^{i+1}$

This procedure is repeated till  $E_k > 1$  and then start a new interval. Using a cautious PID controller, which grows interval  $h_k$  gradually, the convergency of the Newton method is significantly speed up, and at the same time the desired interval size is found. The repeating experiments allowed to specify the following controller parameters:

$$k_I = -0.03 p, k_P = -0.002 p, k_D = 0, \quad (3.27)$$

where  $p = (N - 1)$  is the polynomial order.

### 3.4. Adaptive pseudo spectral method

Detailed description of adaptive pseudo spectral method (APSM) for solution of partial differential equations is presented in Appendix D. Here are only the main aspects outlined. The method is presented for brevity in 1D but it is generally applicable.

Assuming symmetry along y and z, the equation (2.2) is reduced to:

$$\frac{\partial}{\partial t} \mathbf{f}_t + \frac{\partial}{\partial x} \mathbf{f}_x = \mathbf{q}, \quad (3.28)$$

e.g. the conservation equations in cartesian space,  $t = \tau$  and  $x = \xi$  (see eq. (2.5), (2.6), (2.26)):

$$\frac{\partial}{\partial t} \begin{pmatrix} \rho \\ \rho v \\ \rho e \end{pmatrix} + \frac{\partial}{\partial x} \begin{pmatrix} v \rho \\ \rho v^2 + \sigma + \tau_{xx} \\ v(\rho e + \sigma + \tau_{xx}) + q_x \end{pmatrix} = \begin{pmatrix} 0 \\ 0 \\ 0 \end{pmatrix}. \quad (3.29)$$

Please note that the cartesian representation of conservation equations is given here for illustration purposes only. Conservation equation in other coordinate systems can be packed in the same form (see Appendix A), e.g. in spherical coordinates,  $x \rightarrow r$ . The first order tensors  $\mathbf{f}_t$ ,  $\mathbf{f}_x$  and  $\mathbf{q}$  in general coordinates are functions of time  $t$ , space  $x$ , state variables  $\mathbf{u}$  and of space derivative of state variables  $\partial \mathbf{u} / \partial x$ :

$$\begin{aligned} \mathbf{f}_\tau &= \mathbf{f}_\tau \left( \tau, \xi, \mathbf{u}, \frac{\partial \mathbf{u}}{\partial \xi} \right), \\ \mathbf{f}_\xi &= \mathbf{f}_\xi \left( \tau, \xi, \mathbf{u}, \frac{\partial \mathbf{u}}{\partial \xi} \right), \\ \mathbf{q} &= \mathbf{q} \left( \tau, \xi, \mathbf{u}, \frac{\partial \mathbf{u}}{\partial \xi} \right). \end{aligned} \quad (3.30)$$

The solution  $\mathbf{u}$  must be Lipschitz continuous on the interval  $t \in [t_a, t_b]$  and  $x \in [x_a, x_b]$  and that on this interval it can be expanded into series without an error. Then, the solution is approximated as a weighted sum of basis functions:

$$\tilde{\mathbf{u}}(t, x) = \sum_i^N \hat{\mathbf{u}}_i \varphi_i(t, x), \quad (3.31)$$

where  $\hat{\mathbf{u}}_i$  are weights of corresponding basis functions  $\varphi_i(t, x)$ . Please note that the number of basis functions  $N$  can be arbitrary large and in this case  $\tilde{\mathbf{u}} \rightarrow \mathbf{u}$ . Additionally, it is required that functions  $\mathbf{f}_t$ ,  $\mathbf{f}_x$ ,  $\mathbf{q}$  are also expanded into series with the same set of basis functions.

The projection of approximation in functional space  $\hat{U}$  to physical space on the predefined collocation points  $\tilde{U}$  is given as:

$$\tilde{U} = \hat{U} \Phi, \quad (3.32)$$

where  $\Phi_{ij} = \varphi_i(t_j, x_j)$ ,  $\tilde{U} = (\tilde{\mathbf{u}}_1, \tilde{\mathbf{u}}_2, \dots, \tilde{\mathbf{u}}_N)$ ,  $\hat{U} = (\hat{\mathbf{u}}_1, \hat{\mathbf{u}}_2, \dots, \hat{\mathbf{u}}_N)$ .

Using approach presented in §3.3 on the basis of functional approximation eq. (3.31), the following semi-linear system can be derived:

$$F_t B + F_x C - Q A = R, \quad (3.33)$$

where

$$\begin{cases} F_t &= \left( \mathbf{f}_t(t_1, x_1, \tilde{\mathbf{u}}_1), \mathbf{f}_t(t_2, x_2, \tilde{\mathbf{u}}_2), \dots, \mathbf{f}_t(t_N, x_N, \tilde{\mathbf{u}}_N) \right), \\ F_x &= \left( \mathbf{f}_x(t_1, x_1, \tilde{\mathbf{u}}_1), \mathbf{f}_x(t_2, x_2, \tilde{\mathbf{u}}_2), \dots, \mathbf{f}_x(t_N, x_N, \tilde{\mathbf{u}}_N) \right), \\ Q &= \left( \mathbf{q}(t_1, x_1, \tilde{\mathbf{u}}_1), \mathbf{q}(t_2, x_2, \tilde{\mathbf{u}}_2), \dots, \mathbf{q}(t_N, x_N, \tilde{\mathbf{u}}_N) \right). \end{cases} \quad (3.34)$$

Projection matrices A, B and C depend on the applied method (collocation or Gauss-Galerkin) and on type of functional approximation (power series, Chebyshev polynomials, etc).

For *pseudo-spectral method*:  $A = I$ ,  $B = \Phi^{-1} B^*$ ,  $C = \Phi^{-1} C^*$ , where  $I_{ij} = \delta_{ij}$ ,  $B_{ij}^* = \frac{\partial}{\partial t} \varphi_i(t_j, x_j)$ ,  $C_{ij}^* = \frac{\partial}{\partial x} \varphi_i(t_j, x_j)$ .

For *Gauss-Galerkin method*:  $A = \Phi^{-1} A^*$ ,  $B = \Phi^{-1} B^*$ ,  $C = \Phi^{-1} C^*$ , where  $A_{ij}^* = \int \int \varphi_i \varphi_j dx dt$ ,  $B_{ij}^* = \int \int \frac{\partial}{\partial t} \varphi_i \varphi_j dx dt$ ,  $C_{ij}^* = \int \int \frac{\partial}{\partial x} \varphi_i \varphi_j dx dt$ .

As the functional space is defined on a specific interval, e.g. Chebyshev  $\xi \in [-1, 1]$ , and the physical domain can be of a complex shape (not necessary rectangular), coordinate transformation must be also taken into account (see Appendix B). The detailed derivation of projection matrices for pseudo-spectral method is shown in Appendix D.

The solution approximation within the domain U is then sought by minimisation of the residual  $R(U) \rightarrow 0$ , using modified Newton iterations (see §3.3.1).

As the global spectral approximation of stiff system tend to be unstable, it is better to split the time-space domain into a number of subdomains:

$$t_0 < \dots < t_k < \dots < T, \quad k = 1, 2, \dots, (N_t - 1), \quad (3.35)$$

$$x_0 < \dots < x_l < \dots < x_\infty, \quad l = 1, 2, \dots, (N_x - 1). \quad (3.36)$$

Then the solution in time is being sought one time-interval after the other: the initial condition  $\mathbf{u}(t_k)$  on the interval  $t \in [t_k, t_{k+1}]$  is provided from the solution of the previous interval  $t \in [t_{k-1}, t_k]$ . This corresponds to an implicit Runge-Kutta method (see §3.3). It is important to note here, that space and time order, as well as the space width of each subdomain, can be different.

The subdomains in space are matched with the following boundary conditions:

$$\begin{cases} \mathbf{u}^l(t, x_{l-1}) = \mathbf{u}^{l-1}(t, x_{l-1}) \\ \mathbf{u}^l(t, x_l) = \mathbf{u}^{l+1}(t, x_l) \\ \frac{\partial}{\partial x} \mathbf{u}^l(t, x_{l-1}) = \frac{\partial}{\partial x} \mathbf{u}^{l-1}(t, x_{l-1}) \\ \frac{\partial}{\partial x} \mathbf{u}^l(t, x_l) = \frac{\partial}{\partial x} \mathbf{u}^{l+1}(t, x_l), \end{cases} \quad (3.37)$$

where  $\mathbf{u}^l$  is solution within domain  $l$ .

### 3.4.1. Solution of linear system in binary tree

Due to the stiffness of the combustion systems, the system of equations (3.33), equipped the corresponding global boundary conditions, is solved for each time step with modified Newtonian iterations (see §3.3.1). The structure of the required global Jacobian has a block form, i.e. in 1D has a block diagonal form (see fig. 3.6(step 1)). However, the global storage is not required. Computational cells are split/united as required. After that a natural binary tree is created (see fig. 3.5).

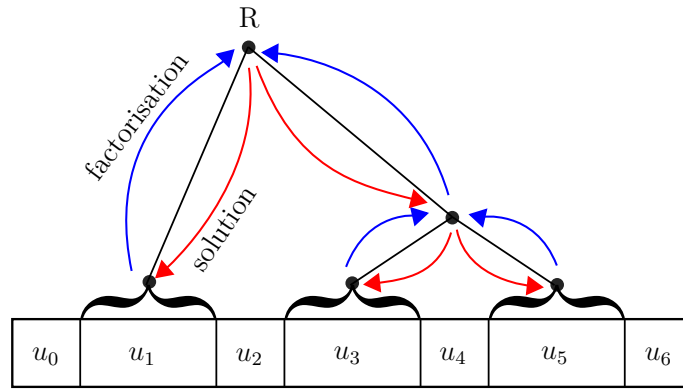


**Figure 3.5.:** Information flow in binary tree for APSM.

In this tree, boundary points are stored in *knots* ( $\mathbf{u}_0, \mathbf{u}_2, \mathbf{u}_4, \mathbf{u}_6$ ), where each split of a computational cell creates a new artificial boundary (knot). Other discretisation points are stored in *cells* ( $\mathbf{u}_1, \mathbf{u}_3$ , and so on). The solution of the resulted linear system can be found with quasi-gaussian elimination, following to:

1. Elimination of inner cell points. The Jacobian system is constructed as shown in fig. 3.6 (Step 1). Inner points corresponding to the lower level of the tree are eliminated, e.g cells  $\mathbf{u}_3$  and  $\mathbf{u}_5$ . Here, we eliminate red blocks and submit information about blue blocks to the parent knot  $\mathbf{u}_4$ . The green blocks are used to reconstruct the solution from known boundary points. The resulting reduced system is shown in fig. 3.6 (Step 2). The procedure is repeated until only global boundary points remain, fig. 3.6 (Step 4).
2. Find solution update of Newtonian iterations at the global boundaries  $\Delta \mathbf{u}_0$  and  $\mathbf{u}_{10}$ .
3. Propagate the solution update to the inner boundaries (knots) and finally to cells by solving local linear systems shown in green on fig. 3.6.

This process is repeated till the relative increment of Newtonian iteration for current time step is small:

$$\frac{\|\Delta \mathbf{u}^l\|_2}{\|\mathbf{u}^l\|_2} \leq \varepsilon, \quad \forall l = 0, 1, \dots, 2Nx_x. \quad (3.38)$$

It is worth to mention that the iterations can be stopped in one part of the system earlier as in the other, as soon as the criteria eq. (3.38) is reached locally. The value  $\varepsilon = 10^{-9}$  was used in computations.

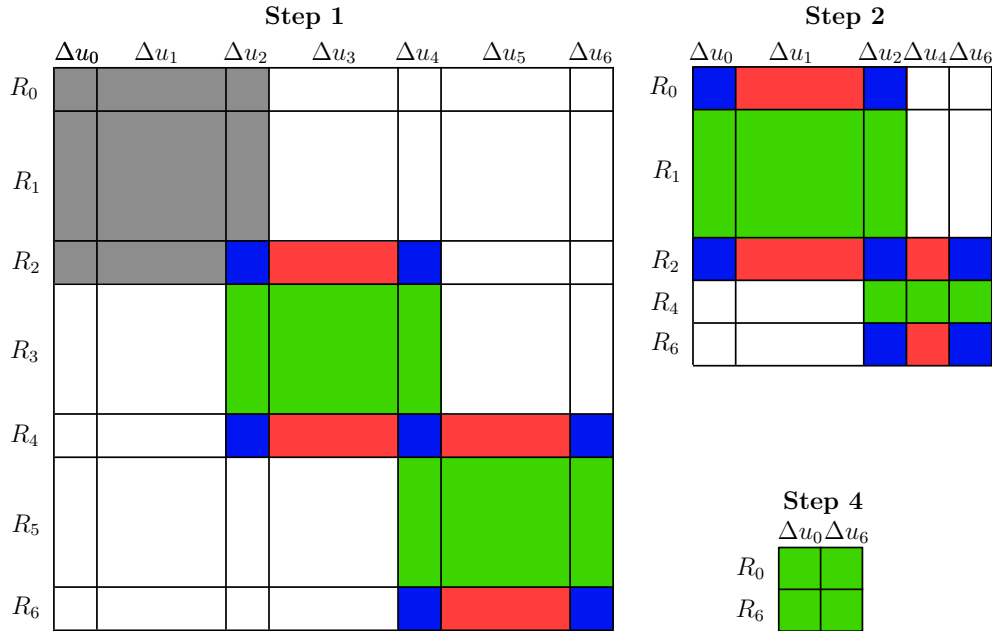


**Figure 3.6.:** Structure of the global Jacobian for APSM and its factorisation. Blocks shown in grey remains unchanged, red blocks are eliminated, modified blue blocks are propagated to the upper level, modified green blocks are used to reconstruct the solution from local boundary values.

The advantages of implemented quasi-gaussian iterations are:

- Localised Jacobian updates. Changes in the structure of the binary tree (polynomial order, number of computational cells) lead to only local update of the matrix factorisation, e.g. the update of Jacobian corresponding cell  $u_1$  leads to an update of points  $u_0$ ,  $u_2$  and  $u_6$  only, leaving  $u_3$ ,  $u_4$  and  $u_5$  unchanged.
- Distributed storage. As the factorisation information is stored nodes and cells, no global storage is required. This allows local modification of the systems, i.e. polynomial order and number of cells.
- Efficient parallelisation. All cells and almost all tree knots can be processed independently with very limited communication between threads (see fig. 3.5).

### 3.4.2. Error estimation and optimal collocation points

The definition of errors is firstly introduced:

The **truncation error**  $E_T(N)$  is defined to be the error made by neglecting all spectral coefficients  $a_i$  with  $i > N$  [Boy89]. It is generally assumed that truncation error is equal to **discretisation error**.

The **interpolation error**  $E_I(N)$  is the error made by approximating a function by an  $(N + 1)$ -term series whose coefficients are chosen to make the approximation agree with the target function exactly at each of  $N + 1$  “interpolation” (“collocation”) points [Boy89]. If the function expansion (infinite) is known:

$$f(x) = \sum_i^{\infty} a_i T_i(x) \quad (3.39)$$

then the truncation error is bounded by the sum of the absolute values of all the neglected coefficients [Boy89]:

$$E_T(N) \leq \sum_{i=N+1}^{\infty} |a_i|. \quad (3.40)$$

Let  $f(x)$  to be a function, which is interpolated by a Chebyshev polynomial  $S_N(x)$  of order  $N$  on the interval  $x \in [-1, 1]$

$$S_N(x) = \sum_i^N a_i T_i(x) \quad (3.41)$$

then the interpolation error is bounded to twice the sum of the absolute values of all the neglected coefficients [Boy89]:

$$E_I(N) = |f(x) - S_N(x)| \leq 2 \sum_{i=N+1}^{\infty} |a_i|. \quad (3.42)$$

This means that interpolation error is in worse case of factor 2 greater than the truncation error.

In order to minimise the reminder error the optimal interpolation points correspond to roots of the Chebyshev polynomial of degree  $(N + 1)$ . This leads to the Gauss-Chebyshev expression for collocation points [Boy89]:

$$x_i = \cos\left(\frac{(2i + 1)\pi}{2N}\right), \quad \forall i = 0, 1, \dots, N - 1, \quad (3.43)$$

which is illustrated in fig. 3.7. Points are actually destributed equidistantly along the perimeter of unit circle. The eq. (3.43). In order to include boundary points a similar expression Gauss-Lobatto can be used:

$$x_i = \cos\left(\frac{i\pi}{N - 1}\right), \quad \forall i = 0, 1, \dots, N - 1. \quad (3.44)$$

Unfortunately the truncated coefficients are not known during the integration. The ultimate test of a numerical solution is to repeat the calculation with different  $N$  and

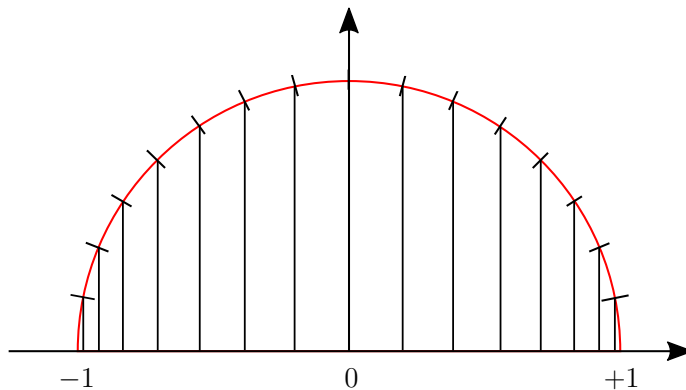


**Figure 3.7.:** Gauss-Lobatto collocation points

compare results. However, the amplitude of the last coefficient  $|a_N|$  can provide a reasonable error estimate (within order of magnitude) [Boy89]:

$$E_T(N) \sim O(|a_N|), \quad (3.45)$$

iff lower coefficients decrease smoothly towards  $a_N$ .

The last coefficient of the approximation can be used as the error measure but precautions must be taken:

- All coefficients must decrease smoothly. Otherwise the approximation might be far off the correct solution;
- Depending on the form of approximated function  $f(x)$  some coefficients may be naturally zero.

Figure 3.8 shows a well converging series, where only odd coefficients are non-zero. However, it is not straightforward to detect that it is converging smoothly and obviously the last coefficient  $a_8 = 0$  but the next coefficient  $a_9$  would be most likely non-zero.

The following estimate for the interpolation error is used:

$$E_I(N) \approx \sqrt{a_N^2 + a_{N-1}^2}. \quad (3.46)$$

This formula avoids the parity of the solution but might overestimate the error.

### 3.4.3. Grid adaptation

The proposed adaptive pseudo spectral method (APSM) allows two types of adaptation:

- p-Refinement: Increase order of polynomial within one or several elements,
- r-Refinement: Increase number of elements by splitting and thus increasing the depth of the binary tree.

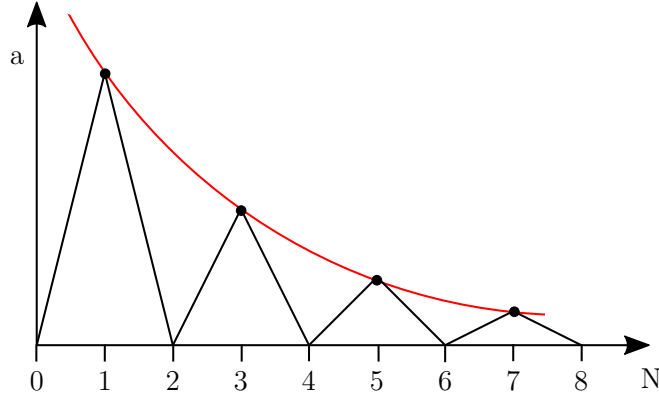


**Figure 3.8.:** Converging series with zero even coefficients.

The first method is advantageous, as it is associated with a faster accuracy increase (exponential) and requires less regriding overheads, e.g. memory allocation. The change of order is a linear operation such that:

$$\tilde{\mathbf{U}}_M^l = \tilde{\mathbf{U}}_N^l \mathbf{P}_{N,M}, \quad (3.47)$$

where  $\tilde{\mathbf{U}}_N^l$  is a solution approximation on corresponding collocation points for  $N$  basis functions,  $\mathbf{P}_{N,M}$  is a projection matrix, which transforms the solution with  $N$  basis function on corresponding collocation points to the solution with  $M$  basis functions on the corresponding points. The order increase corresponds to padding zeros the solution approximation in functional space:

$$\hat{\mathbf{U}}_{M+1}^l = (\hat{\mathbf{u}}_0, \hat{\mathbf{u}}_1, \dots, \hat{\mathbf{u}}_M, \mathbf{0}). \quad (3.48)$$

The procedure of order increase does not produce additional errors to the solution as shown in fig. 3.9.

The order decrease through a truncation of series coefficients, introduces an error which is proportional to the doubled amplitude of the truncated coefficients. In this case the derivatives at the boundaries are particularly affected (see blue line in fig. 3.10), which creates solution inconsistency at the boundaries. Recapitulate, that sub-domains are matched by the equality of gradients at boundaries. Thus additional criteria, preserving boundary gradients were introduced, which leads However, to additional loss of 2 orders, i.e. by a desired reduction of order by one  $N - 1$  leads to loss of accuracy of  $N - 3$ . This is illustrated in fig. 3.10. The latter is However, preferable, if the additional accuracy loss is taken into account. The eq. (3.47) is valid for both order reduction approaches but with different coefficients.

As discussed in the previous section, the error of the order increase is limited to interpolation error:

$$E_I(N) \approx \hat{\mathbf{u}}_N^l. \quad (3.49)$$

The error of order reduction (by one) is then:

$$E_T(N) \approx \hat{\mathbf{u}}_{N-3}^l. \quad (3.50)$$

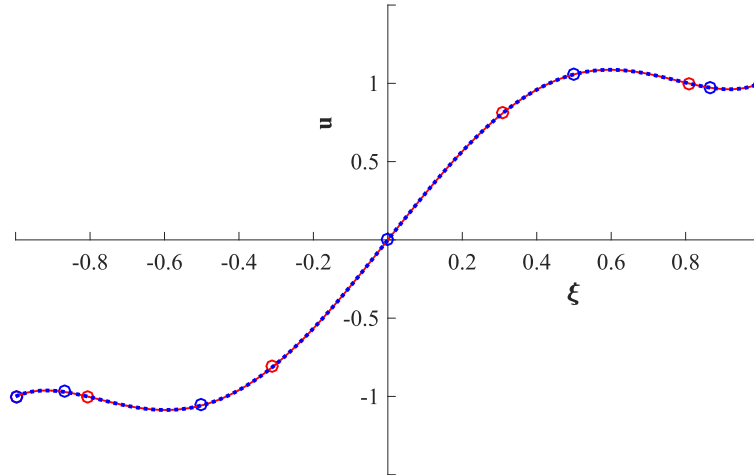


**Figure 3.9.:** Solution approximation after order increase. Red line shows the initial approximation  $O(5)$  with red points showing the collocation points, blue dotted line shows the increased order  $O(6)$  with  $a_6 = 0$ .

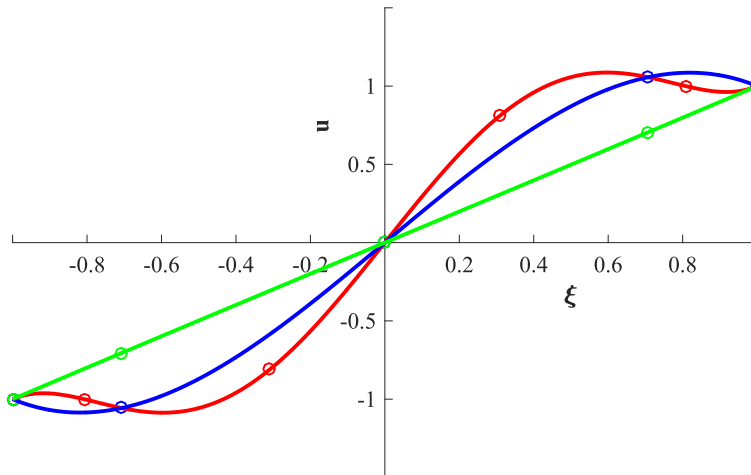


**Figure 3.10.:** Solution approximation after order decrease through interpolation with fixed gradients. Red line shows the initial approximation  $O(5)$  with red points showing the collocation points, blue line shows the decreased order through truncation  $O(4)$  and green line - reinterpolation with fixed boundary gradients.

The procedure of order increase/decrease is in itself efficient (matrix-vector multiplication) and provide little disturbance to the solution, if the trailing coefficient is small. However, the solution of discretised PDE with high orders requires more CPU power because an LU-Decomposition of dense matrix of size  $[N_v(M-1) \times N_v(M-1)]$  is required for each element. This procedure is of computational order  $O((N_v(M-1))^3)$  [QSS00]. Thus infinite increase of polynomial order is not practical, within the proposed scheme. Distributed data storage (within nodes and elements) and processing in binary tree permits a structured straightforward unification and splitting of elements without any distortions in the rest of the domain.

As next, imagine a splitting of an element  $l$ , which produces 2 children  $l-1$  and  $l+1$ . The numeration  $\{l-1, l, l+1\}$  is in the new resulted system after splitting, where the parent element becomes the node  $l$  (consider e.g. node “RO01” in fig. D.9). Each element is split up exactly in the middle, by keeping the order for all 3 elements  $O(M)$ :

$$\begin{cases} x_0^{l-1} = x_0^l, \\ x_M^{l-1} = x_0^{l+1} = \frac{1}{2}(x_0^l + x_M^l), \\ x_M^{l+1} = x_M^l. \end{cases} \quad (3.51)$$

This is described by a familiar linear operation:

$$\begin{cases} \tilde{U}_N^{l-1} = \tilde{U}_N^l S_N^{-1}, \\ \tilde{U}_N^{l+1} = \tilde{U}_N^l S_N^{+1}, \end{cases} \quad (3.52)$$

where  $S_N^{-1}$  and  $S_N^{+1}$  are projection matrices from solution approximation in domain  $l$  on  $x \in [x_0^l, x_N^l]$  to subdomains  $l-1$  on  $x \in [x_0^l, \frac{1}{2}(x_0^l + x_M^l)]$  and  $l+1$  on  $x \in [\frac{1}{2}(x_0^l + x_M^l), x_N^l]$ .

If the approximation order is preserved, then the splitting doesn't distort the solution. See e.g. fig. 3.11. It can be seen that the approximation on sub-intervals (dotted blue and green) overlap identically with the initial approximation (solid red). It comes from the fact that scaling and shifting of the coordinate system does not change the polynomial order.

Surely a split with an unequal width of child elements can be advantageous but it requires a further investigation. Additionally, unequal split results in variable transformation matrices which cannot be precomputed and thus providing an additional overhead.

Similar to the element order reduction, the union of elements leads to an information loss, which is particularly pronounced near the boundaries. Consider fig. 3.12, two elements “green” and “blue” are united. With simple reinterpolation (red dotted line), a relatively good fit is acquired, but as in the case of the order reduction, the gradients at boundaries deviate strongly. With fixed gradients (smooth) at the boundaries, a worse approximation within the volume is achieved, because 2 orders are lost for gradients.

Here again the projection of solution approximation on subdomains  $l-1$  and  $l+1$  to domain  $l$  is described with the following linear operation:

$$\tilde{U}^l = \tilde{U}^{l-1} Q_{M,K}^a + \tilde{U}^{l+1} Q_{N,K}^b, \quad (3.53)$$

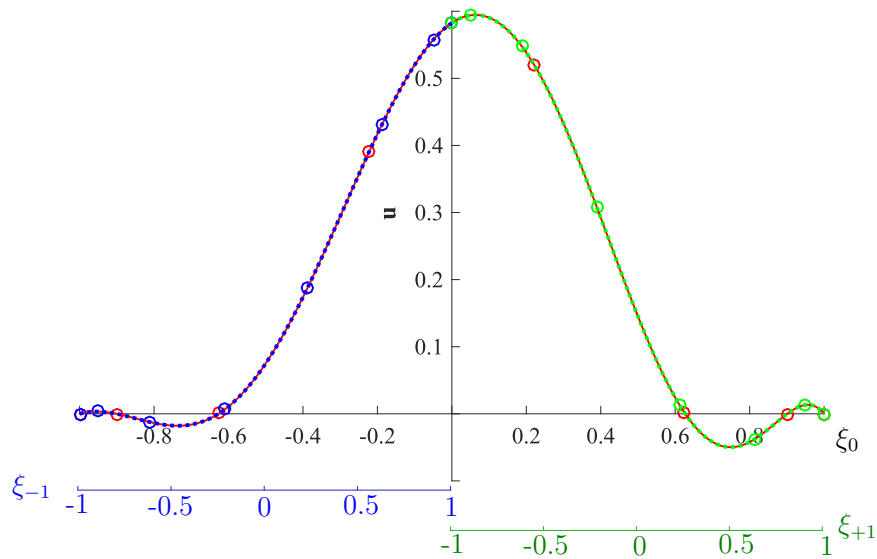


**Figure 3.11.:** Solution approximation before and after element split with  $O(5)$ . Red line shows the initial approximation, blue dotted line shows left child element with and green dotted line – right child. Circles show collocation points.

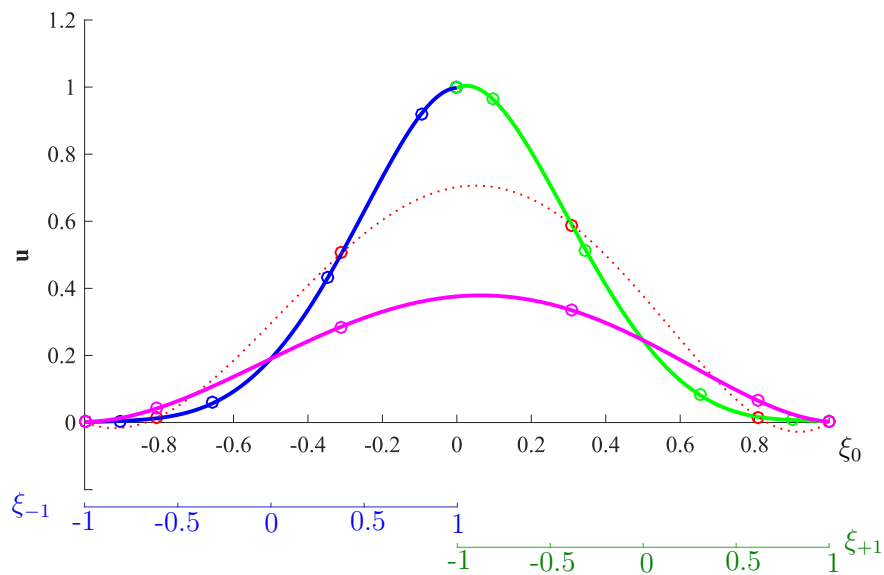


**Figure 3.12.:** Solution approximation before and after element union with  $O(5)$ . Red line shows the approximation after union with, blue dotted line shows initial data of the left child element and green dotted line – initial right child. Circles show collocation points.

where  $Q_{M,K}^a$  and  $Q_{N,K}^b$  are matrices projecting approximation of order  $M$  from the left subdomain  $l - 1$  and approximation of order  $N$  from the right subdomain  $l + 1$  to solution on corresponding points of the united domain  $l$  with order  $K$ .

Obviously order increase/reduction and element split/union are two competitive strategies, which alone can adjust the collocation grid to the required accuracy. For an effective combined strategy, additional factors need to be considered:

- Polynomial order increase has exponential accuracy growth
- Infinite order increase leads to the inversion of large dense matrices,
- Second order is the lowest possible order. Firstly, differential equations of second order impose minimal second order polynomials. Secondly, two degrees of freedom are governed by boundary conditions and at least one degree of freedom must be assigned to PDE. Practically third order (splines) is the minimal order.
- Element split provides a linear accuracy growth.
- Element split/union require expensive memory allocation (reallocation) for elements.
- Element split produces almost twice as much collocation points, compared to only one of order increase.

In order to introduce the grid adaptation strategy, the error control strategy is presented firstly (see §3.4.2). The absolute error of the state variable  $u_i$  for order  $k$  is approximated by:

$$e_i^{\text{abs}}(k) = \sqrt{\hat{u}_{i,k}^2 + \hat{u}_{i,k-1}^2}, \quad \forall i = 1, 2, \dots, N_v, \quad (3.54)$$

where  $\hat{u}_{i,k}$  is the amplitude of the  $k$ -th coefficient, computed from the solution approximation with (see also eq. (D.9)):

$$\hat{\mathbf{u}}_i = \tilde{\mathbf{u}}_i^l \Phi_{N,N}^{-1}. \quad (3.55)$$

The normalised relative error of order  $k$  is more practical, as scales of state variables may change dramatically during the computation, and the scales of variables may be different:

$$E_i(k) = \frac{e_i^{\text{abs}}(k)}{\text{RTOL}_i (\text{ATOL}_i + |\hat{u}_{i,0}|)}. \quad (3.56)$$

Then the measure of error of order  $k$  for all state variables is the maximum:

$$E(k) = \max_{i=1, \dots, N_v} E_i(k). \quad (3.57)$$

The normalised error is  $E(k) = 1$ , if the desired level of accuracy is reached. If  $E(k) > 1$  – the accuracy is insufficient and if  $E(k) < 1$  – the accuracy is superfluous.

Based on this criterion, a heuristic grid adaptation strategy can be defined, which is summarised in the algorithm, fig. 3.13. The limit of orders within one element

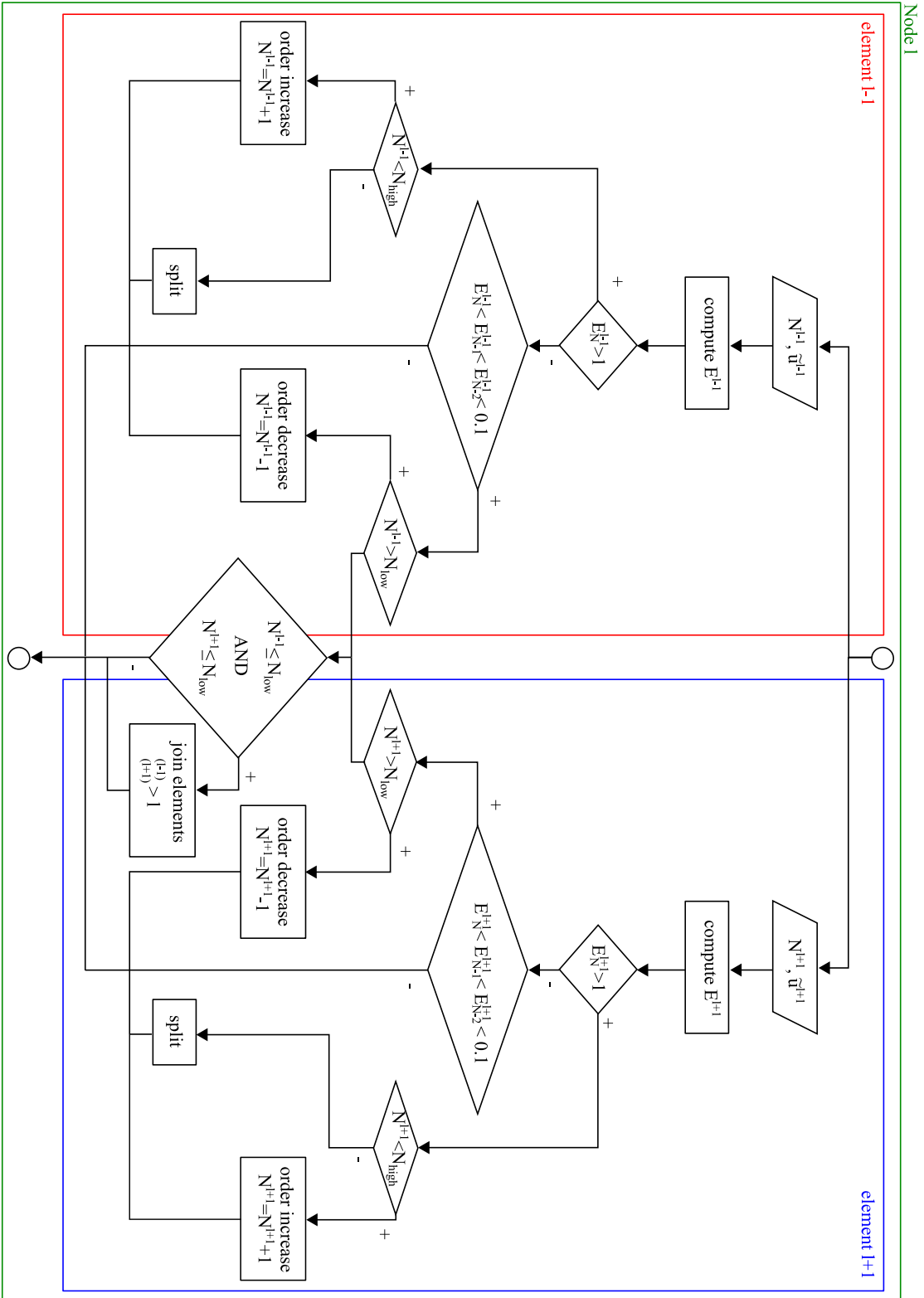


Figure 3.13.: Grid adaptation Algorithm.

$N \in [3, 15]$  provides a good trade-off between the number of total grid points and the computational time. If element order is greater than  $O(3)$  and less than  $O(15)$ , the order increase/decrease is used. If the amplitude of the last coefficient  $E(N) > 1$  is too large, the element order is increased by one. If the accuracy is too high  $E(N) < E(N-1) < E(N-2) < 0.1$ , then the element order is reduced by one. It is important to consider the amplitudes up to the third coefficient from the end, because after the reduction of the polynomial order by 1, the order of accuracy is reduced by 3.

The splitting/unification is a structured process. If the order is  $O(15)$  and the accuracy is still not sufficient  $E(15) > 1$  the element is split up into two smaller elements with  $O(15)$ , which creates a new node in the tree with two sub-elements. If for a node its children have order  $O(3)$  and both have a small error  $E(N) < E(N-1) < E(N-2) < 0.1$ , the elements are united. The elements belonging to different nodes cannot be united.

### 3.4.4. Antialiasing and Filter

If underresolved, the spectral methods are becoming increasingly unstable and may lead to unexpected results, (see §3.2). A possible way to overcome these difficulties was introduced in §3.4.3, where spectral elements are split up till all required waves are resolved. However, the resolution of smallest scales is not always needed, e.g. acoustic waves in laminar regimes. Thus an antialiasing strategy is required.

The simplest antialiasing is accomplished with an artificial diffusion (blurring). See e.g. [Har87]. Consider general conservation equation (see §2.1):

$$\frac{\partial f_t}{\partial t} + \frac{\partial f_x}{\partial x} = q. \quad (3.58)$$

where an artificial diffusion of the conservation quantity  $f_t$  is introduced:

$$\frac{\partial f_t}{\partial t} + \frac{\partial f_x}{\partial x} - \alpha \frac{\partial^2 f_t}{\partial x^2} = q, \quad (3.59)$$

here  $\alpha \rightarrow 0$  is coefficient of artificial viscosity. The diffusion term forces that series coefficients for  $f_t$  decay exponentially [Tad90]:

$$\hat{f}_t(t) \sim e^{-i^2 \alpha t}. \quad (3.60)$$

High coefficients decay even faster, proportionally to the squared coefficient index. Unfortunately, if  $\alpha$  is proportional to interval spacing  $\Delta x$ , the solution remains by the first order approximation  $O(1)$ . Some schemes [Har87] use:

$$\alpha \sim (\Delta x)^N, \quad (3.61)$$

in order to keep the influence of artificial viscosity term of order  $O(N)$ .

Alternatively, one can introduce a low-pass filter, which removes the upper  $(1/3)$  of frequencies either of state variable  $u$  or of fluxes  $f_x$  [Boy89]. However, numerical experiments have shown that this may still lead to blow-up of the solution, as the

“solution” strategy still does not provide a dissipation mechanism for high frequency disturbances.

Spectral viscosity method (SVM), which can be seen as combination of both previous approaches, was introduced by E. Tadmor [Tad90]. The method works as a diffusion operator but damping only the upper frequencies:

$$\frac{\partial f_t}{\partial t} + \frac{\partial f_x}{\partial x} - \alpha Q * \frac{\partial^2 f_t}{\partial x^2} = q, \quad (3.62)$$

here  $Q$  is viscosity kernel which is activated only on high frequencies  $i \geq m$ , where  $m$  is the critical frequency. The meaning of  $Q$  is best explained with Fourier transformation, i.e.

$$Q(x) = \sum_{m \leq |i| \leq N} \hat{Q}_i e^{\sqrt{-1} i x}. \quad (3.63)$$

Then the diffusion operator is

$$\alpha Q * \frac{\partial^2 f_t}{\partial x^2} = -\alpha \sum_{m \leq |i| \leq N} i^2 \hat{Q}_i \hat{f}_{t_i} e^{\sqrt{-1} i x}. \quad (3.64)$$

with theoretically defined optimal activation frequency:

$$m = 2\sqrt{N}, \quad (3.65)$$

where  $N$  is the order of polynomial approximation (number of highest frequency resolved). According to the author [Tad90] the error introduced by the SVM is less than the general error of Fourier approximation of eq. (3.58).

The viscosity kernel is usually defined as a step function in spectral space:

$$\hat{Q}_i = \begin{cases} 0, & \forall i < m, \\ 1, & \forall i \geq m, \end{cases} \quad (3.66)$$

The spectral filter  $W_N$  of order  $N$  according to SVM is defined as:

$$W_N = \Phi_{N,N}^{-1} \text{diag}(\hat{Q}) \left( \frac{\partial^2}{\partial x^2} \Phi_{N,N} \right) \quad (3.67)$$

The modified quasi-linear approximation of PDE with spectral filter takes the following form (compare with eq. (3.33)):

$$F_t(B - \alpha W) + F_x C - Q A = R, \quad (3.68)$$

In order to keep the accuracy of the approximation to  $O(m)$ , the coefficient of artificial viscosity should be

$$\alpha \leq \Delta x. \quad (3.69)$$

Interesting to note, that for power series this filter is exactly null for all  $m \neq 2$ . If  $m = 2$  it corresponds to the common diffusion.

## 4. Computation of reaction rates for isomerisation and decomposition reactions

The solution of partial differential equation with proposed algorithm “Phlogia”, requires to write the conservation equation in form space time divergence

$$\nabla \cdot \mathbf{F} = \mathbf{q}. \quad (4.1)$$

A large number of engineering tasks can be covered by this formulation, e.g. Burnett equation<sup>1</sup>, heat transfer, elastic stress analysis. The methodology of spectral methods (SM) is however not limited to this mathematical formulation. As long as an appropriate functional basis can be found, the SM can be applied to other types of problems. For instance, the canonical transition-state theory (see e.g. [Gla41, TGK96]) can be used to describe unimolecular, recombination, and complex-forming bimolecular reactions. This usually requires the setup and solution of a so-called master equation (ME), see e.g. [GS90, HPR96, For03, Olz13], which is a stiff integro-differential equation.

The problem of reaction rates for bimolecular reactions or unimolecular reactions is very acute for the accurate description of ignition processes. Indeed, a study of chemical mechanisms for hydrocarbons revealed that up to 2/3 of elementary reaction contain unimolecular, recombination and chemical activation reactions [GLT83]. Apart from common temperature dependency these reaction are also strongly influenced by pressure variations. Experimental results are usually limited to a relative small range of temperatures and pressures. Moreover, the uncertainties of experimental results are very high.

Additional problems arise, by constructing of ME and by converting its results to the canonical Arrhenius form. In many cases a reactant can undergo several interconnected isomerisation and decomposition processes, which are covered by a system of MEs. When a solution available, it becomes a challenging task to provide a single rate constant for each reaction. The steady state assumption alone (see discussion below) can lead to errors in rate constants, e.g. when the quasi steady state is reached, there might be just few molecules left in the system to continue the process.

---

<sup>1</sup>High order extension of Navier-Stokes, derived from Chapman–Enskog theory [HCB54]

An analytical solution of ME is possible for a few very specific cases only (see e.g. [GS90]). Realistic applications require a numerical treatment, which requires a large number of discretisation parameters for the resolution of complex distribution of reactant over energy levels. Using a conventional discretisation strategy, see e.g. [GS90, HPR96, For03, Olz13], about 5000 discretisation parameters is required for one ME. This significantly limits the application for realistic multi-well MEs.

The application of SM with Gaussian radial basis functions (GRBFs), suggested in [KYB<sup>+</sup>18], allows significantly, up to several orders, reduce the number of required discretisation parameters. Thus making the study of complex multi-well systems of MEs possible.

## 4.1. Solution of integro-differential equations

The frame work of spectral methods can be easily adapted to other type of problems [KYB<sup>+</sup>18]. Consider the following integro-differential equation:

$$\frac{\partial n(E, t)}{\partial t} = \omega \left[ \int_0^{\infty} P(E, E') n(E', t) dE' - n(E, t) \right] - k(E) n(E, t) + R_a f(E), \quad (4.2)$$

As for other spectral methods, the starting point is the approximation of the solution  $n(E, t)$  as a weighted sum of  $N$  known basis functions:

$$n(E, t) \approx \sum_{j=0}^{N-1} \hat{n}_j(t) \varphi_j(E) \quad (4.3)$$

In order to find  $N$  weights of the solution approximation, the eq. (4.2) is substituted into eq. (4.3), and the inner product is formed with  $N$  test functions  $\psi_i(E)$  over the interval  $x \in [0, \infty]$  [Boy89]. The result is the following linear system of ordinary differential equations (ODE) [KYB<sup>+</sup>18]:

$$\begin{aligned} & \sum_{j=0}^{N-1} \frac{d\hat{n}_j(t)}{dt} \int_E \varphi_j(E) \psi_i(E) dE \\ &= \int_E R_a f(E) \psi_i(E) dE + \omega \sum_{j=0}^{N-1} \hat{n}_j(t) \int_{E'} \varphi_j(E') \int_E P(E, E') \psi_i(E) dE dE' \\ & - \omega \sum_{j=0}^{N-1} \hat{n}_j(t) \int_E \varphi_j(E) \psi_i(E) dE - \sum_{j=0}^{N-1} \hat{n}_j(t) \int_E k_{\Sigma}(E) \varphi_j(E) \psi_i(E) dE, \\ & \forall i = 0, 1, \dots, N-1 \end{aligned} \quad (4.4)$$

that can also be written in vector-matrix notation:

$$\hat{A} \frac{d}{dt} \hat{n}(t) = \left[ \omega(\hat{P} - \hat{A}) - \hat{K} \right] \hat{n}(t) + R_a \hat{f} \quad (4.5)$$

Here  $\hat{n}(t)$  denotes the vector of the unknowns weight functions  $\hat{n}_j(t)$ , the symbols  $\hat{A}$ ,  $\hat{P}$ , and  $\hat{K}$  denote matrices and  $\hat{f}$  represents a vector with the following respective

elements:

$$\hat{A}_{ij} = \int_E \varphi_j(E) \psi_i(E) dE \quad (4.6a)$$

$$\hat{P}_{ij} = \int_{E'} \varphi_j(E') \int_E P(E, E') \psi_i(E) dE dE' \quad (4.6b)$$

$$\hat{K}_{ij} = \int_E k_{\Sigma}(E) \varphi_j(E) \psi_i(E) dE \quad (4.6c)$$

$$\hat{f}_i = \int_E f(E) \psi_i(E) dE. \quad (4.6d)$$

It is instructive to set the basis functions  $\varphi_i(E) = I_i(E)$  with  $I_i(E)$  being an interval indicator-function such that:

$$I_i(E) = \begin{cases} 1 & \text{if } E \in [E_i, E_{i+1}] \\ 0 & \text{otherwise} \end{cases} \quad (4.7)$$

Then, the solution approximation, eq. (4.3), becomes:

$$n(E, t) \approx \sum_{i=0}^{N-1} n_i(t) I_i(E) \quad (4.8)$$

where  $\hat{n}_j(t) = n_i(t)$  is the approximation of  $n(E, t)$  in the  $i$ -th grid interval, and  $N$  is the total number of intervals. The test functions are chosen from the function space of interval indicator-functions by setting  $\psi_i(E) = I_i(E)$ . Then, taking an equidistant energy grid with a small finite increment  $\Delta E_i = \Delta E_j = \text{const}$ , setting an upper boundary  $E_{max} = N\Delta E_i$ , and dividing by  $\Delta E_j$ , one obtains the familiar discrete form of the ME [GS90, HPR96, Olz13]:

$$\frac{d}{dt} \mathbf{n}(t) = \left[ \omega(\mathbf{P} - \mathbf{U}) - \mathbf{K} \right] \mathbf{n}(t) + R_a \mathbf{f} = \mathbf{Jn}(t) + R_a \mathbf{f} \quad (4.9)$$

with

$$P_{ij} = P(E_i, E_j) \Delta E_i \quad (4.10a)$$

$$K_{ii} = k_{\Sigma}(E_i) \quad (4.10b)$$

$$f_i = f(E_i) \quad (4.10c)$$

In this case, matrix  $\hat{A}$  reduces to the identity matrix  $\mathbf{U}$  and matrix  $\hat{K}$  transforms into the diagonal matrix  $\mathbf{K}$ .

The spectral method used in this work projects the solution into the space of arbitrarily spaced GRBFs:

$$\varphi_i(E) = \exp \left[ -\frac{(E - E_i)^2}{\sigma_i^2} \right] \quad (4.11)$$

where  $E_i$  defines a displacement of the function  $\varphi_i$ , and  $\sigma_i$  defines the width of the GRBF. In general, the question regarding the choice of these parameters is complicated and strongly depends on the problem at hand. This choice of GRBFs as basis functions relies on the following properties (reasons):

- GRBFs form a complete set [Boy89], i.e. the set of functions is sufficient to represent the solution with any degree of accuracy,
- GRBFs are smooth because the solution of the continuous ME is in most cases a smooth function.
- GRBFs reflect the general form of the solution particularly well (with a minimum number of basis functions the solution can be represented with maximum accuracy), and
- GRBFs allow for an effective computation, i.e. there is an analytic solution for the integral, eq. (4.6a), and the exponential function is a built-in function in many modern processors.

Practically, results with the highest accuracy can be achieved by using a normalised form of the GRBFs:

$$\varphi_i^n(E) = \frac{\varphi_i(E)}{\sum_j \varphi_j(E)} \quad (4.12)$$

that forces the sum of all basis functions to unity at all points of the energy scale [KYB<sup>+</sup>15]. As numerical tests show that this choice avoids artifactual oscillations of the solution approximation. The use of these normalised GRBFs, however, hampers an efficient calculation of the integrals, eqs. (4.6a)–(4.6d) because in this case setting up these equations is more time consuming.

With much less computational effort than by using GRBFs normalised according to eq. (4.12), a smooth solution can be obtained by an optimal choice of the parameters  $E_i$  and  $\sigma_i$ . By using a homogeneous distribution of GRBFs, i.e., the distances between two adjacent GRBFs,  $E_{i+1} - E_i = \Delta E$ , are constant) with equal width factors  $\sigma_i = \sigma$  and by imposing the condition that each function  $\varphi_i(E)$  crosses its second next neighbours ( $\varphi_{j-2}$  and  $\varphi_{j+2}$ ) at half of the height, it can be achieved that the sum of all basis functions,  $S(E)$ , remains nearly constant over the largest part of the domain with somewhat lower values only close to the boundaries. This is illustrated in fig. 4.1. These choices lead to the following relation between  $\sigma$  and  $\Delta E$  for an equidistant grid:

$$\sigma = \sqrt{\ln(2)} \Delta E \quad (4.13)$$

As test functions, general interval indicator functions are used, that is  $\psi_i(E) = I_i(E)$  (cf. fig. 4.1) because this makes integration of eqs. (4.6a)–(4.6d) very efficient. With the matrix/vector elements  $\hat{A}_{ij}$ ,  $\hat{P}_{ij}$ ,  $\hat{K}_{ij}$ , and  $\hat{\mathbf{f}}_i$  calculated in this way, the time-dependent solution of the linear differential equation system, eq. (4.5), can be found numerically by using, e.g.,

1. an implicit ODE solver because, due to the constant Jacobian, the integration is particularly fast or
2. an eigenvalue decomposition routine because, although computationally expensive, the small size of the linear ODE system resulting from application of the method makes it feasible to use.

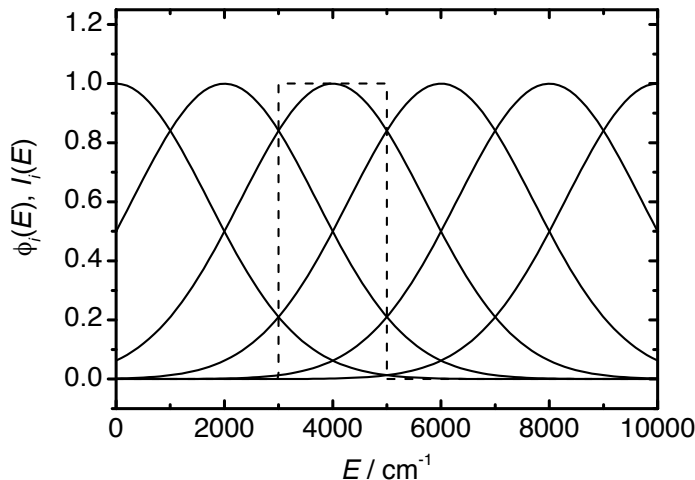


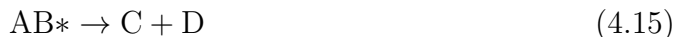
**Figure 4.1.:** Six illustrative GRBFs  $\varphi_i(E)$  (solid lines) with  $\Delta E = 2000 \text{ cm}^{-1}$  and  $\Sigma = 2402 \text{ cm}^{-1}$  from eq. (4.13), sum of the six GRBFs,  $S(E)$  (dashed line), and a test function  $I_j(E)$  for  $j = 2$  (dotted line) [KYB<sup>+</sup>18].

## 4.2. Single-well Master Equation

Consider e.g. following reaction pathway:



In this scenario the bimolecular reaction  $A + B$  is the source of excited complex  $AB^*$ , which can further recombine into molecules  $C$  and  $D$ . If only the right side of the expression (4.14)



is considered, one speaks about thermal activation. The left part of the expression (4.14)



defines a chemical activation and is described by a constant flux of activated complex  $AB^*$ .

The entire process can be described with the ME, which is derived from Lindemann-Hinshelwood mechanism [Hin29] under assumption of continuity of density of states:

$$\frac{\partial n(E, t)}{\partial t} = \omega \left[ \int_0^\infty P(E, E') n(E', t) dE' - n(E, t) \right] - k(E) n(E, t) + R_a f(E), \quad (4.17)$$

with

$$k(E) = \sum_{l=1}^{N_R} k_l(E). \quad (4.18)$$

Here,  $n(E, t)$  is the energy- and time-dependent population of the considered reactant or intermediate,  $\omega$  is the collision frequency with bath gas molecules,  $N_R$  is the

number of unimolecular reaction channels, and  $k_l(E)$  is the energy-specific rate constant of the  $l$ -th channel (e.g. eq. (4.15)). The quantity  $P(E, E')$  represents the probability density of a collision-induced transition from an initial energy in the range  $[E', E' + dE]$  to a final energy within  $[E, E + dE]$ . The symbol  $R_a$  denotes the rate of a reaction that produces the considered species, and  $f(E)$  is the corresponding normalised input flux distribution. This final term is only present for chemically activated reactions (e.g. (4.16)).

The equation (4.17) is so-called 1-Dimensional (1D) ME, which accounts only for internal energy and neglects the collisional energy transfer of rotational energy. The 1D ME is applicable for all reactants with similar moments of inertia, e.g. unimolecular isomerisations and eliminations [GS90].

The kinetic behaviour of the reaction system is governed by  $n(E, t)$ , the solution function of the ME. Since the ME contains the pressure and temperature via the collision frequency  $\omega$  and the collisional energy transfer probability  $P(E, E')$ , the population  $n(E, t)$  parametrically depends on  $T$  and  $p$  as well. Where appropriate this is written in the form  $n(E, t; T, p)$ .

The specific rate constants  $k_l(E)$  for the unimolecular reactions can be calculated from RRKM theory or similar models; for an overview see e.g. ref. [Olz13]. The collisional transition probability function  $P(E, E')$  is typically expressed by heuristic models as for instance the step-ladder [QT77] or exponential-down model [PF77, Rin97]:

$$P(E, E') = \frac{1}{N(E')} \exp \left[ - \left( \frac{E' - E}{C_0 + C_1 E'} \right)^y \right] \rho(E) \rho(E'), \quad (4.19)$$

the parameters  $C_0$ ,  $C_1$  any  $y$  in the exponential-down model are defined empirically as a fit of experimental results. The term  $C_0 + C_1 E'$  is always positive and describes the magnitude of the energy transfer per collision. The exponential down model is only valid for downward transition  $P(E, E')$ . The upward transition  $P(E', E)$  is determined from the detailed balance:

$$\frac{P(E, E')}{P(E', E)} = \frac{n^e(E)}{n^e(E')} = \frac{\rho(E)}{\rho(E')} \exp \left( - \frac{E - E'}{k_B T} \right), \quad (4.20)$$

where  $n^e$  is equilibrium distribution for given temperature:

$$n^e(E) = \frac{\rho(E) \exp \left( - E / (k_B T) \right)}{\int_0^\infty \rho(E') \exp \left( - E' / (k_B T) \right) dE'}, \quad (4.21)$$

with  $\rho$  – density of states and  $k_B$  – Boltzmann constant.

The normalisation factor  $N(E')$  is derived from the principle of completeness:

$$\int_0^\infty P(E, E') dE = 1, \quad (4.22)$$

The collision frequency  $\omega$  describes the average number of collisions between interacting molecules per unit of time and is defined as [GS90]:

$$\omega_{ij} = \Omega_{ij}^{(2,2)*} \sigma_{ij}^2 \sqrt{\frac{8\pi k_B T}{M_{ij}}} \frac{p_B}{RT} N_A, \quad (4.23)$$

where  $\omega_{ij}$  is collision efficiency between molecules  $i$  and  $j$ ,  $\Omega_{ij}^{(2,2)*}$  collision integral (see §2.2.5),  $\sigma_{ij}$  – collision diameter (eq. (2.57)),  $M_{ij}$  – reduced molar mass (eq. (2.56)),  $p_B$  – pressure of the bath gas. In most cases it is assumed that the bath gas is in excess and the total pressure equals the bath gas pressure  $p \approx p_B$ .

For chemically activated processes, the ME has to be extended by a chemical source term,  $R_a > 0$ . It is common to assume  $R_a$  as being time-independent due to the usually significantly slower change of the bimolecular precursor concentrations compared to the population change of the intermediate [GS90, HPR96, For03]. The nascent distribution  $f(E)$  for a formation reaction from thermalised reactants can be expressed by the following relation [GS90, HPR96, For03]:

$$f(E) = \frac{W_{-a}(E - E_{0(-a)}) \exp\left(- (E - E_{0(-a)})/(k_B T)\right)}{\int_0^\infty W_{-a}(E') \exp\left(- E'/(k_B T)\right) dE'}, \quad (4.24)$$

Here,  $E \geq E_{0(-a)}$ , with  $E_{0(-a)}$  denoting the threshold energy and  $W_{-a}$  the cumulative reaction probability (sum of states of the transition state) for the reverse of the formation reaction.

Once a solution  $n(E, t)$  of the equation (4.17) is attained, the time-dependent reaction rate  $k(t; T, p)$  can be attained, considering that:

$$\frac{dc(t)}{dt} = k(E, t) c(t), \quad (4.25)$$

$$k(t) = \frac{\int_0^\infty \frac{d}{dt} n(E, t) dE}{\int_0^\infty n(E, t) dE}, \quad (4.26)$$

where  $c(t) = \int n(E, t) dE$  denotes the total concentration of the reactant, e.g.  $AB^*$  in expression (4.14).

Similarly can be the reaction rate  $k_l(t)$  for each channel  $l$  attained:

$$k_l(t) = \frac{\int_0^\infty k_l(E) n(E, t) dE}{\int_0^\infty n(E, t) dE}. \quad (4.27)$$

It is obvious that the observable rate constant defined in this way is in general time-dependent, but in most cases, it reaches a virtually constant value after a short induction period [GS90, HPR96, For03]. During this induction period, the initial energy distribution  $n(E, 0)$  relaxes into a pseudo-stationary distribution that decays exponentially with time but maintains its shape, which means that the normalised distribution

$$\tilde{n}(E, t) = \frac{n(E, t)}{\int_0^\infty n(E, t) dE} \quad (4.28)$$

remains unchanged

$$k(T, p) = \lim_{t \rightarrow \infty} k(t; T, p) = \lim_{t \rightarrow \infty} \frac{\int_0^{\infty} \frac{d}{dt} n(E, t) dE}{\int_0^{\infty} n(E, t) dE}. \quad (4.29)$$

The customary definition of the rate constant corresponds to this long-time limit. Fortunately, for most practical conditions, the induction period, which is closely related to the reciprocal collision frequency,  $\omega^{-1}$ , is well separated from the timescale of the overall chemical reaction itself [GS90, HPR96, For03].

### 4.2.1. Unimolecular decomposition of 25DMF2H

As a case study to evaluate the performance of spectral method with Gaussian Radial Basis Function (GRBFs) approximation, the unimolecular decomposition of the 25DMF2H radical is chosen (for structure, see fig. 4.2). This radical occurs in the pyrolysis and combustion of 25DMF, which is a biofuel candidate (see, e.g., [LKP<sup>+</sup>17]). The 25DMF2H radical is typically formed by addition of an H atom to 25DMF [FSO13]. The kinetics of the latter reaction under shock tube conditions was recently studied and analysed with ME calculations for chemical activation on the basis of quantum chemical data [FSO13]. The essentials necessary to understand the modelling with the methods of the current work are briefly repeated here.

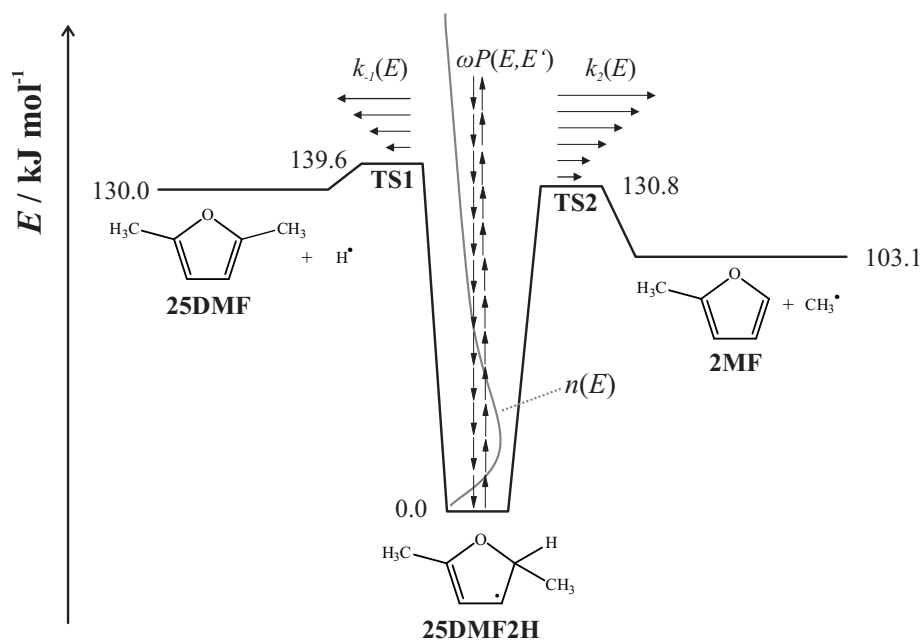
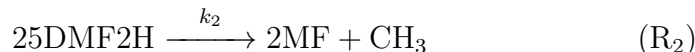


**Figure 4.2.:** Schematic potential energy diagram, including zero-point energy, relative to 25DMF2H (adapted from [FSO13]).

The dominant product channel of the H + 25DMF reaction is (2MF) + CH<sub>3</sub>. These products are formed in a complex-forming mechanism via 25DMF2H (see fig. 4.2). This intermediate radical once formed can either dissociate back to the reactants via C-H bond fission or undergo the energetically favored C-C bond fission to give

2MF + CH<sub>3</sub>:



The input parameters for the ME were essentially taken from [FSO13]. Specific rate coefficients were calculated from RRKM theory [GS90, HPR96, For03] on the basis of an averaged CBS-QB3/CBS-APNO/G3 potential energy diagram (see fig. 4.2) and CBS-QB3 vibrational frequencies and rotational constants. Densities and sums of states were determined with direct counting procedures for a total angular momentum quantum number of  $J = 110$  that corresponds to the thermal average between 950 and 1250 K. For the calculation of the collision frequency,  $\omega$ , argon was chosen as the bath gas with the following binary Lennard-Jones parameters [FSO13]:  $\epsilon_{25\text{DMF2H-Ar}}/k_{\text{B}} = 239$  K and  $\sigma_{25\text{DMF2H-Ar}} = 4.4$  Å.

In contrast to [FSO13], where a stepladder model was used for the collisional energy transfer probability, a density-of-states-weighted [DDHR99] exponential-down model (see §4) was used in the current work:

$$P(E, E') = \frac{1}{N(E')} \exp\left(-\frac{E' - E}{\alpha}\right) \rho(E) \quad \forall E < E'. \quad (4.30)$$

Here,  $N(E')$  is a normalisation function to satisfy the principle of completeness, and  $\alpha$  is a parameter that represents the average energy transferred per down-collision (corresponding to  $\Delta E_{\text{SL}}$  in the stepladder model) [GS90, HPR96, For03]. Weighting by the density of states of 25DMF2H,  $\rho(E)$ , ensures that completeness and detailed balancing can be simultaneously fulfilled at all energies. In the calculations of the present work, it is set  $\alpha = 250$  cm<sup>-1</sup> in analogy to  $\Delta E_{\text{SL}} = 250$  cm<sup>-1</sup> in [FSO13].

It is important to note here that the primary intention of the present work is not to provide highly accurate kinetic data for the thermally and chemically activated 25DMF2H reactions but to demonstrate the performance of the SM with GRBFs for the solution of the ME for a practically relevant unimolecular reaction system of realistic size.

The results are compared with the conventional discretisation method (CDM) [GLT83, HPR96, Olz13, KYB<sup>+</sup>15] for a wide range of temperatures from 800 to 1400 K and pressures from 10<sup>-8</sup> to 10<sup>6</sup> bar. The performance of the SM with the CDM is compared using the size of the corresponding linear system, which represents the number of basis functions of the spectral method and to the number of intervals of the conventional method.

A typical outcome of the solution of the master equation is the pressure and temperature dependence of the rate constant. Figure 4.3 (left) shows the temperature dependence of the cumulative rate constant  $k_{\Sigma}$  and fig. 4.3 (right) shows the pressure dependency of the rate constant. The results of QSM with 50 or more GRBFs are visually indistinguishable from the solution with reference method with several

thousand grids points. The QSM with a smaller number of basis functions is less accurate for low pressures, e.g. with 20 GRBFs the solution deviates significantly below  $10^{-3}$  bar (see fig. 4.3(right)). As the solution approaches the low pressure limit  $p \rightarrow 0$  there are not enough collisions to establish an equilibrium and it can be shown that the mathematical solution is a simple cut-off of the initial distribution at the position of the reaction channel. The required number of basis functions for  $p \rightarrow 0$  approaches infinity.

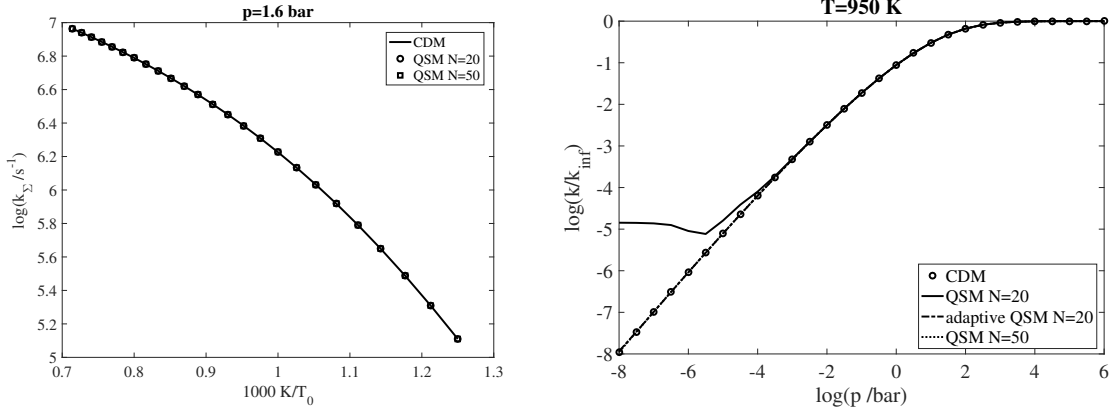


**Figure 4.3.:** Temperature dependence of the rate constant (left) and Pressure dependence of the rate constant (right).

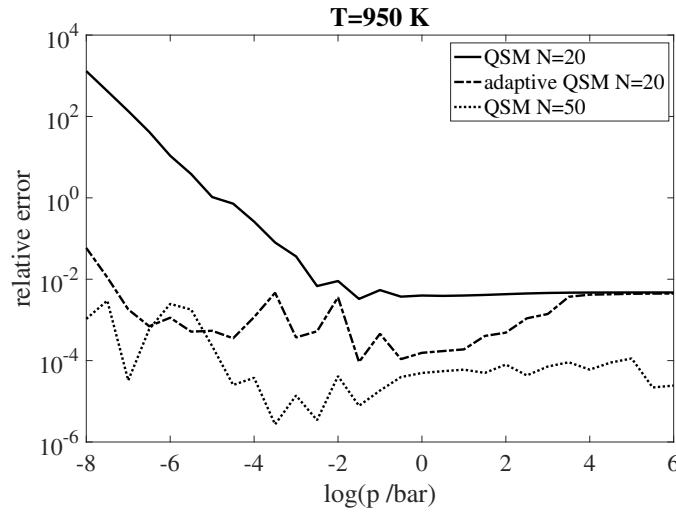
In order to quantify the differences, a relative error is defined as

$$e_{\text{rel}}(t) = \frac{k(t) - k_{\text{REF}}(t)}{k_{\text{REF}}(t)} \quad (4.31)$$

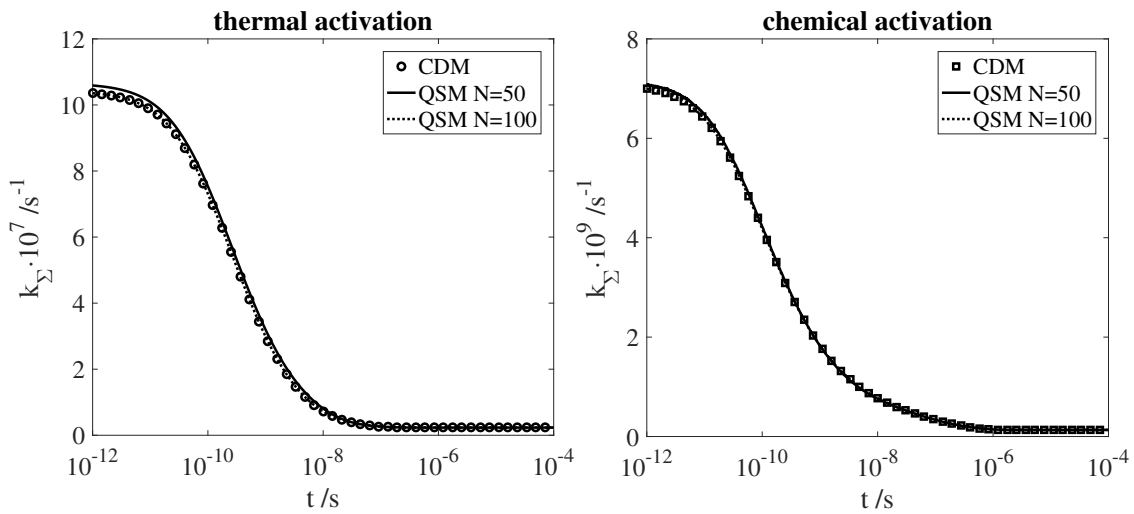
here  $k(t)$  is time-dependent rate constant as defined in eq. (4.26) computed with given method and accuracy,  $k_{\text{REF}}(t)$  is rate constant computed with reference method. Note that the conventional, time-independent rate constant is obtained as the long-time limit as is discussed in the context of eq. (4.29). The reference method to calculate  $k_{\text{REF}}(t)$  is in general CDM with a cutoff energy of  $E_{\text{max}} = 42310 \text{ cm}^{-1}$  and a grid size of  $E = 10 \text{ cm}^{-1}$ .

Figure 4.4 supports the mostly excellent agreement between the results from the different methods. The relative deviations are in most cases well below  $10^{-2}$ . An exception occurs in the case of QSM with a very small number of basis functions  $N = 20$  at pressures below  $10^{-3}$  bar, where the differences strongly increase with decreasing pressure. But by an increase of the number of basis functions, here from  $N = 20$  to  $N = 50$ , or by using the adaptive interval truncation, that is by decreasing the cutoff energy and keeping  $N = 20$ , the situation can be considerably improved as is also obvious from fig. 4.4.

Previous results are valid for quasi-steady state, when the normalised distribution does not change  $t \rightarrow \infty$ . The multiexponential decay occurring at earlier reaction times formally leads to a time dependence of the rate constant. A more general scenario is presented in fig. 4.5, where the rate constant is evolving over time. In this illustrative case, there are relative deviations between QSM and CDM of up to 0.13 with number of basis function  $N = 50$  (see fig. 4.8). For  $N = 100$  these



**Figure 4.4.:** Relative error of pressure dependence of the rate constant



**Figure 4.5.:** Calculated time-dependent rate constants.

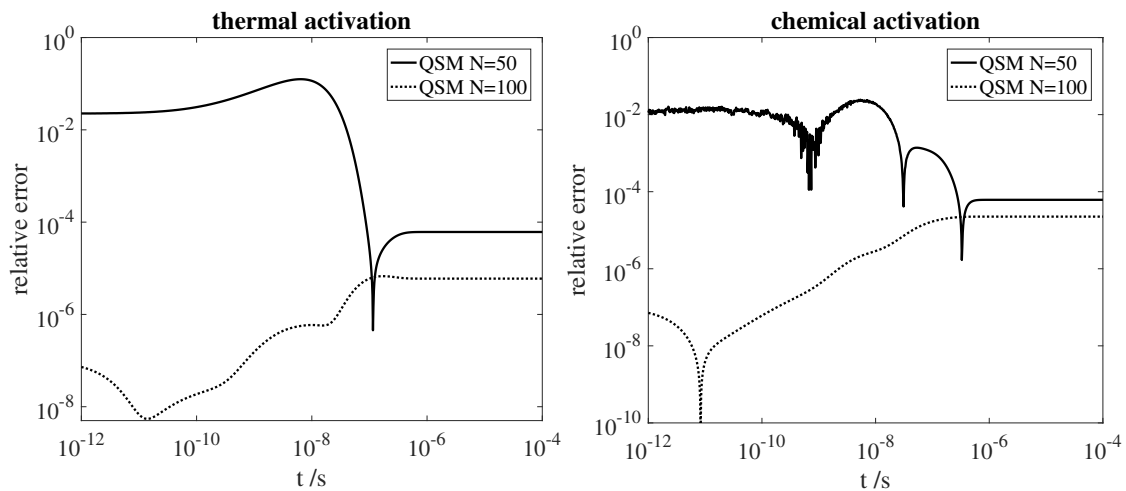


**Figure 4.6.:** Relative error of calculated time-dependent rate constants.

deviations decrease to values below  $10^{-4}$ . Obviously, the kinetically relevant part of the eigenvalue spectrum is calculated by spectral matrix with reasonable accuracy.

In fig. 4.7, relative errors for rate constants  $k(t \rightarrow \infty)$  calculated with the different methods are plotted for typical conditions as a function of the linear size of the corresponding ODE system. In all cases, except adaptive SM, the maximum energy  $E_{max} = 52380 \text{ cm}^{-1}$ . The reference solution was obtained from CDM with a grain size of  $\Delta E = 10 \text{ cm}^{-1}$  that is with  $N = 5238$ . It can be observed that the relative error of CDM scales approximately linearly with the system size whereas the errors of SM and adaptive SM decrease much stronger. Even for a number of basis functions as low as  $N = 20$ , the relative errors of the results from SM and adaptive SM are well below  $10^{-2}$ , a value reached with CDM only for  $N > 700$ .

At about 80 basis functions, SM and adaptive SM seem to reach a round-off plateau, where the relative errors remain nearly unchanged for further increasing number of basis function  $N$ . At this point, the spectral method has virtually reached the accuracy of the reference method with relative deviations below  $10^{-5}$ . With less basis function  $N$ , the decrease in  $N$  through interval adaptation compared to fixed SM is about a factor of 3 and appears to be more pronounced for thermally than for chemically activated reactions. Any further investigation would require either an analytic benchmark or a much finer grid for the reference method. But such differences are unimportant for any practical calculation of rate constants. Please note that a very similar behaviour was observed also for other temperatures and pressures.

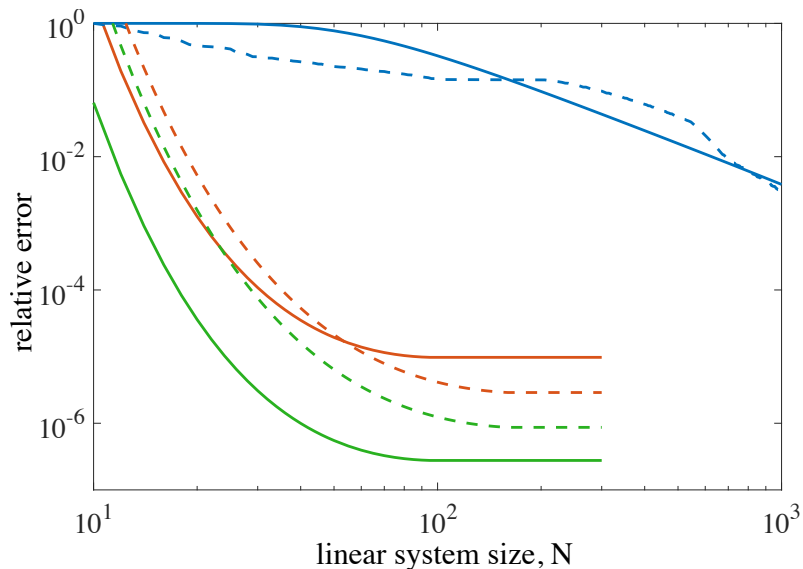


**Figure 4.7.:** Dependence of the relative error on the linear size. System for thermal (solid lines) and chemical (dashed lines) activation conditions, with CDM (blue), fixed SM (red) and adaptive SM (green) at  $T = 1100 \text{ K}$ ,  $p = 1 \text{ bar}$ ,  $E_{max} = 52318 \text{ cm}^{-1}$ , reference method: CDM with  $N = 5238$ .

Relative computation times required to solve the linear ODE systems are shown for comparison in fig. 4.8. Whereas the processor- and software-dependent absolute CPU times are of limited interest, relative values are most useful to assess the efficiencies of the different methods. Here, it is not attempted to perform a quantitative analysis but

note that fixed SM is usually faster by about a factor of three compared to adaptive SM for a given accuracy, whereas adaptive SM finally reaches higher accuracy at the cost of longer CPU times. The reason for the higher speed is that SM with a certain number of basis functions is obviously faster than adaptive SM with an even smaller number of basis functions but with several (three in this example) iterations. This means that adaptive SM is particularly useful for low pressures, where a larger number of basis functions have to be used.

One may also ask about the computational demand for the solution of the ODE system itself as compared to the calculation of the necessary matrix elements. Here, please note that the integrations in eq. (4.6) approximately scale with  $N^2$ . This is negligible compared to effort for the solution of the ODE system by eigenvalue decomposition, which scales with  $N^3$  [QSS00]. In the current work, however, the author refrains from making any more detailed analysis but keep these numerical aspects for future investigations.

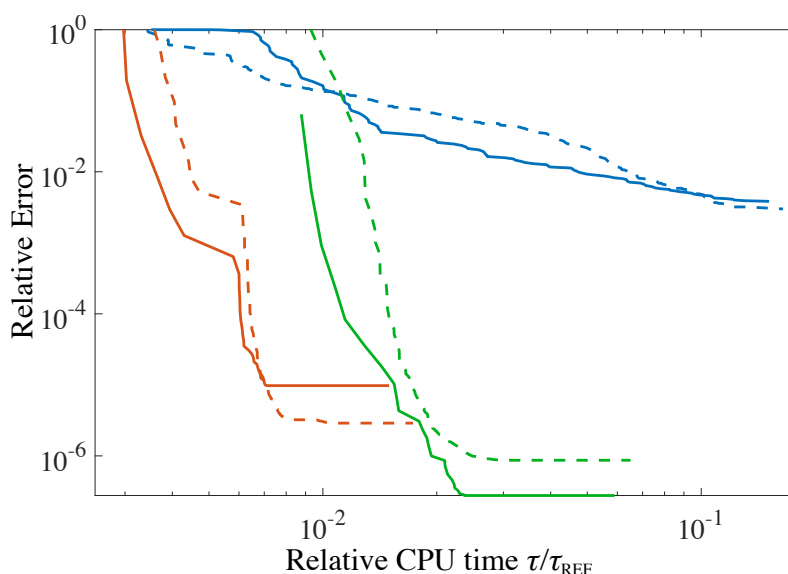


**Figure 4.8.:** Relative computation times for a given method necessary to obtain rate constants with given relative errors. System for thermal (solid lines) and chemical (dashed lines) activation conditions, with CDM (blue), fixed SM (red) and adaptive SM (green) at  $T = 1100$  K,  $p = 1$  bar,  $E_{max} = 52318$  cm $^{-1}$ , reference method: CDM with  $N = 5238$ .

The computation of pressure and temperature dependency of rate constant assumes a sufficiently large separation of first eigenvalue from the rest. As eigenvalues approach each other, the transition period is no longer negligible and thus the quasi stationary solution ( $t \rightarrow \infty$ ) will strongly depend on initial population. In our test case the sufficient eigenvalue separation is guaranteed only for moderate temperatures  $T \leq 1100$  K, where  $\lambda_1/\lambda_2 \geq 7$ . Consider fig. 4.9, solid lines show the evolution of the 25DMF2H through thermal activation with all eigenvalues and dashed lines – with the smallest eigenvalue  $\lambda_1$ . For temperatures 1100 K and below the difference is negligible but at high temperature, i.e. 1400 K, the 0.1% of the initial population is reached within  $0.883 \cdot 10^{-3}$  ms and with only one eigenvalue within  $1.101 \cdot 10^{-3}$  ms, which 1.25 times later. In the latter case eigenvalues are not well separated  $\lambda_1/\lambda_2 = 3.4$ .

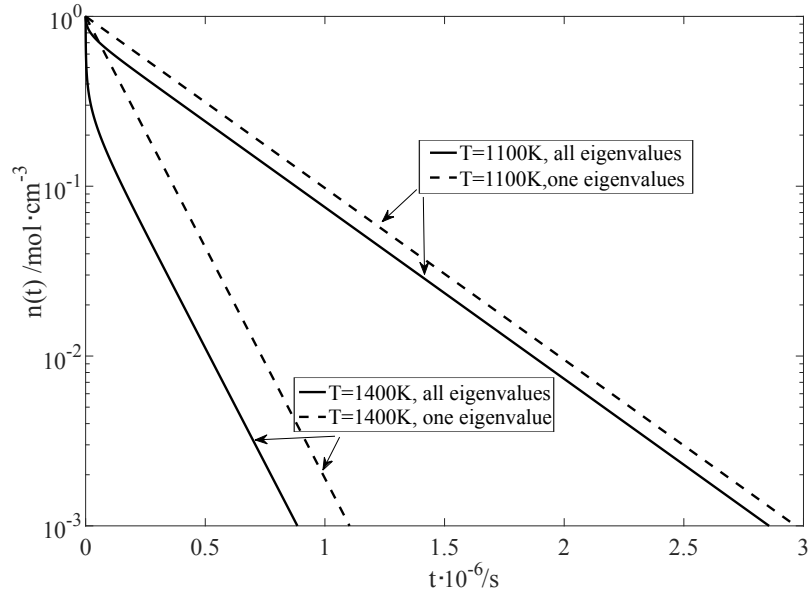
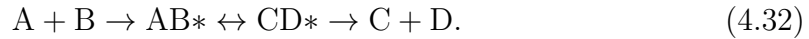


**Figure 4.9.:** Time dependence of the total population.

### 4.3. Multi-well Master Equation

In other scenario a molecule can undergo several isomerisation steps before transition to end products. Consider e.g. following reaction pathway:



In this chain now starting from the bimolecular reaction an excited complex  $AB^*$  is created, which can either decompose back to  $A + B$  or undergo isomerisation to  $CD^*$ . The latter can either decompose to  $C + D$  or isomerise back to  $AB^*$ .

This entire process is described by a set of two master equations:

$$\left\{ \begin{array}{l} \frac{\partial n_{AB}(E, t)}{\partial t} = \omega_{AB} \left[ \int_0^{\infty} P_{AB}(E, E') n_{AB}(E', t) dE' - n_{AB}(E, t) \right] \\ \quad - k_{CD \leftarrow AB}(E) n_{AB}(E, t) + k_{AB \leftarrow CD}(E) n_{CD}(E, t) + R_a f(E) \\ \frac{\partial n_{CD}(E, t)}{\partial t} = \omega_{CD} \left[ \int_0^{\infty} P_{CD}(E, E') n_{CD}(E', t) dE' - n_{CD}(E, t) \right] \\ \quad - \left( k_{C+D \leftarrow CD}(E) + k_{AB \leftarrow CD}(E) \right) n_{CD}(E, t) \\ \quad + k_{CD \leftarrow AB}(E) n_{AB}(E, t) \end{array} \right. , \quad (4.33)$$

here  $\omega_{AB}$  and  $\omega_{CD}$  are collision frequency for interaction of molecule  $AB^*$  and  $CD^*$  with the bath gas respectively, according to eq. (4.23);  $P_{AB}$  and  $P_{CD}$  probability density of a collision-induced transition, calculated with eq. (4.19),  $R_a f(E)$  is the source of chemically activated molecules from the reaction  $A + B \rightarrow AB^*$ , computed with eq. (4.24). Equation (4.33) includes energy dependent reaction rates for dissociation of  $AB^*$  into initial reactants  $A$  and  $B$ ,  $k_{A+B \leftarrow AB}$ , dissociation of  $CD$  into end-products  $C$  and  $D$ ,  $k_{C+D \leftarrow CD}$ . The main difference to single-well master equation

(4.17) are the coefficients of isomerisation from AB to CD,  $k_{\text{CD} \leftarrow \text{AB}}$ , and from CD to AB,  $k_{\text{AB} \leftarrow \text{CD}}$ .

The time dependent phenomenological rate constants can be calculated, if the following rate expressions are considered:

$$\begin{cases} \frac{d}{dt}[\text{AB}^*] = -k_{\text{CD} \leftarrow \text{AB}}(t)[\text{AB}^*] + k_{\text{AB} \leftarrow \text{CD}}(t)[\text{CD}^*] + \dot{q}_{\text{AB}^*} \\ \frac{d}{dt}[\text{CD}^*] = k_{\text{CD} \leftarrow \text{AB}}(t)[\text{AB}^*] - k_{\text{AB} \leftarrow \text{CD}}(t)[\text{CD}^*] - k_{\text{C}+\text{D} \leftarrow \text{CD}}(t)[\text{CD}^*] \end{cases}, \quad (4.34)$$

where  $\frac{d}{dt}[\text{AB}^*]$  and  $\frac{d}{dt}[\text{CD}^*]$  are the change of total population reactant  $\text{AB}^*$  and  $\text{CD}^*$  respectively, which are defined as:

$$\frac{d}{dt}[\text{AB}^*](t) = \frac{\int_0^{\infty} \frac{\partial}{\partial t} n_{\text{AB}}(E, t) dE}{\int_0^{\infty} \left( n_{\text{AB}}(E, t) + n_{\text{CD}}(E, t) \right) dE}, \quad (4.35)$$

$$\frac{d}{dt}[\text{CD}^*](t) = \frac{\int_0^{\infty} \frac{\partial}{\partial t} n_{\text{CD}}(E, t) dE}{\int_0^{\infty} \left( n_{\text{AB}}(E, t) + n_{\text{CD}}(E, t) \right) dE}, \quad (4.36)$$

with the corresponding total population of reactants  $\text{AB}^*$  and  $\text{CD}^*$ :

$$[\text{AB}^*](t) = \frac{\int_0^{\infty} n_{\text{AB}}(E, t) dE}{\int_0^{\infty} \left( n_{\text{AB}}(E, t) + n_{\text{CD}}(E, t) \right) dE}, \quad (4.37)$$

$$[\text{CD}^*](t) = \frac{\int_0^{\infty} n_{\text{CD}}(E, t) dE}{\int_0^{\infty} \left( n_{\text{AB}}(E, t) + n_{\text{CD}}(E, t) \right) dE}. \quad (4.38)$$

The constant flux of chemically activated molecules  $\dot{q}_{\text{AB}^*}$  is seen as:

$$\dot{q}_{\text{AB}^*}(t) = \frac{\int_0^{\infty} R_a f(E) dE}{\int_0^{\infty} \left( n_{\text{AB}}(E, t) + n_{\text{CD}}(E, t) \right) dE}, \quad (4.39)$$

The time (i.e. temperature and pressure) dependent rate constants  $k_{\text{CD} \leftarrow \text{AB}}(t)$ ,  $k_{\text{AB} \leftarrow \text{CD}}(t)$  and  $k_{\text{C}+\text{D} \leftarrow \text{CD}}(t)$  are not independent. If system approaches thermodynamic equilibrium the first two constant are related via an equilibrium constant (see eq. (2.96):

$$K^c = \frac{k_{\text{CD} \leftarrow \text{AB}}(t)}{k_{\text{AB} \leftarrow \text{CD}}(t)}. \quad (4.40)$$

The above permits to write a linear system for computation of time dependent rate constants:

$$\begin{pmatrix} \frac{d}{dt}[\text{AB}^*] - \dot{q}_{\text{AB}^*} \\ \frac{d}{dt}[\text{CD}^*] \end{pmatrix} = \begin{pmatrix} -\left([\text{AB}^*] - \frac{1}{K^c}[\text{CD}^*]\right) & 0 \\ \left([\text{AB}^*] - \frac{1}{K^c}[\text{CD}^*]\right) & [\text{CD}^*] \end{pmatrix} \begin{pmatrix} k_{\text{CD} \leftarrow \text{AB}}(t) \\ k_{\text{C}+\text{D} \leftarrow \text{CD}}(t) \end{pmatrix} \quad (4.41)$$

The two-well ME (4.33) can be written in a more general form [MK06]:

$$\begin{aligned} \frac{\partial n_i(E, t)}{\partial t} = & \omega_i \left[ \int_0^\infty P_i(E, E') n_i(E', t) dE' - n_i(E, t) \right] \\ & + \sum_{\substack{N_W \\ j \neq i}} \left( k_{i \leftarrow j} n_j(E, t) - k_{j \leftarrow i} n_i(E, t) \right) + \sum_P^{N_P} k_{p \leftarrow i} n_i(E, t) + R_{a,i} f_i(E), \\ & \forall i = 1, \dots, N_W, \end{aligned} \quad (4.42)$$

where  $N_W$  is number of potential wells and  $N_P$  – number of products.

Once the solution for the evolution of the population of reactants  $n_i(E, t)$  is available the time dependent rate constants  $k_i(t)$  can be derived in a similar fashion as eq. (4.41).

$$\frac{d}{dt} c_i = \sum_{j \neq i}^{N_W} k_i(t) \quad (4.43)$$

### 4.3.1. Isomerisation of Allene to Propyne

As a second example for computation of reaction rates the isomerisation of allene (a-C<sub>3</sub>H<sub>4</sub>) to propyne (p-C<sub>3</sub>H<sub>4</sub>) is considered.



Both allene and propyne are important in combustion chemistry, as they produce in rich flames propargyl (C<sub>3</sub>H<sub>3</sub>), through abstraction of hydrogen atom. The latter has the ability to react with itself and form cyclic species like benzene, phenyl or fulvene [WMD06].



The simplified potential surface is displayed in fig. 4.10. The isomerisation between allene and propyne can undergo several stages, e.g. cyclopropene (c-C<sub>3</sub>H<sub>4</sub>) [KKM94, MK03]. However this reactant is noticeable only at very high pressures ( $p \rightarrow \infty$ ), because c-C<sub>3</sub>H<sub>4</sub> tend to decompose to a-C<sub>3</sub>H<sub>4</sub> almost instantly, compared to the time scale of other processes.

Specific rate coefficients were calculated from RRKM theory<sup>2</sup> [MJCL98, DLW99, Shi72, Her66] on the basis of an averaged potential energy diagram CCSD(T)/B3LYP (see fig. 4.10). Densities and sums of states were determined with direct counting procedures for a total angular momentum quantum number of  $J = 60$ . For the calculation of the collision frequency,  $\omega$ , argon was chosen as the bath gas with the following binary Lennard-Jones parameters for both allene and propyne:  $\varepsilon_{\text{C}_3\text{H}_4-\text{Ar}}/k_B = 93.3 \text{ K}$  and  $\sigma_{\text{C}_3\text{H}_4-\text{Ar}} = 3.5 \text{ \AA}$ . For collisional energy transfer probability, a density-of-states-weighted exponential-down model, eq. (4.30), with  $\alpha = 250 \text{ cm}^{-1}$ , was used.

<sup>2</sup>Prof. Matthias Olzmann, private communication

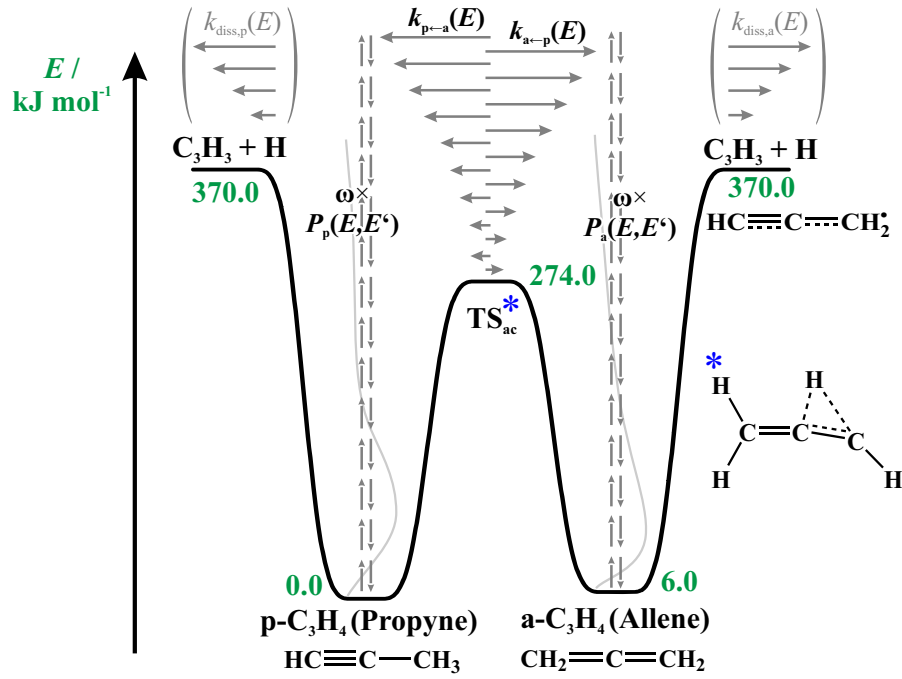


**Figure 4.10.:** Schematic potential energy diagram, including zero-point energy, relative to Propyne.

This process is described by a set of two MEs, compare eq. (4.33):

$$\begin{cases} \frac{\partial n_a(E, t)}{\partial t} = \omega_a \left[ \int_0^\infty P_a(E, E') n_a(E', t) dE' - n_a(E, t) \right] \\ \quad - k_{p \leftarrow a}(E) n_a(E, t) + k_{a \leftarrow p}(E) n_p(E, t) + R_a f(E), \\ \frac{\partial n_p(E, t)}{\partial t} = \omega_p \left[ \int_0^\infty P_p(E, E') n_p(E', t) dE' - n_p(E, t) \right] \\ \quad - \left( k_{o \leftarrow p}(E) + k_{a \leftarrow p}(E) \right) n_p(E, t) + k_{p \leftarrow a}(E) n_p(E, t). \end{cases} \quad (4.44)$$

Here  $n_a$  is population of allene;  $n_p$  – population of propyne;  $P_a$  is collisional energy transfer probability for allene;  $P_p$  is collisional probability for propyne;  $\omega_a$  is collision frequency with bath gas for allene;  $\omega_p$  is collision frequency – for propyne;  $k_{p \leftarrow a}(E)$  is energy dependent reaction rate, describing transition of allene to propyne;  $k_{a \leftarrow p}(E)$  is energy dependent reaction rate, describing transition of propyne to allene;  $k_{o \leftarrow p}(E)$  is energy dependent reaction rate, describing transition of propyne to propargyl;  $R_a f(E)$  is chemical source of allene.

The focus of the current application of spectral method is on isomerisation of allene to propyne, ignoring loses to propargyl radical. In fact, according to experimental observation [HNM<sup>+</sup>89] for lower temperatures propyne is the dominating species in allene isomerisation and decomposition, due to much slower decomposition of allene and propyne to propargyl [MK03]. A typical example of this isomerisation is shown in fig. 4.11. Where starting only with a-C<sub>3</sub>H<sub>4</sub> (left), the process reaches equilibrium where both a-C<sub>3</sub>H<sub>4</sub> and p-C<sub>3</sub>H<sub>4</sub> present. The process is initiated with allene alone distributed with equilibrium Boltzman distribution for the specified temperature (fig. 4.11(right)), reaching new thermo-chemical equilibrium with propyne.

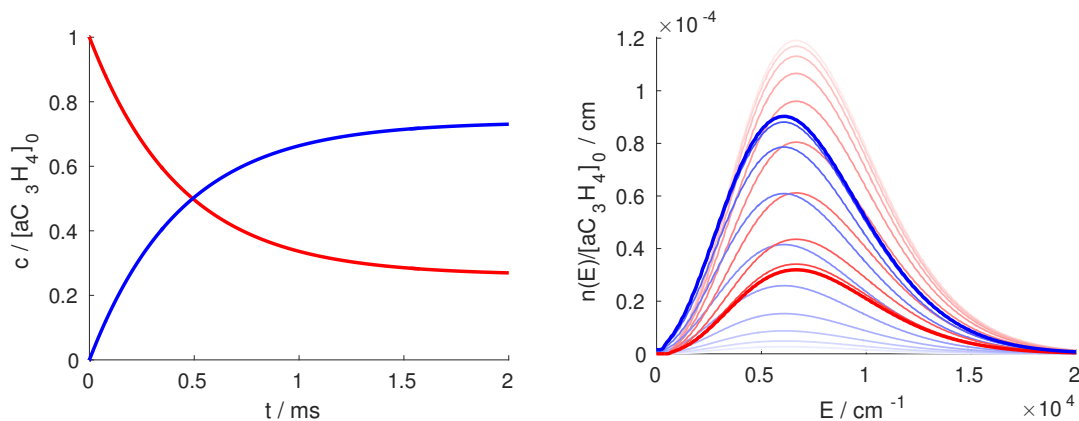


**Figure 4.11.:** Example of allene to propyne isomerisation at  $T = 1400$  K and  $P = 0.5$  bar. Colour intensity represent time evolution.

The question of mutual isomerisation and decomposition of allene and propyne was thoroughly investigated in a number of works both experimentally and theoretically [GFB<sup>+</sup>11, MK03, KMS<sup>+</sup>97, HNM<sup>+</sup>89, KOBGL88, WK87, LFB75]. Low temperature results are summarised in fig. 4.12. Coloured lines represent results of current work for different pressures. They show a good agreement with experimental results of Hidaka et.al.[HNM<sup>+</sup>89] and Lifshitz et.al.[LFB75]. Arrhenius approximation from theoretical study of Miller et.al. [MK03] semi empirical analysis of Wu et.al. [WK87] correlate with the present work within experimental uncertainties.

In order to calculate time dependent reaction rate  $k_{p \leftarrow a}(t)$ , an equilibrium constant  $K^c$  was used (see §4.3), such that:

$$k_{a \leftarrow p} = K^c k_{p \leftarrow a}. \quad (4.45)$$

The equilibrium constant was calculated from thermodynamic data eq. (2.96). The required data was acquired from the NIST Chemistry WebBook<sup>3</sup>. Then according to reaction (R1):

$$\frac{d[\text{a-C}_3\text{H}_4]}{dt} = -k_{p \leftarrow a} ([\text{a-C}_3\text{H}_4] - K^c [\text{p-C}_3\text{H}_4]) \quad (4.46)$$

which leads to (see §4.3):

$$k_{p \leftarrow a}(t) = - \frac{\int_0^\infty \frac{\partial}{\partial t} n_a dE}{\int_0^\infty (n_a - K^c n_p) dE}. \quad (4.47)$$

Figure 4.13 (left) shows an example of time dependent rate constants for  $T = 1200$  K and  $P = 0.5$  bar. Dashed line shows asymptotic rate constant, which is commonly used in reaction mechanisms (see e.g. [GLT83, MK06]) and presented in the Arrhenius plot (fig. 4.12). The use of asymptotic rate constants in mechanisms leads to a systematic error, for low temperatures in particular. Figure 4.13 (right) shows concentration of reactant with time dependent rate constant and with constant asymptotic rate

<sup>3</sup><http://webbook.nist.gov>

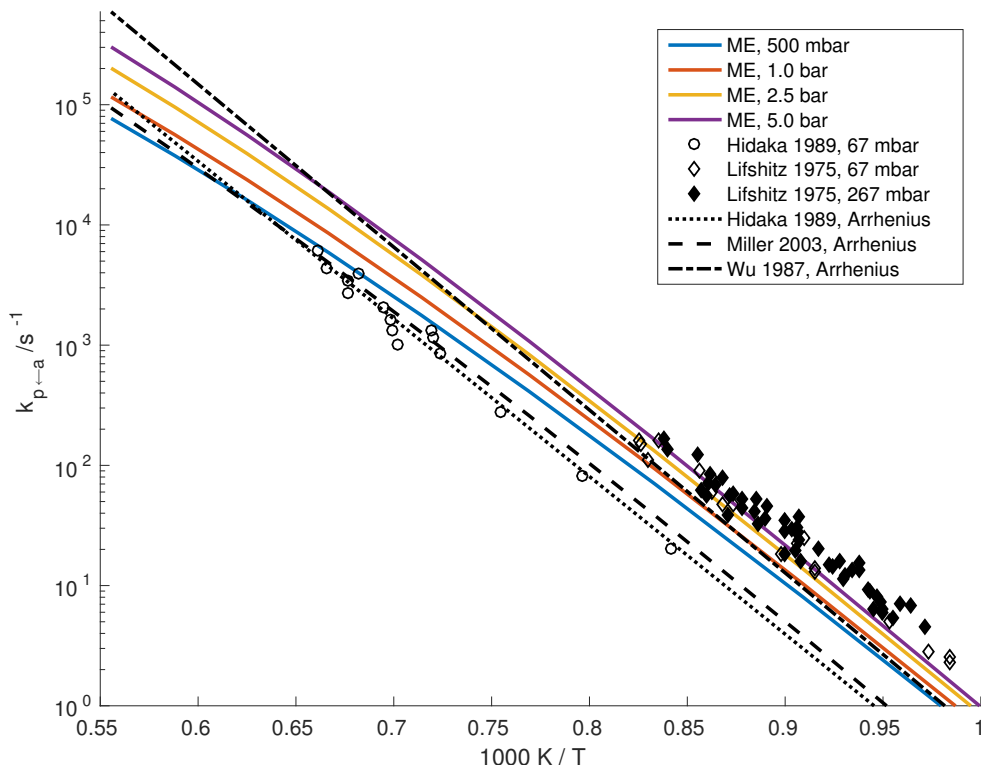


**Figure 4.12.:** Summary of reaction rates of allene isomerisation.

constant. It is to see that the equilibrium concentrations noticeably differ: 6.5 % for a-C<sub>3</sub>H<sub>4</sub> and 2.1 % for p-C<sub>3</sub>H<sub>4</sub>. If a relative error is defined as

$$e = \left| \frac{c_0(\infty) - c(\infty)}{c(\infty)} \right| \quad (4.48)$$

where  $c_0$  is species concentration computed with constant asymptotic rate constant and  $c$  is species concentration computed with time dependent rate constant, then it can be seen that this error is temperature dependent (fig. 4.14) and is approximately proportional to reciprocal of the temperature. No pressure dependency of this error was observed within the studied range. The highest error corresponds to allene concentration at lower temperatures (fig. 4.14 (left)) but the relative error for propyne at this temperature is the lowest.

It is possible to adjust the rate constant, used further in mechanism, that minimises error eq. (4.48) but the concentration of reactants within realistic time remains dependent on initial distribution over energy levels.

The results were verified with different resolutions, i.e. number of basis functions  $N_{BF}$ . The following measure of error for convergence tests was used:

$$e(t) = \left| \frac{c(t) - c_{\text{ref}}}{c_{\text{ref}}} \right|, \quad (4.49)$$

where  $c_{\text{ref}}$  is reference solution with  $N_{BF} = 200$ . fig. 4.15 (left) shows exemplarily error over time for  $T = 1200$  K and  $P = 1$  bar. For other temperature and pressure the

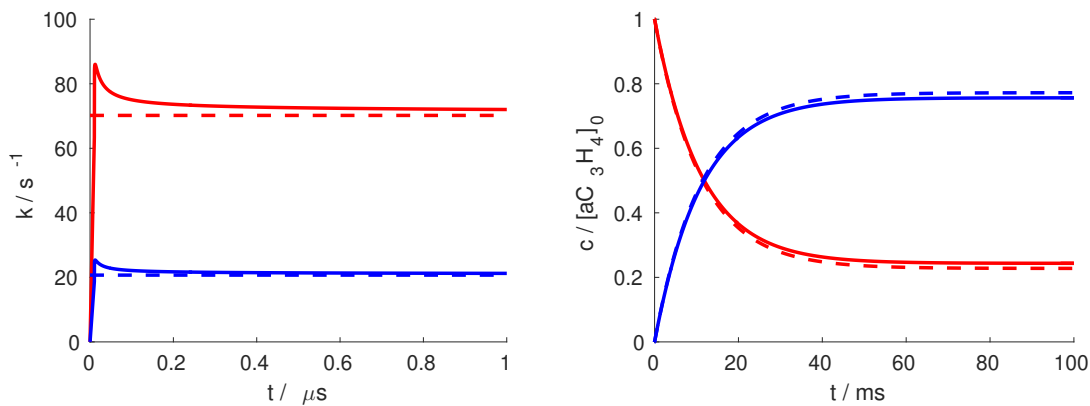


**Figure 4.13.:** Rate constant comparison for  $T = 1200$  K and  $P = 0.5$  bar: Time dependent vs. asymptotic rate constant (left); evolution of concentration with time dependent vs. fixed asymptotic rate constant (right). Red corresponds to allene ( $k_{p \leftarrow a}$  and  $[a-C_3H_4]$ ), blue – propyne ( $k_{a \leftarrow p}$  and  $[p-C_3H_4]$ ). Solid lines represent time dependent values of rate constants, dashed line – fixed asymptotic rate constants.

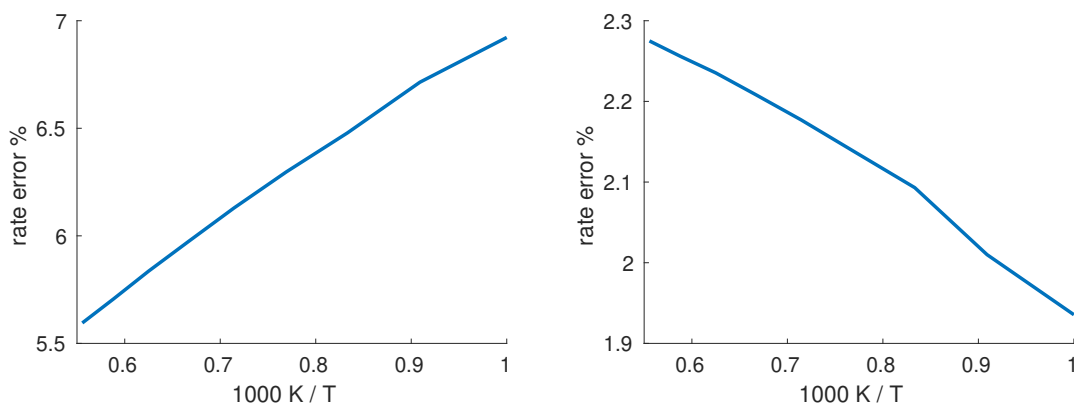


**Figure 4.14.:** Relative error for rate constants at different temperatures: concentration of allene (left); concentration of propyne (right).

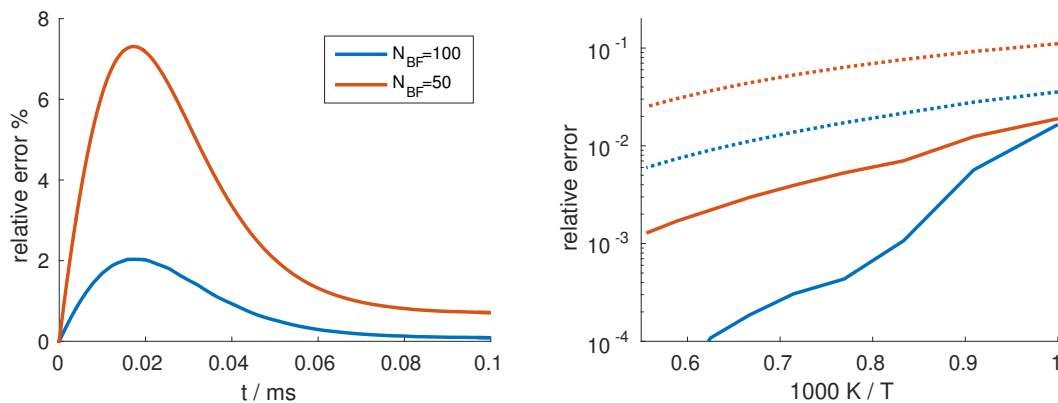


**Figure 4.15.:** Resolution test for computation of rate constant  $k_{p \leftarrow a}$ : relative error over time for  $T = 1200$  K and  $P = 1$  bar (left); dependence of relative error on temperature. All data is in relation to  $N_{BF} = 200$ . Dotted line shows maximum of error, solid line asymptotic error.

---

form remains the same. The results are summarised in fig. 4.15 (right) for  $P = 5$  bar. Results for lower pressures have smaller relative errors. It can be seen that with increase of  $N_{BF}$  from 50 to 100 maximal deviations in results improve by about 5%, by increase of resolution from 100 to 200 the results improve by maximum 2%. The convergence for higher temperatures is of several magnitudes better. The difference in asymptotic results between  $N_{BF} = 100$  and  $N_{BF} = 200$  is below 1%. Meaning that  $N_{BF} = 100$  is more than sufficient for technical applications for temperatures above 1000 K.



# 5. Applications to combustion systems

## 5.1. Benchmarking and code validation

One of the main difficulties in the accurate numerical modelling of ignition is in simultaneous solution of both gas-dynamical and thermochemical processes. Generally these processes are described by conservation laws equipped with source term, representing chemical reactions. This is complicated by molecular diffusion of components, which has a large influence on the development of instabilities [GYC81].

Small changes in initial composition and temperature may lead to large effect on ignition. For this reason a number of benchmarks were created, which allow to evaluate the performance of chemical and transport models, e.g. ignition and flame propagation problems. These benchmark provide such a configuration, that the mathematical model is simplified, e.g. to 0D or 1D. In this section, a validation of thermochemical and hydrodynamical models is conducted, using ignition delay and laminar flame velocities as observable parameters to access the quality of modelling and of computation.

### 5.1.1. Ignition delay of Hydrogen-Oxygen mixtures

For homogeneous systems the ignition can be described by a system of stiff ordinary differential equations (ODE). The general performance and accuracy of the proposed time integration method (see §3.3) was tested in MATLAB<sup>1</sup> on the classical stiff benchmarks (see Appendix C). The main purpose of this section is to validate the implemented chemical kinetics models and asses their sensitivity in respect to initial parameters.

---

<sup>1</sup><http://www.mathworks.com>

### 5.1.1.1. Mathematical model for homogeneous systems

On the basis of the general conservation equations (see §2.1), the following ODEs can be defined [MW88]:

$$\left\{ \begin{array}{l} \frac{d}{dt} \left( V \left( \sum_j c_j \bar{h}_j - P \right) \right) = V \dot{q}, \\ \frac{d}{dt} \left( V c_i \right) = V \dot{\omega}_i, \\ \forall i = 1, \dots, N_S. \end{array} \right. \quad (5.1)$$

In order to close the equation system (5.1), the ideal gas law is applied:

$$PV = nR_0T, \quad (5.2)$$

where the number of moles in gas:

$$n = V \sum_i c_i. \quad (5.3)$$

Two cases for homogeneous systems can be defined, which describe homogeneous auto-ignition problem [MW88]:

- Volume is function of time,  $V = V(t)$ ,

$$\begin{pmatrix} 1 & 0 & 0 & \cdots & 0 \\ 0 & \sum_j (\bar{c}_{P_j} - R_0) c_j & 0 & \cdots & 0 \\ c_1/V & 0 & 1 & \cdots & 0 \\ \vdots & \vdots & \vdots & \ddots & \vdots \\ c_{N_S}/V & 0 & 0 & \cdots & 1 \end{pmatrix} \frac{d}{dt} \begin{pmatrix} V \\ T \\ c_1 \\ \vdots \\ c_{N_S} \end{pmatrix} = \begin{pmatrix} \dot{V} \\ \dot{q} - \sum_j (\bar{h}_j - R_0T) \dot{\omega}_j \\ \dot{\omega}_1 \\ \vdots \\ \dot{\omega}_{N_S} \end{pmatrix} \quad (5.4)$$

- Pressure is function of time,  $P = P(t)$ ,

$$\begin{pmatrix} 1 & -V/T & 0 & \cdots & 0 \\ 0 & \sum_j (\bar{c}_{P_j} - R_0) c_j & 0 & \cdots & 0 \\ c_1/V & 0 & 1 & \cdots & 0 \\ \vdots & \vdots & \vdots & \ddots & \vdots \\ c_{N_S}/V & 0 & 0 & \cdots & 1 \end{pmatrix} \frac{d}{dt} \begin{pmatrix} V \\ T \\ c_1 \\ \vdots \\ c_{N_S} \end{pmatrix} = \begin{pmatrix} V \left( \sum_j \dot{\omega}_j / \sum_j c_j - \dot{P}/P \right) \\ \dot{q} - \sum_j (\bar{h}_j - R_0T) \dot{\omega}_j \\ \dot{\omega}_1 \\ \vdots \\ \dot{\omega}_{N_S} \end{pmatrix} \quad (5.5)$$

For the current study three following combustion models for the reaction hydrogen with oxygen were selected:

- Mechanism of J. Warnatz and U. Maas (Warnatz mechanism), containing 38 elementary reactions and 8 species [MW88];
- Mechanism of A. Keromnes et. al. (Keromnes mechanism), containing 46 elementary reactions and 8 species [KMH<sup>+</sup>13];

- Keromnes mechanism optimised at Institute of Chemistry, Eötvös University, Hungary (ELTE mechanism), containing 58 elementary reactions and 11 species [VNO<sup>+</sup>15].

As an evaluation benchmark the ignition delay, measured at the time of strongest increase of concentration of OH radical, is used. Firstly, the results of ignition delays are compared with the well established codes HOMREA [MW88] and CHEMKIN<sup>2</sup>. Secondly, the performance of the 3 mechanisms using the set of experimental data is evaluated.

For ignition delay studies eq. (5.5) is used, which describes expanding volume with constant pressure inside.

Figure 5.1 shows pressure and temperature dependence of ignition delay predicted by the Warnatz mechanism. The study was performed for temperatures in the range from 900 to 2000 K, and pressures in the range from 1 to 50 bar. Initial composition is the stoichiometric mixture of hydrogen with air:  $X_{\text{H}_2} = 21/71$ ,  $X_{\text{O}_2} = 21/142$  and  $X_{\text{N}_2} = 79/142$ . The same study was performed with Phlogia (solid lines), HOMREA (dotted lines) and CHEMKIN (dashed lines). The results of computation of all programmes are optically identical for all pressure, as seen in the Arrhenius plot fig. 5.1. Marginal difference is to see only for high temperatures.

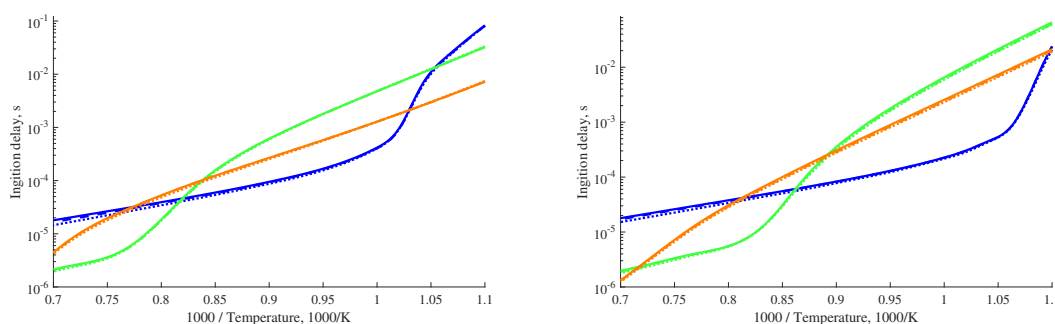


**Figure 5.1.:** Pressure and temperature dependence of ignition delay computed with Warnatz (left) and Keromnes (right) mechanisms for stoichiometric mixture of hydrogen with air. Solid lines correspond to computations with Phlogia, dotted lines – HOMREA, dashed line – CHEMKIN. Blue colour represents pressure 1 bar, green – 10 bar and red – 50 bar.

The following figure shows the dependency on temperature and on equivalence ratio:

$$\Phi = \frac{X_{\text{H}_2}}{X_{\text{O}_2} + X_{\text{N}_2}} \frac{X_{\text{O}_2}^{\text{ST}} + X_{\text{N}_2}^{\text{ST}}}{X_{\text{H}_2}^{\text{ST}}}, \quad (5.6)$$

where the superscript “ST” corresponds to the stoichiometric mixture composition.

Here, Warnatz mechanisms, fig. 5.2 (left) and Keromnes mechanisms are compared, fig. 5.2 (right), within temperature range from 900 to 2000 K, for pressure 1 bar and equivalence ratios 0.2, 1 and 5. The results of all three programmes are also almost identical. Very small differences can be seen only at high temperatures.

<sup>2</sup><http://www.reactiondesign.com/products/chemkin/chemkin-2>

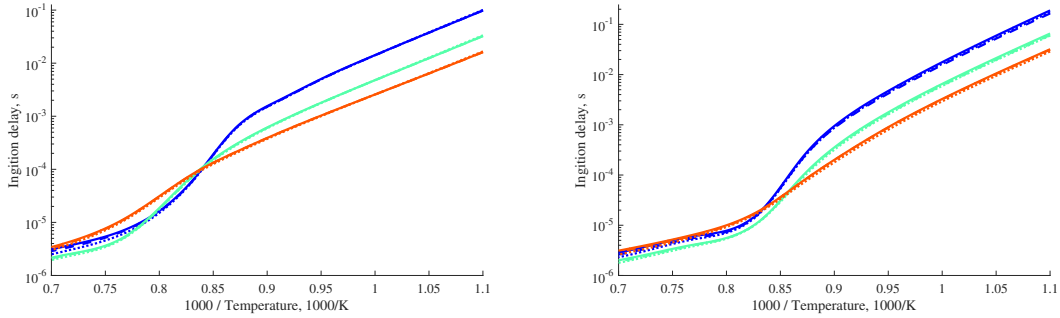


**Figure 5.2.:** Equivalence ratio and temperature dependence of ignition delay computed with Warnatz (left) and Keromnes (right) mechanisms for pressure 10 bar (left). Red represents  $\Phi = 0.2$ , green –  $\Phi = 1$  and blue –  $\Phi = 5$ . Solid lines correspond to computations with Phlogia, dotted lines – HOMREA and dashed lines – CHEMKIN.

Now it is considered, how the three mechanisms perform relative to one another and relative to independent shock tube experiments of J. Herzler and C. Naumann [HN09] and Y. Zhang et. al, [ZHW<sup>+</sup>12]. The mixture of 1 H<sub>2</sub> and 1 O<sub>2</sub> was highly diluted with Argon ( $X_{\text{H}_2} = 0.035$ ,  $X_{\text{O}_2} = 0.035$  and  $X_{\text{Ar}} = 0.932$ ). The ignition delay was investigated for pressures of 1, 4 and 16 bar. Numerical data was prepared with Phlogia, using constant pressure approach eq. (5.5). The results are summarised in Figure 5.3.

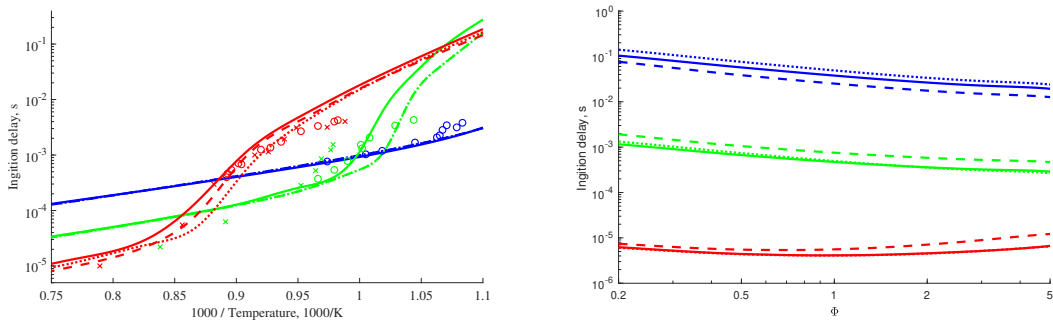


**Figure 5.3.:** Comparison of ignition delay time computed with Warnatz (dashed lines), Keromnes (dotted lines) and ELTE (solid lines) mechanisms: On the left – Temperature dependence for pressure 1 (blue), 4 (green) and 16 bar (red); On the right – Equivalence ratio dependence for temperature 900 (blue), 1100 (green) and 1300 K (red). Circles are experimental results of J. Herzler and C. Naumann [HN09]; Crosses represent experimental data of Y. Zhang et. al. [ZHW<sup>+</sup>12]. Mixture composition  $X_{\text{H}_2} = 0.035$ ,  $X_{\text{O}_2} = 0.035$  and  $X_{\text{Ar}} = 0.932$ .

At pressure of 1 bar (shown in blue) all three mechanisms give almost identical results, with difference not exceeding 6%. At this pressure the simulated results pass directly through the measured points [HN09], starting from 950 K. Below this temperature a large discrepancy of experimental results is observed. In the case of an elevated pressure of 4 bar (shown in green), Warnatz and Keromnes mechanisms are overlapping identically, whilst ELTE mechanism shows a significant deviation up to 80% for temperatures below 1020 K. The ELTE mechanism seems to fit better experimental data of J. Herzler and C. Naumann. However, the discrepancy of experimental data, comparing results of J. Herzler and C. Naumann and Y. Zhang

et. al, is of the same magnitude, 65 %, as the difference between the mechanisms. At relatively high pressure of 16 bar (shown in red), the experimental data is much better correlated: compare red crosses with red circles. However, the results of different mechanisms deviate up to 65 %, with Keromnes mechanism laying in the middle.

In most considered cases Keromnes and Warnatz mechanisms deliver comparable results, whilst the ELTE mechanism has a significant deviation, particularly for elevated pressures. This deviation is within the uncertainty of experimental results. Although there is still a noticeable discrepancy between chemical models, they still show a high sensitivity of ignition delay times on initial mixture composition and temperature. For instance small change of initial temperate of 10 K may lead to change of ignition delay of more than 50 %, which is particularly pronounced by elevated pressures (see fig. 5.3); or a small change in equivalence ratio of 0.1 can lead to a change of ignition delay of more than 25 % (see fig. 5.2).

### 5.1.2. Unconfined hydrogen-air flame

The main purpose of this section is to assess the space-time integration approach and selected hydrodynamic and transport models, coupled with thermochemistry. The method is validated with a well established code INSFLA [MW88, Maa88], which uses Lagrangian coordinate and homogeneous pressure.

For validation purposes, the Warnatz mechanism [MW88] was chosen. As the ignition delay study §5.1.1 has shown that considered mechanism have similar chemical behaviour and the transport coefficients of these mechanism are also identical, the validation results are expected to be similar for Keromnes and ELTE mechanisms.

For validation a closed volume  $x \in [0, 0.5]$  m was chosen. The solution was integrated over the time interval of  $t \in [0, 0.15]$  ms. In order to ignite the mixture, a hot spot near the left boundary was created, while keeping the initial pressure in the whole volume constant:

$$\begin{cases} v_0 = 0, \\ T_0(x) = 300 \text{ K} + (1200 \text{ K})e^{-(x/l)^2}, \\ c_{0,i}(x) = X_{i,0} \frac{1 \text{ bar}}{R_0 T_0(x)}, \quad i = 1, \dots, N_S, \end{cases} \quad (5.7)$$

The hot spot width  $l = 0.5$  mm was chosen such that the minimal ignition energy is provided. The ignition problem was considered for  $X_{H_2} = 2/3$ ,  $X_{O_2} = 1/3$  and other species were set to zero.

The boundary conditions, representing symmetry relation ( $r = 0$ ) and adiabatic “wall” ( $r = L$ ) are given as:

$$\begin{cases} v(t, 0) = v(t, L) = 0, \\ \frac{\partial}{\partial \xi} T(t, 0) = \frac{\partial}{\partial \xi} T(t, L) = 0, \\ \frac{\partial}{\partial \xi} c_i(t, 0) = \frac{\partial}{\partial \xi} c_i(t, L) = 0, \quad \forall i = 1, \dots, N_s. \end{cases} \quad (5.8)$$

In order to assess the error, the following relative error definition is used:

$$\epsilon_{rel} = \frac{\int_0^L (u(x) - u_{ref}(x)) dx}{L \max_x u(x)}, \quad (5.9)$$

where  $u(x)$  considered state variable, e.g. temperature, pressure or species concentration,  $u_{ref}(x)$  – reference solution for the state variable.

During the ignition a pressure wave is generated, which propagates ahead of the flame front and preheated the initial mixture from 300 K to 318 K (see fig. 5.4 (left)) and raised the pressure to 1.2 bar (see fig. 5.4 (right)). At the current stage the primary focus is on stationary flame profiles. For this reason the comparison was conducted in the isobaric regime of INSFLA, with adjusted initial values of temperature  $T_0 = 318$  K and pressure  $P = 1.2$  bar.

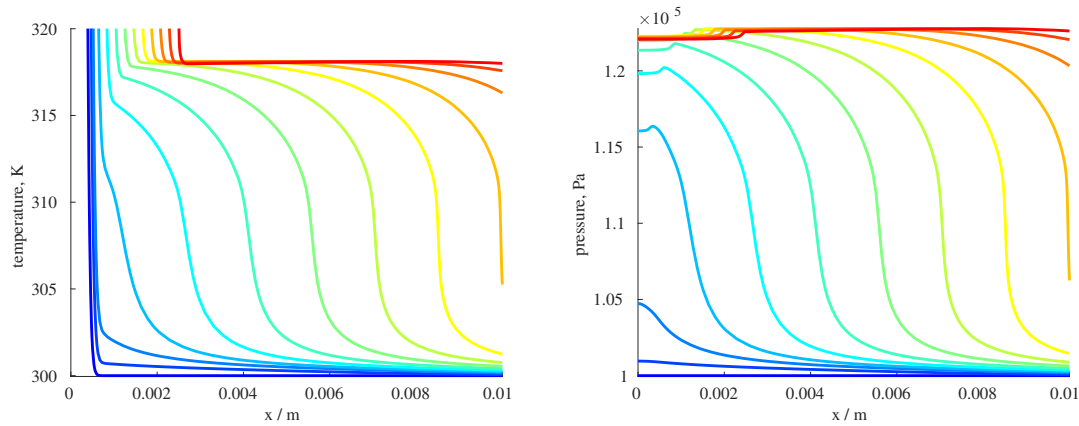


**Figure 5.4.:** Pressure wave propagation after ignition shown on profiles of temperature (left) and pressure (right) for  $t \in [0, 10^{-5}]$

It was observed that stationary profiles for species concentration are optically almost indistinguishable (see fig. 5.5). The mole fraction of OH radical near adiabatic limit has the largest deviation. The relative difference is however less than 0.2%, which can be attributed to the isobaric approximation in INSFLA. The computed flame front velocity is also close: INSFLA is 87.1 m/s and Phlogia – 90.5 m/s.

The resulted stationary profile for temperature is also virtually identical between INSFLA and Phlogia calculations, compare fig. 5.6 (left). Obviously the pressure profile in INSFLA is constant over the space, which is seen as dotted line in fig. 5.6 (right), but the compressibility leads to a tiny jump in pressure at the flame position of 500 Pa (around 0.4%). The effects of RTOL (specified relative tolerance in space) on computation are best seen on this pressure jump. The RTOL provides an equivalent to the spacial resolution. Solution with  $RTOL=10^{-4}$  is characterised by an optically perfectly smooth jump; with  $RTOL=10^{-3}$  – little oscillations are seen near the jump; and with  $RTOL=10^{-2}$  – the oscillations are getting significantly stronger. Meanwhile the other profiles like temperature or species are optically indistinguishable for all three tolerances. In fact the solution with  $RTOL=10^{-4}$  is also a subject to oscillations, which are of the order of magnitude of 0.01%. These oscillation come from the spectral nature of the method.

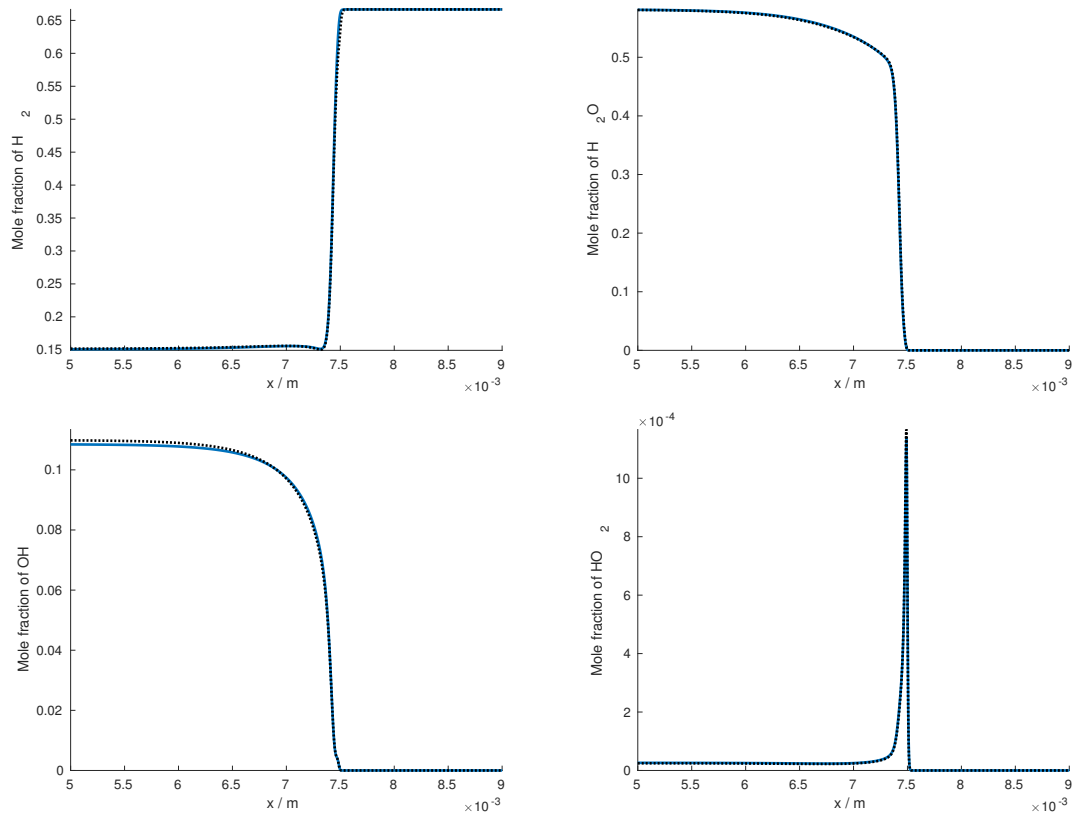


**Figure 5.5.:** Stationary profiles of hydrogen-oxygen flame for species: Mole fraction of  $H_2$  (top-left), mole fraction of  $H_2O$  (top-right), mole fraction of  $OH$  (bottom-left) and mole fraction of  $HO_2$  (bottom-right). Solid line correspond to Phlogia results and dotted line – INSFLA.

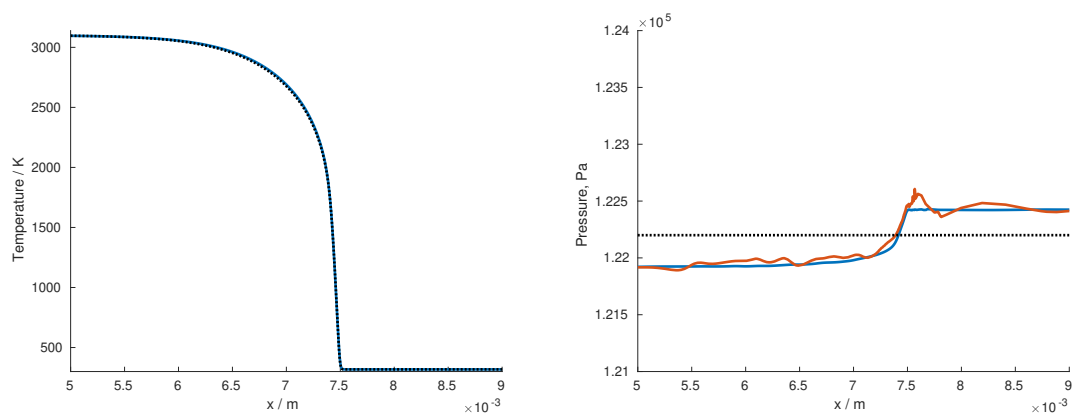


**Figure 5.6.:** Stationary profiles of hydrogen-oxygen flame for temperature (left) and pressure (right). Solid line corresponds to Phlogia results and dotted line – INSFLA. Blue colour represents  $RTOL=10^{-4}$ , red –  $RTOL=10^{-3}$ .

The RTOL parameter describes the maximum of the amplitude of the last coefficient of the truncated series (see §D.4) and can be used as a measure for numerical error of the method. The relative error eq. (5.9) shows the same characteristic behaviour as the oscillation amplitude. This is illustrated in fig. 5.7, where the relative error for pressure is compared to the amplitude of the oscillations and shown as function of the RTOL parameter. Here, as a reference solution  $P_{ref}$  the solution with  $RTOL=10^{-5}$  has been employed.

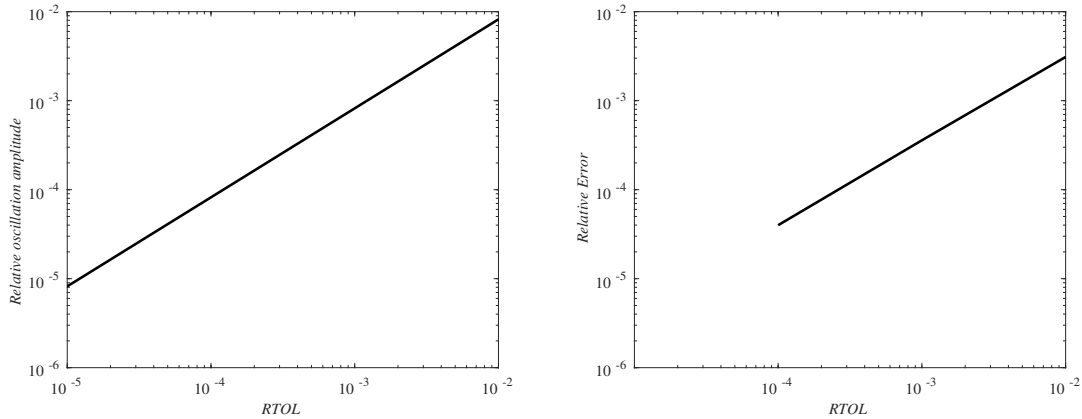


**Figure 5.7.:** Relative amplitude of numerical oscillations (left) and relative error for pressure (right).

Typical computational time with accuracy  $RTOL = 10^{-3}$  accounts for 30 minutes on Intel®Core™i7-4960HQ CPU @ 2.60GHz, with most computational efforts given to the resolution of the pressure wave created after the ignition. Thickness of the pressure wave is accounted to  $6 \mu\text{m}$  and it travels with  $\propto 500 \text{ m/s}$ , which reduces the maximal time increment through CFL condition to  $\propto 10^{-8} \text{ s}$ . During the physical time of  $0.15 \text{ ms}$  the pressure wave has travelled  $7 \text{ cm}$ , whilst the flame – only  $1 \text{ cm}$ . Smoothing the pressure wave with frequency damping filter §3.4.4 or choosing a smaller domain, e.g.  $10 \text{ mm}$ , with non-reflecting outflow [PL92] allows reducing the computational time to a few minutes, without affecting the presented results.

### 5.1.3. Laminar flame speed of hydrogen-air mixtures

The laminar burning velocity is the basic characteristic of combustion systems [WMD06]. There are numerous algorithms how to estimate the laminar burning rate on the basis of data registered experimentally including the flame speed in the laboratory referenced frame, flame front curvature, stretch factor etc. [WLC<sup>+</sup>15]. A straightforward algorithm offers the Mikhelson<sup>3</sup> formula for the flame speed:

$$v_f = u_L \frac{\rho_0}{\rho_b}, \quad (5.10)$$

where  $u_L$  is the laminar burning velocity and  $\rho_0/\rho_b$  is expansion ratio. Here  $\rho_0$  density of fresh mixture and  $\rho_b$  is density of combustion products.

In order to observe a steady propagating flame, a large vessel is chosen. The vessel is filled with a test mixture of given composition at given thermodynamic state. The

<sup>3</sup>Mikhelson, V.A., “O normal’noy skorosti vosplameneniya gazovykh smesey”, 1927

dimensions of the vessel are chosen as large as  $L = 10$  m, such that to minimise the effects of boundary conditions on flame dynamics, during early stages of its development. Boundary conditions representing symmetry condition and adiabatic wall are given by eq. (5.8). The initial conditions are similar to the previous section §5.1.2. The ignition is initiated with a hot-spot of 1500 K in the region of 2 mm radius adjacent to the left wall.

Both initial mixture composition and pressure were imposed to be constant in the whole computational domain. Herewith,  $p_0 = 1.0$  bar and  $T_0 = 300$  K. The mixture was assumed to be quiescent. The calculation was performed with different codes:

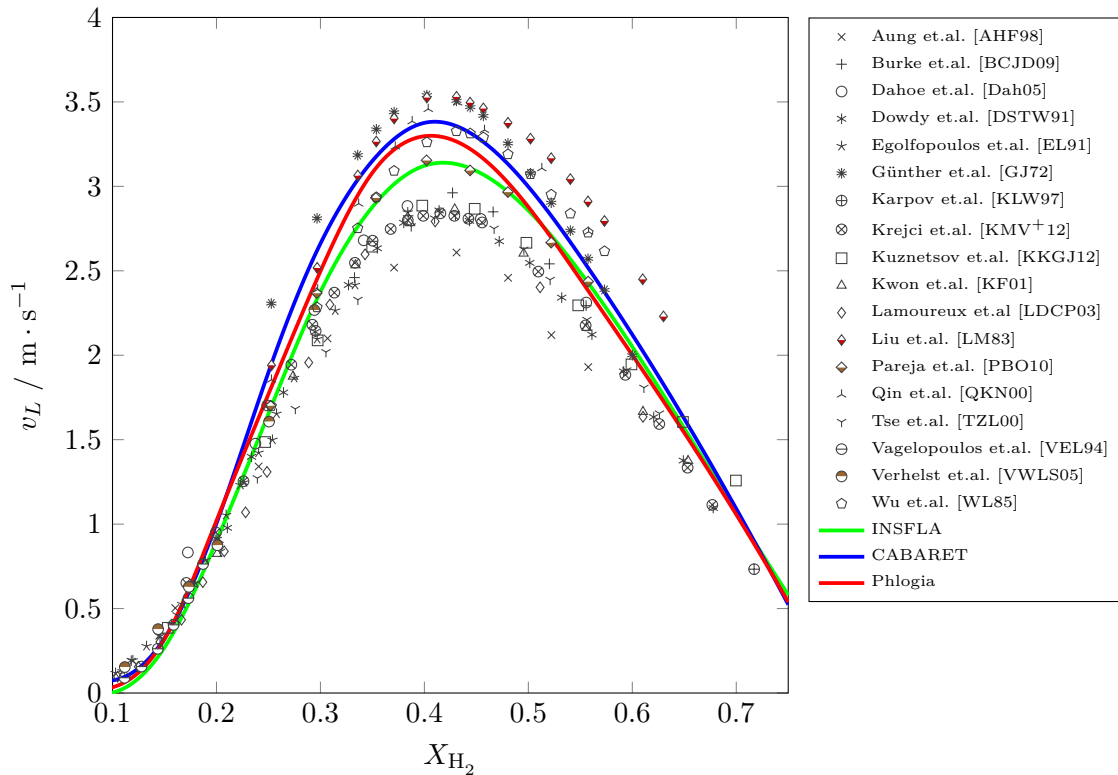
- Flame burning velocity as eigenvalue problem, computed with INSFLA using isobaric approximation [MW88, Maa88],
- Flame propagation from adiabatic wall, as described above, using full compressible code CABARET [GZKK13, KG09]. The code is based on high order finite differences method. Here a shorter domain  $L = 50$  mm had to be used, with imposed non-reflecting NSCBC [PL92] at the right wall.
- Flame propagation from adiabatic wall in a very large vessel  $L = 10$  m using proposed algorithm Phlogia.

Figure 5.8 shows the calculated burning velocities for the wide range of hydrogen-air mixture compositions. The calculations are compared with experimental data adopted from [SW14] and [PBO10]. Here rather a good quantitative agreement between all the calculations is observed.

Because of the special character of the spectral methods standard algorithms to access the accuracy and convergence of numerical schemes are not straightforwardly applicable. It is clear the discretisation mesh can be fixed and a standard mesh refinement procedure can be performed, but then all advantages of the suggested approach will be absent. The proposed algorithm automatically adjust the number spectral elements and the polynomial order within them for each time step. The process is governed by user specified accuracy requirements ATOL and RTOL (see §D.4). In order to see the effect of the tolerance criteria, a number of resolution tests have been performed. The result of these tests for flame propagation in unconfined settings are summarised in table 5.1. The absolute tolerance is kept constant  $ATOL=10^{-6}$  for all state variables. The table presents values for stoichiometric mixture of hydrogen and air but the results for other mixtures behave identically.

The table 5.1 shows also flame thickness  $\delta_f$ , computed from the slope of temperature profile, and required number of collocation points  $N_P$ . A data for outwardly propagating spherical flame at radius  $r = 20$  mm is also added for comparison.

The difference in computed values for laminar flame speed  $v_L$  and for flame thickness  $\delta_f$  lies between  $RTOL=10^{-4}$  and  $RTOL=10^{-3}$  in fourth decimal and between  $RTOL=10^{-3}$  and  $RTOL=10^{-2}$  in the third decimal place. The number of required grid points  $N_P$  almost doubles for each order of accuracy. Note additionally that  $N_P$  is given for the whole computational domain  $x = [0, 10]$  m. Please note that the number of points correspond to the quasi-stationary regime of flame propagation and



**Figure 5.8.:** Comparison of computed laminar burning velocities with experimental measurements, adopted from [BKKY]

vary significantly during initial stages.

The computation of pure burning velocity is a well posed mathematical eigenvalue problem, available in several well established programmes like INSFLA or CHEMKIN (Premix). Unfortunately, a physical experiment cannot be completely separated from neighbour effects, like flame surface curvature, burner-flame interaction or effects of walls of the combustion vessel. Moreover, there is a difficulty separating of laminar burning velocity speed from flame propagation speed, which is hydrodynamically driven (see e.g. [WLC<sup>+</sup>15]).

Figure 5.9 presents previously discussed experimental results, grouped according to experimental method. Red symbols correspond to bombs, e.g. spherical bombs or cylindrical bombs; blue symbols represent burner experiments, e.g. bunsen burner; and green symbols depict several other experiments, e.g. particle image velocimetry or counterflow flames. The grouping of experimental results is obvious, with bomb experiments, possibly underestimating the burning velocity and open burner experiments, possibly overestimating the burning velocity. The flame propagation in such experiments is accompanied with a number of phenomena, which influence the burning velocity.

For instance, the measurements of burning velocity in closed vessel (bomb) experiments encounter flame folding and flame-wall interaction. For this reason measurements are conducted at relatively small radius of spherically expanding flame, e.g. 20 mm. However, at this conditions the flame is not yet completely stationary and

RTOL	spherical, $r = 20$ mm			planar		
	$N_P$	$\delta_f$ mm	$v_l$ cm/s	$N_P$	$\delta_f$ mm	$U_f$ cm/s
$10^{-4}$	1249	0.3560	219.50	934	0.3397	243.84
$10^{-3}$	665	0.3570	219.46	491	0.3400	243.92
$10^{-2}$	365	0.3572	218.67	386	0.3422	245.54

**Table 5.1.:** Resolution test with APSM in unconfined settings for stoichiometric conditions.

is still influenced by initial conditions. Figure 5.9 shows also the computed with Phlogia flame burning velocity in the spherical symmetry at the flame position of  $r = 20$  mm, which goes perfectly through experimental results in closed vessels. Naturally, conducting the numerical measurements at larger radii, the burning velocity is approaching the planar case, shown as blue line. Unfortunately, laminar spherical flames of large size are not feasible in experiment, due to various destabilisation effects.

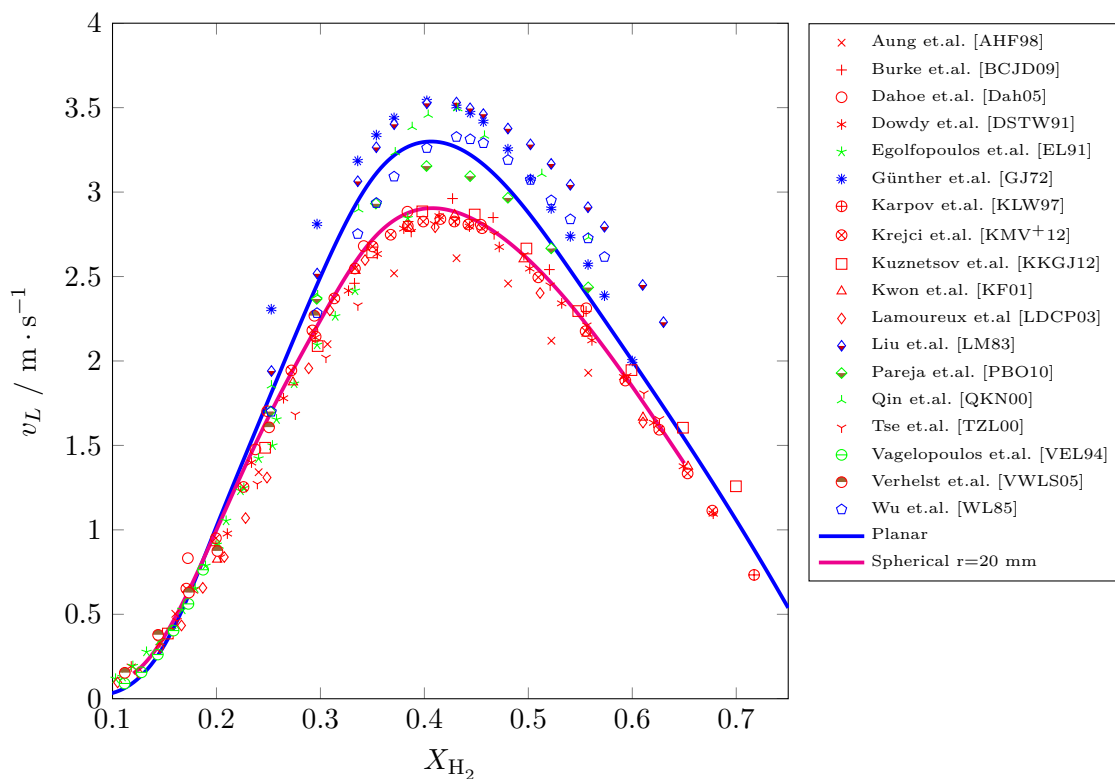


**Figure 5.9.:** Laminar burning velocities vs. experiment type, adopted from [BKKY].

Results shown in fig. 5.9 indicate that a more accurate modelling physical experiments is required, in order to extract the laminar burning velocity.

## 5.2. Ignition and flame propagation in narrow channels

Another case, where the transient regimes play important roles, is ignition in narrow channels. In the first part is investigated, how a flame is developing in narrow closed and semi-open ducts with adiabatic walls. In the second part, a combustion in micro flow reactor with isothermal walls is studied.

### 5.2.1. Flame development in narrow ducts

The problem of premixed flame propagation in ducts has relevance for safety applications, e.g. in the petro-chemical industry, mining and power generation. There arise situations, where a mixture of fuel and air coexist in a duct with the possibility of ignition and flame propagation. The propagating flame can undergo spontaneous acceleration and even a transition to detonation [KS03], which has a very destructive potential.

The problem of flame propagation in ducts attracted interest of scientific society since end of XIX century, when Mallard and Le Chatelier studied the explosions in tunnels and coal mines [ML85]. The development of photographic equipment showed that flame is asymmetric and has non-uniform movement. Particularly interesting are the photographic observation of Ellis [Ell28]. He studied ignition in vessels of different shapes. All vessels provided interesting visual results but particularly interesting were interesting observation in closed tubes of, what is now called, "tulip" flames. Stroboscopic images showed that flame develops firstly as a hemisphere. Later, as it approaches the walls of the duct, it get the characteristic elongated form of "finger" flame, which in the last phase flattens and turn the convex towards the burned gas.

The dynamics of flame propagation in closed pipes or ducts is influenced by a large number of phenomena, e.g.:

1. Finger flames – a transition from finger to tulip flame [XHO15] leads to a rapid increase of the flame surface ratio accelerating the flame;
2. Wall friction, hydraulic resistance (G. Sivashinsky [BS00, BGG<sup>+</sup>04]) leading to momentum and energy losses – following ideas of Ya.B. Zel'dovich [ZR47], the pressure increase in the flame induction zone govern the acceleration;
3. Delayed burning phenomena – secondary reaction in the product side pushes the flame forward driving the flame acceleration [BVE08, BVAL12];
4. Acoustic instabilities – flame instabilities [CH96, Cla00] courses the flame surface growth and, in turn, accelerating the flame;
5. Turbulence and compression waves interaction – strong interaction of the reaction flame front and accumulating shock waves [VBA<sup>+</sup>10], see e.g. [OG07] for more details.

Most experimental observations available in the literature were conducted in relatively long square ducts. It has been observed that the tulip inversion is best seen for the ratio of the length of the duct to width of the square cross section  $L/W$  ranging

Type	Width, mm	Length, mm
Open	15	100
Open	10	100
Open	5	100
Open	2.5	100
Closed	10	100
Closed	5	100
Closed	5	50
Closed	5	25
Closed	2.5	100

**Table 5.2.:** Duct configurations used in study.

between 4 and 20 [Ell28, DR09]. In the current work, the formation of the flame front in two configurations of relatively long and narrow square channel is investigated. The ratio of width of the square to length  $L/W$  is ranging from 10 to 20. One numerical sample for  $L/W = 40$  is taken, in order to investigate, what happens outside the experimentally proposed range. Table 5.2 summarised investigated configurations.

The majority of experimental data are available for rectangular cross sections. Moreover previously conducted 2D simulations compared to 3D simulations can still represent important features of the combustion wave in narrow ducts [XMSM12, XHO17]. For the current study is thus limited to 2D planar geometry. For numerical test, two rectangular channels with width  $W$  and length  $L$  are introduced. They are shown in fig. 5.10. In one configuration the right side is open and in the other the duct is closed from all directions.

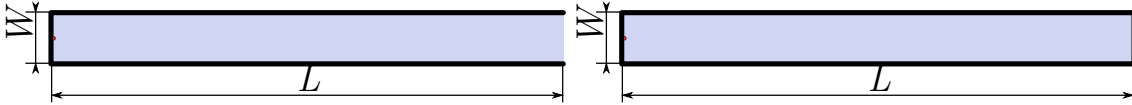


**Figure 5.10.:** Geometrical configuration of narrow duct: half-open (left) and closed (right). Red point indicates the hot spot position.

For ignition a small hot spot with width of 0.2 mm and temperature of 2500 K is used, whilst the rest of the mixture has temperature of 300 K. The initial pressure is kept uniform of 1 bar. The initial hot spot is tend to represent a spark or a laser pulse. At the time zero, only stoichiometric mixture of hydrogen and air is present:

**Initial condition,  $t = 0$**

$$\left\{ \begin{array}{l} v_x(0, x, y) = 0, \\ v_y(0, x, y) = 0, \\ T(0, x, y) = 300 + 2200 \exp\left(- (x/0.2 \text{ mm})^2 - (y/0.2 \text{ mm})^2\right), \\ c_{\text{H}_2}(0, x, y) = \frac{21}{71} \frac{1 \text{ bar}}{R_0 T(0, x, y)}, \\ c_{\text{O}_2}(0, x, y) = \frac{21}{142} \frac{1 \text{ bar}}{R_0 T(0, x, y)}, \\ c_{\text{N}_2}(0, x, y) = \frac{79}{142} \frac{1 \text{ bar}}{R_0 T(0, x, y)}. \end{array} \right. \quad (5.11)$$

Assuming that heat transfer is much slower as the combustion process, the walls are taken adiabatic. However, it is important to resolve the boundary layer and thus the non-slip boundary condition for velocity is imposed.

**Bottom boundary,  $y = -W/2$**

$$\left\{ \begin{array}{l} v_x(t, x, -\frac{W}{2}) = 0, \\ v_x(t, x, -\frac{W}{2}) = 0, \\ \frac{\partial}{\partial y} T(t, x, -\frac{W}{2}) = 0, \\ \frac{\partial}{\partial y} c_i(t, x, -\frac{W}{2}) = 0, \\ \forall i = 1, \dots, N_S \end{array} \right. \quad (5.12)$$

**Top boundary,  $y = W/2$**

$$\left\{ \begin{array}{l} v_x(t, x, \frac{W}{2}) = 0, \\ v_x(t, x, \frac{W}{2}) = 0, \\ \frac{\partial}{\partial y} T(t, x, \frac{W}{2}) = 0, \\ \frac{\partial}{\partial y} c_i(t, x, \frac{W}{2}) = 0, \\ \forall i = 1, \dots, N_S \end{array} \right. \quad (5.13)$$

**Left boundary,  $x = 0$**

$$\left\{ \begin{array}{l} v_x(t, 0, y) = 0, \\ v_y(t, 0, y) = 0, \\ \frac{\partial}{\partial x} T(t, 0, y) = 0, \\ \frac{\partial}{\partial x} c_i(t, 0, y) = 0, \\ \forall i = 1, \dots, N_S \end{array} \right. \quad (5.14)$$

**Right boundary for closed configuration,  $x = L$**

$$\left\{ \begin{array}{l} v_x(t, L, y) = 0, \\ v_y(t, L, y) = 0, \\ \frac{\partial}{\partial x} T(t, L, y) = 0, \\ \frac{\partial}{\partial x} c_i(t, L, y) = 0, \\ \forall i = 1, \dots, N_S \end{array} \right. \quad (5.15)$$

**Right boundary for open configuration (NSCBC),  $x = L$**

$$\left\{ \begin{array}{l} \frac{\partial}{\partial t} (\rho v_x) + \frac{\partial}{\partial y} (\rho v_x v_y + \tau_{xy}) = -(v_x d_1 + \rho d_3), \\ \frac{\partial}{\partial t} (\rho v_y) + \frac{\partial}{\partial y} (\rho v_y^2 + \sigma + \tau_{xy}) = -(v_y d_1 + \rho d_4), \\ \frac{\partial}{\partial t} (\rho e) + \frac{\partial}{\partial y} (v_x \tau_{yx} + v_y (\rho e + \sigma + \tau_{yy}) + q_y) = - \left( \left( h + \frac{1}{2} v_x^2 \right) d_1 + \rho v (\dot{h} + v \dot{v}) \right) \\ \frac{\partial}{\partial t} c_i + \frac{\partial}{\partial y} (c_i v_y + \bar{j}_{i,y}) = \dot{\omega}_i - \left( (d_1 - v_x \dot{\rho}) c_i + v \dot{c}_i \right), \end{array} \right. \quad (5.16)$$

Here the abbreviation  $(\dot{\phantom{x}}) = \partial(\phantom{x})/\partial x$  is used for space derivative. All variables, unless specified, are computed from the solution approximation within the domain at the corresponding boundary. Mass specific boundary derivatives [PL92]:

$$\begin{aligned} d_1 &= \frac{1}{a^2} \left( \mathcal{L}_2 + \frac{1}{2} (\mathcal{L}_5 + \mathcal{L}_1) \right), \\ d_3 &= \frac{1}{2\rho a} (\mathcal{L}_5 - \mathcal{L}_1), \\ d_4 &= v_x \frac{\partial v_y}{\partial x}, \end{aligned} \quad (5.17)$$

The amplitudes of characteristic waves for outflow:

$$\begin{aligned} \mathcal{L}_1 &= K (P - P_\infty), \\ \mathcal{L}_2 &= v (a^2 \dot{\rho} - \dot{P}), \\ \mathcal{L}_5 &= (a + v) (\dot{P} + \rho a \dot{v}_x), \end{aligned} \quad (5.18)$$

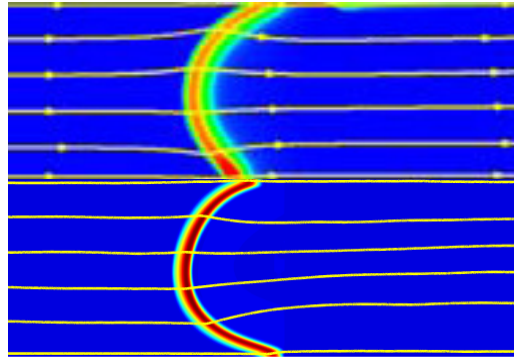
For more information on NSCBC for non-reflecting outflow see discussion in §6.2. Here, the following parameters are used: pressure at the outflow  $P_\infty = 1$  bar, the parameter  $\sigma = 0.5$  (used in  $K$ ) and the characteristic length  $L^* = 2$  cm.

### 5.2.1.1. Flame tip inversion in closed channel

Under particular conditions, depending on mixture composition and channel configuration, convex “tulip” shape becomes characteristic for a propagating flame in narrow channels. Fig. 5.11 shows a stationary tulip flame in channel with width 10 mm under stoichiometric hydrogen-air conditions. Results attained in [MR04] correspond to a stationary propagating “free” flame and the results of current work correspond to closed channel with length  $L = 25$  mm.

C. Clanet and G. Searby [CS96] distinguished four stages of tulip flame development, which are also observed by other researches [DRS98, XWH<sup>+</sup>11]:

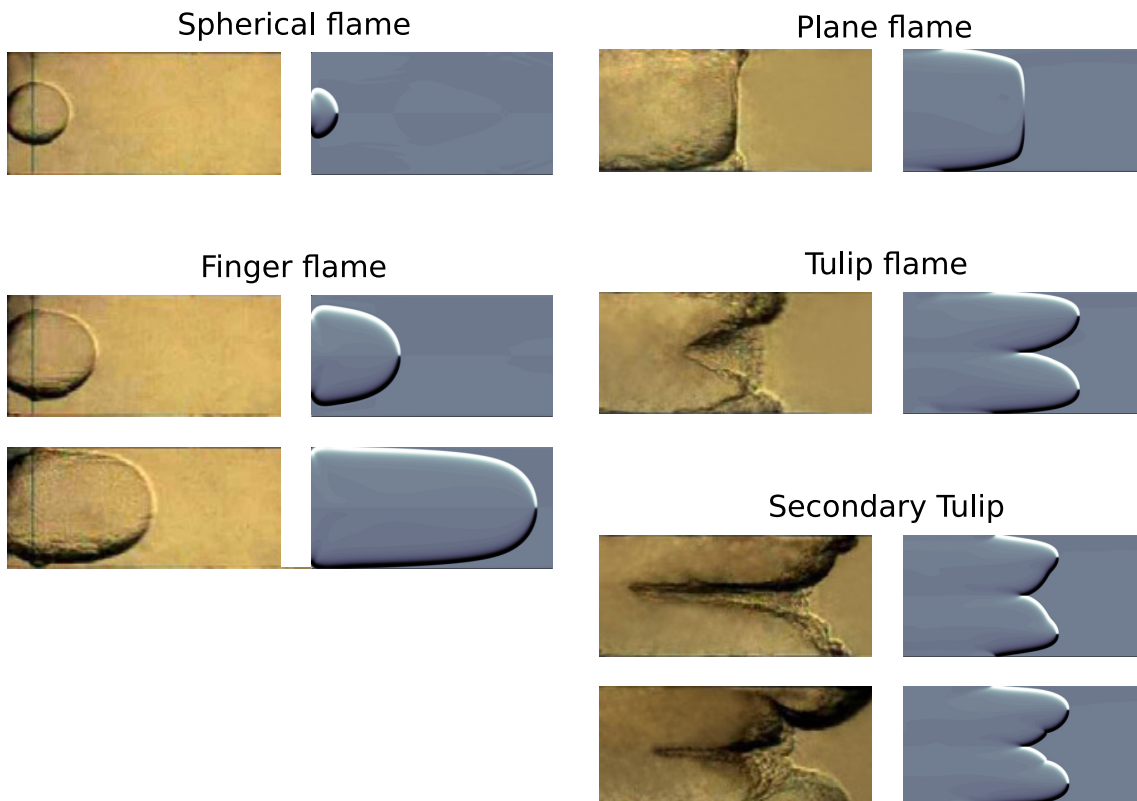
1. Hemispherical flame. Unaffected by the presence of the walls. Flame is expanding with small velocity close to laminar flame speed.
2. Finger flame. Flame approaches side walls. Flame velocity is growing exponentially, reaching value exceeding several times the laminar flame speed.



**Figure 5.11.:** Comparison of stationary tulip flame with heat release rate and flow lines. Upper half results attained in [MR04], lower half – this work.

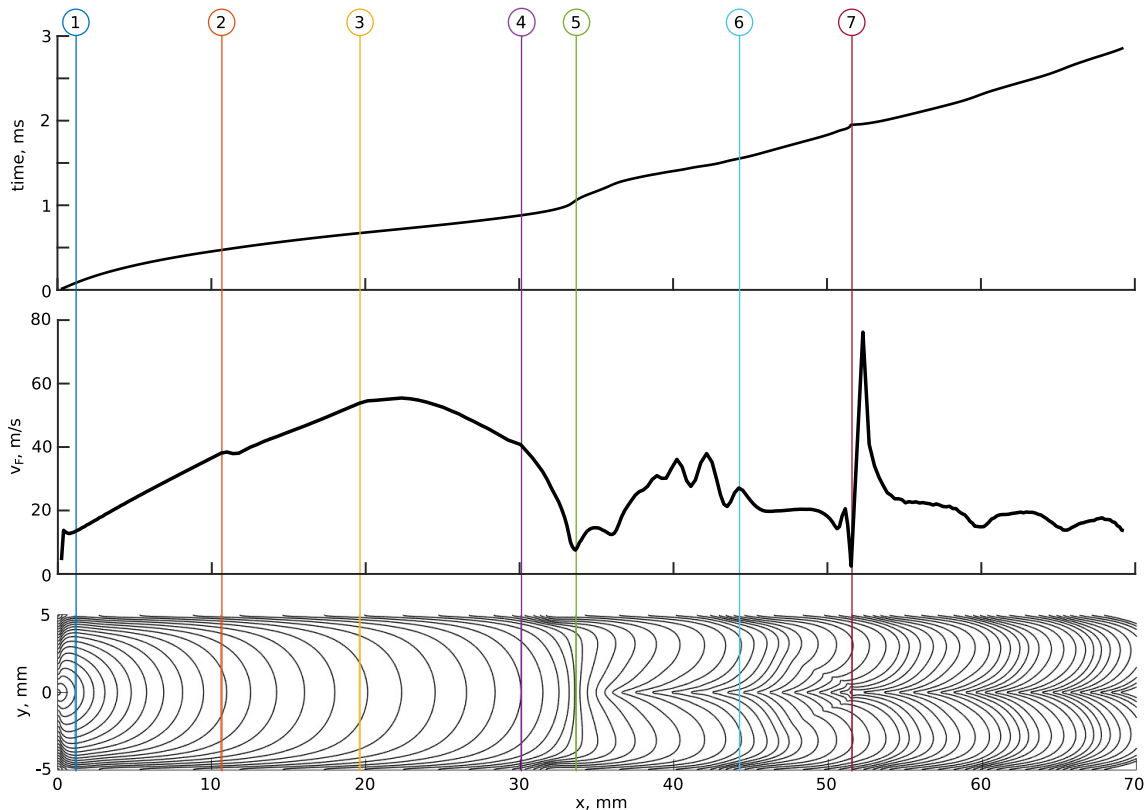
3. Tulip formation. As the skirt of flame touches the side walls, the inversion of tulip begins. During this stage of propagation, the flame surface area and the propagation velocity decrease steadily.
4. Tulip propagation. The dynamics of the front propagation after the tulip inversion.

Figure 5.12 provide illustration to C. Clanet and G. Searby classification (CSC). On the left are flame development stages observed in experiment [XMSM12] and on the right results of the current work. Interesting that during the last stage “tulip propagation” secondary tulips can be formed.



**Figure 5.12.:** Stages of tulip flame formation. Left half schlieren images adapted from [XMSM12], right half are computational schlieren images (this work).

Consider now fig. 5.13, which shows flame development process along the axis of symmetry for stoichiometric hydrogen air flame in closed channel 10 mm. The top image show flame tip position at different time instances, the middle image shows the velocity of the flame tip over duct length and the bottom images shows the contours of flame every  $40 \mu\text{s}$ . The coloured lines show the critical points of flame evolution (1 through 7). These points are addressed in details:



**Figure 5.13.:** Flame position (top), flame velocity (middle) and sequence of flame front contours (bottom).

1. Pressure from initial ignition reflected top and bottom walls of the duct, has reached the flame ( $t = 0.08 \text{ ms}$ ). Compare also fig. 5.17 (top most frame), the pressure wave, reflected from walls collapses in the middle. At this point ended the first stage of hemispherical flame propagation, according to CSC. Before that point, the flame is growing with about  $v_F = 13 \text{ m/s}$ . From this point on, the flame is developing a typical “finger” configuration. Flame velocity, starting from this point, is growing linearly with  $x$ . Here starts the second stage, according to CSC.
2. Flame approaches top/bottom walls of the duct ( $t = 0.48 \text{ ms}$ ) which is accompanied with a short drop of flame velocity. Pressure, “locked” in top-left and bottom-left pockets, thwarts shortly flame acceleration.
3. Flame touches the top/bottom walls of vessel ( $t = 0.67 \text{ ms}$ ). Starting from this point flame surface is shrinking, releasing the overpressure region, which was behind the flame. Here the acceleration of the flame tip becomes negative and the flame tip eventually drops velocity. At this point the flame tip velocity has almost reached its maximum of about  $v_F = 55 \text{ m/s}$ . Here begins the actual

tulip formation, according to the third stage of CSC. At this point the flame surface is reduced almost instantly, creating secondary expansion waves.

4. Released, at the previous point, pressure wave reaches the right wall of the duct ( $t = 0.88$  ms). Beginning from this point, the flame tip velocity drops dramatically, by more than 5 times (see also fig. 5.17).
5. Plane flame is formed ( $t = 1.05$  ms). Maximum, of the reflected from the right wall, pressure wave reaches the flame tip (see also fig. 5.17). At this point the flame velocity reaches its minimum of  $v_F = 7.5$  m/s. Shortly after that, the classical tulip flame is formed, where begins final stage of tulip flame propagation, according CSC, where the flame motion is governed by hydrodynamic processes. Interesting, that the flame tip, as it becomes sharp, begins to flatten, as seen on the velocity profile, which indicates presence of some sort instability. The secondary expansion waves created at the 3. critical point do not affect integral flame front propagation, as seen in fig. 5.13 (top) but there are nonetheless marginal fluctuations of flame front velocity due to this waves.
6. Formation of the secondary tulip ( $t = 1.55$  ms). Pressure wave reflected again from the right wall, reaches the flame front to the second time. At this point, the tulip front starts to curve at both sides, forming two additional cusps, which propagate towards the main cusp.
7. Collapse of the secondary tulip ( $t = 1.95$  ms). Secondary cups are reaching the tip of the flame. Here the unburned gas are captured at the tip, explodes, creating a strong but short flame tip acceleration. After this point the pressure in the vessel is almost homogeneous and the flame gradually relaxes to the steady propagating tulip flame with velocity about  $v_F = 15$  m/s.

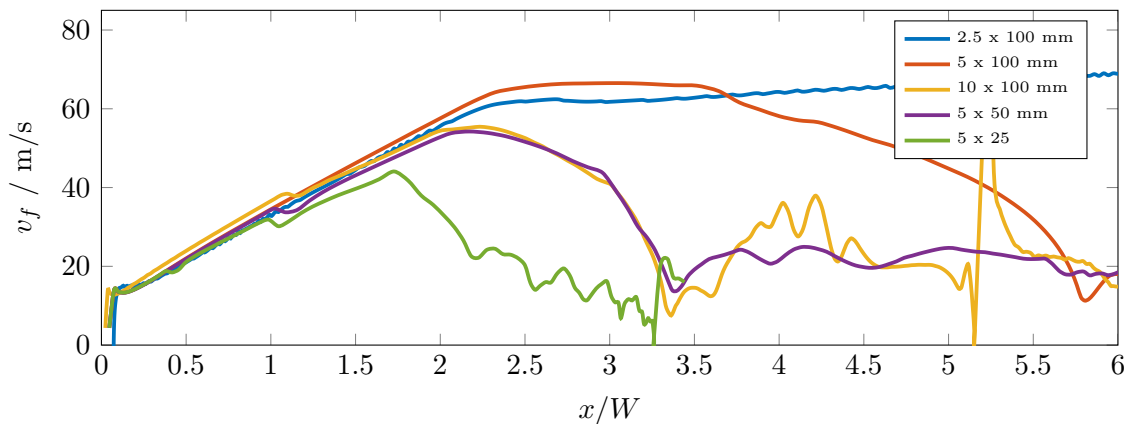


**Figure 5.14.:** Comparison of flame tip velocities for different width/length ratios.

Figure 5.14 shows comparison of flame tip velocities of different channel configurations (width/length). The x-axis is normalised to the width of the channel  $L$ . Flame front velocity develops in the normalised space almost identically, till flame skirt touches side walls. This however, happens at the different points along the trajectory. What is interesting, is that the formation of the plane flame (lowest point in velocity profile after flame acceleration,  $x/x_{max} \approx 0.32$ ) for equal  $W/L$  ( $5 \times 50$  and  $10 \times 100$ ) happens

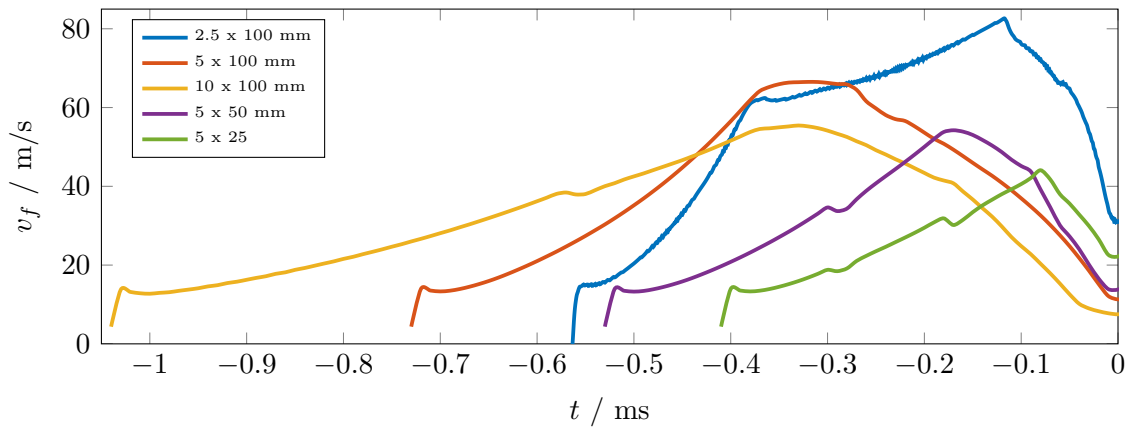


**Figure 5.15.:** Comparison of flame tip inversion times for different width/length ratios. Zero corresponds to plane flame.

exactly at the same position. Meanwhile, for smaller  $W/L$  ( $5 \times 100$ ) the transition position is shifted to the right and for large  $W/L$  ( $5 \times 25$ ) is shifted to the left.

The actual tip inversion type depend only on channel length, which is illustrated in fig. 5.15. The moment as the flame becomes “plane” is taken here as reference point  $t = 0$ . It can be seen that for channels with equal length ( $L = 100$  mm), the time range between flame skirt touching the side wall (kink in the velocity profile) and the formation of plane flame is equal  $\Delta t = 0.37$  ms.

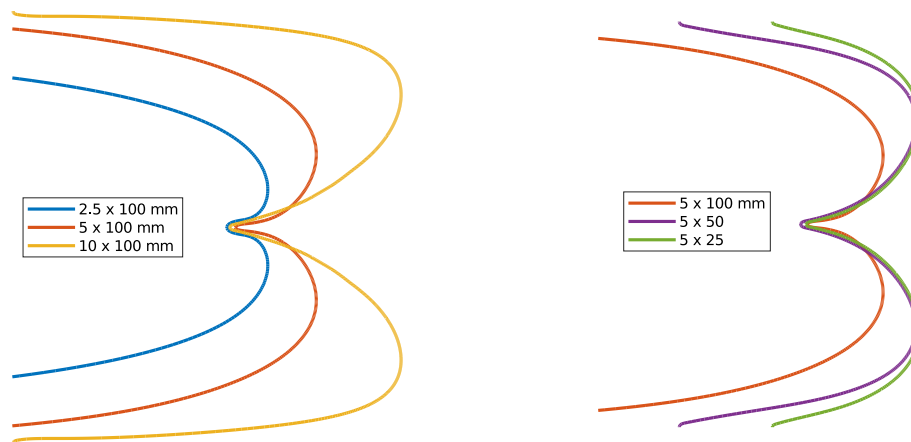


**Figure 5.16.:** Comparison of quasi-stationary tulip configurations for different width/length ratios.

Figure 5.16 shows a comparison of quasi stationary tulip flame shapes. All profiles are normalised in  $x$  and  $y$  direction by channel width  $W$ . Left picture shows effect of channel width: with larger cross-section of the channel, the tip inversion is getting stronger. The right picture shows the effect of channel length on tulip configuration. Longer channels have a somewhat deeper tip inversion but the effect is much less pronounced as in case of channel width variations.

There are a number of explanation of the tulip phenomenon. Some authors emphasise the importance of Darrieus-Landau instability [NFGLC93]. The others put forward radial gradient axial velocity just ahead of the curved flame front [DRBS88] but the appearance of the gradient is not explained. In [GBS92] the so-called “squish” flaw

was observed and put responsible for flame tip inversion. In [RO88] by studying flames in enclosures, considered the generated vorticity (Rayleigh–Taylor instability) in the burned gas, as responsible for tulip flame formation. Similar observation was done in [XHO17]. Finally in [Lee77], by studying initiation of detonation in gas mixtures half-open tubes, the importance of Taylor interface instability for the folding of the flame to a tulip shape.

In order to investigate the driving force, hydrodynamic processes are firstly analysed. Figure 5.17 shows sequence of overlapped pressure distribution (colours) with velocity field (small cyan arrows). Additionally, the actual flame position is put, for reference, as a solid black line. In the first frame the pressure wave, reflected from top/bottom walls, arriving to the hemispherical flame. From this point on, the mass flux initiated through thermal expansion is increasingly dominated in x-direction, given a rise to finger flame.

The finger flame is a prevailing effect, till the flame skirt touches the top/bottom walls (0.7 ms). From this time on, the flame surface is rapidly decreasing, with corresponding lower heat release. This triggers the release of overpressure, blocked previously by the growing flame (see 0.7 and 0.8 ms in fig. 5.17).

Once the released pressure wave reaches the right wall, the speed of the flame tip starts to decrease, and eventually a negative flow is built behind the flame, as the pressure wave approaches the flame (1.0 ms). Here the inversion of the flame tip begins. One may expect, when reflected from the left wall (1.2 and 1.3 ms), the pressure wave should inverse the tulip. However, by passing through the flame of the pressure wave, the tulip configuration remains almost unchanged. More over, as mentioned before, by passing again through the flame from the right ( $t > 1.5$  ms) the flame surface is distorted again, by creating secondary cusps on the flame front (see fig. 5.13).

Although the pressure wave triggers the formation of tulip, it is not the effect responsible for tulip existence. In order to investigate the driving force in more detail, consider a quasi-stationary tulip flame, when pressure in the vessel is homogeneous  $P = 3.286 \pm 0.005$  bar. Figure 5.18 shows vorticity field  $\omega$  with overlapped velocity field (left) and vorticity generation  $\partial\omega/\partial t$  with neglected viscosity (right) [CM00]:

$$\begin{aligned}\omega &= \frac{\partial v_x}{\partial x} - \frac{\partial v_y}{\partial y}, \\ \frac{\partial\omega}{\partial t} &= \frac{1}{\rho^2} \left( \frac{\partial\rho}{\partial x} \frac{\partial P}{\partial y} - \frac{\partial\rho}{\partial y} \frac{\partial P}{\partial x} \right).\end{aligned}\tag{5.19}$$

Pressure and density fields were smoothed before using eq. (5.19) in order to filter out small acoustic perturbations. In this quasi-stationary state, the velocity at the flame front is zero, with stronger flow behind the flame front (see fig. 5.18 (left)). This flow is perpendicular to the flame front but, due to the non-slip boundary conditions, this flow is forced to rotate near the walls. This creates high vorticity region, where flame front touches top/bottom walls of the duct. The high vorticity is further stimulated by disparity of pressure and density gradients in these regions (see vorticity generation in fig. 5.18 (right)). The vorticity driven instabilities are attributed to Rayleigh–Taylor instability.

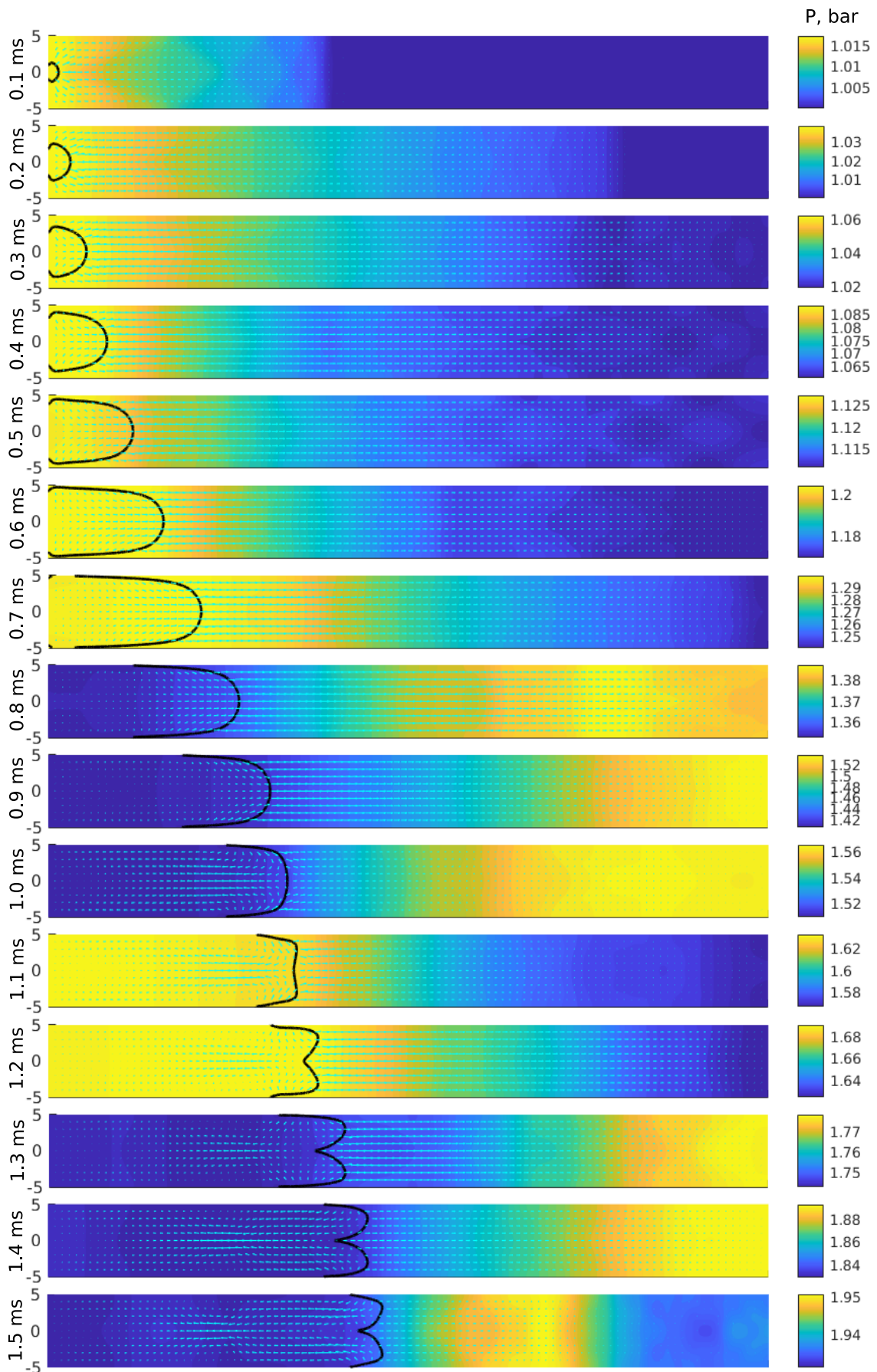


**Figure 5.17.:** Flame development in closed duct  $10 \times 100$  mm. Solid black line shows flame front, colour codes the pressure, cyan arrows represent velocity field.

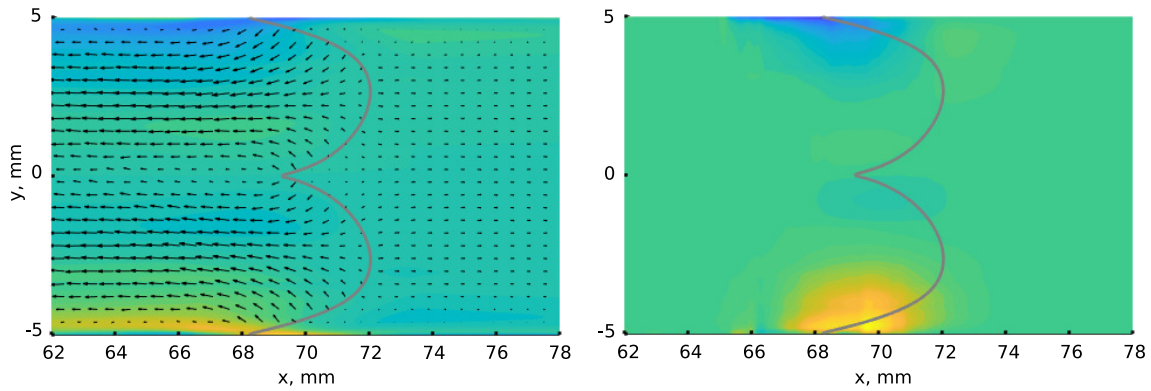


**Figure 5.18.:** Vorticity of quasi-stationary tulip flame: vorticity with overlapped velocity field  $\omega$  (left), vorticity generation  $\partial\omega/\partial t$  (right). Black arrows represent local velocity vector, grey line corresponds to flame position.

By passing second time through the tulip flame, reflected from the right side, pressure wave, disturbs the flame front again and the secondary tulip is generated (see fig. 5.13). Figure 5.19 shows the vorticity field and vorticity generation term during the secondary tulip formation (top) and during the quasi-steady propagation of the secondary tulip towards the main cusp (bottom). The top frame corresponds to the moment, as the traversing the flame front, which disturbs the flame front through misalignment of velocity vectors of different layers near the flame, with different densities. As a result, a secondary vorticity generation region at the flame front (see fig. 5.19 (top)). The created Kelvin–Helmholtz instability curves the flame front. As the pressure wave is relatively far away from the flame, the secondary vorticity source reduces almost to zero, whilst the main vorticity near the walls remains. Nonetheless, the secondary tulip did not cease to exist, even when the pressure wave is traveling back trough the flame. Persistence of the secondary tulip, indicate on the existence of other instability, e.g. Darrieus-Landau insatbility.

Now the attention is given to thermochemical state space. The same (seven) critical points are considered, as discussed in relation to fig. 5.13. Few first several stages are shown in fig. 5.20 in projections to  $\text{H}_2\text{O}$ ,  $\text{H}_2$ ,  $\text{OH}$  (left) and in projections to  $\text{H}$ ,  $\text{O}$ ,  $\text{OH}$  (right). First projection, shown in green, is captured at  $t = 0.03$  ms as the flame started to expand. Second projection, coloured with blue, is at  $t = 0.08$  ms as the reflected from top/bottom walls pressure wave reaches the flame (1. critical point). Till now, there was a little difference in thermochemical state space is observed. Projections are practically identical, if properly scaled. However, as the finger flame is formed, the projections took completely different shape (cyan), which was developed further, as the flame was approaching top/bottom walls (red). The cyan projection can be seen as a part of a more complex red state space formed near the wall. The red profile corresponds to the 2. critical point.

In the next snap shot, fig. 5.21, the point of flame wall approach is shown now in green and used as reference point. The next point is at the time moment  $t = 0.68$  ms (blue), just after the flame touches top/bottom walls (3. critical point). Within very short time 0.03 ms the projections to specific mole numbers have changed dramatically. As the pressure wave reaches the right wall at  $t = 0.88$  ms (fourth critical point), the thermochemical state reaches the state shows in cyan projections. After that

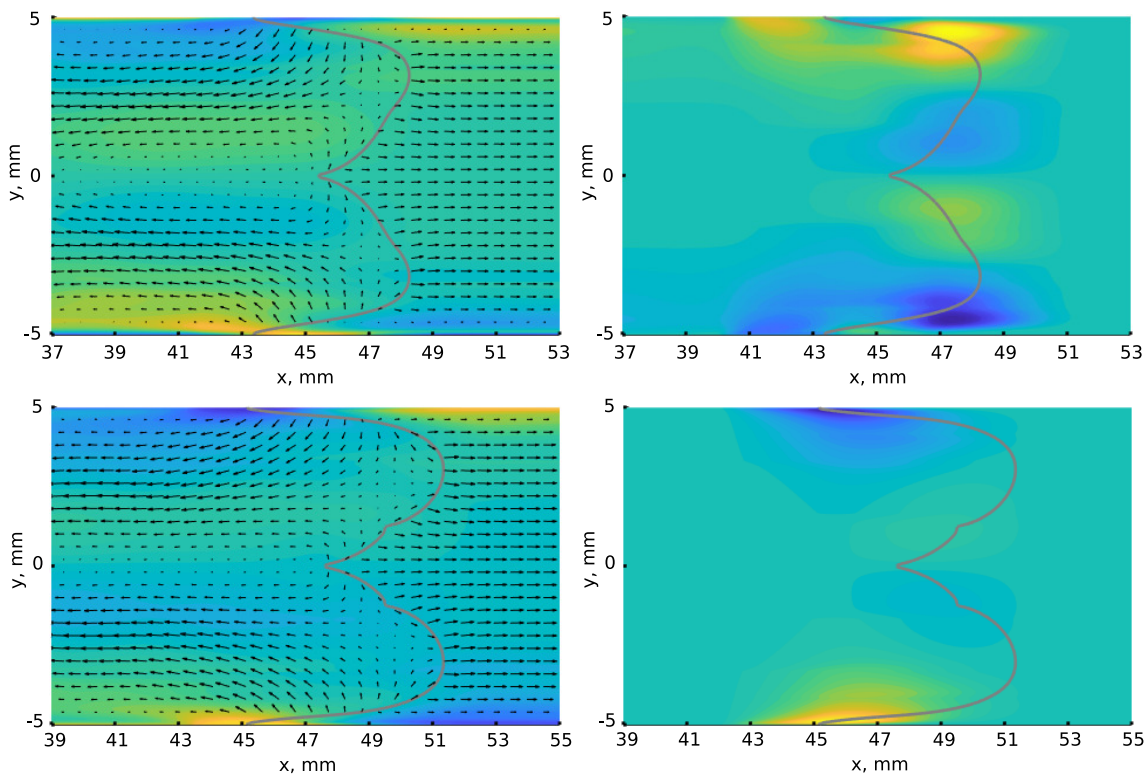


**Figure 5.19.:** Vorticity of forming secondary tulip flame: vorticity with overlapped velocity field  $\omega$  (left), vorticity generation  $\partial\omega/\partial t$  (right), initiation of the secondary tulip (top), later stages of secondary tulip (bottom). Black arrows represent local velocity vector, grey line corresponds to flame position.

point the thermochemical state space remains unchanged, if appropriate scaling is chosen. The last, in this snapshot, is the moment, as the flame becomes plane shape,  $t = 1.05$  ms (5. critical point). Here is to see, that projection have the same shape but have only somewhat shrunk.

The following snapshot, fig. 5.22, shows the development of tulip flame from plane flame. Green projections shows plane flame ( $t = 1.05$  ms) and red – tulip flame ( $t = 1.45$  ms). It is to see that the thermochemical state did not change shape during the tip inversion, but only shrank.

The final snapshot, fig. 5.23, shows the moment, when the secondary cusp in tulip flame is present (blue) and the final quasi-steady tulip flame (red). The last moment from the previous snapshot (fig. 5.22 (red)) is show here in green for reference. During the time between formation  $t = 1.55$  ms (6. critical point) and disappearance of the secondary cusp on tulip flame  $t = 1.95$  ms (7. critical point), the thermochemical state state is, as shown in blue in fig. 5.23. The projections are also practically identical to the moment as the pressure wave touches the right wall, when properly scaled. The last projection, shown in red, corresponds to the steady propagating tulip flame  $t = 2.03$  ms.

From the moment as the pressure wave reached the right end of the duct, the thermochemical state space was fully developed. In late times the shape of projections to specific mole numbers of species remains unchanged but only shrinks along some

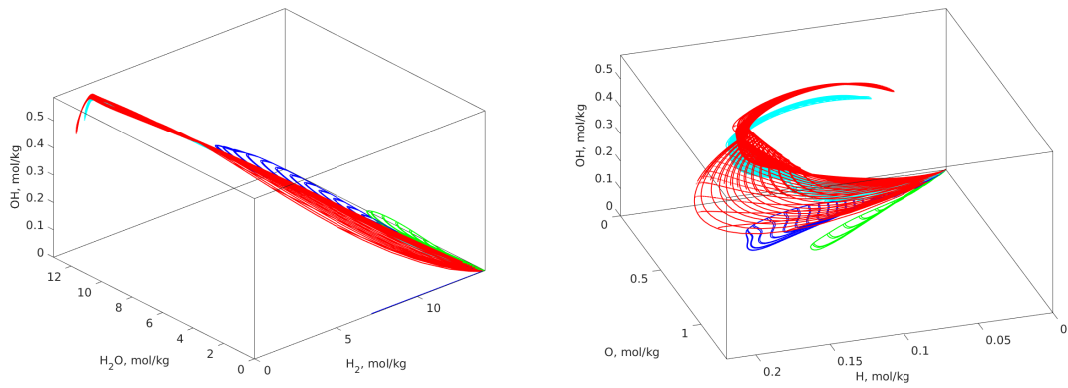


**Figure 5.20.:** Development of finger flame in thermochemical state space in projection to  $\text{H}_2\text{O}$ ,  $\text{H}_2$ ,  $\text{OH}$  (left) and to  $\text{H}$ ,  $\text{O}$ ,  $\text{OH}$  (right).

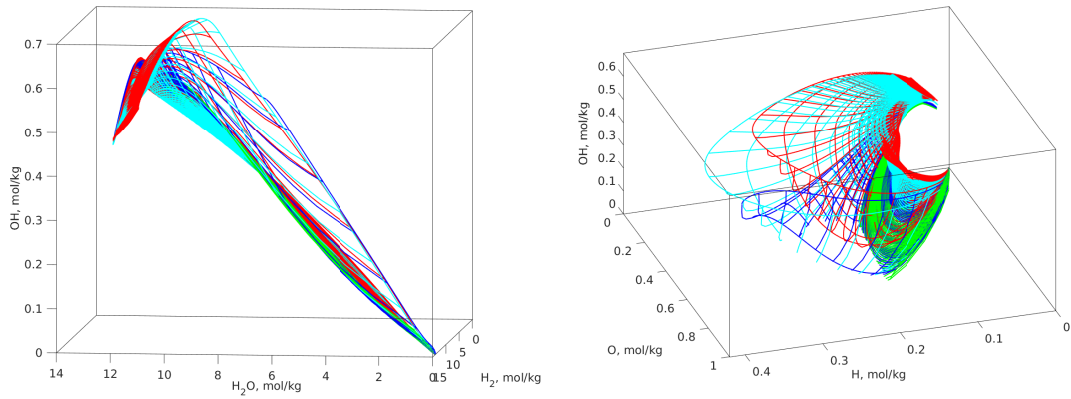


**Figure 5.21.:** Development of plane flame in thermochemical state space in projection to  $\text{H}_2\text{O}$ ,  $\text{H}_2$ ,  $\text{OH}$  (left) and to  $\text{H}$ ,  $\text{O}$ ,  $\text{OH}$  (right).

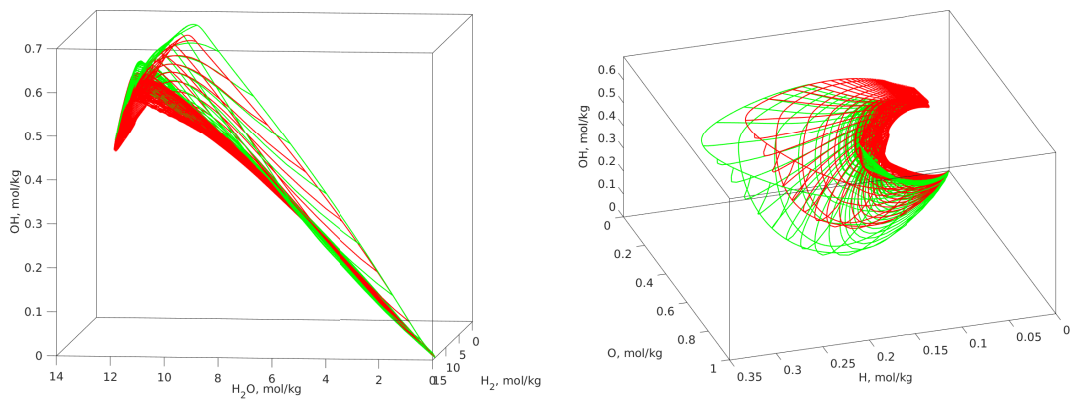


**Figure 5.22.:** Development of tulip flame in thermochemical state space in projection to  $\text{H}_2\text{O}$ ,  $\text{H}_2$ ,  $\text{OH}$  (left) and to  $\text{H}$ ,  $\text{O}$ ,  $\text{OH}$  (right).

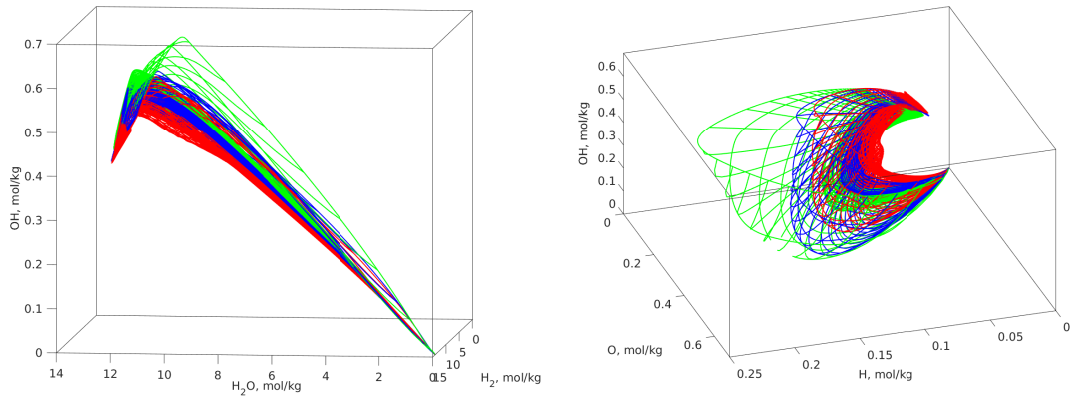


**Figure 5.23.:** Development of secondary tulip and quasi-steady tulip flame in thermochemical state space in projection to  $\text{H}_2\text{O}$ ,  $\text{H}_2$ ,  $\text{OH}$  (left) and to  $\text{H}$ ,  $\text{O}$ ,  $\text{OH}$  (right).

axes. This implies that the flame tip inversion and the appearance of secondary cusps is pure hydrodynamical effect.

### 5.2.1.2. Flame acceleration in open channel

Now, the same duct configurations (width, length) is considered but the right end is kept left open (see fig. 5.10), whilst the other sides have adiabatic walls. The flame development in half-open channel undergoes stages similar to CSC of tulip flame development, which is also illustrated in fig. 5.24.

1. Hemispherical flame.
2. Finger flame, until flame touches the side walls.
3. Turbulent flame

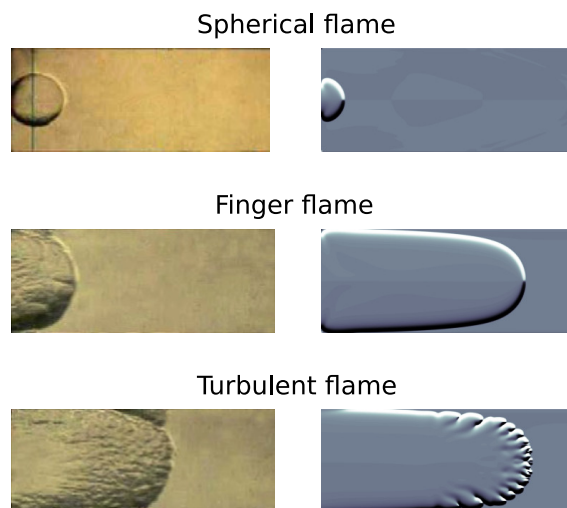


**Figure 5.24.:** Stages of flame development in half-open channel. On the left schlieren images of experimental observations [XWH<sup>+</sup>11]; On the right are computational schlieren images (this work).

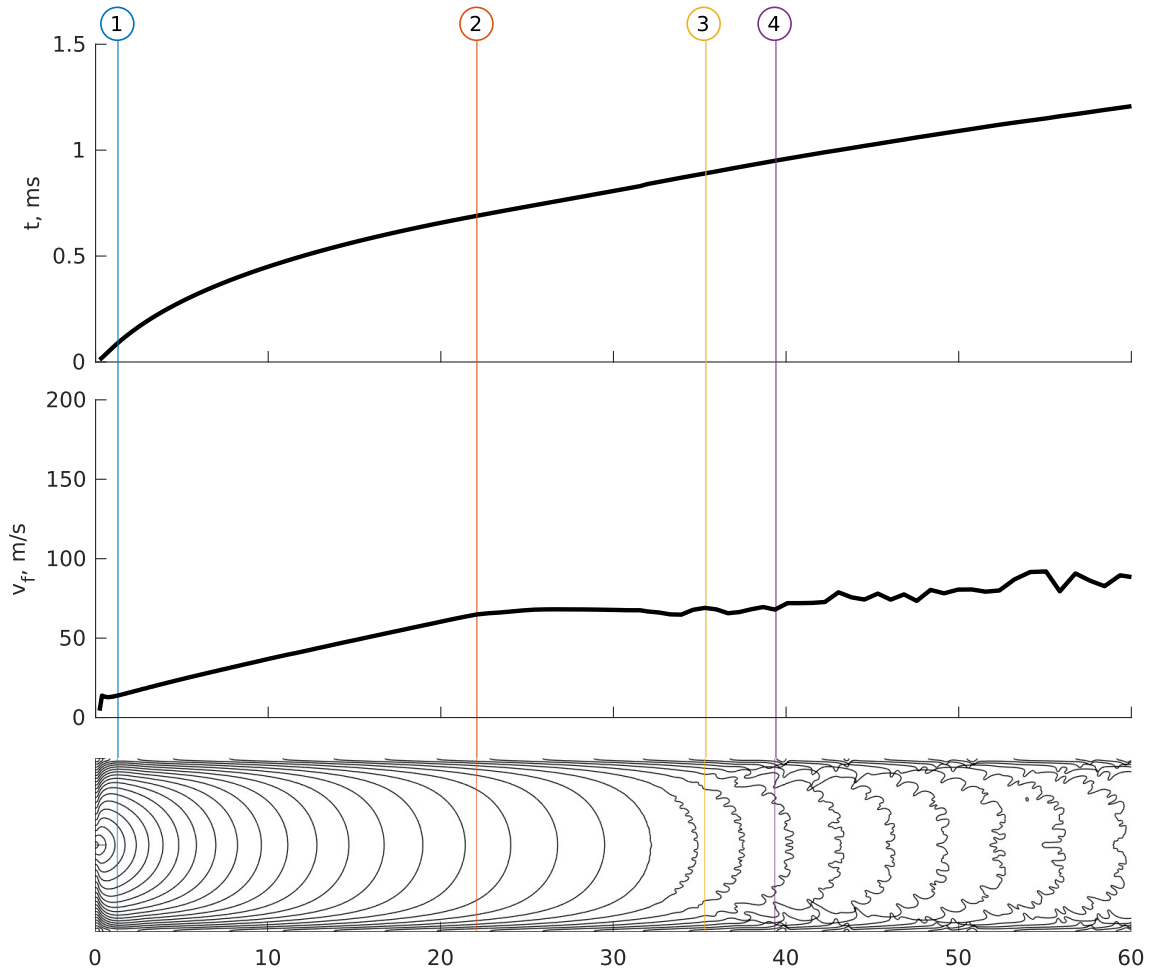
The development of turbulent flame in open duct is now compared with development of tulip flame in closed duct of the same geometry. Compare figs. 5.13 and 5.25. At the top is the position of flame along the symmetry axis, in the middle is flame velocity along symmetry axis and at the bottom are flame contours, taken every  $40 \mu\text{s}$ . Coloured lines show the critical points in flame velocity profile:

1. Pressure from initial ignition reflected top and bottom walls of the duct, has reached the flame ( $t = 0.08 \text{ ms}$ ). This point, in both closed and open configurations, is identical, because hydrodynamic effects could not yet influence the flame development. From this moment on, a laminar finger flame is being developed.
2. Flame skirt touches top/bottom walls of the vessel ( $t = 0.68 \text{ ms}$ ). This point almost identical to third point in closed vessel configuration. However, in the closed vessel, velocity is shortly reduced, during approach to the wall, which can be seen as kink on the velocity profile (fig. 5.13, point 2). Before this point the small overpressure was captured behind rapidly growing flame front, as seen in fig. 5.27, is, at this very moment, released and travels ahead of the flame. In the fully confined configuration, this wave is reflected from the right end of the duct (see fig. 5.17) and by approaching to flame, the flame is reducing its speed and eventually reverses its tip. In the open configuration, the pressure wave travels out of the domain (fig. 5.27,  $t = 0.9, \dots, 1.0 \text{ ms}$ ), and flame can undisturbed propagate further.
3. Flame speed, being almost constant from the previous point, starts rapidly reducing ( $t = 0.88 \text{ ms}$ ).  $0.05 \text{ ms}$  ( $\Delta x = 3.36 \text{ mm}$ ) before that the flame front started to curve.
4. Pressure is slowly increasing behind the flame, due to flame surface increase of the curved flame, creating the second round of flame acceleration ( $t \approx 0.94 \text{ ms}$ ).

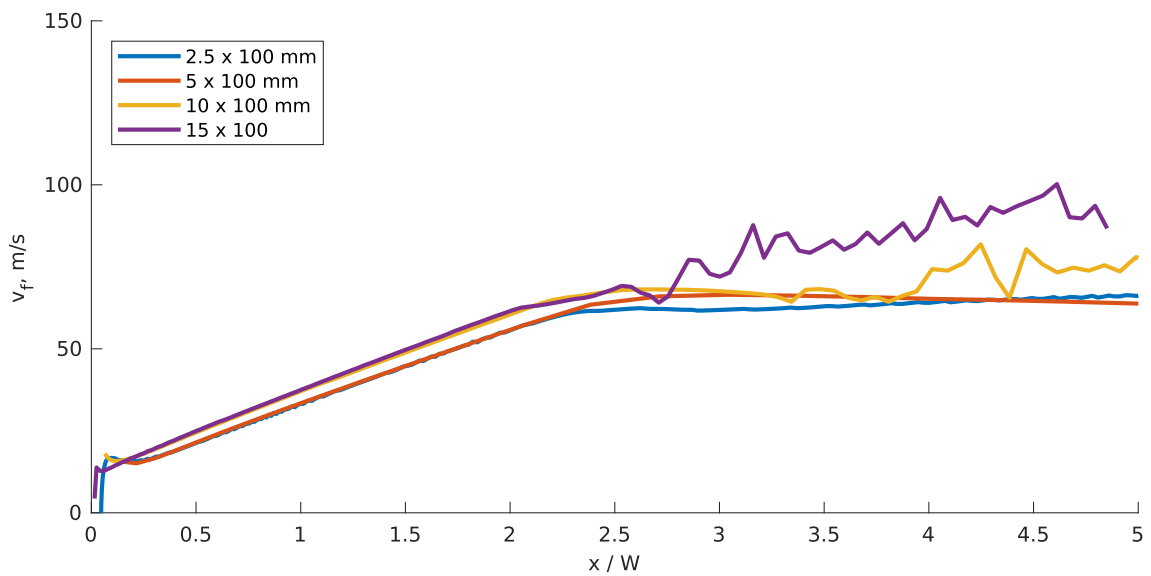
Experimentally, two other flame configuration were observed for open channels. One is so called  $\Gamma$ -flame and the other – classical tulip flame. In order to observe on of these configurations, probably a longer duct is required.

Figure 5.26 compares how velocity profiles depend on different  $W/L$  ratios. It can be observed that when x-axis is scaled with the width of duct  $W$ , velocity profiles are identical till the flame skirt reaches outer walls. After that, the shorter the channel width, the longer it takes for the turbulence to kick off. For channel  $W = 15 \text{ mm}$  the turbulence commences, straight after the flame touches the walls. In narrow channel  $W = 2.5 \text{ mm}$  the flame propagates relatively long undisturbed, after its skirt touches side walls.

If the attention is given to thermochemical state-space, fig. 5.28, it can be seen that initial stages of flame development, before the flame skirt touches top/bottom walls, are identical to the closed duct (compare fig. 5.20). Figure 5.28 shows hemispherical flame (green), flame distorted through acoustic reflection from top/bottom walls (blue, first critical point), developed finger flame (cyan) and the flame approaching top/bottom walls (red, second critical point). At this stages, in closed duct, the acoustic disturbances have not yet reflected from the right end of the duct, and thus both



**Figure 5.25.:** Flame position (top), flame velocity (middle) and sequence of flame front contours (bottom).



**Figure 5.26.:** Comparison of turbulent flame tip velocities for different width/length ratios.

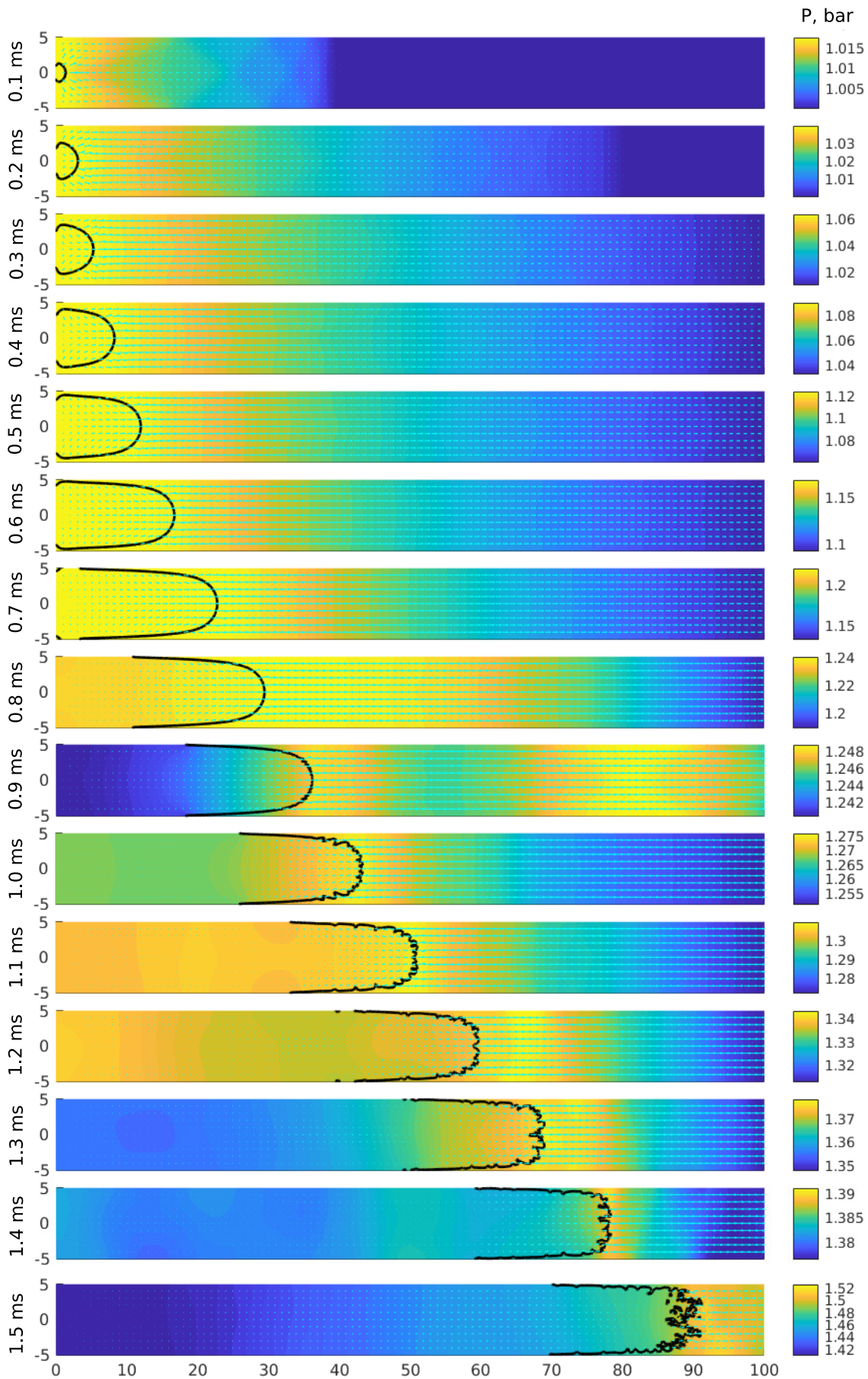


**Figure 5.27.:** Flame development in half open duct  $10 \times 100$  mm. Solid black line shows flame front, colour codes the pressure, cyan arrows represent velocity field.

open and closed configurations have identical hydrodynamical and thermochemical behaviour.

In the next stage, as the flame skirt touches the walls and the flame surface starts to reduce, fig. 5.29, the identical thermochemical state space, as in closed duct, is observed (compare fig. 5.21). Green projections shows here the state, as the flame approaches top/bottom walls, blue projection shows the state, just after the wall approach, and red projections correspond the fourth critical point on the velocity profile, as the flame speed reaches local minimum. The third critical does not have any distinguished features in thermochemical state space. The fourth points corresponds approximately the time moment, when in closed duct the reflected wave from the right end reaches the flame and the plane is formed. Meanwhile, in the open duct at this moment the flame front starts to curve. The reached here thermochemical state space is also identical to the closed duct.

In contrast, to closed duct, where projections of the thermochemical state space in previous step to mole fraction of species, preserves its shape for the rest of flame propagation, the thermochemical state space in open configuration is perturbed through the turbulence. It can be well observed in fig. 5.30, where green projections correspond to the fourth critical point and green, followed by red – represent the later stages of turbulent flame.

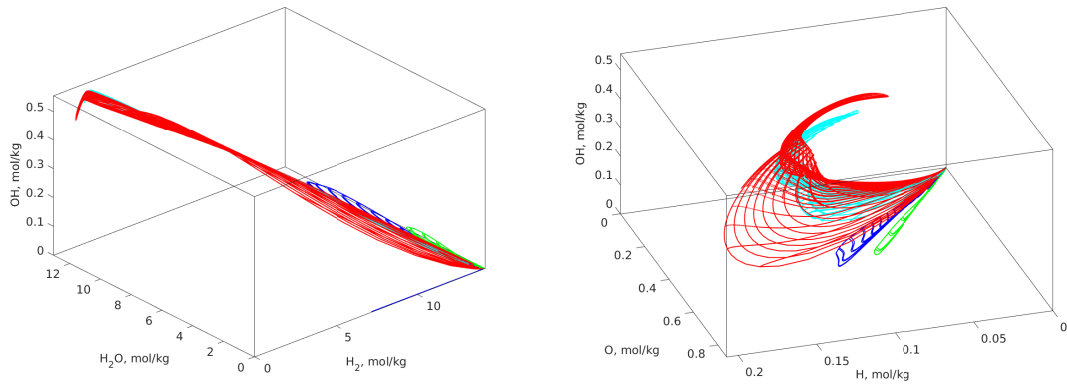


**Figure 5.28.:** Development of finger flame of half open duct in thermochemical state space in projection to  $\text{H}_2\text{O}$ ,  $\text{H}_2$ ,  $\text{OH}$  (left) and to  $\text{H}$ ,  $\text{O}$ ,  $\text{OH}$  (right).

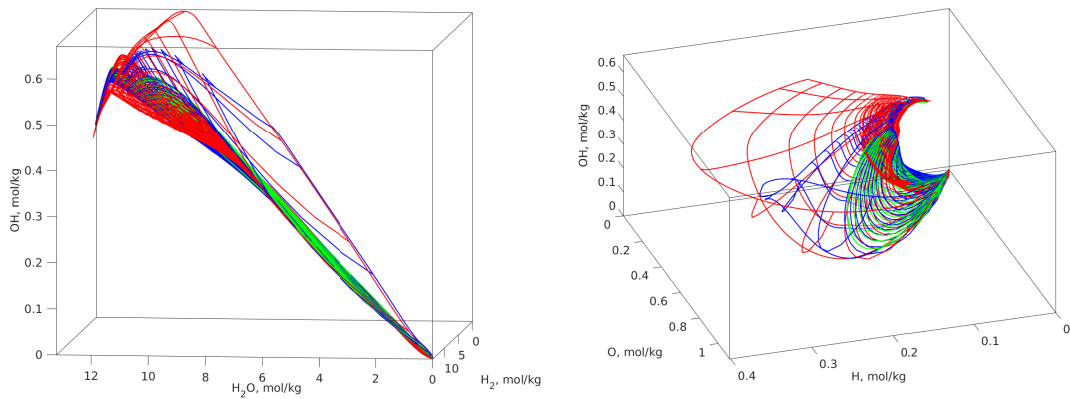


**Figure 5.29.:** Last stages of finger flame of half open duct in thermochemical state space, in projection to  $\text{H}_2\text{O}$ ,  $\text{H}_2$ ,  $\text{OH}$  (left) and to  $\text{H}$ ,  $\text{O}$ ,  $\text{OH}$  (right).

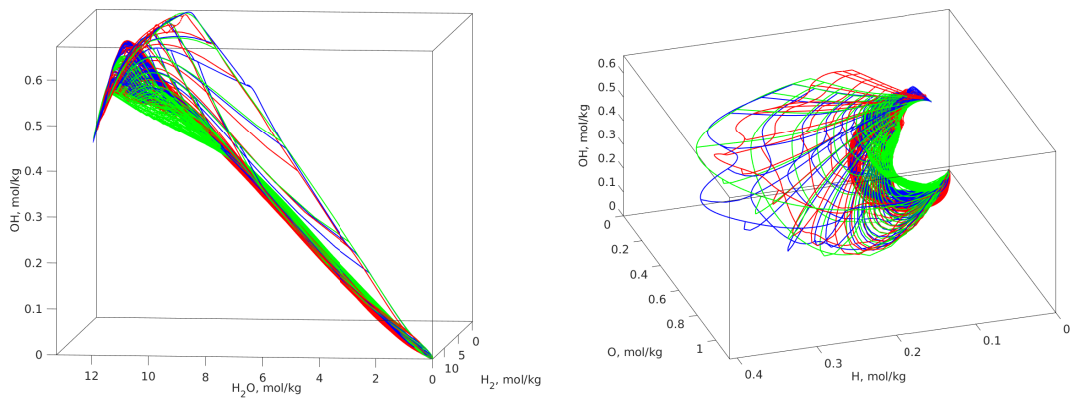


**Figure 5.30.:** Development of turbulent flame of half open duct in thermochemical state space in projection to  $\text{H}_2\text{O}$ ,  $\text{H}_2$ ,  $\text{OH}$  (left) and to  $\text{H}$ ,  $\text{O}$ ,  $\text{OH}$ .

### 5.2.2. Combustion in micro flow reactor

There is a trend to downsize combustion facilities but to sustain the combustion, with the reduction of the facility size, is a very complicated task due the heat losses, flame-wall interaction and heterogeneous chemical effects at the boundary. Nevertheless, there are practical application which showed stable flames in chambers smaller than the quenching radius [JLW78]. In order to stabilise and to study such micro combustion systems in details, an experimental setup with micro flow channel was developed [MPO<sup>+</sup>04]. Over the past decades different chemical mechanisms were studied extensively in this micro flow channel under controlled isothermal conditions, i.e. CH<sub>4</sub>, NH<sub>4</sub>, dimethyl ether, syngas, etc. [SHN<sup>+</sup>13, KNT<sup>+</sup>14, KNT<sup>+</sup>15, NTT<sup>+</sup>16]. It was shown that not all mechanisms perform well under micro scale conditions and this setup can be used efficiently as an additional validation tool.

The experimental work with micro flow reactor covers a large number of phenomena, i.e. flammability and extinction limits, flame quenching and stability effects of lean mixtures [MKK<sup>+</sup>05]. Three regimes of combustion were observed: normal flame, Flames with Repetitive Extinction and Ignition (FREI) and weak flames, depending on the inlet mixture composition and initial and boundary conditions. Normal flame is observed at a high velocity regime. FREI occurs at an intermediate velocity regime where the unstable middle-branch solution exists. Stable weak flames appear at a low flow velocity regime and give a possibility to study and verify low temperature oxidation mechanisms. However, a special attention in the past was given to weak flames. Although experimental findings were well supported by stationary 1D simulations [SHN<sup>+</sup>13, KNT<sup>+</sup>14, KNT<sup>+</sup>15, NTT<sup>+</sup>16, MKK<sup>+</sup>05] there is still a question of applicability of such models.

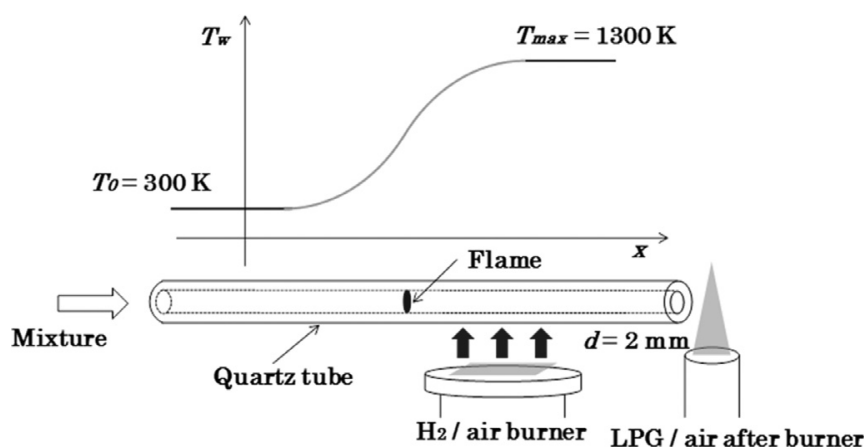


**Figure 5.31.:** Schematic of experimental setup of micro scale combustor, adapted from [NTT<sup>+</sup>16].

Figure 5.31 shows the schematic of the experimental setup [NTT<sup>+</sup>16]. A quartz tube with inner diameter of 2 mm and length 100 mm is used as a reactor channel. A hydrogen/air flat-flame burner was employed as an external heat source and the stationary temperature profile from ambient temperature 300 to 1300 K is formed along the inner surface of the reactor channel. Optical observations of the flame are conducted through a band-pass filter (transparent wavelength: 431.4 nm, half bandwidth: 6.4 nm). In this observation, UV chemiluminescence from the hydrogen oxidation is filtered out and part of broad spectrum from the CO–O radiation (350–450

nm) can be captured [NTT<sup>+</sup>16]. All experiments were conducted at atmospheric pressure and given mixtures were supplied to the reactor at inlet mean flow velocity of  $v_0 = 2$  cm/s.

In order to create a numerical model of the experimental setup (fig. 5.31), the configuration shown in fig. 5.32 is proposed. The channel is modelled in 2D with rotational symmetry (see §A.3 cylindrical, axial). The symmetry is assumed along rotation angle  $\theta$ ,  $x$  is axial direction,  $r$  is radial. The wall of the channel (top) is assumed isothermal and non-slip. At the inflow (left) a fresh mixture with given velocity is provided. The outflow simulates a large open space and at the bottom symmetrical boundary condition. The mathematical model of this boundaries is described below:

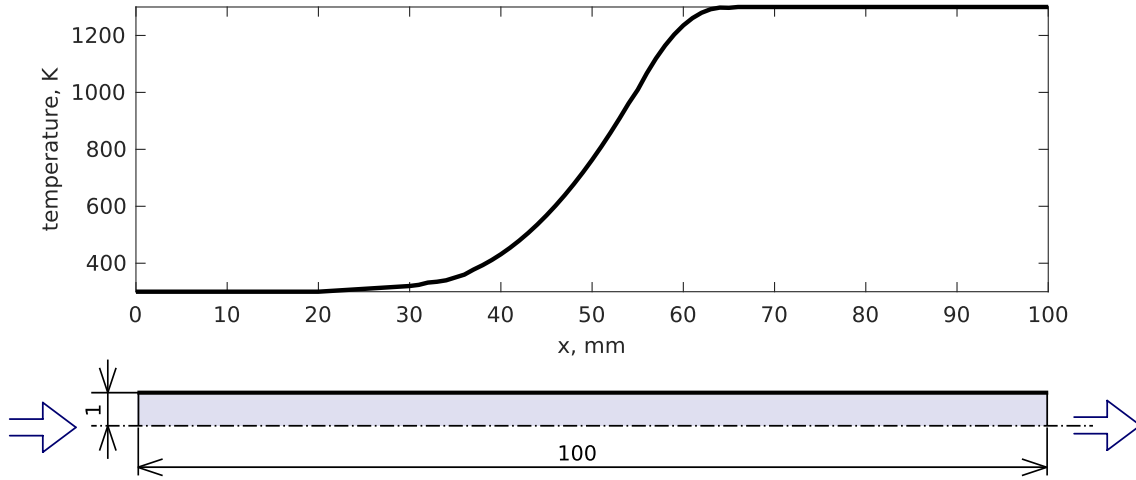


**Figure 5.32.:** Modelling configuration of micro flow channel.

**Isothermal wall**,  $r = 1$  mm, adapted from [PL92].

$$\left\{ \begin{array}{l} v_x(t, x, 1 \text{ mm}) = 0 \\ v_r(t, x, 1 \text{ mm}) = 0 \\ T(t, x, 1 \text{ mm}) = T_{\text{wall}}(x) \\ \frac{\partial}{\partial t} (g_\theta c_i) + \frac{\partial}{\partial x} (g_\theta \bar{j}_{x,i}) = g_\theta \left( \dot{\omega}_i - \frac{d_1}{\rho} c_i \right), \end{array} \right. \quad (5.20)$$

where  $T_{\text{wall}}$  is provided temperature profile at the wall (see fig. 5.32),  $g_\theta = r$  is coordinate transformation parameter <sup>4</sup> (see §A.2 and §A.3), and the mass specific boundary derivative is given [PL92] as:

$$d_1 = \frac{1}{a} \left( \frac{\partial P}{\partial r} + \rho a \frac{\partial v_r}{r} \right), \quad (5.21)$$

with  $a = \sqrt{\gamma P / \rho}$  representing speed of sound.

<sup>4</sup> $g_x = g_y = 1$  are omitted in the equation for more compact representation

**Symmetry axis,  $r = 0$**

$$\begin{cases} \frac{\partial}{\partial r} v_x(t, x, r_0) = 0 \\ \frac{\partial}{\partial r} v_r(t, x, r_0) = 0 \\ \frac{\partial}{\partial r} T(t, x, r_0) = 0, \\ \frac{\partial}{\partial r} c_i(t, x, r_0) = 0. \end{cases} \quad (5.22)$$

In order to avoid singularity in coordinate transformation, the left boundary was placed at  $r_0 = 0.01$  mm.

**Inflow (NSCBC),  $x = 0$**

This boundary condition is adapted from NSCBC subsonic inflow [PL92], where the inflow velocity  $v_x$ ,  $v_r$ , temperature  $T_{in}$  and mixture composition as mole fractions  $X_{in,i}$  are imposed:

$$\begin{cases} v_x(t, 0, r) = v_{in}(t, r) \\ v_r(t, 0, r) = 0 \\ T(t, 0, r) = T_{in}(t, r), \\ \frac{\partial}{\partial t} c_i(t, 0, r) = g_\theta \left( \dot{\omega}_i - \frac{1}{M} (d_1 - v_{in} \rho) X_{in,i} - \dot{c}_i v_{in} \right). \end{cases} \quad (5.23)$$

here  $M$  is mean molar mass and the abbreviation  $(\dot{\phantom{x}}) = \partial(\phantom{x})/\partial x$  denotes space derivative at the boundary, computed from inner points. The inflow velocity  $v_{in}$  is given with parabolic profile, such that mean value in through the circular surface is equal to desired value, e.g. experimental  $\bar{v}_0 = 0.02$  m/s:

$$v_{in}(t, r) = 2 \frac{\bar{v}_0(t)}{r_\infty - r_0} (r_\infty(r_\infty - 2r_0) + 2r_0 r - r^2) \quad (5.24)$$

with  $r$  given in meters, and  $r_\infty = 1 \times 10^{-3}$  m,  $r_0 = 1 \times 10^{-5}$  m. Mean inflow velocity  $v_0$  is allowed to be time dependent. Here the mass specific boundary derivative is given as [PL92]:

$$d_1 = \frac{1}{a^2} \left( \mathcal{L}_2 + \frac{1}{2} (\mathcal{L}_5 + \mathcal{L}_1) \right), \quad (5.25)$$

where  $\mathcal{L}_i$  are amplitudes of characteristic waves, give as

The amplitudes of characteristic waves for outflow:

$$\begin{aligned} \mathcal{L}_1 &= (v_{in} - a) \left( \frac{\partial P}{\partial x} - \rho a \frac{\partial v_x}{\partial x} \right), \\ \mathcal{L}_5 &= \mathcal{L}_1 - 2\rho a \frac{\partial v_{in}}{\partial t}, \\ \mathcal{L}_2 &= \frac{1}{2} (\gamma - 1) (\mathcal{L}_5 + \mathcal{L}_1). \end{aligned} \quad (5.26)$$

The eq. (5.24) was derived under consideration that stationary flows in pipes tend to take parabolic form (see e.g. [CM00]):

$$v_{in}(r) = b_0 + b_1 r + b_2 r^2. \quad (5.27)$$

The velocity at the wall is zero, due to non-slip condition, eq. (5.20), the gradient of velocity at the symmetry boundary should be zero, eq. (5.22), and the mean velocity over the surface of circular inflow  $\bar{v}_0$  is imposed by the user:

$$\left\{ \begin{array}{l} \bar{v}_0 = \frac{\int_{r_0}^{r_\infty} 2\pi v(r) r dr}{\int_{r_0}^{r_\infty} 2\pi r dr} \\ v_{\text{in}}(r_\infty) = 0 \\ \frac{\partial}{\partial r} v_{\text{in}}(r_0) = 0. \end{array} \right. \quad (5.28)$$

Solving system eqs. (5.27) and (5.28) for coefficients  $b_0$ ,  $b_1$  and  $b_2$  leads to the expression for inflow velocity (5.24).

**Outflow (NSCBC),  $x = 100$  mm**

$$\left\{ \begin{array}{l} \frac{\partial}{\partial t} (g_\theta \rho v_x) + \frac{\partial}{\partial r} \left( g_\theta (\rho v_x v_r + \tau_{xr}) \right) = -g_\theta (v_x d_1 + \rho d_3), \\ \frac{\partial}{\partial t} (g_\theta \rho v_r) + \frac{\partial}{\partial r} \left( g_\theta (\rho v_r^2 + \sigma + \tau_{rr}) \right) = -g_\theta (v_r d_1 + \rho d_4), \\ \frac{\partial}{\partial t} (g_\theta \rho e) + \frac{\partial}{\partial r} \left( g_\theta (v_x \tau_{rx} + v_r (\rho e + \sigma + \tau_{rr}) + q_r) \right) = -g_\theta \left( \left( h + \frac{1}{2} v_x^2 \right) d_1 + \rho v (\dot{h} + v \dot{v}) \right) \\ \frac{\partial}{\partial t} (g_\theta c_i) + \frac{\partial}{\partial r} \left( g_\theta (c_i v_r + \bar{j}_{i,r}) \right) = g_\theta \left( \dot{\omega}_i - \left( (d_1 - v_x \dot{\rho}) c_i + v \dot{c}_i \right) \right), \end{array} \right. \quad (5.29)$$

Here, the abbreviation  $(\dot{\phantom{x}}) = \partial(\phantom{x})/\partial x$  for space derivative is used. All variables, unless specified, are computed from the solution approximation within the domain at the corresponding boundary. Mass specific boundary derivatives  $d_1$ ,  $d_3$ ,  $d_4$  and required amplitudes of characteristic waves were discussed in §6.2, eqs. (6.8), (6.9), and §5.2.1, (5.17), (5.18).

The reacting system and species transport were modelled with data provided for Warnatz synthesis gas mechanism [MW88]. The mechanism contains 13 species and 68 elementary reactions. In the focus of this study is the composition of fuel (CO, H<sub>2</sub>) at stoichiometric conditions. The list of conditions is summarised in the table 5.3. The listed conditions are covered by experimental study of Nakamura et.al. [NTT<sup>+</sup>16]. Here, the parameter  $\alpha$  describes fuel composition:

$$\alpha = \frac{X_{\text{CO}}}{X_{\text{CO}} + X_{\text{H}_2}}. \quad (5.30)$$

In the physical experiment, the mixture in the channel is ignited with significantly higher flow velocity and then the mean velocity is reduced to 0.02 m/s. In order to simulate this behaviour the experiments are split in two stages.

1. Acquire a steady flow for mixture composition shown in table 5.3 with disabled reactions. The mean inflow velocity  $\bar{v}_0 = \bar{v}_{0,a}$ .
2. Acquire a steady reacting flow. The solution from the previous stage is taken as an initial condition but reactions are now enabled. The inflow velocity

$\alpha$	$X_{\text{CO}}$	$X_{\text{H}_2}$	$X_{\text{O}_2}$	$X_{\text{N}_2}$	$\bar{v}_{0,a}$	$\bar{v}_{0,b}$
0.1	2 %	18 %	10 %	70 %	0.5 m/s	0.02 m/s
0.25	5 %	15 %	10 %	70 %	0.5 m/s	0.02 m/s
0.5	10 %	10 %	10 %	70 %	0.2 m/s	0.02 m/s
0.75	15 %	5 %	10 %	70 %	0.2 m/s	0.02 m/s
0.9	18 %	2 %	10 %	70 %	0.2 m/s	0.02 m/s

**Table 5.3.:** Micro flow channel configurations used in study.

is gradually reduced from  $\bar{v}_{0,a}$  to  $\bar{v}_{0,b}$ . At the time  $t = 0$ , mole fractions of components are redistributed, linearly with temperature, such at  $T = 300$  K only initial fuel is present, and at  $T = 1300$  only products are present.

As mentioned above, the experimental data is available in form of optical observation at wave length  $431.4 \pm 6.4$  nm. This wave length corresponds, in case of hydrocarbons, to electronically excited CH species (CH\*) [NS07, GAB14]. In synthesis gas the filter wave length corresponds approximately to the maximum of spectral intensity [NS07]. Previous work on this subject, i.e. [SHN<sup>+</sup>13, KNT<sup>+</sup>14, KNT<sup>+</sup>15, NTT<sup>+</sup>16], used local heat release rate as an approximation for the location maximal luminosity of the flame. The heat release rate  $Q$  is given as:

$$Q = - \sum_i \bar{h}_i \dot{\omega}_i. \quad (5.31)$$

where  $\bar{h}_i$  is molar enthalpy of species  $i$  and  $\dot{\omega}_i$  is molar production rate of species  $i$ .

As seen in fig. 5.33(left), observed luminescence is an integral value along optical lines. If the distance between the camera and the channel is much large than the diameter of the channel, then it can be assume the optical lines of the camera are parallel to each other. Then the camera view can be approximated by a projection to the middle plane, as shown in fig. 5.33(right):

$$I(r) = 2 \int_0^{\pi/2} u \left( \frac{r}{\cos \theta} \right) d\theta, \quad (5.32)$$

where  $u(r)$  is a studied variable in (2D) symmetry plane and  $I(r)$  is observed signal intensity.

The experimental and numerical data are summarised in figs. 5.34. The figure compares experimental luminescence images (top half of frames) with total energy release through reaction (bottom part of frames). The experimental results are adopted from [NTT<sup>+</sup>16]. The deviation of flame position between experimental and computational results is within 1 mm, with better agreement for higher concentration of carbon monoxide in the fuel. The comparison of flame position measured with heat release rate (HRR) signal is shown in fig. 5.35. Points are experimental measurements of the location of maximal light intensity, green line corresponds to results of simplified

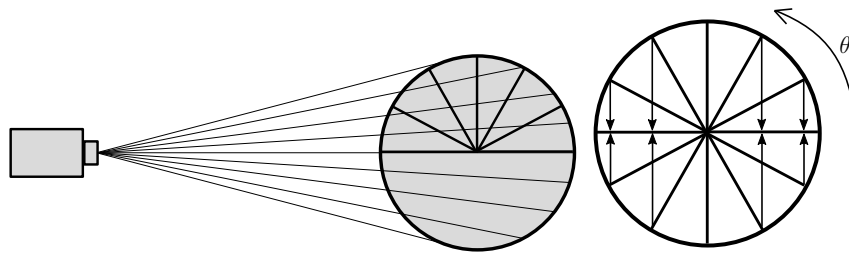


**Figure 5.33.:** Integral camera image: camera view through cylinder (left), projection of rotated layers to horizontal plane (right).

1D model [NTT<sup>+</sup>16] and red line are results of 2D simulations (this work). It can be seen that the trend and locations of flame position is captured well by both models but the 2D model is somewhat closer to the experimental results, which indicate the importance of transport processes in different directions. A small kink in experimental data for temperatures below 1010 K could not be reproduced neither with 1D nor with 2D models. Large uncertainties of experimental data of  $\pm 10$  K, indicate that an additional experimental study for this temperature range is required.

Figure 5.36 shows thermochemical profiles in more details for 50% CO and for 50% H<sub>2</sub> in fuel. The top frame shows specific mole number of CH\* modelled with a small extension to the syngas mechanism [NS07]. The concentration of this species is proportional to the chemiluminescence of excited CH radical. The pick of chemiluminescence for CH lays at wave length 430 nm, which corresponds to the optical filter pass band. It can be observed that the position of CH\* and of HRR do not match. The maxima of CH\* lays at  $x = 56.20$  mm (wall temperature  $T = 1079$  K) and the maximum of HRR lays at  $x = 54.75$  mm (wall temperature  $T = 997$  K). The position of maximal HRR correlates well with the position of O radical and formaldehyde (CH<sub>2</sub>O). However, the modelled concentration of this species is as small as  $\sim 10^{-19}$  mol/kg, that it unlikely can contribute to the light emission, seen in the experiment.

It can be seen in fig. 5.36 that most species have maximum near the maximum of HRR and are concentrated near the symmetry axis. However, two species exhibit a different behaviour. Species OH appears in much later stages, compared to other intermediates and its maximum lays near the wall. The primary source of OH radicals is the decomposition reaction  $\text{OH} + \text{OH} + (\text{M}) \rightleftharpoons \text{H}_2\text{O}_2 + (\text{M})$  which become significant from 1000 K – further downstream of the reaction zone. Although, formaldehyde (CH<sub>2</sub>O) appears near the maximum of HRR but this species is concentrated also more near walls of the channel, where the temperature is somewhat higher as in the middle of the channel.

Figure 5.38 shows species profiles along the symmetry axis for various fuel compositions. It can be seen that hydrogen is consumed earlier than carbon monoxide and water is produced somewhat earlier than carbon dioxide. This can explain that maximum of HRR for fuels with higher hydrogen content lays before those with lower hydrogen content. The maximum of the O-atom and H-atom concentrations for fuel compositions with CO less than 50% lays is shifted to the left relative to the higher CO contents. The location of HCO radical has little dependence on fuel composition. The position of OH radical is shifted more to the right with increase of CO content

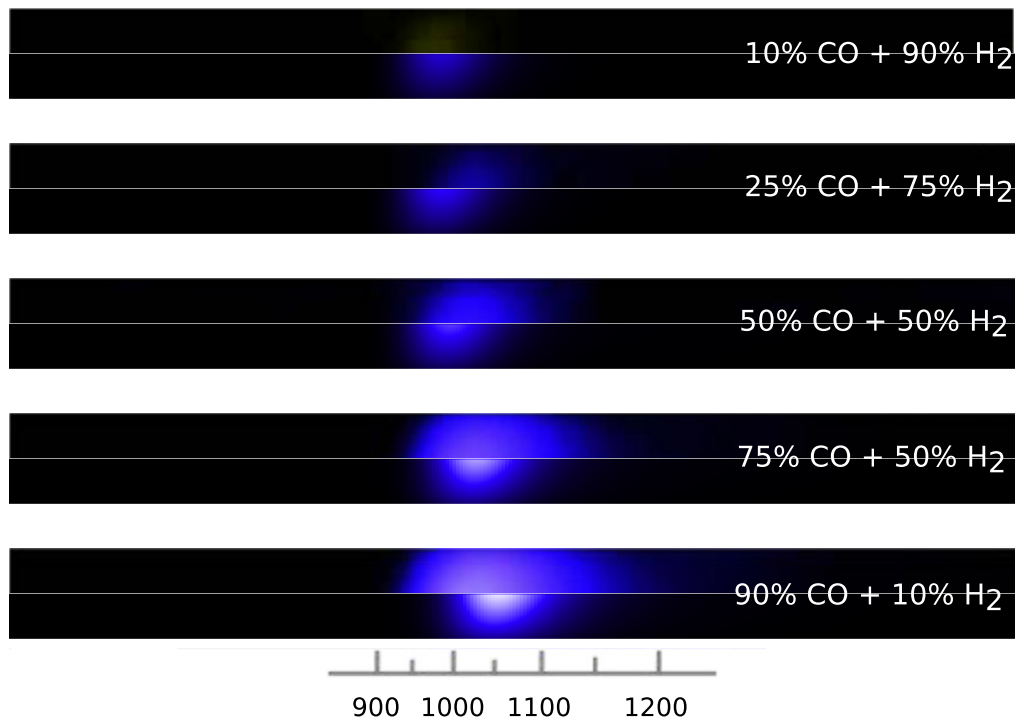


**Figure 5.34.:** Chemiluminescence in micro flow reactor for various fuel composition. In each frame, the upper half corresponds to experimental results [NTT<sup>+</sup>16], the lower half – numerical energy release rate (this work)

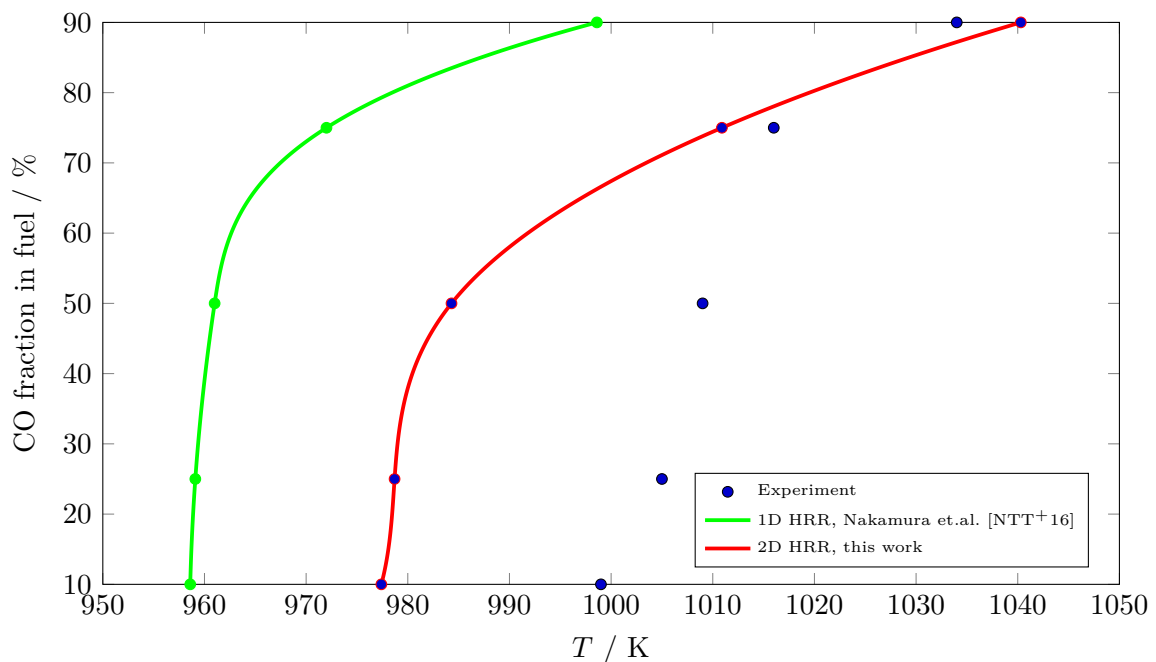


**Figure 5.35.:** Comparison of computed flame position with experimental measurements, adopted from [NTT<sup>+</sup>16].

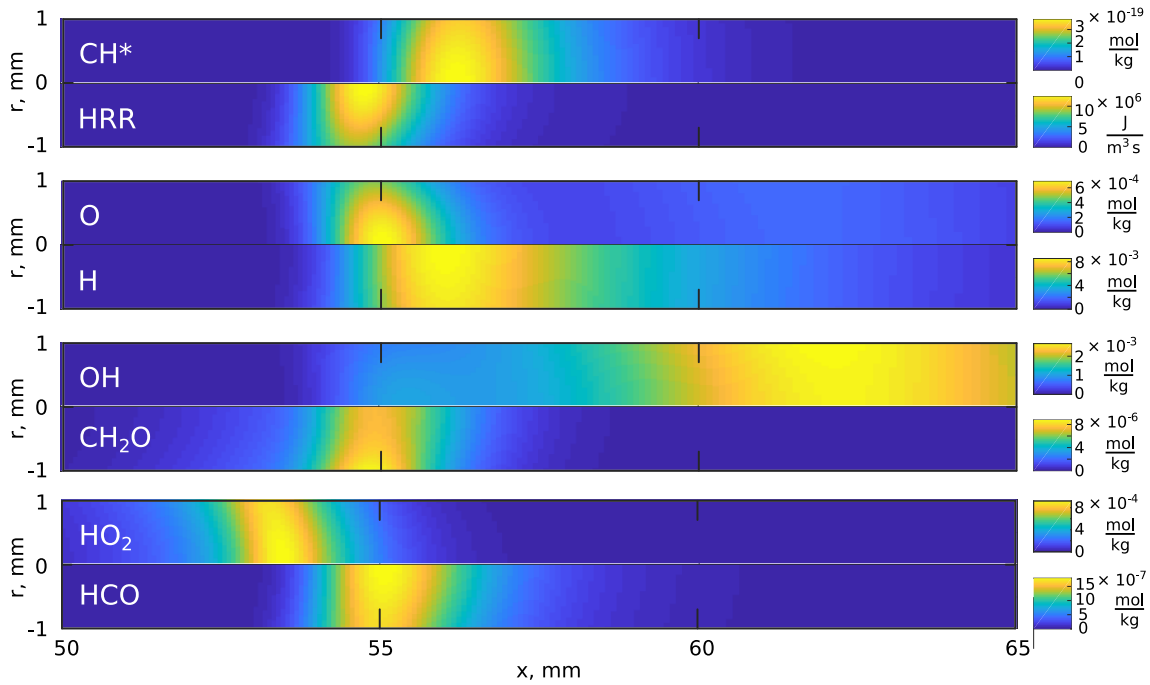


**Figure 5.36.:** Weak flame stationary profiles in 2D for volume ratios of CO=50 % and H<sub>2</sub>=50 % in fuel.

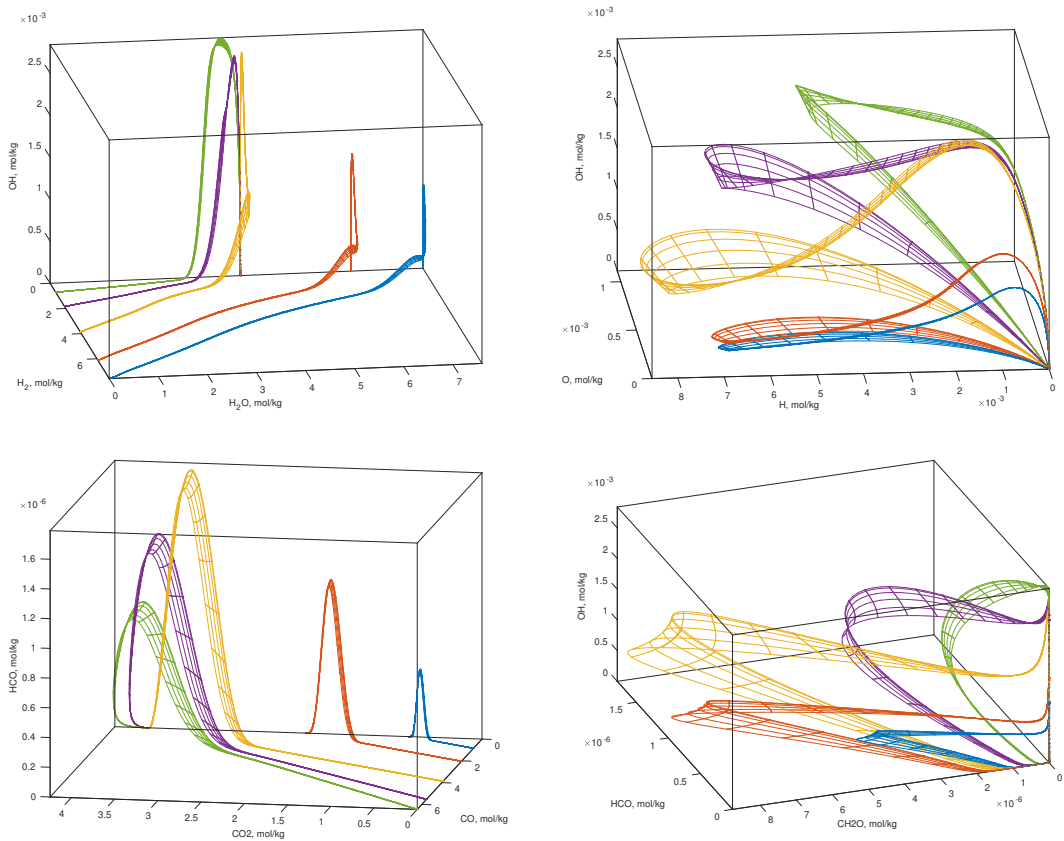


**Figure 5.37.:** Projection of thermochemical state of stationary flame for various CO to H<sub>2</sub> ratios: blue – 10 %, red – 25 %, orange – 50 %, violet – 75 %, green – 90 % CO.

in the fuel, which corresponds to the position of strongest consumption of CO and production of CO<sub>2</sub>. This indicates that the reaction  $\text{CO} + \text{OH} \rightleftharpoons \text{H} + \text{CO}_2$  is the main path for oxidation of carbon monoxide. It is interesting, that for fuels with CO content less than 50 %, the shape of OH profile is very similar but between CO content 50 and 75 % the profile changes its form significantly. Although, the position of CH<sub>2</sub>O is almost independent on fuel content, its maximum corresponds to 50 % CO and 50 % H<sub>2</sub> in fuel. For other fuel compositions the production of formaldehyde is reduced. The concentration of HO<sub>2</sub> is growing with the ratio of H<sub>2</sub> in fuel.

The effects of fuel composition are best seen in projections of thermochemical state space to radical concentrations, fig. 5.37. It can be seen that the thermochemical state space is identical, if appropriately scaled, for fuel compositions CO 50 % and less. However, for higher CO content in fuel the state space is changed significantly.

Although, the numerical results are very close to experimental measurements, the exact position does not match nonetheless. It may be due to the following reasons:

- Chemical model (mechanism). Previous study [NTT<sup>+</sup>16] indicates that the position of maximal HRR can vary significantly from model to model, which means that some improvements of Warnatz mechanism could be done.
- Heterogeneous reactions. As indicated in [PMF<sup>+</sup>09] heterogeneous reactions have a stabilising effect on flame and thus may affect the position of the flame in micro channels. Currently heterogeneous reaction is missing in the 2D model.
- Light intensity position. The model of light emission through excited CH radical, predicts different position of visible chemiluminescence and of heat release rate.

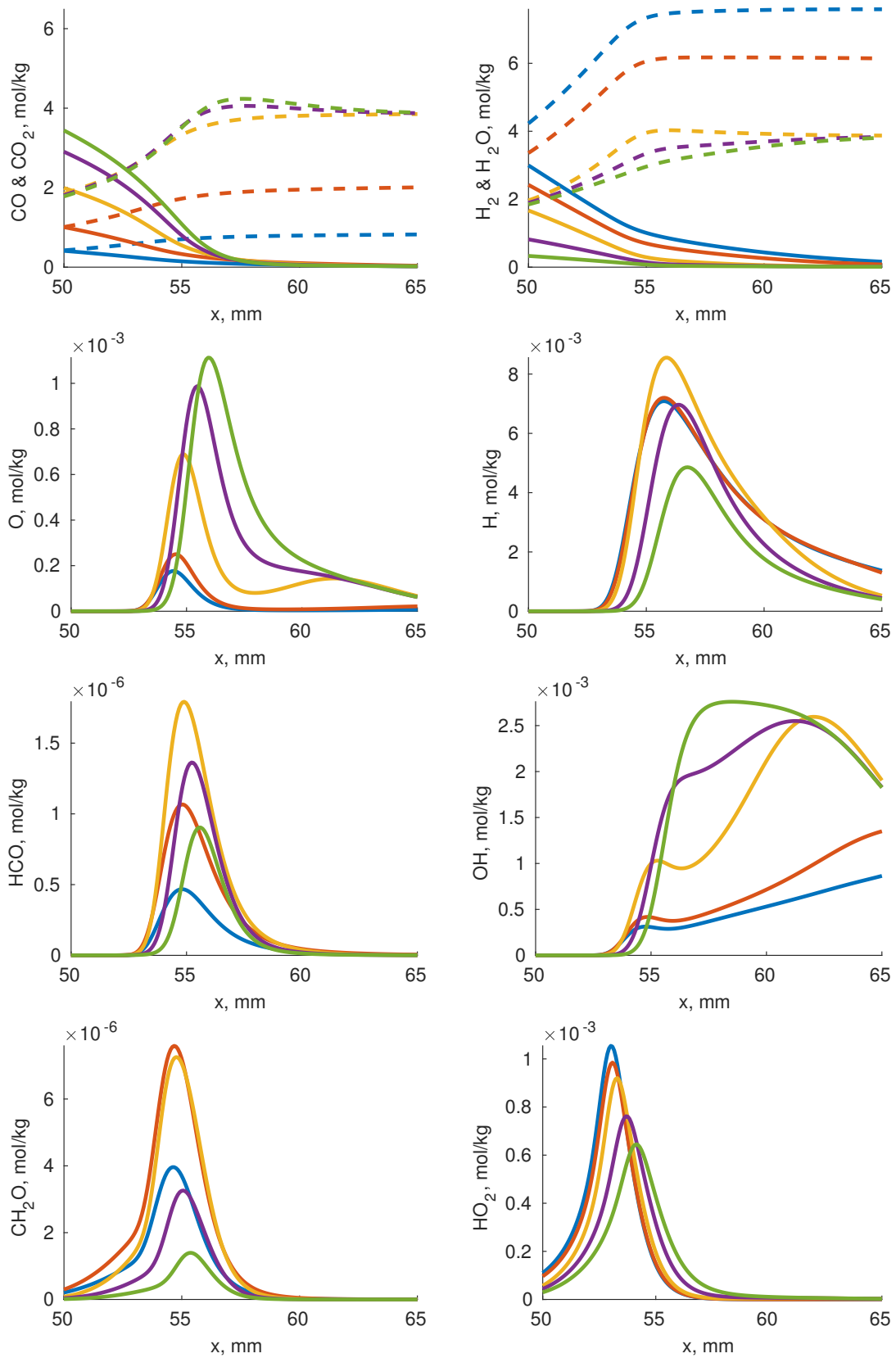


**Figure 5.38.:** Species profiles for various CO to H<sub>2</sub> ratios: blue – 10 %, red – 25 %, orange – 50 %, violet – 75 %, green – 90 % CO. Dashed lines correspond to reaction products CO<sub>2</sub> and H<sub>2</sub>O.

## 6. Modelling of flame acceleration in unconfined settings

Flame acceleration is probably one of the most complex problems in combustion. Under particular conditions this acceleration leads to detonation. In order to treat the flame acceleration quantitatively, all possible phenomena should be taken into account because hydrodynamical and combustion processes becomes extremely coupled having enormous differences in characteristic time and space scales. In spite a considerable progress in understanding of combustion processes has been made in the past and recently, the problem remains open.

The problem is very important for applications and for safety issues. On one hand uncontrolled detonation is a very destructive phenomenon and it is important in risk assessment [Net12]. The detonation can be accounted for engine knock and engine damage [ZWX<sup>+</sup>12]. On the other hand controlled detonation offers a new perspective in propulsion, such as pulse detonation and rotation detonation engines, which promise higher thermal and exergetic efficiency [Kai03].

In study of the problem a central role plays the so-called mechanism of the flame acceleration. In this respect, there are two principle scenarios. In the first scenario, when a large energy deposition happens within a very short time, which is shorter than the acoustic time scale, a direct initiation of the detonation occurs [KNL10, SP17, He96]. In a more interesting and general case the detonation occur after an unsteady deflagration stage of the flame acceleration [ZR47, FK63, KRB<sup>+</sup>11]. At present, there is no quantitative and predictive theory for the second scenario.

It is straightforward to assume that turbulence is the driving force [Lee08]. The flame surface grows increasing the flame speed, which has positive feedback on the flame acceleration. In [KOW97] the author links turbulence intensity with DDT based on gradient of chemical reactivity [ZLMS70]. There is a number of numerical investigations [KLM10, OG07] supporting this theory. However, in this context the mechanism of turbulence initiation and sufficient flame acceleration remains open.

In unconfined settings shock-wave interaction is negligible, due to this the other weaker mechanism such as Darrieus-Landau, thermal-diffusive and Rayleigh-Taylor instabilities gain more importance for turbulence generation [PLS69, KLAM17, KKIL13, IKL11]. This motivated to implement and to study the 1D  $\Sigma$ -model introduced in [DJ89] and extensively studied in later works [KS17b, KS17a, KS16].

Within this approach the complex phenomenon of flame wrinkling can be still described as an integral effect on the flame structure with 1D formulation, using flame folding factor  $\Sigma$ . This factor represents the ratio of the total area of the wrinkled front to the area associated with its average radius. It is implemented as a simple amplification of the chemical source term by  $\Sigma^2$ , compare with eq. (A.18):

$$\frac{\partial}{\partial t}(g c_i) + \frac{\partial}{\partial \xi} \left( g_{\eta} g_{\zeta} (v c_i + \bar{j}_i) \right) = g \Sigma^2 \omega_i. \quad (6.1)$$

Within the sigma-model the flame folding represents an integral factor used to study accelerating flame dynamics. Keeping in mind that, a critical factor is looked for, when the deflagration cannot be sustained, and following the Zeldovich's analysis of flame propagation [Zel48], the same impact can be achieved either by enhancing reaction rate or diffusivity (by  $\Sigma^2$ ) because flame velocity  $v_L$  is proportional to square root of diffusivity  $d$  and reaction rate  $\dot{\omega}$ :

$$v_L \propto \sqrt{d \dot{\omega}}. \quad (6.2)$$

The 1D model of full compressible fluid applied for this study. This model in general orthogonal coordinates is described in §A.1.

## 6.1. Flame acceleration near wall

In this setup, a sufficiently large computational domain is chosen, such that the acoustic waves do not disturb the solution by the reflection from the opposite boundary. For the current case, the domain length  $L = 0.5$  m (see eq. (6.3)) was chosen. This domain allows a simulation time of about 1 ms till acoustic disturbances reach the opposite side, taking into account the speed of sound of about 500 m/s in the fresh mixture. The mixture is ignited at the left boundary  $L = 0$  and the flame acceleration is studied by varying flame folding parameter  $\Sigma$  (see eq. (6.1)).

The whole process is described by the governing equations eqs. (A.13) – (A.18) and (6.1). The boundary conditions, representing adiabatic “walls” are given by eq. (6.3):

$$\begin{cases} v(t, 0) = v(t, L) = 0, \\ \frac{\partial}{\partial \xi} T(t, 0) = \frac{\partial}{\partial \xi} T(t, L) = 0, \\ \frac{\partial}{\partial \xi} c_i(t, 0) = \frac{\partial}{\partial \xi} c_i(t, L) = 0, \quad \forall i = 1, \dots, N_s. \end{cases} \quad (6.3)$$

The Warnatz mechanism [MW88] containing 8 species and 38 elementary reactions was used. The ignition is initiated with the hot spot of a specified width, keeping the pressure constant in space at time  $t = 0$ :

$$\begin{cases} v_0 = 0, \\ T_0(x) = 300 \text{ K} + (1200 \text{ K}) e^{-(x/l)^2}, \\ c_{0,i}(x) = X_{i,0} \frac{1 \text{ bar}}{R_0 T_0(x)}, \quad i = 1, \dots, N_s, \end{cases} \quad (6.4)$$

Natural sensitivity of the ignition processes to initial parameters is additionally amplified by the flame folding ratio. In many cases for elevated  $\Sigma$  an instantaneous

detonation was observed, if too much energy was deposited in the initial hot spot. For example, at  $\Sigma = 5$  with hot width  $l = 0.08$  mm, the detonation is initiated instantaneously but with the hot spot width  $l = 0.039$  no detonation is observed at all. Thus, in order to minimise the influence of hot-spot on unsteady flame propagation, a minimal ignition energy has to be provided.

The energy deposition in the initial hot-spot can be adjusted by varying the hot-spot parameters (see eq. (6.3)). In computations it was implemented by a detailed study of the hot spot width  $l$ , keeping the hot spot temperature constant, for different values of  $\Sigma$  such that minimising the chosen value of width of the hot spot by 1% leads to an ignition failure. Interesting that the resulting  $l$  has a linear dependency on  $\Sigma$  in logarithmic scale, which is shown in fig. 6.1.

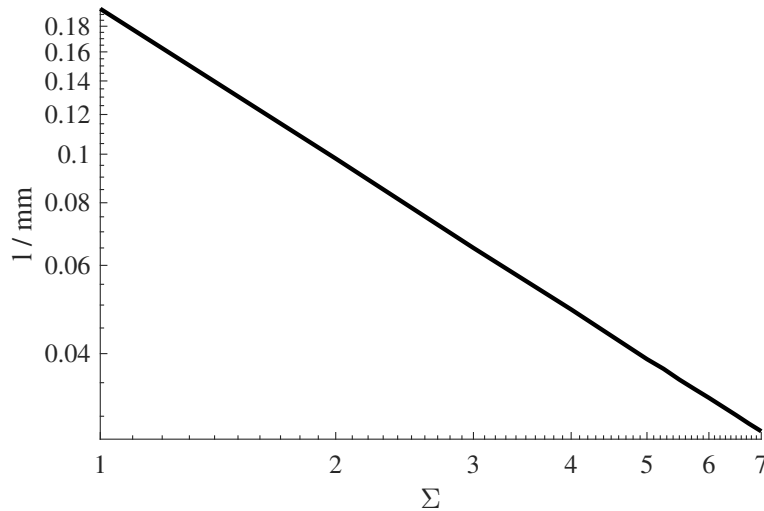


**Figure 6.1.:** Width of the initiation hot spot  $l$  mm vs. folding factor  $\Sigma$ .

According to seminal Gostintsev's experimental observation [GIS88] the flame folding in spherical geometry depends strongly on the flame radius. However, the current study investigates the existence of a critical folding factor, when the deflagration flame propagation cannot be sustained [KS17a], and the role of detailed chemical reaction under such conditions. The PDE system is integrated for different constant values of  $\Sigma$ , starting with unity, and internal structure of the accelerating flame front is investigated.

As it was predicted and was shown in a number of works [KS17b, KBKS18], there is a critical value of  $\Sigma$  leading to very strong DDT, when an over-driven detonation is formed. Until this critical value is reached, flames with deflagration flame structure are observed with only a moderate pressure increase between the precursor shock and the flame front.

Figure 6.2 illustrates the flame front speed depending on  $\Sigma$ , where actual observed flame front speed is shown together with the one extrapolated from the normal deflagration velocity for  $\Sigma = 1$  as  $v_L(\Sigma) = v_L(1)\Sigma$ , where  $v_L(1) = 90.5$  m/s. It can be seen that starting from  $\Sigma \approx 3$  the actual flame velocity begin to deviate significantly from the extrapolated value. After reaching a critical value of  $\Sigma^* \approx 6.1$ , the flame front drastically accelerates with following DDT. The dashed line shows

the quasi-stationary speed of the shock wave after ignition with  $\Sigma = 1$ . This speed of 590 m/s is an overlapped expansion of the gas through reaction heat and the speed of sound.

Considering that the transport of acoustic disturbances is limited to the speed of sound and the reaction heat pro time unit is controlled with  $\Sigma$ , the intersection of extrapolated shock wave velocity (dashed line) and the extrapolated flame speed (dotted line), can provide a criterion for the estimation of the critical value of flame folding ratio,  $\Sigma = 6.5$ .

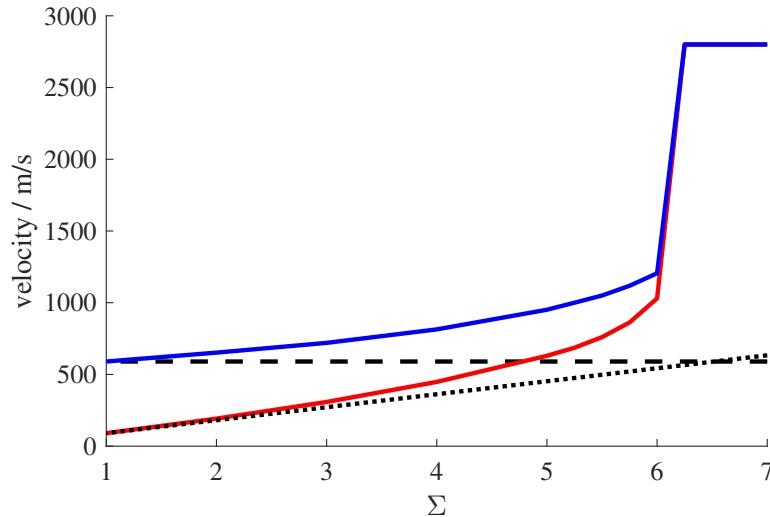


**Figure 6.2.:** Flame speed as a function of  $\Sigma$ : red solid line – actual flame front speed, blue solid line – quasi stationary ignition shock wave speed, dotted line – extrapolated from laminar flame speed with  $\Sigma = 1$ , dashed line – shock wave speed for  $\Sigma = 1$ .

As shown in fig. 6.3 (right), with flame folding ratio  $\Sigma = 6.0$ , the flame was accelerating till it reached saturation about 1000 m/s. Meanwhile the shock wave created at the ignition has reached velocity plateau of about 1200 m/s. This means that the shock and the flame waves are traveling away from one another with constant velocity of 200 m/s. Figure 6.3 (left) shows this fact.

With the flame folding ratio  $\Sigma = 6.25$ , the velocity of the ignition shock behaves similar, almost reaching plateau about 1300 m/s (see fig. 6.4 (right)). However, the flame front accelerates perpetually and about  $2.7 \mu s$  ( $r_{DDT} = 1.919 \text{ mm}$ ) the front experiences a rush acceleration and catches up with the shock wave. The process of DDT for described for  $\Sigma = 6.25$  is similar for all flame folding ratio above  $\Sigma \geq 6.25$ , with radius of transition  $r_{DDT}$  getting shorter.

The criteria proposed in [KYI16, KKIL13] provides an additional tool for comparison and validation. Figs. 6.5 show evolution of the speed of the flame front, the sound speed at the maximum of the pressure and the sound speed in products. One can see that in the first scenario with  $\Sigma = 5.75$  (left), after the initial ignition period, all three characteristics remain almost constant. Thus, the quasi-steady deflagration regime is reached. However, in the second scenario (right) the flame front accelerates further in a very short time. During the acceleration the sound velocity of the Neumann

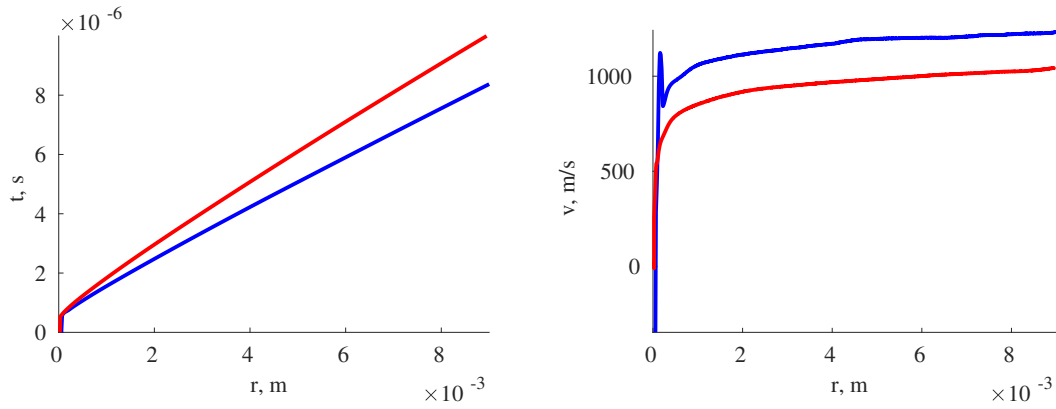


**Figure 6.3.:** Flame and shock for  $\Sigma = 6.0$ . On the Left: Position of the flame front (red) and the ignition shock wave (red); On the right Velocity of the flame front (red) and the velocity of the ignition shock wave (blue).

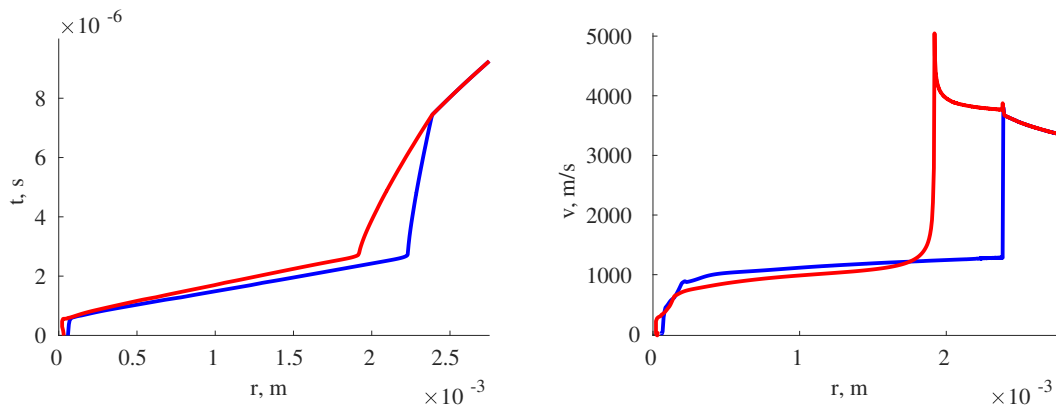


**Figure 6.4.:** Flame and shock for  $\Sigma = 6.25$ . On the Left: Position of the flame front (red) and the ignition shock wave (red); On the right Velocity of the flame front (red) and the velocity of the ignition shock wave (blue).

state (right behind the shock, where the pressure reaches maximal values) grows very slowly and when the front velocity reaches the sound velocity in the products rapid flame front acceleration is observed with subsequent DDT.

By using generic algorithm for interval splitting, uniting and adaptive truncation of the approximating polynomial within the interval the new code can resolve the detonation wave structure with a high accuracy. A limited number of collocation points is used. The evolution of the pressure profile during the DDT can be seen in fig. 6.6. It shows the resolved pressure profile at the moment of the DDT. The whole solution at this moment requires 1106 collocation points on the interval  $x = [0, 0.1]$  m, however, the relative amplitude of the truncated Chebyshev series does not exceed  $10^{-4}$  on each sub-interval (see eq. (3.56)). Required time for this computation till the DDT point is accounted for 3 days on Intel i5-2310 CPU @2.90GHz with 2 cores. The computation with  $\text{RTOL}=10^{-3}$  requires twice as less points and 1.6 times shorter CPU time but the results remain almost identical to  $\text{RTOL}=10^{-4}$ . The relative difference for profiles between these two computations is less than  $10^{-3}$ . The time of DDT can be seen as an integral indicator of accumulated error. The difference between  $\text{RTOL}=10^{-4}$  and  $\text{RTOL}=10^{-3}$  accounts for 0.6%. Even with  $\text{RTOL}=10^{-2}$

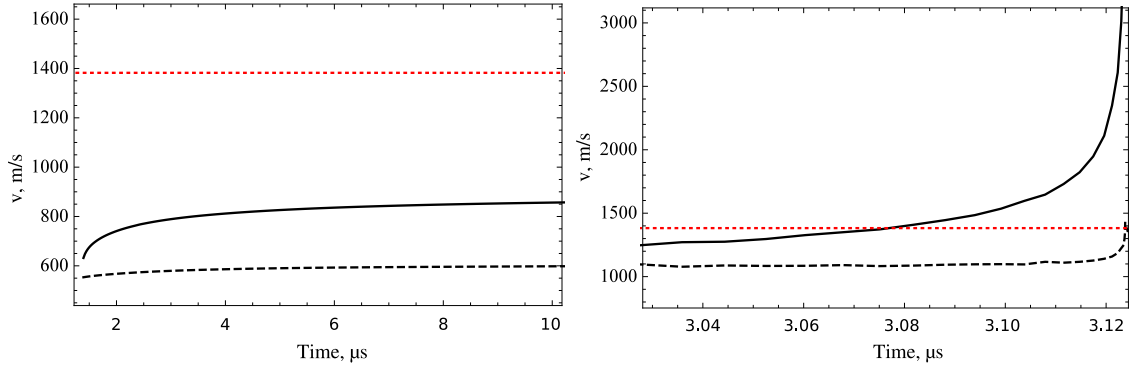


**Figure 6.5.:** Comparison of critical velocities for  $\Sigma = 5.75$  (left) and  $\Sigma = 6.25$  (right). Solid line – flame speed, dashed line – sound velocity at the position of maximal pressure, dotted line – sound velocity in the products.

RTOL	DDT time, $\mu\text{s}$	Grid Points <sup>1</sup>
$10^{-4}$	3.12	1106
$10^{-3}$	3.10	563
$10^{-2}$	3.01	442

**Table 6.1.:** Effect of tolerances on solution of DDT.

the accuracy in estimation of DDT point lays within 5%. These performance criteria are summarised in table 6.1.

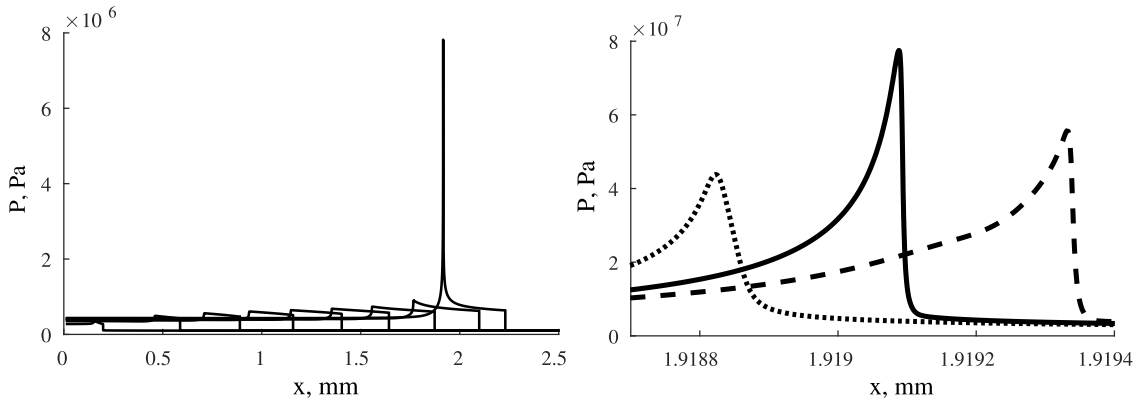


**Figure 6.6.:** On the left: evolution of pressure profile for  $\Sigma = 6.25$  before and at the DDT. On the right: zoom of the pressure profile for  $\Sigma = 6.25$  at the DDT: solid line  $t=3.12378 \mu\text{s}$ , dotted line  $t=3.12373 \mu\text{s}$ , dashed line  $t=3.12382 \mu\text{s}$ .

In order to investigate the flame front structure, several values of flame folding ratio were chosen: one is shortly before the critical value  $\Sigma = 5.75$  and the second one is slightly large than the critical value estimated by  $\Sigma^* = 6.1$ , namely,  $\Sigma = 6.25$ . All results for other values will be qualitatively very similar. The evolution of the system eqs. (A.12)–(A.18) is considered in the system state space, which in the case of detailed chemical kinetics is composed of species concentrations. It can be also

<sup>1</sup>This is the number of points at the moment of DDT. During the solution process, the number of grid points is a subject of strong variation, depending on the solution itself.

visualised, using specific mole numbers  $\phi_i = Y_i/W_i = c_i/\rho$ ,  $i = 1, \dots, n_s$ , to avoid additional strong dependence on the pressure variation.

First of all, the evolution of the system during the ignition and during the initial stage of flame propagation is analysed, when a quasi-steady evolving profile of the flame front establishes. Figure 6.7 shows the profile evolution for minor species in the initial stage of the flame propagation. The profiles are shown for several but different instances in time for both  $\Sigma = 5.75$  (left) and  $\Sigma = 6.25$  (right). The profiles are shown for the same time instances. Although the profiles for  $\Sigma = 5.75$  and  $\Sigma = 6.25$  differ in time and space (flame with  $\Sigma = 6.26$  is obviously faster) they still similar even for minor species like  $\text{H}_2\text{O}_2$ . It is particularly good to see on projections to gas components. Figure 6.8 shows such projections for specific mole number of  $\text{H}_2$ ,  $\text{H}_2\text{O}$  and  $\text{OH}$ . It can be seen that at the initial stage the profiles follow the same path and converge to the same (stationary) profile.

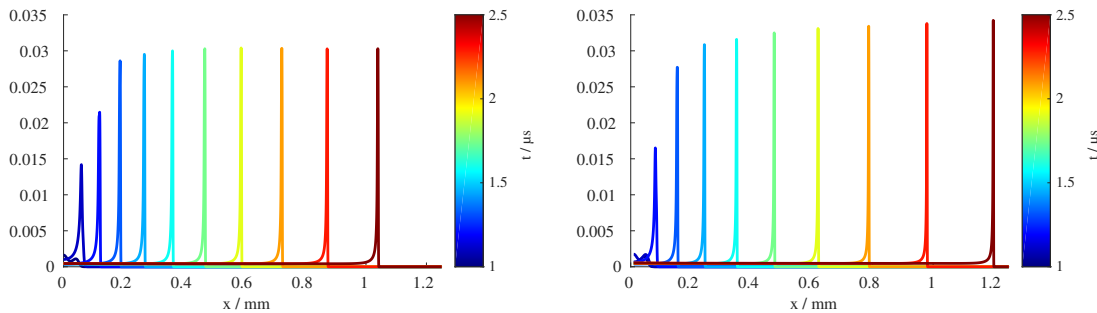


**Figure 6.7.:** The radical profile of  $\text{H}_2\text{O}_2$  specific mole numbers with the folding factor  $\Sigma = 5.75$  (left) and  $\Sigma = 6.25$  (right) over several instances of time.

If the stationary deflagration profiles in projection to specific mole numbers of components are considered for all flame folding ratio  $\Sigma < 6$  (fig. 6.9) they may appear different, which is particularly good to see on projection to radical species  $\text{H}$ ,  $\text{O}$  and  $\text{OH}$  (bottom). However, they have identical shape and with appropriate scale, e.g. maximum of each component, they do not differ one from another.

The situation starts to change, when the transition point is approached. By comparison of the system solution profiles (see fig. 6.10) in this transient regime in the plane projection of the system thermochemical state space, one can see how the quasi-stationary profile (lower solid blue line in fig. 6.10) changes over time while the flame acceleration establishes. Both cases ( $\Sigma = 5.75$  and  $\Sigma = 6.25$ ), until this stage is reached, look very similar and remain identical. They start to deviate strongly from the quasi-stationary profile for  $\Sigma = 5.75$  as the transition point is approached. Finally, after the transition (shown by dashed lines) a new stationary profile establishes (shown by the upper solid red line in fig. 6.10). The drastic change seen in all species projections (compare top and bottom images in fig. 6.10) it is more pronounced for  $\text{O}$ ,  $\text{H}$  and  $\text{OH}$  radicals.

In the deflagration phase, for both  $\Sigma = 5.75$  and  $\Sigma = 6.25$ , system profiles are the same and lay on one dimensional path in the state space (shown in blue in fig. 6.10). Later on during the stages of transition, the states scatter and have multidimensional structure. Furthermore after the transition the solution profile becomes one dimensional again but the solution follows now a different path in the

stat space, shown with solid red line in fig. 6.10. Although initial and final solutions are one dimensional in the state space, these states are completely different, and simple scaling cannot align them. The transition phase (dashed red lines) lays on a complex two (or possibly more) dimensional surface.

## 6.2. Acceleration of a free flame

Flame acceleration near the wall, which was studied in the previous section, is facilitated by the flame-wall interaction. In the current section, another extreme case of free propagating flame is considered, where no external mechanisms influence the flame acceleration. For this task introduced an observer frame, which is moving with the speed  $v_o$ . In this frame the conservation equations in planar geometry read (see §A.1):

$$\begin{cases} \frac{\partial}{\partial t}(\rho v) + \frac{\partial}{\partial x} \left( (v - v_o) \rho v + P - \frac{4}{3} \mu \dot{v} \right) = 0, \\ \frac{\partial}{\partial t}(\rho e) + \frac{\partial}{\partial x} \left( (v - v_o) \rho e + v \left( P - \frac{4}{3} \mu \dot{v} \right) - \lambda \dot{T} + \sum_i \bar{h}_i \bar{j}_i \right) = 0, \\ \frac{\partial}{\partial t}(c_i) + \frac{\partial}{\partial x} \left( (v - v_o) c_i + \bar{j}_i \right) = \dot{\omega}_i. \end{cases} \quad (6.5)$$

Here the abbreviation  $\dot{(\ )} = \partial(\ )/\partial x$  for space derivative is used.

At the left boundary  $x = 0$  the fresh mixture is imposed through Dirichlet boundary conditions:

$$\begin{cases} v(t, 0) = 0, \\ T(t, 0) = 300 \text{ K}, \\ c_{\text{H}_2}(t, 0) = \frac{2}{3} P / R_0 T, \\ c_{\text{O}_2}(t, 0) = \frac{1}{3} P / R_0 T, \end{cases} \quad (6.6)$$

where the conditions on concentration include the pressure  $P$  from solution approximation within the domain at the boundary, which necessary for computation of pressure drop at the flame.

The boundary conditions for the right boundary  $x = L$  are adopted from NSCBC non-reflecting pressure outflow [PL92]:

$$\begin{cases} \frac{\partial}{\partial t} \rho v(t, L) = - \left( (v - v_o) d_1 + \rho d_3 \right), \\ \frac{\partial}{\partial t} \rho e(t, L) = - \left( \left( h + \frac{1}{2} v^2 \right) (d_1 - v_o \dot{\rho}) + \rho (v - v_o) (\dot{h} + v \dot{v}) + \rho v_o (d_3 + v \dot{v}) \right) \\ \frac{\partial}{\partial t} c_i(t, L) = \dot{\omega}_i - \left( (d_1 - v \dot{\rho}) c_i + (v - v_o) \dot{c}_i \right), \end{cases} \quad (6.7)$$

All variables, unless specified, are computed from the solution approximation within the domain at the corresponding boundary. Mass specific boundary derivatives:

$$\begin{aligned} d_1 &= \frac{1}{a^2} \left( \mathcal{L}_2 + \frac{1}{2} (\mathcal{L}_5 + \mathcal{L}_1) \right), \\ d_3 &= \frac{1}{2 \rho a} (\mathcal{L}_5 - \mathcal{L}_1), \end{aligned} \quad (6.8)$$

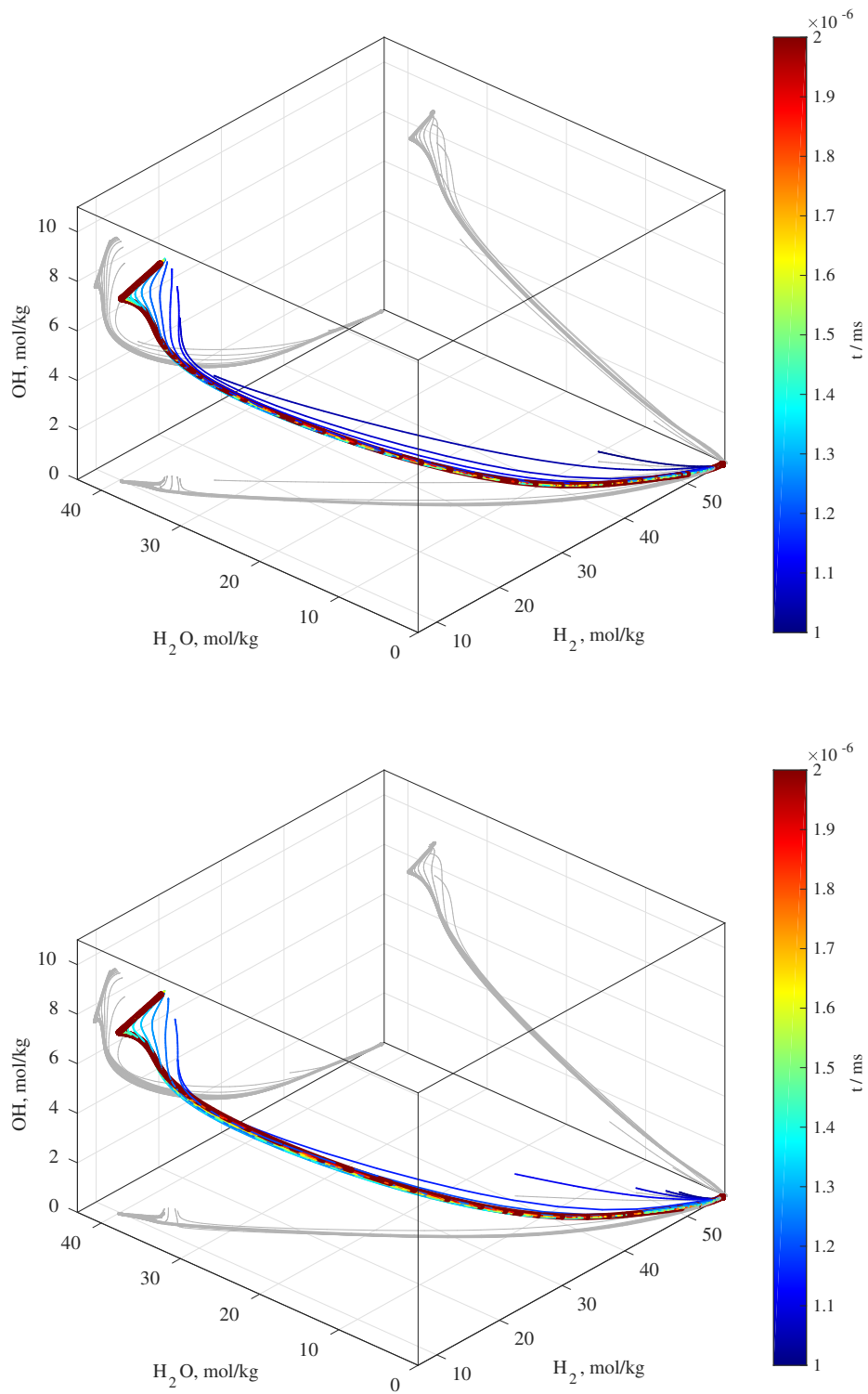


**Figure 6.8.:** 3D projections of the profiles during ignition and deflagration stages of specific mole numbers of  $\text{H}_2$ ,  $\text{H}_2\text{O}$  and  $\text{OH}$  for  $\Sigma = 5.75$  (top) and for  $\Sigma = 6.25$  (bottom). Solid line indicate stationary deflagration. Grey lines represent corresponding 2D projections.

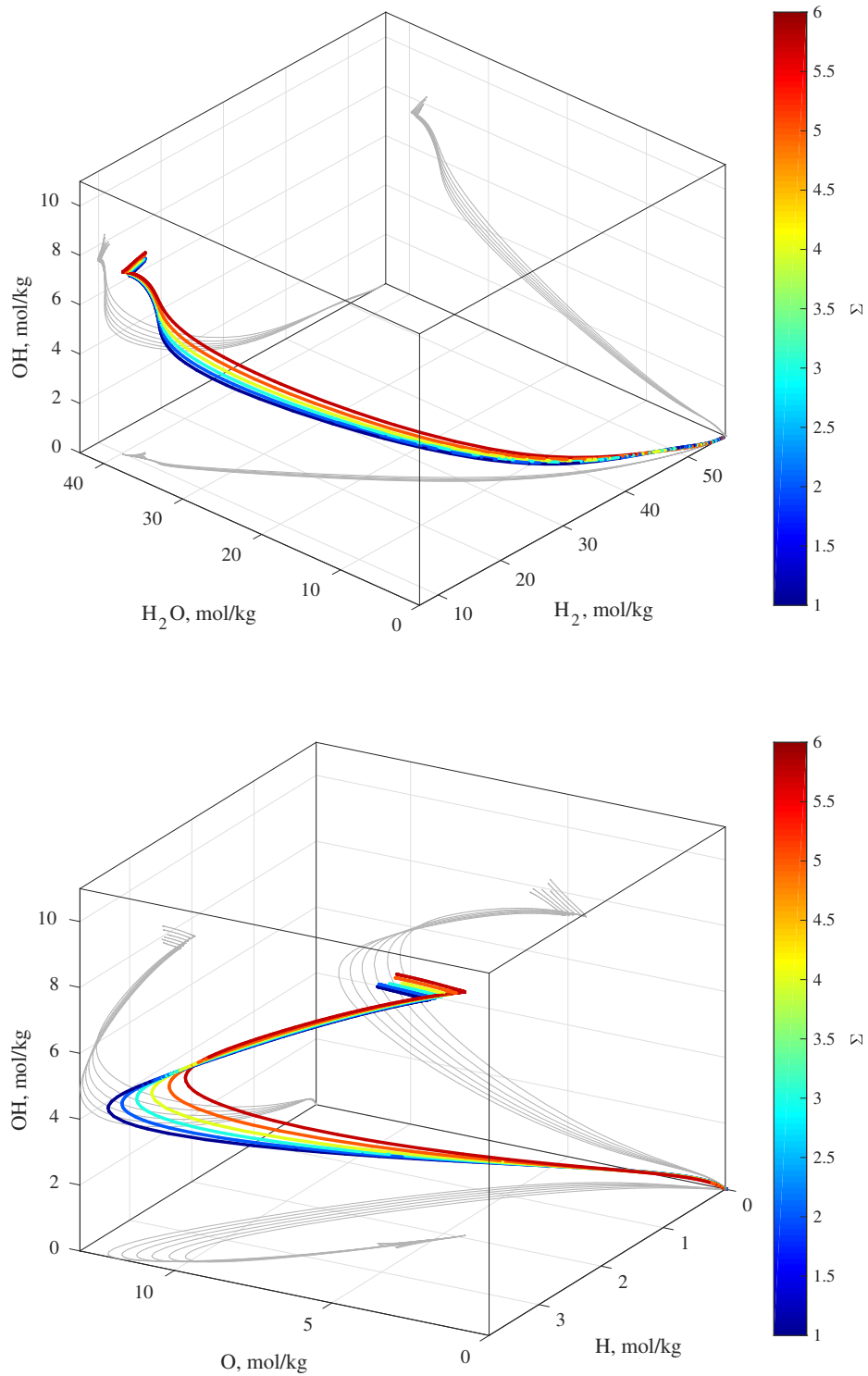


**Figure 6.9.:** Sigma dependence of stationary deflagration profiles in projection to specific mole numbers of H<sub>2</sub>, H<sub>2</sub>O, OH (top) and H, O, OH (bottom). Grey lines represent corresponding 2D projections.

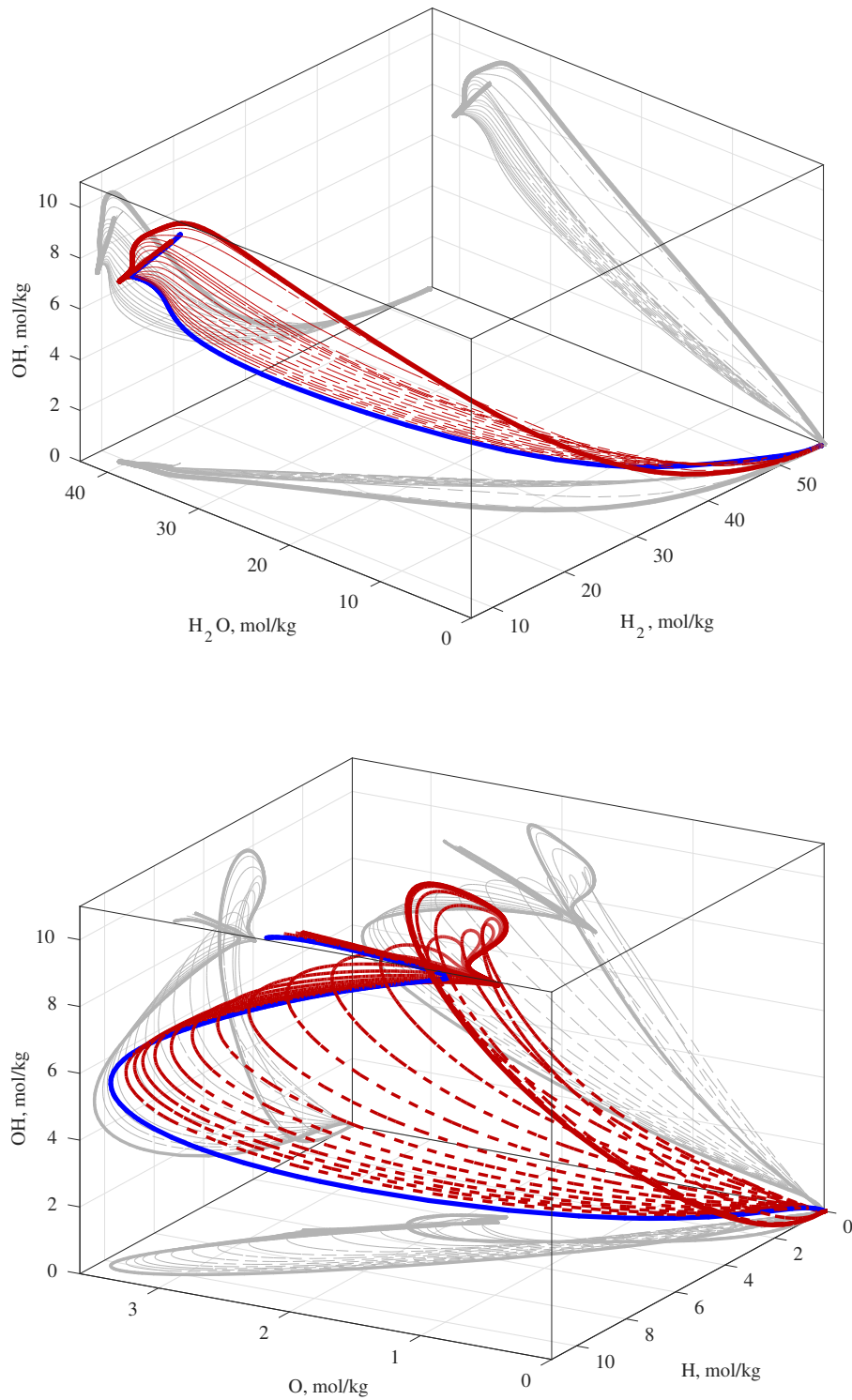


**Figure 6.10.:** 3D projections of the profiles during transition of specific mole numbers of  $H_2$ ,  $H_2O$ ,  $OH$  (top) and  $H$ ,  $O$ ,  $OH$  (bottom). Blue lines correspond to deflagration regime, dashed red lines – transition phase and solid red line – detonation. Grey lines represent corresponding 2D projections.

where  $a = \sqrt{\gamma P/\rho}$  is speed of sound and  $\mathcal{L}_i$  are amplitudes of characteristic waves.

The amplitudes of characteristic waves for outflow:

$$\begin{aligned}\mathcal{L}_1 &= K(P - P_\infty), \\ \mathcal{L}_2 &= v(a^2\dot{\rho} - \dot{P}), \\ \mathcal{L}_5 &= (a + v)(\dot{P} + \rho a\dot{v}),\end{aligned}\tag{6.9}$$

where the pressure relaxation parameter is computed with:

$$K = \sigma \frac{a(1 - \mathcal{M}^2)}{L^*},\tag{6.10}$$

here  $\mathcal{M} = v/a$  is Mach number at the boundary,  $L^*$  is characteristic length of the domain, e.g. is often taken equal to physical length of the domain,  $\sigma$  is relaxation parameter, is something between  $[0, 0.58]$ , where 0 is perfectly non-reflecting boundary. Generally  $\sigma/L^*$  determine how fast the pressure at the boundary is drifting towards  $P_\infty$ , with  $\sigma/L^* = 0$  no pressure correction is applied.

The adiabatic index in the above formuli is computed from internal points:

$$\gamma = \frac{\sum_i \bar{c}_{P,i} c_i}{\sum_i (\bar{c}_{P,i} - R_0) c_i}.\tag{6.11}$$

For all computations, at the pressure  $P_\infty = 1$  bar was imposed at the outflow, with  $\sigma = 0.5$  and  $L^* = L = 10$  mm. At the inflow, the fresh unburned mixture  $X_{\text{H}_2} = 2/3$ ,  $X_{\text{O}_2} = 1/3$  with temperature  $T_{in} = 300$  K and velocity  $v = 0$  was provided. The observer velocity  $v_o$  was variated as described below.

The initial temperature and species profiles for  $\Sigma = 1$  was generated with INSFLA [Maa88]. The observer velocity was set to laminar flame speed computed with INSFLA  $v_o(1) = v_L^{\text{INSFLA}} = 10.300$  m/s. The resulted flame speed was computed from the relative flame speed in the reference flame  $v_L(1) = v_o(1) + v_L^{\text{ref}}(1) = 10.103$  m/s. After that, the flame folding ratio was increased with step  $\Delta\Sigma = 0.5$  and the new value for the speed of reference frame was extrapolated. The following process is repeated till the detonation is observed:

1. Estimate observer velocity for current flame folding ratio  $\Sigma_i$  from the flame speed at the previous iteration  $v_L(\Sigma_{i-1})$ :  $v_o(\Sigma_i) = v_L(\Sigma_{i-1}) \Sigma_i / \Sigma_{i-1}$ ;
2. Compute relative speed of stationary flame from relative flame speed in the reference frame:  $v_L(\Sigma_i) = v_L^{\text{ref}} + v_o(\Sigma)$ .

The result of flame speed dependence on flame folding ratio  $v_L(\Sigma)$  just before the transition point is shown in fig. 6.11 (left). The flame speed is growing almost linearly with  $\Sigma$  but for a value just before the transition, a small deviation of 6% can be observed. Which may be an artefact of the specified boundary conditions. As the transition point is approached, the solution is getting increasingly unstable with significant fluctuation of the flame position, which were persistent over a large period of time, making the estimation of laminar flame speed a difficult task.

At  $\Sigma = 8.4$  a strong flame acceleration was observed, which ended in the transition to detonation, see fig. 6.11 (right). In order to understand the underlying physics, it is important to consider the speed of burned gases behind the flame (blue line), which is growing almost linearly with  $\Sigma$  before the DDT point. However, as the speed of burned gases is reaching the speed of sound in products, at this very moment the transition to detonation takes place. The speed of sound in the burned gas (dashed line) provides a theoretical limit for the propagation of disturbances and thus, being unable to flow in the direction of the outflow, the gas is pushed towards the unburned gas and thus the flame is accelerated.

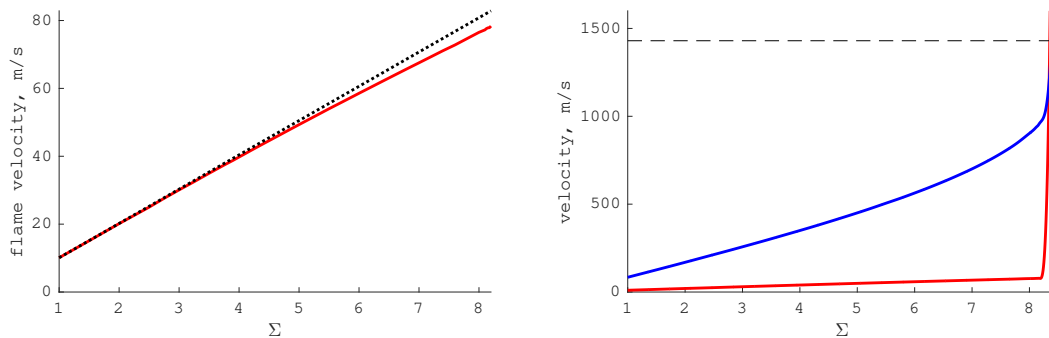


**Figure 6.11.:** Comparison of critical velocities of free flame depending on  $\Sigma$ . On the left: deflagration regimes, on the right: regimes including transition. Velocity of flame front (red), velocity of burned gases (blue), speed of sound in products (dashed), extrapolated flame speed (dotted).

The pressure jump at the position of flame for  $\Sigma = 1$  is negligible,  $\Delta P = 0.004$  bar. However, as seen from fig. 6.12, as the flame folding ratio grows, so does the pressure drop before flame. For  $\Sigma = 8$  the drop is  $\Delta P = 0.451$  bar, which impediments flame acceleration and is a possible explanation of non-linear dependence of flame velocity from  $\Sigma$ . As seen on the temperature profile (fig. 6.12 (right)), with increase of  $\Sigma$ , the flame is getting thinner.

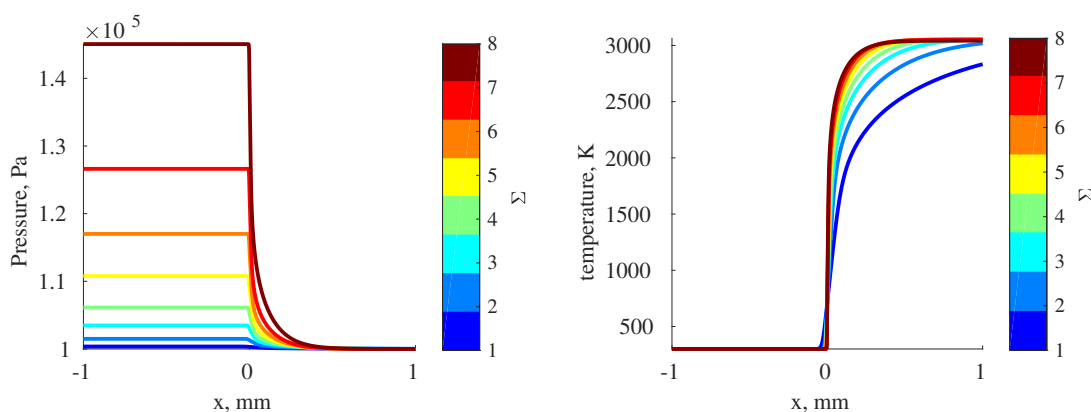


**Figure 6.12.:** Dependence of thermodynamic properties on  $\Sigma$ : pressure (left) and temperature (right)

Now consider fig. 6.13. With increase of flame folding ratio the species profiles are also changing significantly. They are not only getting narrower but also changing their shape. However, if projections on thermochemical state space are considered

(fig. 6.14), all points for stationary flame propagation lay on one 1D curve (a proper linear scaling may be required). However, the detonation point  $\Sigma = 8.4$  (black line) lays far away from the deflagration regimes. The steady deflagration regimes of free flame, as seen in projection to thermochemical state space, appear very similar to steady propagating flame initiated near the wall (compare fig. 6.8 and 6.14).

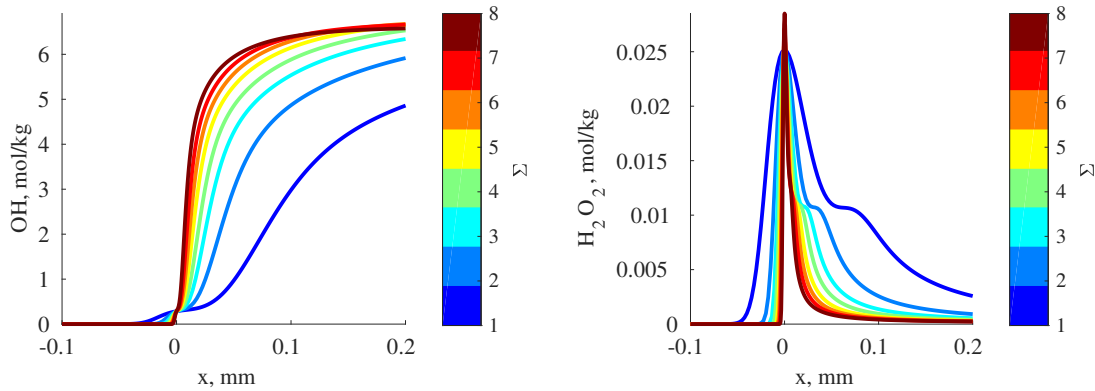


**Figure 6.13.:** Dependence of intermediate species profiles on  $\Sigma$ : OH (left) and H<sub>2</sub>O<sub>2</sub> (right).

The process of transition to detonation itself is shown in projection to thermochemical state space on fig. 6.15. The process of transition occupies a complex 2D (or probably higher dimensional) surface. However, initial (deflagration) and final (detonation) stage belong to a 1D state space. The transition surface appears to be different to DDT initiated near a wall (compare fig. 6.10 and fig. 6.15).

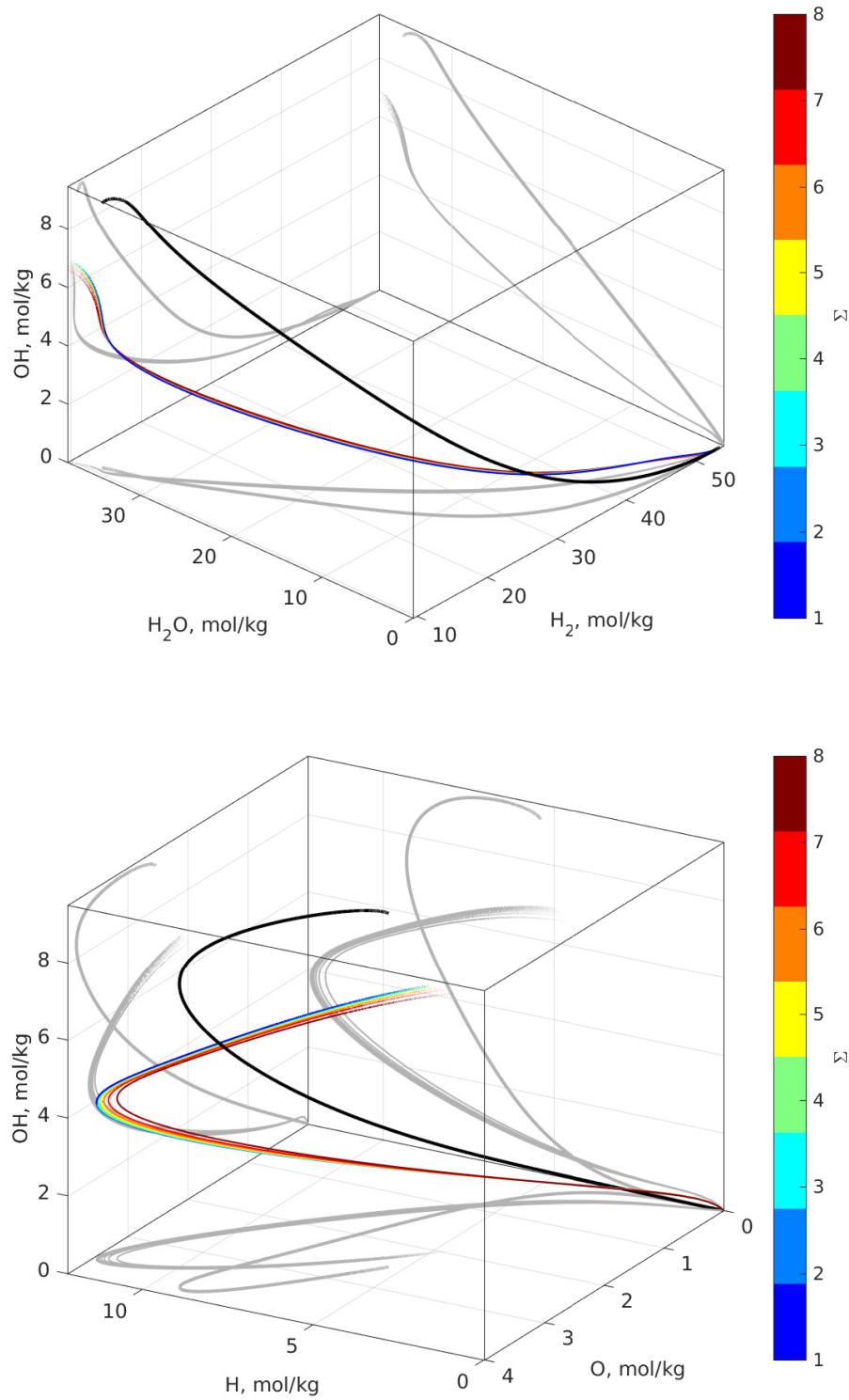


**Figure 6.14.:** 3D projections of stationary profiles for different  $\Sigma$  of specific mole numbers of  $H_2$ ,  $H_2O$ ,  $OH$  (top) and  $H$ ,  $O$ ,  $OH$  (bottom). Black lines show state  $\Sigma = 8.4$ . Grey lines represent corresponding 2D projections.

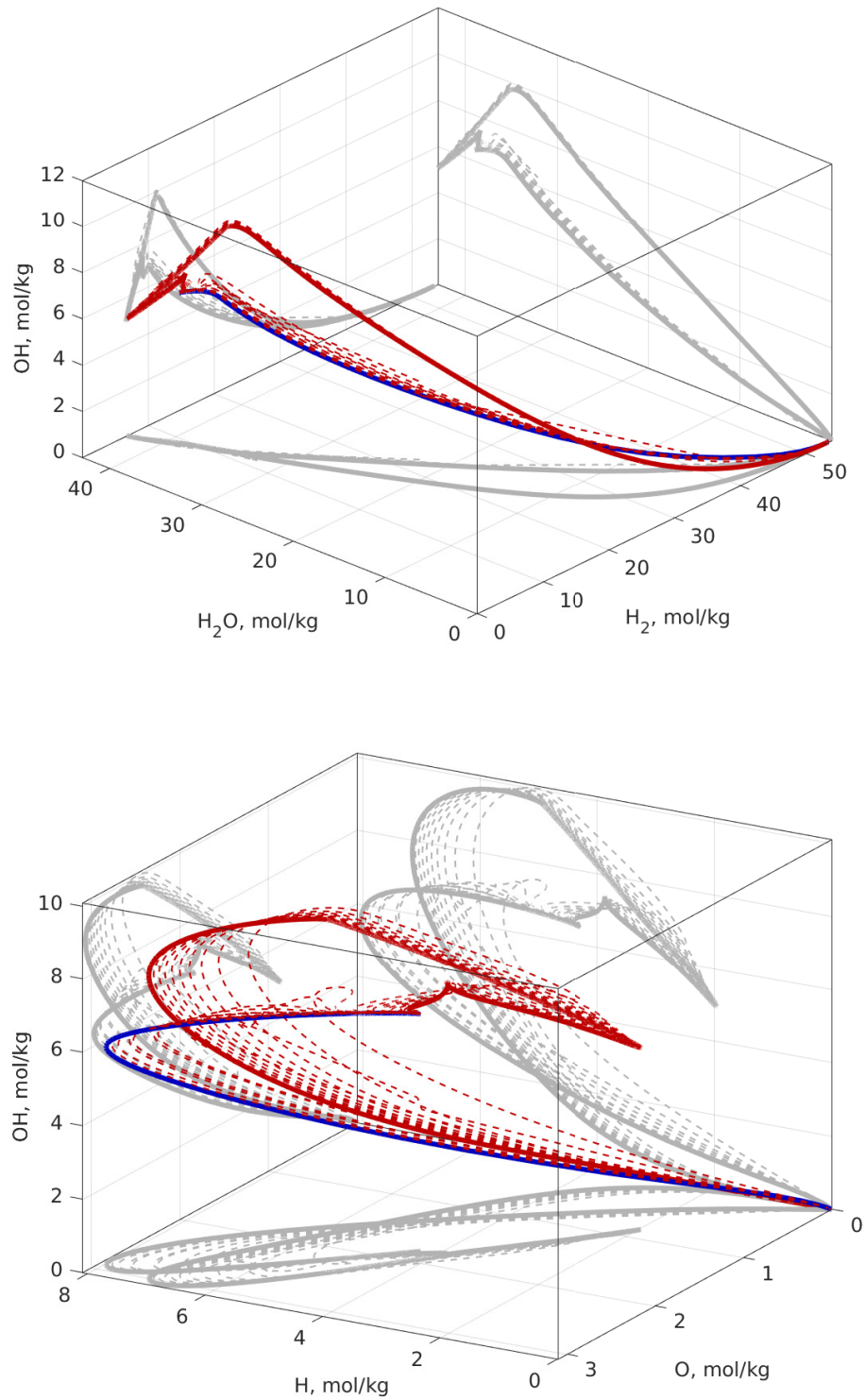


**Figure 6.15.:** 3D projections during DDT of a free flame for specific mole numbers of H<sub>2</sub>, H<sub>2</sub>O, OH (top) and H, O, OH (bottom). Solid blue lines show initial stationary deflagration mode and solid red line – the final detonation regime. Grey lines represent corresponding 2D projections.

## 7. Conclusions

This work was occupied with the study of ignition and transient combustion processes in gas phases. This is defined as a process between initial energy deposition, e.g. through a laser pulse, and quasi-steady flame propagation. Ignition processes are characterised by a strong coupling between hydrodynamic and thermochemistry with a large difference in time and space scales of underlying physical processes.

In order to model such processes Navier-Stokes equations is implemented and extended by conservation of energy and of individual chemical components. In chapter 2, the state of the art for mathematical description of combustible gas flows is presented. The description includes fundamental conservation laws of continuum mechanics augmented by thermodynamic properties of gas mixtures, their transport properties and the model for chemical reactions in accordance with kinetic gas theory.

The resulting system of partial differential equations is very stiff, has a large number of dependent state variables, has high sensitivity to system parameters and is characterised by high gradients of state-space variables. All this introduce very hard requirements and restrictions on computational solution methods because typically a numerical method had to be employed to treat such systems. The numerical method has to:

- posses sufficient accuracy in order to resolve all time and space scales;
- use limited number of discretisation parameters in order to solve the system for large number of state variables within a reasonable CPU time;
- have relatively low numerical viscosity due to the high sensitivity to system parameters;
- use a variable functional basis, which is adapting to rapidly changing conditions.

Spectral methods appear to be an ideal candidate to meet the requirements listed above, when an appropriate basis in functional space can be constructed. They require less discretisation points for the same accuracy as their low order counterparts, like finite differences or finite volumes, and introduce virtually no numerical viscosity. However, they tend to become increasingly unstable, when under-resolved. The current work presents two approaches to overcome this problem. One is structured functional space adaptation, implemented in adaptive pseudo-spectral method (APSM). Within APSM the functional space is adapted dynamically to changing

combustion conditions, using user specified tolerances. The nature of structural adaptation allowed also efficiently solve resulted linear system, with localised updates of the Jacobian inverse. Because the resolution of smallest scales is not always necessary, e.g. acoustic waves, a filtering strategy is presented, which removes high frequency modes but keeps the solution accurate.

The application of the spectral method to the solution of master equation (ME) of chemical kinetics led to speed-up of at least the factor 100 compared to classical discretisation approach, which now permits detailed study of complex multi-well MEs. ME is a stiff integro-differential equation. This equation allows calculation of rate constants from quantum-mechanical properties. In this work, estimations of rate constant for the unimolecular decomposition of 2,3-dihydro-2,5-dimethylfuran-3-yl (25DMF2H) and for the mutual isomerisation between allene and propyne were provided, which are in very good agreement with experimental measurements. Furthermore, by using the suggested method quasi-steady state assumption for the estimation of the elementary reaction rate parameters has been verified. It was shown that reaction rate parameters depend strictly not only on pressure and temperature, but also on the non-equilibrium distributions (by e.g. internal energies) of components involved. This demonstrates the need to improve the elementary reaction rates modelling and the fact that the suggested methodology can be efficiently employed to cope with this problem.

Further on, a number of combustion systems were considered, where the ignition process plays a key role in the combustion system dynamics. Such, that it has to be very accurately modelled and treated in numerical computations. Firstly, the proposed numerical approach and the mathematical description of combustible gas mixtures were extensive validated on classical benchmarks, i.e. the problems of ignition and steady flame propagation. The results showed good agreement with well established software packages and with experimental measurements. Additionally, resolution tests were conducted in order to check their correlation with user specified tolerances. In the presented benchmarks, ignition delay and burning velocity showed high sensitivity of hydrogen-air system to initial conditions, such as temperature and mixture composition.

Main attention was given to ignition and flame propagation in closed narrow channels, which can be accurately described within 2D formulation, equipped with proper symmetry conditions. It was confirmed that for particular ratios of channel length to width, an inversion of flame tip occurs ("tulip" flame). Analysis of the flow structure and the thermochemical state space reveals, that this effect has pure hydrodynamic nature, whereby thermochemical state space is being almost identical to outward propagating finger flame. From this analysis, four critical stages of flame development were also identified: spherical flame (till reflections from side walls reach the flame), finger flame (till the flame reaches side walls), transient period of tulip formation and tulip flame propagation. The obtained results showed a good qualitative agreement with experimental observations.

Then, half open channels with similar configuration were investigated. However, in this case, the outward propagating finger flame did not inverted its tip but instead kept accelerating and folding its surface, which was also in accordance with experimental

observations. Four critical stages of flame development could be also identified, where first two stages are identical to the tulip flame. The third stage corresponds to increasing flame folding and finally turbulent flame propagation. Interesting, that the moment the flame starts folding corresponds to the moment of tip inversion in closed channel with the same geometrical configuration. Moreover, the thermochemical space of tulip flame is also very close, only in the turbulent mode it appears somewhat distorted.

After that, the flame structure in micro flow channel was studied, where the channel width is well below the flame quenching radius. In this case, the combustion can be only facilitated by using hot channel walls. It was observed that depending on mixture composition, the flame position and heat release rate vary significantly. The flame in this regime exhibits very complex dynamics, e.g. extinguishing and re-ignition, which is extremely important to model and to treat numerically as accurate as possible, in order to be able to compare experiments and improve the quality of applied chemical models (mechanisms of chemical kinetics).

The results were also in a very good agreement with experimental measurements and showed significant improvement compared to previously used 1D models, which indicates the importance of transport processes in different directions. The analysis of thermochemical state space revealed that the flame develops along two dimensional surface, supporting the importance of flame-wall interactions. Very smooth velocity and pressures profiles indicate that simplified gas dynamic models, e.g. projections methods, can be used here in order to increase efficiency of calculations.

Finally, the attention was given to the problem of flame acceleration in unconfined settings. Typically combustion flame fronts tend to self stabilise, but sometimes when the gas dynamics and chemical reaction becomes unbalanced, they may start unbounded acceleration with a rapid flame surface grow. Although this is a multidimensional effect, it can be qualitatively modelled with the so called “flame folding ratio” within 1D formulation. Within this framework the chemical reaction is amplified to model the flame folding effects, that intensifies the chemical reaction until the intrinsic balance breaks down.

Special emphasis has been made on the influence of the ignition process and transient behaviour on the critical flame folding ratio. A critical range of the flame folding ratio was identified between 6.5 and 8.4, beyond which a rush flame acceleration, followed by transition to detonation, occurs. The lower limit corresponds to flame propagation from the wall (symmetry centre) and the upper limit describes “free” propagating flame. The analysis of thermochemical state space revealed the importance of detailed modelling of chemical kinetics for the flame acceleration. Whilst during the laminar flame propagation and final detonation the thermochemical state space is one-dimensional, but during the transition the multitude of states covers a complex two-dimensional surface.



# Appendix

## A. Conservation laws in general orthogonal coordinates

Using mapping of a curved computational domain to a rectangular domain offers several advantages for computations, e.g. simplified representation, projection of available solution to different domains, better interpretation of results, etc. General transformations are presented in Appendix B. The general transformations introduce a large number of non-linear terms to the conservation equations. However, using orthogonal coordinates, the form of the conservation equations does not change. Up to 2D a conformal map can be found for virtually any complex regions through the solution of Schwarz-Christoffel equation (see e.g. [DT02]).

The orthogonal coordinates may be non-linear but local tangential vectors  $\mathbf{x}, \mathbf{y}$  are orthogonal to each other. Consider fig. A.1, coordinate lines  $\xi, \eta$  are curved but at each point they are orthogonal to each other.

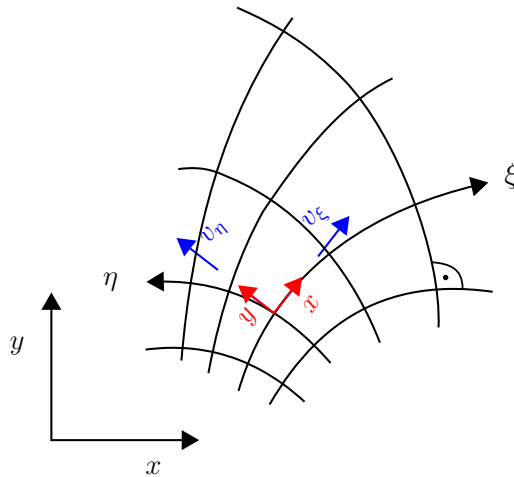


**Figure A.1.:** General orthogonal coordinates.

If velocity components ( $v_\xi, v_\eta$ ) in physical units along the coordinate lines is introduced and eq. (B.38) for orthogonal coordinates is applied, the following set of conservation equations (for more details see [KK68, KCG03]) can be derived:

### Continuity

$$\frac{\partial}{\partial t} (g \rho) + \frac{\partial}{\partial \xi} (g_\eta g_\zeta v_\xi \rho) + \frac{\partial}{\partial \eta} (g_\xi g_\zeta v_\eta \rho) + \frac{\partial}{\partial \zeta} (g_\xi g_\eta v_\zeta \rho) = 0. \quad (\text{A.1})$$

where the following abbreviations are used:

$$g_\xi = \frac{\partial x}{\partial \xi}, \quad g_\eta = \frac{\partial y}{\partial \eta}, \quad g_\zeta = \frac{\partial z}{\partial \zeta}, \quad g = g_\xi g_\eta g_\zeta. \quad (\text{A.2})$$

### Momentum

$$\begin{aligned} & \frac{\partial}{\partial t} (g \rho v_\xi) \\ & + \frac{\partial}{\partial \xi} \left( g_\eta g_\zeta (\rho v_\xi^2 + \sigma_{\xi\xi}) \right) + \frac{\partial}{\partial \eta} \left( g_\xi g_\zeta (\rho v_\xi v_\eta + \sigma_{\xi\eta}) \right) + \frac{\partial}{\partial \zeta} \left( g_\eta g_\zeta (\rho v_\xi v_\zeta + \sigma_{\xi\zeta}) \right) \\ & = -g_\eta g_\zeta \frac{\partial P}{\partial \xi} + g_\zeta \frac{\partial g_\eta}{\partial \xi} (\rho v_\eta^2 + \sigma_{\eta\eta}) + g_\eta \frac{\partial g_\zeta}{\partial \xi} (\rho v_\zeta^2 + \sigma_{\zeta\zeta}) \\ & \quad - g_\zeta \frac{\partial g_\xi}{\partial \eta} (\rho v_\xi v_\eta + \sigma_{\xi\eta}) - g_\eta \frac{\partial g_\xi}{\partial \zeta} (\rho v_\xi v_\zeta + \sigma_{\xi\zeta}), \quad (\text{A.3}) \end{aligned}$$

$$\begin{aligned} & \frac{\partial}{\partial t} (g \rho v_\eta) \\ & + \frac{\partial}{\partial \xi} \left( g_\eta g_\zeta (\rho v_\eta v_\xi + \sigma_{\eta\xi}) \right) + \frac{\partial}{\partial \eta} \left( g_\xi g_\zeta (\rho v_\eta^2 + \sigma_{\eta\eta}) \right) + \frac{\partial}{\partial \zeta} \left( g_\eta g_\zeta (\rho v_\eta v_\zeta + \sigma_{\eta\zeta}) \right) \\ & = -g_\xi g_\zeta \frac{\partial P}{\partial \eta} + g_\zeta \frac{\partial g_\xi}{\partial \eta} (\rho v_\xi^2 + \sigma_{\xi\xi}) + g_\xi \frac{\partial g_\zeta}{\partial \eta} (\rho v_\zeta^2 + \sigma_{\zeta\zeta}) \\ & \quad - g_\zeta \frac{\partial g_\eta}{\partial \xi} (\rho v_\eta v_\xi + \sigma_{\eta\xi}) - g_\xi \frac{\partial g_\eta}{\partial \zeta} (\rho v_\eta v_\zeta + \sigma_{\eta\zeta}), \quad (\text{A.4}) \end{aligned}$$

$$\begin{aligned} & \frac{\partial}{\partial t} (g \rho v_\zeta) \\ & + \frac{\partial}{\partial \xi} \left( g_\eta g_\zeta (\rho v_\zeta v_\xi + \sigma_{\zeta\xi}) \right) + \frac{\partial}{\partial \eta} \left( g_\xi g_\zeta (\rho v_\zeta v_\eta + \sigma_{\zeta\eta}) \right) + \frac{\partial}{\partial \zeta} \left( g_\eta g_\zeta (\rho v_\zeta^2 + \sigma_{\zeta\zeta}) \right) \\ & = -g_\xi g_\eta \frac{\partial P}{\partial \zeta} + g_\eta \frac{\partial g_\xi}{\partial \zeta} (\rho v_\xi^2 + \sigma_{\xi\xi}) + g_\xi \frac{\partial g_\eta}{\partial \zeta} (\rho v_\eta^2 + \sigma_{\eta\eta}) \\ & \quad - g_\eta \frac{\partial g_\zeta}{\partial \xi} (\rho v_\zeta v_\xi + \sigma_{\zeta\xi}) - g_\xi \frac{\partial g_\zeta}{\partial \eta} (\rho v_\zeta v_\eta + \sigma_{\zeta\eta}), \quad (\text{A.5}) \end{aligned}$$

where the components of the stress tensor are:

$$\left\{ \begin{array}{l} \sigma_{\xi\xi} = \sigma - \frac{2\mu}{g_\xi} \left( \frac{\partial v_\xi}{\partial \xi} + \frac{v_\eta}{g_\eta} \frac{\partial g_\xi}{\partial \eta} + \frac{v_\zeta}{g_\zeta} \frac{\partial g_\xi}{\partial \zeta} \right), \\ \sigma_{\eta\eta} = \sigma - \frac{2\mu}{g_\eta} \left( \frac{\partial v_\eta}{\partial \eta} + \frac{v_\xi}{g_\xi} \frac{\partial g_\eta}{\partial \xi} + \frac{v_\zeta}{g_\zeta} \frac{\partial g_\eta}{\partial \zeta} \right), \\ \sigma_{\zeta\zeta} = \sigma - \frac{2\mu}{g_\zeta} \left( \frac{\partial v_\zeta}{\partial \zeta} + \frac{v_\xi}{g_\xi} \frac{\partial g_\zeta}{\partial \xi} + \frac{v_\eta}{g_\eta} \frac{\partial g_\zeta}{\partial \eta} \right), \\ \sigma_{\xi\eta} = \sigma_{\eta\xi} = -\mu \left[ \frac{1}{g_\xi} \left( \frac{\partial v_\eta}{\partial \xi} - \frac{v_\eta}{g_\eta} \frac{\partial g_\eta}{\partial \xi} \right) + \frac{1}{g_\eta} \left( \frac{\partial v_\xi}{\partial \eta} - \frac{v_\xi}{g_\xi} \frac{\partial g_\xi}{\partial \eta} \right) \right], \\ \sigma_{\eta\zeta} = \sigma_{\zeta\eta} = -\mu \left[ \frac{1}{g_\eta} \left( \frac{\partial v_\zeta}{\partial \eta} - \frac{v_\zeta}{g_\zeta} \frac{\partial g_\zeta}{\partial \eta} \right) + \frac{1}{g_\zeta} \left( \frac{\partial v_\eta}{\partial \zeta} - \frac{v_\eta}{g_\eta} \frac{\partial g_\eta}{\partial \zeta} \right) \right], \\ \sigma_{\xi\zeta} = \sigma_{\zeta\xi} = -\mu \left[ \frac{1}{g_\zeta} \left( \frac{\partial v_\xi}{\partial \zeta} - \frac{v_\xi}{g_\xi} \frac{\partial g_\xi}{\partial \zeta} \right) + \frac{1}{g_\xi} \left( \frac{\partial v_\zeta}{\partial \xi} - \frac{v_\zeta}{g_\zeta} \frac{\partial g_\zeta}{\partial \xi} \right) \right], \end{array} \right. \quad (\text{A.6})$$

with

$$\begin{aligned} \sigma = & \frac{2}{3}\mu \left[ \frac{1}{g_\xi} \frac{\partial v_\xi}{\partial \xi} + \frac{1}{g_\eta} \frac{\partial v_\eta}{\partial \eta} + \frac{1}{g_\zeta} \frac{\partial v_\zeta}{\partial \zeta} \right. \\ & \left. + \frac{v_\xi}{g_\xi} \left( \frac{1}{g_\eta} \frac{\partial g_\eta}{\partial \xi} + \frac{1}{g_\zeta} \frac{\partial g_\zeta}{\partial \xi} \right) + \frac{v_\eta}{g_\eta} \left( \frac{1}{g_\xi} \frac{\partial g_\xi}{\partial \eta} + \frac{1}{g_\zeta} \frac{\partial g_\zeta}{\partial \eta} \right) + \frac{v_\zeta}{g_\zeta} \left( \frac{1}{g_\xi} \frac{\partial g_\xi}{\partial \zeta} + \frac{1}{g_\eta} \frac{\partial g_\eta}{\partial \zeta} \right) \right]. \end{aligned} \quad (\text{A.7})$$

## Energy

$$\begin{aligned} & \frac{\partial}{\partial t} (g \rho e) \\ & + \frac{\partial}{\partial \xi} \left( g_\eta g_\zeta (v_\xi (\rho e + P + \sigma_{\xi\xi}) + v_\eta \sigma_{\eta\xi} + v_\zeta \sigma_{\zeta\xi} + q_\xi) \right) \\ & + \frac{\partial}{\partial \eta} \left( g_\xi g_\zeta (v_\eta (\rho e + P + \sigma_{\eta\eta}) + v_\xi \sigma_{\xi\eta} + v_\zeta \sigma_{\zeta\eta} + q_\eta) \right) \\ & + \frac{\partial}{\partial \zeta} \left( g_\xi g_\eta (v_\zeta (\rho e + P + \sigma_{\zeta\zeta}) + v_\xi \sigma_{\xi\zeta} + v_\eta \sigma_{\eta\zeta} + q_\zeta) \right) \\ & = 0. \end{aligned} \quad (\text{A.8})$$

where the energy flux through the surface of control volume is:

$$\begin{cases} q_\xi = -\frac{1}{g_\xi} \lambda \frac{\partial T}{\partial \xi} + \sum_i \bar{h}_i \bar{j}_{\xi,i}, \\ q_\eta = -\frac{1}{g_\eta} \lambda \frac{\partial T}{\partial \eta} + \sum_i \bar{h}_i \bar{j}_{\eta,i}, \\ q_\zeta = -\frac{1}{g_\zeta} \lambda \frac{\partial T}{\partial \zeta} + \sum_i \bar{h}_i \bar{j}_{\zeta,i}. \end{cases} \quad (\text{A.9})$$

## Species $i$ conservation

$$\begin{aligned} & \frac{\partial}{\partial t} (g c_i) \\ & + \frac{\partial}{\partial \xi} \left( g_\eta g_\zeta (v_\xi c_i + \bar{j}_{i,\xi}) \right) + \frac{\partial}{\partial \eta} \left( g_\xi g_\zeta (v_\eta c_i + \bar{j}_{i,\eta}) \right) + \frac{\partial}{\partial \zeta} \left( g_\xi g_\eta (v_\zeta c_i + \bar{j}_{i,\zeta}) \right) \\ & = g \omega_i, \end{aligned} \quad (\text{A.10})$$

where the molar diffusion flux is computed with:

$$\begin{cases} \bar{j}_{\xi,i} = -\frac{1}{g_\xi} D_{ij}^c \frac{\partial c_j}{\partial \xi}, \\ \bar{j}_{\eta,i} = -\frac{1}{g_\eta} D_{ij}^c \frac{\partial c_j}{\partial \eta}, \\ \bar{j}_{\zeta,i} = -\frac{1}{g_\zeta} D_{ij}^c \frac{\partial c_j}{\partial \zeta}. \end{cases} \quad (\text{A.11})$$

### A.1. 1D symmetry

For symmetrical configuration along  $\eta$  and  $\zeta$ , the following simplified equations in general orthogonal coordinates are valid:

**Continuity**

$$\frac{\partial}{\partial t} (g \rho) + \frac{\partial}{\partial \xi} (g_\eta g_\zeta v \rho) = 0. \quad (\text{A.12})$$

**Momentum**

$$\begin{aligned} \frac{\partial}{\partial t} (g \rho v) + \frac{\partial}{\partial \xi} \left( g_\eta g_\zeta (\rho v^2 + \sigma_{\xi\xi}) \right) \\ = -g_\eta g_\zeta \frac{\partial P}{\partial \xi} + g_\zeta \frac{\partial g_\eta}{\partial \xi} \sigma_{\eta\eta} + g_\eta \frac{\partial g_\zeta}{\partial \xi} \sigma_{\zeta\zeta} - g_\zeta \frac{\partial g_\xi}{\partial \eta} \sigma_{\xi\eta} - g_\eta \frac{\partial g_\xi}{\partial \zeta} \sigma_{\xi\zeta}, \end{aligned} \quad (\text{A.13})$$

where the stress tensor is described by:

$$\left\{ \begin{array}{l} \sigma_{\xi\xi} = \sigma - \frac{2\mu}{g_\xi} \frac{\partial v}{\partial \xi}, \\ \sigma_{\eta\eta} = \sigma - 2\mu \frac{v}{g_\eta g_\xi} \frac{\partial g_\eta}{\partial \xi}, \\ \sigma_{\zeta\zeta} = \sigma - 2\mu \frac{v}{g_\zeta g_\xi} \frac{\partial g_\zeta}{\partial \xi}, \\ \sigma_{\xi\eta} = \sigma_{\eta\xi} = \mu \frac{v}{g_\eta g_\xi} \frac{\partial g_\xi}{\partial \eta}, \\ \sigma_{\xi\zeta} = \sigma_{\zeta\xi} = \mu \frac{v}{g_\zeta g_\xi} \frac{\partial g_\xi}{\partial \zeta}, \end{array} \right. \quad (\text{A.14})$$

with

$$\sigma = \frac{2}{3}\mu \left[ \frac{1}{g_\xi} \frac{\partial v}{\partial \xi} + \frac{v}{g_\xi} \left( \frac{1}{g_\eta} \frac{\partial g_\eta}{\partial \xi} + \frac{1}{g_\zeta} \frac{\partial g_\zeta}{\partial \xi} \right) \right]. \quad (\text{A.15})$$

**Energy**

$$\frac{\partial}{\partial t} (g \rho e) + \frac{\partial}{\partial \xi} \left( g_\eta g_\zeta (v (\rho e + P + \sigma_{\xi\xi}) + q) \right) = 0, \quad (\text{A.16})$$

with

$$q = -\frac{1}{g_\xi} \lambda \frac{\partial T}{\partial \xi} + \sum_i \bar{h}_i \bar{j}_i. \quad (\text{A.17})$$

**Species  $i$  conservation**

$$\frac{\partial}{\partial t} (g c_i) + \frac{\partial}{\partial \xi} \left( g_\eta g_\zeta (v c_i + \bar{j}_i) \right) = g \omega_i, \quad (\text{A.18})$$

where

$$\bar{j}_i = -\frac{1}{g_\xi} D_{ij}^c \frac{\partial c_j}{\partial \xi}. \quad (\text{A.19})$$

**A.2. 2D symmetry**

For symmetrical configuration along  $\zeta$ , the following simplified equations in general orthogonal coordinates are valid:

**Continuity**

$$\frac{\partial}{\partial t} (g \rho) + \frac{\partial}{\partial \xi} (g_\eta g_\zeta v_\xi \rho) + \frac{\partial}{\partial \eta} (g_\xi g_\zeta v_\eta \rho) = 0. \quad (\text{A.20})$$

**Momentum**

$$\begin{aligned}
& \frac{\partial}{\partial t} (g \rho v_\xi) + \frac{\partial}{\partial \xi} \left( g_\eta g_\zeta (\rho v_\xi^2 + \sigma_{\xi\xi}) \right) + \frac{\partial}{\partial \eta} \left( g_\xi g_\zeta (\rho v_\xi v_\eta + \sigma_{\xi\eta}) \right) \\
&= -g_\eta g_\zeta \frac{\partial P}{\partial \xi} + g_\zeta \frac{\partial g_\eta}{\partial \xi} (\rho v_\eta^2 + \sigma_{\eta\eta}) - g_\zeta \frac{\partial g_\xi}{\partial \eta} (\rho v_\xi v_\eta + \sigma_{\xi\eta}) + g_\eta \frac{\partial g_\zeta}{\partial \xi} \sigma_{\zeta\zeta} - g_\eta \frac{\partial g_\xi}{\partial \zeta} \sigma_{\xi\zeta},
\end{aligned} \tag{A.21}$$

$$\begin{aligned}
& \frac{\partial}{\partial t} (g \rho v_\eta) + \frac{\partial}{\partial \xi} \left( g_\eta g_\zeta (\rho v_\eta v_\xi + \sigma_{\eta\xi}) \right) + \frac{\partial}{\partial \eta} \left( g_\xi g_\zeta (\rho v_\eta^2 + \sigma_{\eta\eta}) \right) \\
&= -g_\xi g_\zeta \frac{\partial P}{\partial \eta} + g_\zeta \frac{\partial g_\xi}{\partial \eta} (\rho v_\xi^2 + \sigma_{\xi\xi}) - g_\zeta \frac{\partial g_\eta}{\partial \xi} (\rho v_\eta v_\xi + \sigma_{\eta\xi}) + g_\xi \frac{\partial g_\zeta}{\partial \eta} \sigma_{\zeta\zeta} - g_\xi \frac{\partial g_\eta}{\partial \zeta} \sigma_{\eta\zeta},
\end{aligned} \tag{A.22}$$

where the components of the stress tensor are

$$\left\{ \begin{array}{l} \sigma_{\xi\xi} = \sigma - \frac{2\mu}{g_\xi} \left( \frac{\partial v_\xi}{\partial \xi} + \frac{v_\eta}{g_\eta} \frac{\partial g_\xi}{\partial \eta} \right), \\ \sigma_{\eta\eta} = \sigma - \frac{2\mu}{g_\eta} \left( \frac{\partial v_\eta}{\partial \eta} + \frac{v_\xi}{g_\xi} \frac{\partial g_\eta}{\partial \xi} \right), \\ \sigma_{\zeta\zeta} = \sigma - \frac{2\mu}{g_\zeta} \left( \frac{v_\xi}{g_\xi} \frac{\partial g_\zeta}{\partial \xi} + \frac{v_\eta}{g_\eta} \frac{\partial g_\zeta}{\partial \eta} \right), \\ \sigma_{\xi\eta} = \sigma_{\eta\xi} = -\mu \left[ \frac{1}{g_\xi} \left( \frac{\partial v_\eta}{\partial \xi} - \frac{v_\eta}{g_\eta} \frac{\partial g_\eta}{\partial \xi} \right) + \frac{1}{g_\eta} \left( \frac{\partial v_\xi}{\partial \eta} - \frac{v_\xi}{g_\xi} \frac{\partial g_\xi}{\partial \eta} \right) \right], \\ \sigma_{\eta\zeta} = \sigma_{\zeta\eta} = \mu \frac{v_\eta}{g_\zeta g_\eta} \frac{\partial g_\eta}{\partial \zeta}, \\ \sigma_{\xi\zeta} = \sigma_{\zeta\xi} = \mu \frac{v_\xi}{g_\zeta g_\xi} \frac{\partial g_\xi}{\partial \zeta}, \end{array} \right. \tag{A.23}$$

with

$$\sigma = \frac{2}{3} \mu \left[ \frac{1}{g_\xi} \frac{\partial v_\xi}{\partial \xi} + \frac{1}{g_\eta} \frac{\partial v_\eta}{\partial \eta} + \frac{v_\xi}{g_\xi} \left( \frac{1}{g_\eta} \frac{\partial g_\eta}{\partial \xi} + \frac{1}{g_\zeta} \frac{\partial g_\zeta}{\partial \xi} \right) + \frac{v_\eta}{g_\eta} \left( \frac{1}{g_\xi} \frac{\partial g_\xi}{\partial \eta} + \frac{1}{g_\zeta} \frac{\partial g_\zeta}{\partial \eta} \right) \right]. \tag{A.24}$$

**Energy**

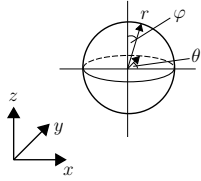
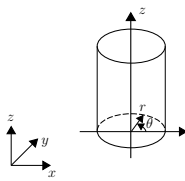
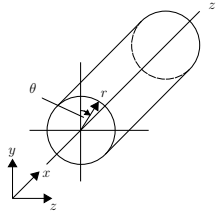
$$\begin{aligned}
& \frac{\partial}{\partial t} (g \rho e) + \frac{\partial}{\partial \xi} \left( g_\eta g_\zeta (v_\xi (\rho e + P + \sigma_{\xi\xi}) + v_\eta \sigma_{\eta\xi} + q_\xi) \right) \\
& \quad + \frac{\partial}{\partial \eta} \left( g_\xi g_\zeta (v_\eta (\rho e + P + \sigma_{\eta\eta}) + v_\xi \sigma_{\xi\eta} + q_\eta) \right) = 0.
\end{aligned} \tag{A.25}$$

**Species  $i$  conservation**

$$\frac{\partial}{\partial t} (g c_i) + \frac{\partial}{\partial \xi} \left( g_\eta g_\zeta (v_\xi c_i + \bar{j}_{i,\xi}) \right) + \frac{\partial}{\partial \eta} \left( g_\xi g_\zeta (v_\eta c_i + \bar{j}_{i,\eta}) \right) = g \omega_i. \tag{A.26}$$

### A.3. Standard geometric symmetry relations

Cartesian, spherical and cylindrical coordinates are probably most often used orthogonal coordinates. The necessary computational parameters are summarised below.

				
	Cartesian	Spherical	Cylindrical (radial)	Cylindrical (axial)
$\xi$	$x$	$r$	$r$	$z$
$\eta$	$y$	$\theta$	$\theta$	$r$
$\zeta$	$z$	$\varphi$	$z$	$\theta$
$g_\xi$	1	1	1	1
$g_\eta$	1	$r \sin(\varphi)$	$r$	1
$g_\zeta$	1	$r$	1	$r$
$\frac{\partial g_\xi}{\partial \eta}$	0	0	0	0
$\frac{\partial g_\xi}{\partial \zeta}$	0	0	0	0
$\frac{\partial g_\eta}{\partial \xi}$	0	$\sin(\varphi)$	1	0
$\frac{\partial g_\eta}{\partial \zeta}$	0	$r \cos(\varphi)$	0	0
$\frac{\partial g_\zeta}{\partial \xi}$	0	1	0	0
$\frac{\partial g_\zeta}{\partial \eta}$	0	0	0	1
$x$	$x$	$r \cos(\theta) \sin(\varphi)$	$r \cos(\theta)$	$z$
$y$	$y$	$r \sin(\theta) \sin(\varphi)$	$r \sin(\theta)$	$r \cos(\theta)$
$z$	$z$	$r \cos(\varphi)$	$z$	$r \sin(\theta)$

**Table A.1.:** Spherical and Cylindrical coordinate transformations.

## B. General coordinate transformations

It is practical to optimise a numerical solver to work in one particular computational domain, e.g. rectangular. This however, doesn't limit the application of such a solver for realistic complex domains, when coordinate transformation is applied. In this section, it is shown how differential operations are affected by this transformation.

### B.1. 1D transformation

Most simple example of coordinate transformation is static 1D transformation. One can imagine, it as local stretch and shrink. See fig. B.2, where irregular intervals in physical domain  $x \in [0, L]$  are mapped to computational domain  $\xi \in [0, 1]$  with regular intervals. In this case one can see physical coordinate as a function of computational coordinate:

$$x = x(\xi), \quad (\text{B.1})$$

then the derivative of  $x$  is:

$$dx = \frac{\partial x}{\partial \xi} d\xi, \quad (\text{B.2})$$

or equivalently:

$$d\xi = \left( \frac{\partial x}{\partial \xi} \right)^{-1} dx. \quad (\text{B.3})$$

Following that, the space derivative of a function  $f = f(x)$  corresponds to scaling of derivative of this function in the computational domain:

$$\frac{\partial f}{\partial x} = \left( \frac{\partial x}{\partial \xi} \right)^{-1} \frac{\partial f}{\partial \xi}. \quad (\text{B.4})$$

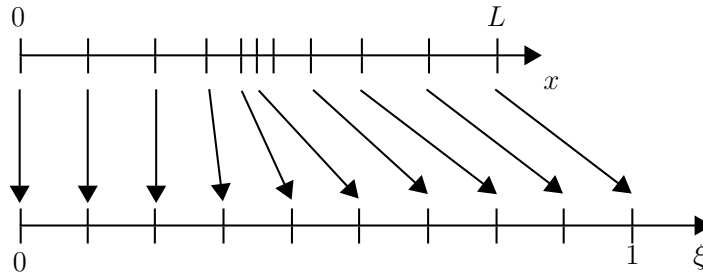


**Figure B.2.:** Static 1D coordinate transformation.

In other scenario the mapping between physical and computational coordinate may evolve with the time, e.g. follow the flame front. See fig. B.3, where the coordinate  $x$  is firstly shrink and then expand. In this case the space coordinate is a function of  $\xi$  and  $\tau$ :

$$x = x(\tau, \xi). \quad (\text{B.5})$$

The space derivative is a linear combination of computational time  $\tau$  and space  $\xi$ :

$$\begin{pmatrix} dt \\ dx \end{pmatrix} = \begin{pmatrix} \frac{\partial t}{\partial \tau} & \frac{\partial t}{\partial \xi} \\ \frac{\partial x}{\partial \tau} & \frac{\partial x}{\partial \xi} \end{pmatrix} \begin{pmatrix} d\tau \\ d\xi \end{pmatrix} \quad (\text{B.6})$$

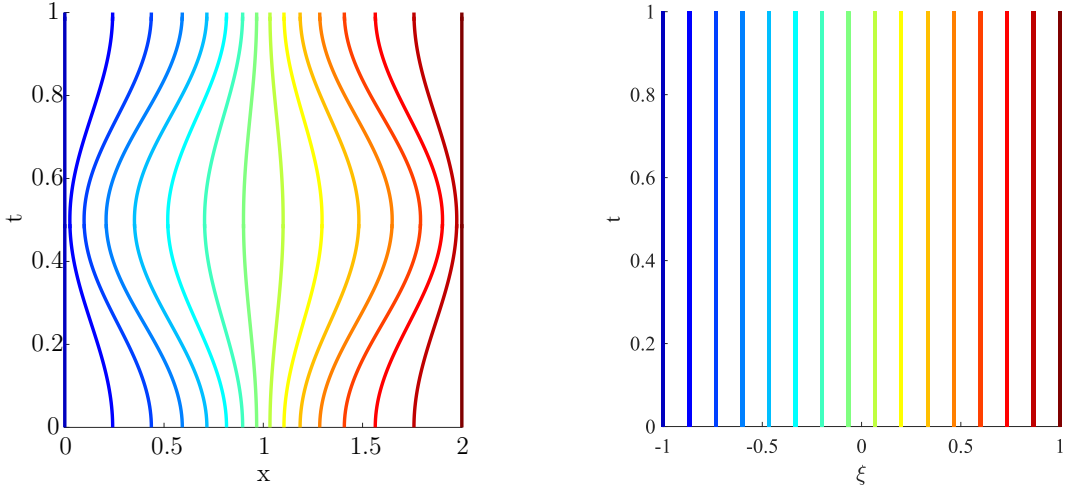


**Figure B.3.:** Dynamic 1D coordinate transformation.

The inverse mapping of derivative is then:

$$\begin{pmatrix} d\tau \\ d\xi \end{pmatrix} = \frac{1}{g} \begin{pmatrix} \frac{\partial x}{\partial \xi} & -\frac{\partial t}{\partial \xi} \\ -\frac{\partial x}{\partial \tau} & \frac{\partial t}{\partial \tau} \end{pmatrix} \begin{pmatrix} dt \\ dx \end{pmatrix}, \quad (\text{B.7})$$

where  $g$  is the determinant of the transformation:

$$g = \frac{\partial t}{\partial \tau} \frac{\partial x}{\partial \xi} - \frac{\partial t}{\partial \xi} \frac{\partial x}{\partial \tau}. \quad (\text{B.8})$$

When coordinates  $x$  and  $t$  are orthogonal (although they can be curvilinear):

$$\begin{cases} \frac{\partial t}{\partial \xi} = 0, \\ \frac{\partial x}{\partial \tau} = 0, \end{cases} \quad (\text{B.9})$$

then eq. (B.7) reduces to eq. (B.3):

$$\begin{pmatrix} d\tau \\ d\xi \end{pmatrix} = \begin{pmatrix} \left(\frac{\partial t}{\partial \tau}\right)^{-1} & 0 \\ 0 & \left(\frac{\partial x}{\partial \xi}\right)^{-1} \end{pmatrix} \begin{pmatrix} dt \\ dx \end{pmatrix}, \quad (\text{B.10})$$

From the mapping eq. (B.7) it is straightforward to derive the partial derivatives of a function  $f = f(t, x)$  in physical coordinates from derivatives in the computational domain:

$$\begin{cases} \frac{\partial f}{\partial t} = \frac{1}{g} \left( \frac{\partial x}{\partial \xi} \frac{\partial f}{\partial \tau} - \frac{\partial x}{\partial \tau} \frac{\partial f}{\partial \xi} \right), \\ \frac{\partial f}{\partial x} = \frac{1}{g} \left( \frac{\partial t}{\partial \tau} \frac{\partial f}{\partial \xi} - \frac{\partial t}{\partial \xi} \frac{\partial f}{\partial \tau} \right). \end{cases} \quad (\text{B.11})$$

In most situation it is useful to take:

$$t = \tau, \quad (\text{B.12})$$

then eq. (B.11) is simplified to

$$\begin{cases} \frac{\partial f}{\partial t} = \frac{1}{g} \left( \frac{\partial x}{\partial \xi} \frac{\partial f}{\partial \tau} - \frac{\partial x}{\partial \tau} \frac{\partial f}{\partial \xi} \right), \\ \frac{\partial f}{\partial x} = \frac{1}{g} \frac{\partial f}{\partial \xi}. \end{cases} \quad (\text{B.13})$$

Using expression eq. (B.13), the conservation equation, eq. (2.2), can be rewritten in moving 1D coordinate system:

$$\frac{\partial}{\partial t} \left( \frac{\partial x}{\partial \xi} f_t \right) + \frac{\partial}{\partial \xi} (f_x - \dot{x} f_t) = \frac{\partial x}{\partial \xi} q, \quad (\text{B.14})$$

where

$$\dot{x} = \frac{\partial x}{\partial t} \quad (\text{B.15})$$

is grid velocity in the global coordinate system.

It is straightforward to show, using differentiation rules, that the last expression is identical to:

$$\frac{\partial f_t}{\partial t} + \left( \frac{\partial x}{\partial \xi} \right)^{-1} \left( \frac{\partial f_x}{\partial \xi} - \dot{x} \frac{\partial f_t}{\partial \xi} \right) = q. \quad (\text{B.16})$$

## B.2. 2D transformation

Firstly, static curvilinear coordinates are considered. Figure B.4 shows coordinate lines in physical spaces  $(x, y)$  and in the computational space  $(\xi, \eta)$ .

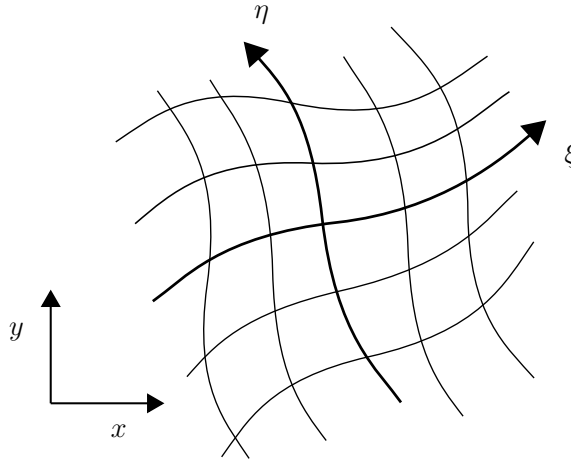


**Figure B.4.:** Static 2D coordinate transformation.

The physical coordinates are the function of computational coordinates:

$$\begin{cases} x = x(\xi, \eta), \\ y = y(\xi, \eta). \end{cases} \quad (\text{B.17})$$

The derivatives of coordinates are linked with one another as (compare with eq. (B.6)):

$$\begin{pmatrix} dx \\ dy \end{pmatrix} = \begin{pmatrix} \frac{\partial x}{\partial \xi} & \frac{\partial x}{\partial \eta} \\ \frac{\partial y}{\partial \xi} & \frac{\partial y}{\partial \eta} \end{pmatrix} \begin{pmatrix} d\xi \\ d\eta \end{pmatrix}. \quad (\text{B.18})$$

Using formal matrix inversion one can compute the reverse operation:

$$\begin{pmatrix} d\xi \\ d\eta \end{pmatrix} = \frac{1}{g} \begin{pmatrix} \frac{\partial y}{\partial \eta} & -\frac{\partial x}{\partial \eta} \\ -\frac{\partial y}{\partial \xi} & \frac{\partial x}{\partial \xi} \end{pmatrix} \begin{pmatrix} dx \\ dy \end{pmatrix}, \quad (\text{B.19})$$

where

$$g = \frac{\partial x}{\partial \xi} \frac{\partial y}{\partial \eta} - \frac{\partial x}{\partial \eta} \frac{\partial y}{\partial \xi}. \quad (\text{B.20})$$

Using the latter, one can calculate the partial derivatives of a function  $f = f(x, y)$  in physical domain from partial derivatives in computational domain (compare eq. (B.13)):

$$\begin{cases} \frac{\partial f}{\partial x} = \frac{1}{g} \left( \frac{\partial y}{\partial \eta} \frac{\partial f}{\partial \xi} - \frac{\partial y}{\partial \xi} \frac{\partial f}{\partial \eta} \right), \\ \frac{\partial f}{\partial y} = \frac{1}{g} \left( \frac{\partial x}{\partial \xi} \frac{\partial f}{\partial \eta} - \frac{\partial x}{\partial \eta} \frac{\partial f}{\partial \xi} \right), \end{cases} \quad (\text{B.21})$$

If coordinates are orthogonal, then  $\frac{\partial x}{\partial \eta} = \frac{\partial y}{\partial \xi} = 0$ , and the expression (B.21) reduces to an expression equivalent to eq. (B.4).

The general conservation equation can be written in general curvilinear 2D coordinates:

$$\frac{\partial}{\partial t} (g f_t) + \frac{\partial}{\partial \xi} \left( \frac{\partial y}{\partial \eta} f_x - \frac{\partial x}{\partial \eta} f_y \right) + \frac{\partial}{\partial \eta} \left( \frac{\partial x}{\partial \xi} f_y - \frac{\partial y}{\partial \xi} f_x \right) = g q, \quad (\text{B.22})$$

which is equivalent to:

$$\frac{\partial f_t}{\partial t} + \frac{1}{g} \left[ \frac{\partial y}{\partial \eta} \frac{\partial f_x}{\partial \xi} - \frac{\partial x}{\partial \eta} \frac{\partial f_y}{\partial \xi} + \frac{\partial x}{\partial \xi} \frac{\partial f_y}{\partial \eta} - \frac{\partial y}{\partial \xi} \frac{\partial f_x}{\partial \eta} \right] = q. \quad (\text{B.23})$$

Next, the dynamic 2D coordinates are presented, which are also the function of time:

$$\begin{cases} t = t(\tau, \xi, \eta), \\ x = x(\tau, \xi, \eta), \\ y = y(\tau, \xi, \eta). \end{cases} \quad (\text{B.24})$$

The derivatives of physical coordinates in time dependent computational coordinates are then:

$$\begin{pmatrix} dt \\ dx \\ dy \end{pmatrix} = \begin{pmatrix} \frac{\partial t}{\partial \tau} & \frac{\partial t}{\partial \xi} & \frac{\partial t}{\partial \eta} \\ \frac{\partial x}{\partial \tau} & \frac{\partial x}{\partial \xi} & \frac{\partial x}{\partial \eta} \\ \frac{\partial y}{\partial \tau} & \frac{\partial y}{\partial \xi} & \frac{\partial y}{\partial \eta} \end{pmatrix} \begin{pmatrix} d\tau \\ d\xi \\ d\eta \end{pmatrix}, \quad (\text{B.25})$$

and the reverse operation:

$$\begin{pmatrix} d\tau \\ d\xi \\ d\eta \end{pmatrix} = \frac{1}{g} \begin{pmatrix} \frac{\partial x}{\partial \xi} \frac{\partial y}{\partial \eta} - \frac{\partial x}{\partial \eta} \frac{\partial y}{\partial \xi} & \frac{\partial t}{\partial \eta} \frac{\partial y}{\partial \xi} - \frac{\partial t}{\partial \xi} \frac{\partial y}{\partial \eta} & \frac{\partial t}{\partial \xi} \frac{\partial x}{\partial \eta} - \frac{\partial t}{\partial \eta} \frac{\partial x}{\partial \xi} \\ \frac{\partial \eta}{\partial \tau} \frac{\partial \tau}{\partial \xi} - \frac{\partial \tau}{\partial \xi} \frac{\partial \eta}{\partial \tau} & \frac{\partial \tau}{\partial \eta} \frac{\partial \tau}{\partial \xi} - \frac{\partial \tau}{\partial \xi} \frac{\partial \tau}{\partial \eta} & \frac{\partial \eta}{\partial \tau} \frac{\partial \tau}{\partial \eta} - \frac{\partial \tau}{\partial \eta} \frac{\partial \tau}{\partial \xi} \\ \frac{\partial \tau}{\partial \tau} \frac{\partial \xi}{\partial \xi} - \frac{\partial \xi}{\partial \tau} \frac{\partial \tau}{\partial \xi} & \frac{\partial \xi}{\partial \tau} \frac{\partial \xi}{\partial \xi} - \frac{\partial \xi}{\partial \xi} \frac{\partial \tau}{\partial \tau} & \frac{\partial \tau}{\partial \tau} \frac{\partial \xi}{\partial \eta} - \frac{\partial \xi}{\partial \eta} \frac{\partial \tau}{\partial \tau} \end{pmatrix} \begin{pmatrix} dt \\ dx \\ dy \end{pmatrix}, \quad (\text{B.26})$$

where the determinant of the transformation Jacobian:

$$g = \frac{\partial t}{\partial \tau} \frac{\partial x}{\partial \xi} \frac{\partial y}{\partial \eta} - \frac{\partial t}{\partial \tau} \frac{\partial x}{\partial \eta} \frac{\partial y}{\partial \xi} + \frac{\partial t}{\partial \eta} \frac{\partial x}{\partial \tau} \frac{\partial y}{\partial \xi} - \frac{\partial t}{\partial \eta} \frac{\partial x}{\partial \xi} \frac{\partial y}{\partial \tau} + \frac{\partial t}{\partial \xi} \frac{\partial x}{\partial \eta} \frac{\partial y}{\partial \tau} - \frac{\partial t}{\partial \xi} \frac{\partial x}{\partial \tau} \frac{\partial y}{\partial \eta}. \quad (\text{B.27})$$

These leads to expressions for partial derivatives of a function  $f = f(t, x, y)$  in physical coordinates

$$\begin{pmatrix} \frac{\partial f}{\partial t} \\ \frac{\partial f}{\partial x} \\ \frac{\partial f}{\partial y} \end{pmatrix} = \frac{1}{g} \begin{pmatrix} \frac{\partial x}{\partial \xi} \frac{\partial y}{\partial \eta} - \frac{\partial x}{\partial \eta} \frac{\partial y}{\partial \xi} & \frac{\partial y}{\partial \tau} \frac{\partial x}{\partial \eta} - \frac{\partial x}{\partial \tau} \frac{\partial y}{\partial \eta} & \frac{\partial x}{\partial \tau} \frac{\partial y}{\partial \xi} - \frac{\partial y}{\partial \tau} \frac{\partial x}{\partial \xi} \\ \frac{\partial \tau}{\partial t} \frac{\partial \eta}{\partial y} - \frac{\partial \tau}{\partial t} \frac{\partial \xi}{\partial y} & \frac{\partial \tau}{\partial t} \frac{\partial \eta}{\partial \tau} - \frac{\partial \tau}{\partial t} \frac{\partial \xi}{\partial \tau} & \frac{\partial \tau}{\partial t} \frac{\partial \xi}{\partial \tau} - \frac{\partial \tau}{\partial t} \frac{\partial \eta}{\partial \tau} \\ \frac{\partial \eta}{\partial t} \frac{\partial \xi}{\partial x} - \frac{\partial \xi}{\partial t} \frac{\partial \eta}{\partial x} & \frac{\partial \eta}{\partial t} \frac{\partial \tau}{\partial x} - \frac{\partial \xi}{\partial t} \frac{\partial \tau}{\partial x} & \frac{\partial \eta}{\partial t} \frac{\partial \tau}{\partial y} - \frac{\partial \xi}{\partial t} \frac{\partial \tau}{\partial y} \\ \frac{\partial \xi}{\partial \tau} \frac{\partial \eta}{\partial \eta} - \frac{\partial \eta}{\partial \tau} \frac{\partial \xi}{\partial \eta} & \frac{\partial \xi}{\partial \tau} \frac{\partial \tau}{\partial \eta} - \frac{\partial \eta}{\partial \tau} \frac{\partial \xi}{\partial \tau} & \frac{\partial \xi}{\partial \tau} \frac{\partial \tau}{\partial \xi} - \frac{\partial \eta}{\partial \tau} \frac{\partial \xi}{\partial \xi} \end{pmatrix} \begin{pmatrix} \frac{\partial f}{\partial \tau} \\ \frac{\partial f}{\partial \xi} \\ \frac{\partial f}{\partial \eta} \end{pmatrix}. \quad (\text{B.28})$$

If one takes that  $t = \tau$ , then eq. (B.28) is reduced to:

$$\begin{pmatrix} \frac{\partial f}{\partial t} \\ \frac{\partial f}{\partial x} \\ \frac{\partial f}{\partial y} \end{pmatrix} = \frac{1}{g} \begin{pmatrix} g & \frac{\partial y}{\partial \tau} \frac{\partial x}{\partial \eta} - \frac{\partial x}{\partial \tau} \frac{\partial y}{\partial \eta} & \frac{\partial x}{\partial \tau} \frac{\partial y}{\partial \xi} - \frac{\partial y}{\partial \tau} \frac{\partial x}{\partial \xi} \\ 0 & \frac{\partial y}{\partial \eta} & -\frac{\partial y}{\partial \xi} \\ 0 & -\frac{\partial x}{\partial \eta} & \frac{\partial x}{\partial \xi} \end{pmatrix} \begin{pmatrix} \frac{\partial f}{\partial \tau} \\ \frac{\partial f}{\partial \xi} \\ \frac{\partial f}{\partial \eta} \end{pmatrix}, \quad (\text{B.29})$$

with

$$g = \frac{\partial x}{\partial \xi} \frac{\partial y}{\partial \eta} - \frac{\partial x}{\partial \eta} \frac{\partial y}{\partial \xi}. \quad (\text{B.30})$$

Applying expression eq. (B.29) one can derive the general conservation equation in dynamic curvilinear coordinates:

$$\begin{aligned} \frac{\partial}{\partial t} (g f_t) + \frac{\partial}{\partial \xi} \left[ \frac{\partial y}{\partial \eta} (f_x - \dot{x} f_t) - \frac{\partial x}{\partial \eta} (f_y - \dot{y} f_t) \right] \\ + \frac{\partial}{\partial \eta} \left[ \frac{\partial x}{\partial \xi} (f_y - \dot{y} f_t) - \frac{\partial y}{\partial \xi} (f_x - \dot{x} f_t) \right] = g q, \end{aligned} \quad (\text{B.31})$$

with grid velocity:

$$\begin{pmatrix} \dot{x} \\ \dot{y} \end{pmatrix} = \begin{pmatrix} \frac{\partial x}{\partial t} \\ \frac{\partial y}{\partial t} \end{pmatrix}. \quad (\text{B.32})$$

The eq. (B.31) is equivalent to:

$$\begin{aligned} \frac{\partial f_t}{\partial t} + \frac{1}{g} \left[ \frac{\partial y}{\partial \eta} \frac{\partial f_x}{\partial \xi} - \frac{\partial x}{\partial \eta} \frac{\partial f_y}{\partial \xi} + \left( \dot{y} \frac{\partial x}{\partial \eta} - \dot{x} \frac{\partial y}{\partial \eta} \right) \frac{\partial f_t}{\partial \xi} \right. \\ \left. + \frac{\partial x}{\partial \xi} \frac{\partial f_y}{\partial \eta} - \frac{\partial y}{\partial \xi} \frac{\partial f_x}{\partial \eta} + \left( \dot{x} \frac{\partial y}{\partial \xi} - \dot{y} \frac{\partial x}{\partial \xi} \right) \frac{\partial f_t}{\partial \eta} \right] = q. \end{aligned} \quad (\text{B.33})$$

### B.3. 3D transformation

Similarly to 2D, one can imaging static 3D coordinates  $(x, y, z)$  as a function of computational coordinates  $(\xi, \eta, \zeta)$

$$\begin{cases} x = x(\xi, \eta, \zeta), \\ y = y(\xi, \eta, \zeta), \\ z = z(\xi, \eta, \zeta). \end{cases} \quad (\text{B.34})$$

Then the derivative are linked with linear transformation:

$$\begin{pmatrix} dx \\ dy \\ dz \end{pmatrix} = \begin{pmatrix} \frac{\partial x}{\partial \xi} & \frac{\partial x}{\partial \eta} & \frac{\partial x}{\partial \zeta} \\ \frac{\partial y}{\partial \xi} & \frac{\partial y}{\partial \eta} & \frac{\partial y}{\partial \zeta} \\ \frac{\partial z}{\partial \xi} & \frac{\partial z}{\partial \eta} & \frac{\partial z}{\partial \zeta} \end{pmatrix} \begin{pmatrix} d\xi \\ d\eta \\ d\zeta \end{pmatrix}, \quad (\text{B.35})$$

with the corresponding inverse transformation:

$$\begin{pmatrix} d\xi \\ d\eta \\ d\zeta \end{pmatrix} = \frac{1}{g} \begin{pmatrix} \frac{\partial y}{\partial \eta} \frac{\partial z}{\partial \zeta} - \frac{\partial y}{\partial \zeta} \frac{\partial z}{\partial \eta} & \frac{\partial x}{\partial \eta} \frac{\partial z}{\partial \zeta} - \frac{\partial x}{\partial \zeta} \frac{\partial z}{\partial \eta} & \frac{\partial x}{\partial \eta} \frac{\partial y}{\partial \zeta} - \frac{\partial x}{\partial \zeta} \frac{\partial y}{\partial \eta} \\ \frac{\partial \zeta}{\partial \xi} \frac{\partial \eta}{\partial \zeta} - \frac{\partial \xi}{\partial \zeta} \frac{\partial \eta}{\partial \xi} & \frac{\partial \xi}{\partial \xi} \frac{\partial \zeta}{\partial \zeta} - \frac{\partial \xi}{\partial \zeta} \frac{\partial \zeta}{\partial \xi} & \frac{\partial \xi}{\partial \xi} \frac{\partial \eta}{\partial \zeta} - \frac{\partial \xi}{\partial \zeta} \frac{\partial \eta}{\partial \xi} \\ \frac{\partial \zeta}{\partial \eta} \frac{\partial \xi}{\partial \zeta} - \frac{\partial \eta}{\partial \zeta} \frac{\partial \xi}{\partial \eta} & \frac{\partial \xi}{\partial \eta} \frac{\partial \zeta}{\partial \zeta} - \frac{\partial \xi}{\partial \zeta} \frac{\partial \zeta}{\partial \eta} & \frac{\partial \xi}{\partial \eta} \frac{\partial y}{\partial \zeta} - \frac{\partial \xi}{\partial \zeta} \frac{\partial y}{\partial \eta} \\ \frac{\partial \xi}{\partial \xi} \frac{\partial \eta}{\partial \zeta} - \frac{\partial \eta}{\partial \zeta} \frac{\partial \xi}{\partial \xi} & \frac{\partial \xi}{\partial \xi} \frac{\partial \zeta}{\partial \zeta} - \frac{\partial \xi}{\partial \zeta} \frac{\partial \zeta}{\partial \xi} & \frac{\partial \xi}{\partial \xi} \frac{\partial \eta}{\partial \zeta} - \frac{\partial \xi}{\partial \zeta} \frac{\partial \eta}{\partial \xi} \end{pmatrix} \begin{pmatrix} dx \\ dy \\ dz \end{pmatrix}, \quad (\text{B.36})$$

with

$$g = \frac{\partial x}{\partial \xi} \frac{\partial y}{\partial \eta} \frac{\partial z}{\partial \zeta} - \frac{\partial x}{\partial \eta} \frac{\partial y}{\partial \xi} \frac{\partial z}{\partial \zeta} + \frac{\partial x}{\partial \eta} \frac{\partial y}{\partial \zeta} \frac{\partial z}{\partial \xi} - \frac{\partial x}{\partial \xi} \frac{\partial y}{\partial \zeta} \frac{\partial z}{\partial \eta} - \frac{\partial x}{\partial \zeta} \frac{\partial y}{\partial \eta} \frac{\partial z}{\partial \xi} + \frac{\partial x}{\partial \zeta} \frac{\partial y}{\partial \xi} \frac{\partial z}{\partial \eta}. \quad (\text{B.37})$$

The latter leads to the formulæ for partial derivatives of function  $f = f(x, y, z)$  in physical coordinates:

$$\begin{pmatrix} \frac{\partial f}{\partial x} \\ \frac{\partial f}{\partial y} \\ \frac{\partial f}{\partial z} \end{pmatrix} = \frac{1}{g} \begin{pmatrix} \frac{\partial y}{\partial \eta} \frac{\partial z}{\partial \zeta} - \frac{\partial y}{\partial \zeta} \frac{\partial z}{\partial \eta} & \frac{\partial x}{\partial \eta} \frac{\partial z}{\partial \zeta} - \frac{\partial x}{\partial \zeta} \frac{\partial z}{\partial \eta} & \frac{\partial x}{\partial \eta} \frac{\partial y}{\partial \zeta} - \frac{\partial x}{\partial \zeta} \frac{\partial y}{\partial \eta} \\ \frac{\partial \zeta}{\partial \xi} \frac{\partial \eta}{\partial \zeta} - \frac{\partial \xi}{\partial \zeta} \frac{\partial \eta}{\partial \xi} & \frac{\partial \xi}{\partial \xi} \frac{\partial \zeta}{\partial \zeta} - \frac{\partial \xi}{\partial \zeta} \frac{\partial \zeta}{\partial \xi} & \frac{\partial \xi}{\partial \xi} \frac{\partial \eta}{\partial \zeta} - \frac{\partial \xi}{\partial \zeta} \frac{\partial \eta}{\partial \xi} \\ \frac{\partial \zeta}{\partial \eta} \frac{\partial \xi}{\partial \zeta} - \frac{\partial \eta}{\partial \zeta} \frac{\partial \xi}{\partial \eta} & \frac{\partial \xi}{\partial \eta} \frac{\partial \zeta}{\partial \zeta} - \frac{\partial \xi}{\partial \zeta} \frac{\partial \zeta}{\partial \eta} & \frac{\partial \xi}{\partial \eta} \frac{\partial y}{\partial \zeta} - \frac{\partial \xi}{\partial \zeta} \frac{\partial y}{\partial \eta} \\ \frac{\partial \xi}{\partial \xi} \frac{\partial \eta}{\partial \zeta} - \frac{\partial \eta}{\partial \zeta} \frac{\partial \xi}{\partial \xi} & \frac{\partial \xi}{\partial \xi} \frac{\partial \zeta}{\partial \zeta} - \frac{\partial \xi}{\partial \zeta} \frac{\partial \zeta}{\partial \xi} & \frac{\partial \xi}{\partial \xi} \frac{\partial \eta}{\partial \zeta} - \frac{\partial \xi}{\partial \zeta} \frac{\partial \eta}{\partial \xi} \end{pmatrix} \begin{pmatrix} \frac{\partial f}{\partial \xi} \\ \frac{\partial f}{\partial \eta} \\ \frac{\partial f}{\partial \zeta} \end{pmatrix}. \quad (\text{B.38})$$

Last but not least, the derivatives in dynamic curvilinear coordinates are presented:

$$\begin{cases} t = t(\tau, \xi, \eta, \zeta), \\ x = x(\tau, \xi, \eta, \zeta), \\ y = y(\tau, \xi, \eta, \zeta), \\ z = z(\tau, \xi, \eta, \zeta). \end{cases} \quad (\text{B.39})$$

The derivatives in physical coordinates  $(t, x, y, z)$  and computational coordinates  $(\tau, \xi, \eta, \zeta)$  are linked through  $4 \times 4$  transformation Jacobian:

$$\begin{pmatrix} dt \\ dx \\ dy \\ dz \end{pmatrix} = \begin{pmatrix} \frac{\partial t}{\partial \tau} & \frac{\partial t}{\partial \xi} & \frac{\partial t}{\partial \eta} & \frac{\partial t}{\partial \zeta} \\ \frac{\partial x}{\partial \tau} & \frac{\partial x}{\partial \xi} & \frac{\partial x}{\partial \eta} & \frac{\partial x}{\partial \zeta} \\ \frac{\partial y}{\partial \tau} & \frac{\partial y}{\partial \xi} & \frac{\partial y}{\partial \eta} & \frac{\partial y}{\partial \zeta} \\ \frac{\partial z}{\partial \tau} & \frac{\partial z}{\partial \xi} & \frac{\partial z}{\partial \eta} & \frac{\partial z}{\partial \zeta} \end{pmatrix} \begin{pmatrix} d\tau \\ d\xi \\ d\eta \\ d\zeta \end{pmatrix}, \quad (\text{B.40})$$

with the inverse transformation shown in eq. (B.41).



Here applies the determinant of the transformation Jacobian:

$$\begin{aligned}
g = & \frac{\partial t}{\partial \tau} \left[ \frac{\partial x}{\partial \xi} \frac{\partial y}{\partial \eta} \frac{\partial z}{\partial \zeta} - \frac{\partial x}{\partial \xi} \frac{\partial y}{\partial \zeta} \frac{\partial z}{\partial \eta} + \frac{\partial x}{\partial \eta} \frac{\partial y}{\partial \zeta} \frac{\partial z}{\partial \xi} - \frac{\partial x}{\partial \eta} \frac{\partial y}{\partial \xi} \frac{\partial z}{\partial \zeta} + \frac{\partial x}{\partial \zeta} \frac{\partial y}{\partial \xi} \frac{\partial z}{\partial \eta} - \frac{\partial x}{\partial \zeta} \frac{\partial y}{\partial \eta} \frac{\partial z}{\partial \xi} \right] \\
& + \frac{\partial t}{\partial \xi} \left[ \frac{\partial x}{\partial \tau} \left( \frac{\partial y}{\partial \zeta} \frac{\partial z}{\partial \eta} - \frac{\partial y}{\partial \eta} \frac{\partial z}{\partial \zeta} \right) + \frac{\partial y}{\partial \tau} \left( \frac{\partial x}{\partial \eta} \frac{\partial z}{\partial \zeta} - \frac{\partial x}{\partial \zeta} \frac{\partial z}{\partial \eta} \right) + \frac{\partial z}{\partial \tau} \left( \frac{\partial x}{\partial \zeta} \frac{\partial y}{\partial \eta} - \frac{\partial x}{\partial \eta} \frac{\partial y}{\partial \zeta} \right) \right] \\
& + \frac{\partial t}{\partial \eta} \left[ \frac{\partial x}{\partial \tau} \left( \frac{\partial y}{\partial \xi} \frac{\partial z}{\partial \zeta} - \frac{\partial y}{\partial \zeta} \frac{\partial z}{\partial \xi} \right) + \frac{\partial y}{\partial \tau} \left( \frac{\partial x}{\partial \zeta} \frac{\partial z}{\partial \xi} - \frac{\partial x}{\partial \xi} \frac{\partial z}{\partial \zeta} \right) + \frac{\partial z}{\partial \tau} \left( \frac{\partial x}{\partial \xi} \frac{\partial y}{\partial \zeta} - \frac{\partial x}{\partial \zeta} \frac{\partial y}{\partial \xi} \right) \right] \\
& + \frac{\partial t}{\partial \zeta} \left[ \frac{\partial x}{\partial \tau} \left( \frac{\partial y}{\partial \eta} \frac{\partial z}{\partial \xi} - \frac{\partial y}{\partial \xi} \frac{\partial z}{\partial \eta} \right) + \frac{\partial y}{\partial \tau} \left( \frac{\partial x}{\partial \xi} \frac{\partial z}{\partial \eta} - \frac{\partial x}{\partial \eta} \frac{\partial z}{\partial \xi} \right) + \frac{\partial z}{\partial \tau} \left( \frac{\partial x}{\partial \eta} \frac{\partial y}{\partial \xi} - \frac{\partial x}{\partial \xi} \frac{\partial y}{\partial \eta} \right) \right].
\end{aligned} \tag{B.42}$$

It is more practical to use again:

$$t = \tau, \tag{B.43}$$

then eq. (B.40) and particularly eq. (B.41) can be simplified considerably:

$$\begin{pmatrix} dt \\ dx \\ dy \\ dz \end{pmatrix} = \begin{pmatrix} 1 & 0 & 0 & 0 \\ \frac{\partial x}{\partial \tau} & \frac{\partial x}{\partial \xi} & \frac{\partial x}{\partial \eta} & \frac{\partial x}{\partial \zeta} \\ \frac{\partial y}{\partial \tau} & \frac{\partial y}{\partial \xi} & \frac{\partial y}{\partial \eta} & \frac{\partial y}{\partial \zeta} \\ \frac{\partial z}{\partial \tau} & \frac{\partial z}{\partial \xi} & \frac{\partial z}{\partial \eta} & \frac{\partial z}{\partial \zeta} \\ \frac{\partial \tau}{\partial \tau} & \frac{\partial \tau}{\partial \xi} & \frac{\partial \tau}{\partial \eta} & \frac{\partial \tau}{\partial \zeta} \end{pmatrix} \begin{pmatrix} d\tau \\ d\xi \\ d\eta \\ d\zeta \end{pmatrix}, \tag{B.44}$$

and

$$\begin{pmatrix} d\tau \\ d\xi \\ d\eta \\ d\zeta \end{pmatrix} = \frac{1}{g} \begin{pmatrix} g & 0 & 0 & 0 \\ a_1 & \frac{\partial y}{\partial \eta} \frac{\partial z}{\partial \zeta} - \frac{\partial y}{\partial \zeta} \frac{\partial z}{\partial \eta} & \frac{\partial x}{\partial \eta} \frac{\partial z}{\partial \zeta} - \frac{\partial x}{\partial \zeta} \frac{\partial z}{\partial \eta} & \frac{\partial x}{\partial \zeta} \frac{\partial y}{\partial \eta} - \frac{\partial x}{\partial \eta} \frac{\partial y}{\partial \zeta} \\ a_2 & \frac{\partial y}{\partial \xi} \frac{\partial z}{\partial \zeta} - \frac{\partial y}{\partial \zeta} \frac{\partial z}{\partial \xi} & \frac{\partial x}{\partial \xi} \frac{\partial z}{\partial \zeta} - \frac{\partial x}{\partial \zeta} \frac{\partial z}{\partial \xi} & \frac{\partial x}{\partial \zeta} \frac{\partial y}{\partial \xi} - \frac{\partial x}{\partial \xi} \frac{\partial y}{\partial \zeta} \\ a_3 & \frac{\partial y}{\partial \eta} \frac{\partial z}{\partial \xi} - \frac{\partial y}{\partial \xi} \frac{\partial z}{\partial \eta} & \frac{\partial x}{\partial \eta} \frac{\partial z}{\partial \xi} - \frac{\partial x}{\partial \xi} \frac{\partial z}{\partial \eta} & \frac{\partial x}{\partial \xi} \frac{\partial y}{\partial \eta} - \frac{\partial x}{\partial \eta} \frac{\partial y}{\partial \xi} \end{pmatrix} \begin{pmatrix} dt \\ dx \\ dy \\ dz \end{pmatrix}, \tag{B.45}$$

where

$$\begin{cases} g = \frac{\partial x}{\partial \xi} \frac{\partial y}{\partial \eta} \frac{\partial z}{\partial \zeta} - \frac{\partial x}{\partial \xi} \frac{\partial y}{\partial \zeta} \frac{\partial z}{\partial \eta} + \frac{\partial x}{\partial \eta} \frac{\partial y}{\partial \zeta} \frac{\partial z}{\partial \xi} - \frac{\partial x}{\partial \eta} \frac{\partial y}{\partial \xi} \frac{\partial z}{\partial \zeta} + \frac{\partial x}{\partial \zeta} \frac{\partial y}{\partial \xi} \frac{\partial z}{\partial \eta} - \frac{\partial x}{\partial \zeta} \frac{\partial y}{\partial \eta} \frac{\partial z}{\partial \xi}, \\ a_1 = \dot{x} \left( \frac{\partial y}{\partial \zeta} \frac{\partial z}{\partial \eta} - \frac{\partial y}{\partial \eta} \frac{\partial z}{\partial \zeta} \right) + \dot{y} \left( \frac{\partial x}{\partial \eta} \frac{\partial z}{\partial \zeta} - \frac{\partial x}{\partial \zeta} \frac{\partial z}{\partial \eta} \right) + \dot{z} \left( \frac{\partial x}{\partial \zeta} \frac{\partial y}{\partial \eta} - \frac{\partial x}{\partial \eta} \frac{\partial y}{\partial \zeta} \right), \\ a_2 = \dot{x} \left( \frac{\partial y}{\partial \xi} \frac{\partial z}{\partial \zeta} - \frac{\partial y}{\partial \zeta} \frac{\partial z}{\partial \xi} \right) + \dot{y} \left( \frac{\partial x}{\partial \xi} \frac{\partial z}{\partial \zeta} - \frac{\partial x}{\partial \zeta} \frac{\partial z}{\partial \xi} \right) + \dot{z} \left( \frac{\partial x}{\partial \zeta} \frac{\partial y}{\partial \xi} - \frac{\partial x}{\partial \xi} \frac{\partial y}{\partial \zeta} \right), \\ a_3 = \dot{x} \left( \frac{\partial y}{\partial \eta} \frac{\partial z}{\partial \xi} - \frac{\partial y}{\partial \xi} \frac{\partial z}{\partial \eta} \right) + \dot{y} \left( \frac{\partial x}{\partial \eta} \frac{\partial z}{\partial \xi} - \frac{\partial x}{\partial \xi} \frac{\partial z}{\partial \eta} \right) + \dot{z} \left( \frac{\partial x}{\partial \xi} \frac{\partial y}{\partial \eta} - \frac{\partial x}{\partial \eta} \frac{\partial y}{\partial \xi} \right). \end{cases} \tag{B.46}$$

The eq. (B.45) leads to expressions for partial derivatives of a function  $f = f(t, x, y, z)$  in physical coordinates  $(t, x, y, z)$  from partial derivatives in computational coordinates



## C. Benchmarking of time integration scheme

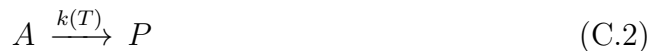
Generally, the spectral ODE solver tend to outperform classical low order schemes, if higher accuracies are required. In order to test the proposed method, a simple MATLAB code was designed. The several tests were run on a number of well known benchmark problems. The solution with the MATLAB implementation of the Rosenbrock method (ode23s) [SR97] is then compared. The following criteria are used: the number of function calculations, the number of Jacobian calculations and the computational time needed to achieve the desired accuracy. The accuracy is measured with an analytical solution, if available, or with a numerical solution to which the "ode23s" is striving with strictest tolerances, on a large set ( $N = 10^6$ ) of control points:

$$error = \arg \max_{v=1, \dots, n_v} \frac{\sum_{i=1}^N (u_v(t_i) - x_v(t_i))^2}{\sum_{i=1}^N (u_v(t_i))^2}, \quad (C.1)$$

where  $n_v$  number of variable (unknowns) in the system,  $u_v$  is the ideal solution of the variable  $v$  and  $x_v$  - the actual numerical solution.

### C.1. Semenov's explosion model

In the late thirties N. Semenov developed a phenomenological model of a chemical system, which can either be either slow reacting or exploding [Sem28]. The reacting system is represented by a homogeneous flammable mixture, which undergoes a one-step reaction:



and is a subject of Newtonian cooling. The dimensionless form of the problem is given by:

$$\begin{cases} \gamma \dot{\theta} + \dot{\eta} &= -\alpha \theta \\ \dot{\eta} &= -\eta \exp\left(\frac{\theta}{1+\beta\theta}\right) \end{cases}, \quad (C.3)$$

where  $\eta$  is the dimensionless concentration of reactants  $\theta$  - dimensionless temperature. The properties of the system are described by coefficients  $\alpha$ ,  $\beta$  and  $\gamma$ , which represent energy dissipation through cooling, activation temperature and adiabatic temperature respectively. Depending on the set of parameters  $\alpha$ ,  $\beta$  and  $\gamma$ , the system can be from very smooth (slow reaction) to extremely stiff (explosion).

The Semenov's explosion model is studied on the interval  $t \in [0, 0.15]$ . On this interval at around  $t = 0.06$  concentration suddenly drops to zero and after that the temperature, obeying the Newtonian law of cooling, gradually decreases also quasi zero at  $t = 0.15$ . Numerical tests show that higher order polynomials tend to reduce number of function evaluations (feval), Jacobian evaluations (jeval) and thus reduce computational time (see figures C.5). Although polynomial of order 11 requires the same number of function evaluations than polynomials of order 7 but the number Jacobian calculations is noticeably lower, which results in a higher computational time. Legendre series seems to be more appropriate for this problem, especially for low order case. At around  $t = 0.06$  the reactant concentration drops to zero. The proposed approach can also manage this sudden drop of the concentration for all reasonable tolerances ( $TOL > 10^{-2}$ ): with  $TOL = 10^{-8}$  the zero is captured with the absolute accuracy of  $10^{-11}$ .

The proposed method outperform the Rosenbrock (ODE23s) algorithm starting from error about  $10^{-2}$  for polynomials of order 7 or higher. However, the low order

polynomials appear to be very inefficient compared to the classical method. The proposed method reaches the bottom line of achieved relative error at about  $10^{-9}$ , that signalise that the reference solution, acquired with ODE23s with minimal possible tolerance  $RTOL = 2 \cdot 10^{-14}$ , can be insufficient. It was also observed that 35 polynomial segments are sufficient to achieve relative error below  $10^{-9}$ . Most of this segments are located near the singularity.

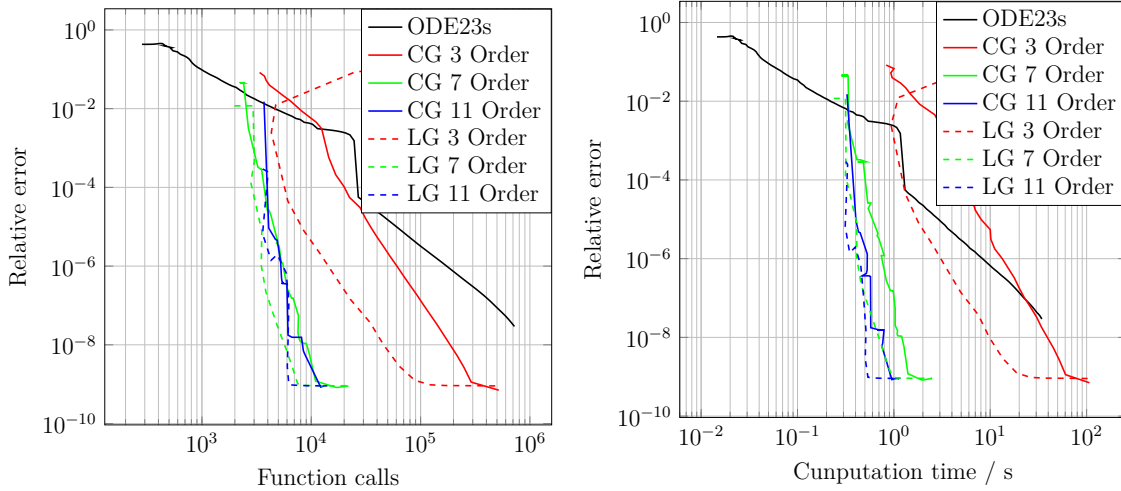
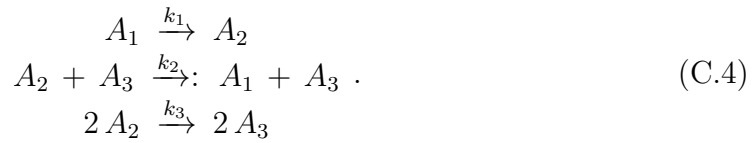


**Figure C.5.:** ODE Solver performance for Semenov's Explosion

## C.2. The reaction of Robertson

This example, borrowed from H. Robertson [Rob66], describes the following simple reaction mechanism:



With initial concentration of reactants  $[A_1] = 1$ ,  $[A_2] = 0$  and  $[A_3] = 0$ . The reaction rates ( $k_1 = 4 \cdot 10^{-2}$ ,  $k_2 = 10^4$ ,  $k_3 = 1.5 \cdot 10^7$ ) vary over nine order of magnitude, which results in a very stiff non-linear ODE system:

$$\begin{cases} \dot{x}_1 = -k_1 x_1 + k_2 x_2 x_3 \\ \dot{x}_2 = k_1 x_1 - k_2 x_2 x_3 - 2k_3 x_2^2, \\ \dot{x}_3 = 2k_3 x_2^2 \end{cases} \tag{C.5}$$

where  $x_i$  is the concentration of the reactant  $i$ .

This problem is considered on the interval  $t \in [0, 10]$ . The most dramatic change happens with the second variable, which jumps from zero to about  $3.6 \cdot 10^{-5}$  within  $t < 5 \cdot 10^3$ , meanwhile the other two variables express quite a smooth behaviour. After  $t = 5 \cdot 10^3$  the solution is fully smooth. On one side, a similar behaviour can be observed, as in case of Semenov's explosion problem and in case of Robertson's Reaction: the higher the polynomial order of the proposed method, the more efficient is the proposed algorithm (see figures C.6). It occurs due to lower function and Jacobian evaluations. On the other side, the method is not able to achieve crude tolerances by high order polynomials. This happens due to the difficulty of finding an appropriate interval length near the singularity in the solution, which results in

high computational efforts (s. fig. C.6, the blue curve is bended significantly to the right for low accuracy).

In this case, both types of polynomial approximations provide almost identical results and the proposed method outperform the classical Rosenbrock method just from relative error of  $10^{-7}$ . This problem seems to be relatively simple, considering the computational effort and the number of required segments (only 9 segments required).

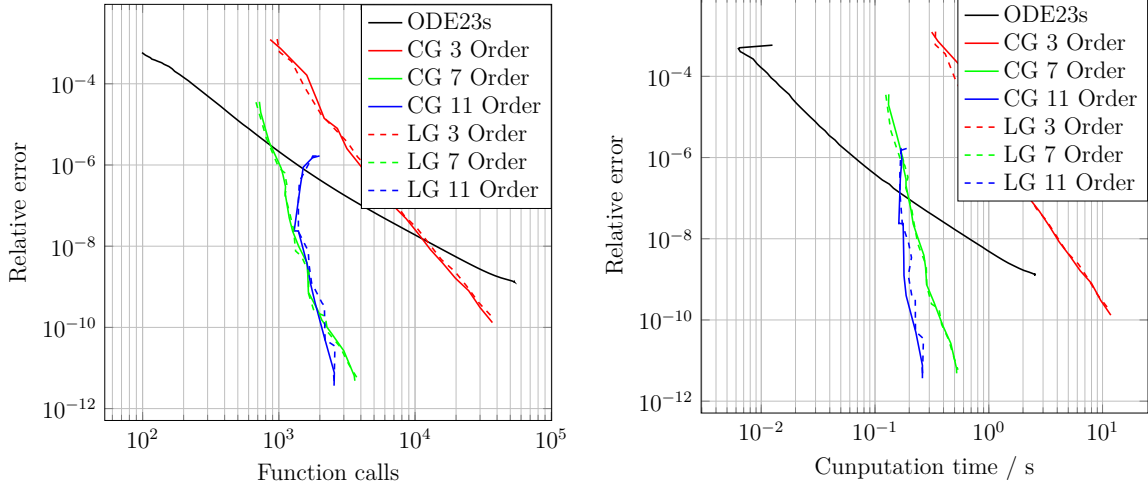
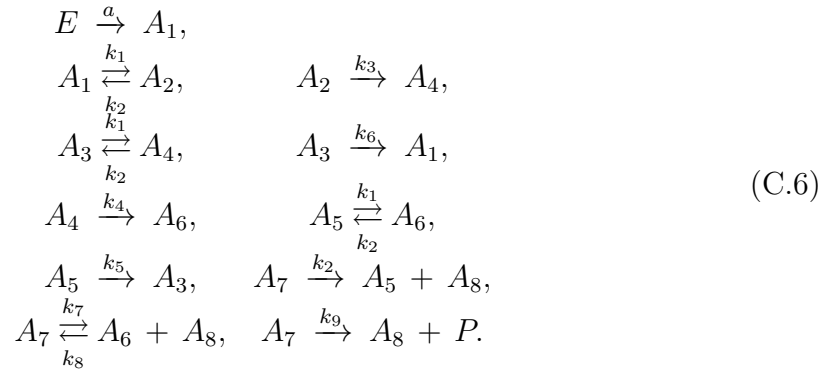


**Figure C.6.:** ODE Solver performance for Reaction of Robertson

### C.3. HIRES

This chemical model was proposed by Schafer in 1975 [Sch75] and refers to “High Irradiance RESponse”. The name HIRES was given by Hairer & Wanner [Hai10]. This chemical system can be described by the following mechanism:



Then, the production rate of the species  $A_1$  from  $E$  is taken constant and the concentration of  $P$  is not considered. As a result the following system of ODE can be derived:

$$\begin{cases}
 \dot{x}_1 = -k_1x_1 + k_2x_2 + k_6x_3 + a, \\
 \dot{x}_2 = k_1x_1 - (k_2 + k_3)x_2, \\
 \dot{x}_3 = -(k_1 + k_6)x_3 + k_2x_4 + k_5x_5, \\
 \dot{x}_4 = k_3x_2 + k_1x_3 - (k_2 + k_4)x_4, \\
 \dot{x}_5 = -(k_1 + k_5)x_5 + k_2x_6 + k_2x_7, \\
 \dot{x}_6 = k_4x_4 + k_1x_5 - k_2x_6 + k_7x_7 - k_8x_6x_8, \\
 \dot{x}_7 = -(k_2 + k_7 + k_9)x_7 + k_8x_6x_8, \\
 \dot{x}_8 = (k_2 + k_7 + k_9)x_7 - k_8x_6x_8.
 \end{cases} \tag{C.7}$$

Here  $x_i$  represents the concentration of the species  $A_i$ . The reaction rates are given:

$$\begin{aligned} a &= 0.0007, k_1 = 1.71, k_2 = 0.43, k_3 = 8.32, k_4 = 0.69, \\ k_5 &= 0.035, k_6 = 8.32, k_7 = 0.69, k_8 = 280, k_9 = 0.69. \end{aligned} \quad (\text{C.8})$$

The initial values were taken  $\vec{x} = (1, 0, 0, 0, 0, 0, 0, 0.0057)^T$ . This model shows a typical behaviour of a realistic chemical system with consumed educts, short living intermediates and emerging products. Moreover, some components shows strong oscillations with frequent zero crossing.

For the ‘‘High Irradiance RESponse’’ problem, the interval  $t \in [0, 10]$  is considered. This problem is more complicated than all previous, not only because it has 8 unknowns, but also because the smallest variables  $x_7$  and  $x_8$  are significantly oscillating. The results (s. fig. C.7) show again that higher order polynomials are suited better. However, there is no noticeable difference between Chebyshev and Legendre Polynomials. It can be also observed here, that high order polynomials are getting very inefficient for low tolerances (low relative errors), as it could be seen in case of the reaction of Robertson. This fact has the same explanation: finding an appropriate interval with the desired low tolerance near a singularity of the solution is a challenging problem. The HIRES was the most difficult problem, of the studied examples, to tackle. It required most CPU efforts and 24 elements to achieve relative accuracy below  $1^{-7}$ .

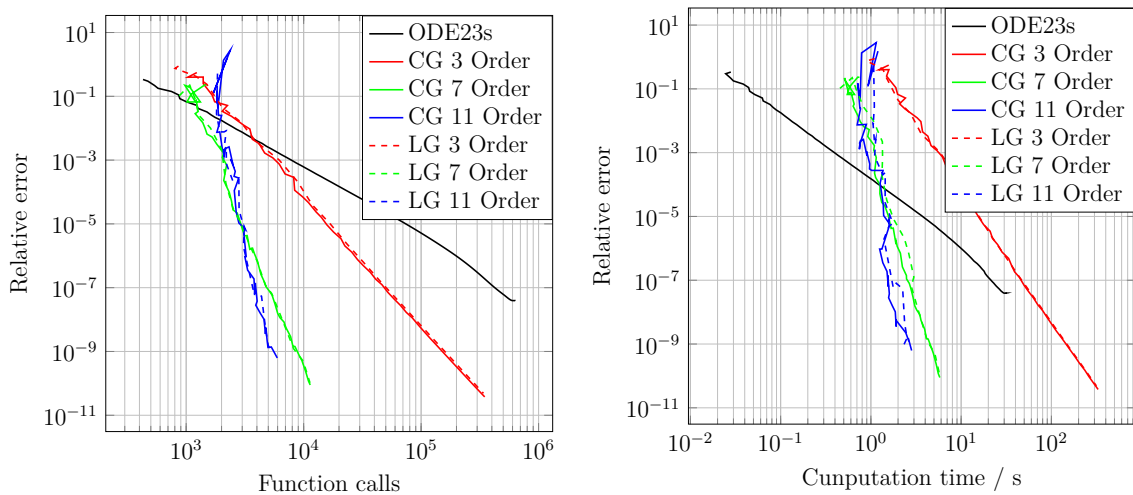


**Figure C.7.:** ODE Solver performance for HIRES

## D. Adaptive pseudo spectral method

Although the main component of the proposed method is the pseudo spectral method [Boy89], the developed framework allows easily to adapt other spectral methods like Galerkin weighted residual method [Boy89]. In order to derive the numerical method, the conservation equation can be rewritten in the following form, with corresponding boundary and initial conditions:

$$\left\{ \begin{array}{ll} \frac{\partial}{\partial t} [\mathbf{f}_t(t, x, \mathbf{u}, \dot{\mathbf{u}})] + \frac{\partial}{\partial x} [\mathbf{f}_x(t, x, \mathbf{u}, \dot{\mathbf{u}})] = \mathbf{q}(t, x, \mathbf{u}, \dot{\mathbf{u}}), & t \in [t_0, T], \quad x \in [x_0, x_\infty] \\ \frac{\partial}{\partial t} [\mathbf{f}_0(t, \mathbf{u}, \dot{\mathbf{u}})] = \mathbf{q}_0(t, x, \mathbf{u}, \dot{\mathbf{u}}), & t \in [t_0, T] \quad x = x_0 \\ \frac{\partial}{\partial t} [\mathbf{f}_\infty(t, \mathbf{u}, \dot{\mathbf{u}})] = \mathbf{q}_\infty(t, x, \mathbf{u}, \dot{\mathbf{u}}), & t \in [t_0, T], \quad x = x_\infty \\ \mathbf{u}(t_0, x) = \mathbf{u}_0(x), & x \in [x_0, x_\infty] \end{array} \right. , \quad (\text{D.1})$$

where  $\mathbf{f}_t, \mathbf{f}_x, \mathbf{q} : \mathbb{R} \times \mathbb{R}^{n_v} \rightarrow \mathbb{R}^{n_v}$  are given vector functions and  $\mathbf{u} \in \mathbb{R}^{n_v}$  is the solution vector. Here for brevity the following notations for partial derivatives over time and space coordinates are used:

$$\dot{(\quad)} = \frac{\partial}{\partial t}(\quad), \quad (\text{D.2})$$

$$\acute{(\quad)} = \frac{\partial}{\partial x}(\quad). \quad (\text{D.3})$$

The solution  $\mathbf{u}$  must be also Lipschitz continuous on the interval  $t \in [t_a, t_b]$  and  $x \in [x_a, x_b]$ , and that on this interval it can be expanded into series without an error:

$$\mathbf{u}(t, x) = \sum_i^N \hat{\mathbf{u}}_i \varphi_i(t, x), \quad (\text{D.4})$$

where  $\hat{\mathbf{u}}_i$  are weights of corresponding basis functions  $\varphi_i(t, x)$ . Please note that the number of basis functions  $N$  can be arbitrary large.

Using a set of test functions  $\psi_i$  a weak formulation can be written:

$$\int_{t_0}^T \int_{x_0}^{x_\infty} \left[ \frac{\partial}{\partial t} (f_t) + \frac{\partial}{\partial x} (f_x) \right] \psi_i dt dx = \int_{t_0}^T \int_{x_0}^{x_\infty} \dot{q} \psi_i dt dx. \quad (\text{D.5})$$

Additionally, it is required that functions  $\mathbf{f}_t, \mathbf{f}_x, \dot{\mathbf{q}}$  to be also expanded into series with the same set of basis functions:

$$\mathbf{f}(t, x) = \sum_i^N \hat{\mathbf{f}}_i \varphi_i(t, x). \quad (\text{D.6})$$

Introducing (D.4) in (D.5) and choosing test functions from the space of Dirac-delta functions  $\psi_i(t, x) = \delta_i(t, x)$ , a discrete form of conservation equations is obtained:

$$\sum_j \hat{\mathbf{f}}_{t,i} \dot{\varphi}_j(t_i, x_i) + \sum_j \hat{\mathbf{f}}_{x,i} \acute{\varphi}_j(t_i, x_i) = \sum_j \hat{\mathbf{q}}_i \varphi_j(t_i, x_i), \quad \forall i = 1, \dots, N_p \quad (\text{D.7})$$

or in a more compact matrix-vector notation:

$$\hat{\mathbf{f}}_t \dot{\Phi} + \hat{\mathbf{f}}_x \acute{\Phi} = \hat{\mathbf{q}} \Phi, \quad (\text{D.8})$$

where  $N_p$  is the number of collocation points (test functions).

Observing that series coefficients connected to the function approximation on the collocation points through a linear operation (see eq. (D.6)):

$$\tilde{\mathbf{f}} = \hat{\mathbf{f}}\Phi, \quad (\text{D.9})$$

where  $\tilde{\mathbf{f}} = (\mathbf{f}(t_1, x_1), \dots, \mathbf{f}(t_{N_p}, x_{N_p}))$  is an approximation of the vector function  $\mathbf{f}$  at the collocation points specified by Dirac-delta functions  $\delta_i$ , and choosing number of basis functions  $N$  equal to the number of collocation points  $N_p$ , the eq. (D.8) can be written in semi-linear form as:

$$\tilde{\mathbf{f}}_t \dot{\mathbf{H}} + \tilde{\mathbf{f}}_x \dot{\mathbf{H}} = \tilde{\mathbf{q}}, \quad (\text{D.10})$$

with

$$\dot{\mathbf{H}} = \Phi^{-1} \dot{\Phi}, \quad (\text{D.11})$$

$$\dot{\mathbf{H}} = \Phi^{-1} \dot{\Phi}. \quad (\text{D.12})$$

The projector matrices  $\dot{\mathbf{H}}$  and  $\dot{\mathbf{H}}$  depend only on the polynomial type and collocation points and therefore are computed in advance. As the solution approximation is sought on the same set of collocation points, it is valid:

$$\tilde{\mathbf{u}} = \tilde{\mathbf{u}} \dot{\mathbf{H}} \quad (\text{D.13})$$

and thus, the approximations  $\tilde{\mathbf{f}}_t$ ,  $\tilde{\mathbf{f}}_x$  and  $\tilde{\mathbf{q}}$  depend on only the solution approximation  $\tilde{\mathbf{u}}$  at these locations:

$$\begin{aligned} \tilde{\mathbf{f}}_t &= \tilde{\mathbf{f}}_t(\tilde{\mathbf{u}}) \\ \tilde{\mathbf{f}}_x &= \tilde{\mathbf{f}}_x(\tilde{\mathbf{u}}) \\ \tilde{\mathbf{q}} &= \tilde{\mathbf{q}}(\tilde{\mathbf{u}}) \end{aligned} \quad (\text{D.14})$$

The quasi-linear system (D.10) is a non-linear algebraic equation, which is solved implicitly with modified Newton method (see fig. 3.4). The essence of the method is that the eq. (D.10) is linearised at the current solution estimate  $\tilde{\mathbf{u}}^0$  and a better approximation is sought along the gradient:

$$R_0 + \mathbf{J} \Delta \tilde{\mathbf{u}} = 0, \quad (\text{D.15})$$

where

$$R_0 = \tilde{\mathbf{f}}_t \dot{\mathbf{H}} + \tilde{\mathbf{f}}_x \dot{\mathbf{H}} - \tilde{\mathbf{q}} \quad (\text{D.16})$$

is residual for current solution estimate and

$$\mathbf{J} = \frac{\partial R}{\partial \mathbf{u}} \quad (\text{D.17})$$

is the Jacobian of the residual. In order to explain the construction of the Jacobian, the data structure of solution is introduced:

$$\mathbf{u}_{j,i}, \quad (\text{D.18})$$

here  $j$  is the index of the space coordinate and  $i$  is the index of the time coordinate. Each space-time cell  $j, i$  contains a vector of  $n_v$  state variables. The solution can be casted into a single vector:

$$\mathbf{u}_l = \mathbf{u}_{j,i}, \quad (\text{D.19})$$

where the global index is then defined as:

$$l = j + n_x i, \quad (\text{D.20})$$

with  $n_x$  is the number of collocation points along the space coordinate. The analytical global Jacobian can be constructed from the known local Jacobians of  $\mathbf{f}_t$ ,  $\mathbf{f}_x$  and  $\mathbf{q}$ :

$$\begin{aligned} J_{ij} = & \dot{H}_{ij} \left( \frac{\partial \mathbf{f}_t}{\partial \mathbf{u}} \right)_j + \dot{H}_{ij} \left( \frac{\partial \mathbf{f}_x}{\partial \mathbf{u}} \right)_j + \delta_{ij} \left( \frac{\partial \mathbf{q}}{\partial \mathbf{u}} \right)_j \\ & + \sum_k \dot{H}_{ik} \dot{H}_{kj} \left( \frac{\partial \mathbf{f}_t}{\partial \mathbf{u}} \right)_k + \sum_k \dot{H}_{ik} \dot{H}_{kj} \left( \frac{\partial \mathbf{f}_x}{\partial \mathbf{u}} \right)_k + \dot{H}_{ij} \left( \frac{\partial \mathbf{q}}{\partial \mathbf{u}} \right)_i, \end{aligned} \quad (\text{D.21})$$

here  $J_{ij}$  is a cell with the size  $n_v \times n_v$  in the global Jacobian.

### D.1. Domain matching and boundary conditions

As the global spectral approximation of stiff system tend to be unstable, it is better to split the time-space domain into a number of subdomains:

$$t_0 < \dots < t_k < \dots < T, \quad k = 1, 2, \dots, (N_t - 1), \quad (\text{D.22})$$

$$x_0 < \dots < x_l < \dots < x_\infty, \quad l = 1, 2, \dots, (N_x - 1). \quad (\text{D.23})$$

Then the solution in time is being sought one time-interval after the other: the initial condition  $\mathbf{u}(t_k)$  on the interval  $t \in [t_k, t_{k+1}]$  is provided from the solution of the previous interval  $t \in [t_{k-1}, t_k]$ . This corresponds to an implicit Runge-Kutta method (see §3.3).

The subdomains in space are matched with the following boundary conditions:

$$\begin{cases} \mathbf{u}^l(t, x_{l-1}) = \mathbf{u}^{l-1}(t, x_{l-1}) \\ \mathbf{u}^l(t, x_l) = \mathbf{u}^{l+1}(t, x_l) \\ \frac{\partial}{\partial x} \mathbf{u}^l(t, x_{l-1}) = \frac{\partial}{\partial x} \mathbf{u}^{l-1}(t, x_{l-1}) \\ \frac{\partial}{\partial x} \mathbf{u}^l(t, x_l) = \frac{\partial}{\partial x} \mathbf{u}^{l+1}(t, x_l), \end{cases} \quad (\text{D.24})$$

where  $\mathbf{u}^l$  is solution within domain  $l$ .

One collocation point is placed exactly at the boundary. The evolution of the point  $l$  is govern by the equality of gradients in the adjacent regions:

$$\begin{cases} \frac{\partial}{\partial t} [\mathbf{f}_0(t, \mathbf{u}^1)] = \mathbf{q}_0(t, \mathbf{u}^1, \dot{\mathbf{u}}^1), & x = x_0, \\ \frac{\partial}{\partial x} \mathbf{u}^l(t, x_l) = \frac{\partial}{\partial x} \mathbf{u}^{l+1}(t, x_l), & \forall l = 1, 3, \dots, N_x - 1, \\ \frac{\partial}{\partial t} [\mathbf{f}_\infty(t, \mathbf{u}^{N_x})] = \mathbf{q}_\infty(t, \mathbf{u}^{N_x}, \dot{\mathbf{u}}^{N_x}), & x = x_\infty. \end{cases} \quad (\text{D.25})$$

Using the same spectral approximation eq. (D.4) and eq. (D.6) the boundary conditions can be rewritten into an algebraic equation:

$$\begin{cases} \tilde{\mathbf{f}}_0 \dot{H}_a^1 = \tilde{\mathbf{q}}_0 \\ \tilde{\mathbf{u}}^l \dot{H}_b^l = \tilde{\mathbf{u}}^{l+1} \dot{H}_a^{l+1} \\ \tilde{\mathbf{f}}_\infty \dot{H}_b^{N_x} = \tilde{\mathbf{q}}_\infty \end{cases}, \quad (\text{D.26})$$

here  $\dot{H}_a^l$  and  $\dot{H}_b^l$  are linear operators for time derivative at the left boundary of the element  $l$ :

$$\begin{aligned} \dot{H}_a^l &= \Phi_l^{-1} \dot{\Phi}_l^a, \\ \dot{H}_b^l &= \Phi_l^{-1} \dot{\Phi}_l^b, \end{aligned} \quad (\text{D.27})$$

where each element of matrices  $\dot{\Phi}_l^a$  and  $\dot{\Phi}_l^b$  is defined as:

$$\begin{aligned} (\dot{\Phi}_l^a)_{ij} &= \dot{\varphi}_i^l(t_j^l, x_0^l), \\ (\dot{\Phi}_l^b)_{ij} &= \dot{\varphi}_i^l(t_j^l, x_{n_x}^l). \end{aligned} \quad (\text{D.28})$$

Similarly,  $\dot{H}_a^l$  and  $\dot{H}_b^l$  are linear operators for space derivative at the boundaries:

$$\begin{aligned} \dot{H}_l^a &= \Phi_l^{-1} \dot{\Phi}_l^a, \\ \dot{H}_l^b &= \Phi_l^{-1} \dot{\Phi}_l^b, \end{aligned} \quad (\text{D.29})$$

where each element of matrices  $\dot{\Phi}_l^a$  and  $\dot{\Phi}_l^b$  is defined as:

$$\begin{aligned} (\dot{\Phi}_l^a)_{ij} &= \dot{\varphi}_i^l(t_j^l, x_0^l), \\ (\dot{\Phi}_l^b)_{ij} &= \dot{\varphi}_i^l(t_j^l, x_{n_x}^l). \end{aligned} \quad (\text{D.30})$$

After linearisation the global system takes the block diagonal form shown in fig. D.8. It is important to note here, that space and time order, as well as the space width of each element can be different.

## D.2. Solution of the linear system for spectral elements

Imagine a binary tree, which describes splitting of elements (see fig. D.9). The element points  $\mathbf{u}_1$ ,  $\mathbf{u}_3$ ,  $\mathbf{u}_5$ ,  $\mathbf{u}_7$  and  $\mathbf{u}_9$  are governed by algebraic eq. (D.10) and boundary points  $\mathbf{u}_0$ ,  $\mathbf{u}_2$ ,  $\mathbf{u}_4$ ,  $\mathbf{u}_6$ ,  $\mathbf{u}_8$  and  $\mathbf{u}_{10}$  are described by the expression (D.26). The structure of the linear system has a block diagonal form (fig. D.8). The tree is created such, that the element ‘‘R’’ is split into elements ‘‘R0’’ and ‘‘R1’’, which creates a virtual boundary  $\mathbf{u}_6^B$ , where equality of gradients from left and right to the boundary are imposed. Each element (node) is split up further till elements ‘‘R00’’, ‘‘R010’’, ‘‘R011’’, ‘‘R10’’ and ‘‘R11’’, and virtual boundaries  $\mathbf{u}_2$ ,  $\mathbf{u}_4$ ,  $\mathbf{u}_6$  and  $\mathbf{u}_8$  are created. The boundaries  $\mathbf{u}_0$  and  $\mathbf{u}_{10}$  correspond to physical boundary conditions. For the solution of the global linear system a modified Gauss elimination is applied. Elements and virtual boundaries, both described as nodes in the binary tree, are eliminated upwards starting from the bottom level of the tree. In order to illustrate this, consider first the element ‘‘R011’’, corresponding to  $\mathbf{u}_5$ . The structure of the linear system for that element is shown in fig. D.13. Empty cells in the diagram represents zero submatrices in the system. The residual  $R_5$  for inner element points depend only on values at these points  $\mathbf{u}_5$  and boundary points  $\mathbf{u}_4$  and  $\mathbf{u}_6$ . The residual at the boundary points however, is a linear combination of the adjacent elements and boundaries, i.e. the residual of the boundary point  $\mathbf{u}_4$  depend on the element values  $\mathbf{u}_3$ ,  $\mathbf{u}_5$  and boundaries  $\mathbf{u}_2$ ,  $\mathbf{u}_6^B$ . After the elimination of the entries of matrix corresponding to ‘‘R011’’ the structure shown in fig. D.14 is achieved, where  $I$  is identity matrix and

$$\left\{ \begin{array}{l} J'_{5,4} = J_{5,5}^{-1} J_{5,4}, \\ J'_{5,6} = J_{5,5}^{-1} J_{5,6}, \\ J'_{4,4} = J_{4,4} - J_{4,5} J'_{5,4} - J_{4,3} J'_{3,4}, \\ J'_{4,6} = J_{4,6} - J_{4,5} J'_{5,6}, \\ J'_{6,4} = J_{6,4} - J_{6,5} J'_{5,4}, \\ J'_{6,6} = J_{6,6} - J_{6,5} J'_{5,6}, \\ R'_5 = J_{5,5}^{-1} R_5, \\ R'_4 = R_4 - J_{4,5} R'_5 - J_{4,3} R'_3. R'_6 = R_6 - J_{6,5} R'_5. \end{array} \right. \quad (\text{D.31})$$

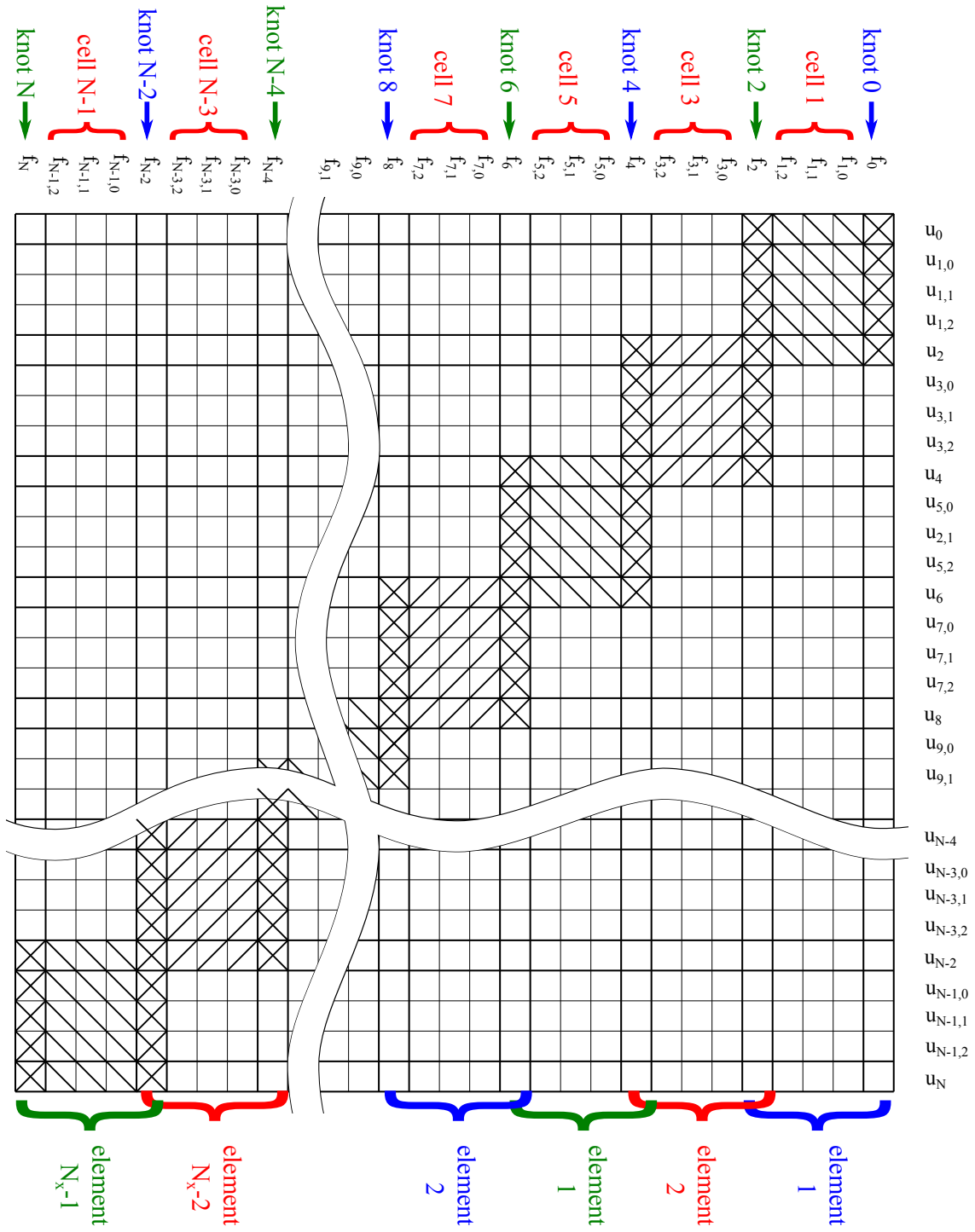


Figure D.8.: Structure of the Jacobian of the global spectral element system.

In a similar fashion, the linear system is constructed for element “R010”, which is shown in fig. D.11. The identical elimination procedure leads also to the similar structure as in case of “R010” (compare figs. D.12 and D.14). The elements are:

$$\left\{ \begin{array}{l} J'_{3,2} = J_{3,3}^{-1} J_{3,2}, \\ J'_{3,4} = J_{3,3}^{-1} J_{3,4}, \\ J'_{2,2} = J_{2,2} - J_{2,3} J'_{3,2}, \\ J'_{2,4} = J_{2,4} - J_{2,3} J'_{3,4}, \\ J'_{4,2} = J_{4,2} - J_{4,3} J'_{3,2}, \\ J'_{4,4} = J_{4,4} - J_{4,3} J'_{3,4} - J_{4,5} J'_{5,4}, \\ R'_3 = J_{3,3}^{-1} R_3, \\ R'_2 = R_2 - J_{2,3} R'_3, \\ R'_4 = R_4 - J_{4,3} R'_3 - J_{4,5} R'_5. \end{array} \right. \quad (\text{D.32})$$

Next, the data of the node “R01” corresponding  $\mathbf{u}_4$  can be eliminated. The data structure of this node after elimination of “R010” ( $\mathbf{u}_3$ ) and “R011” ( $\mathbf{u}_5$ ) is shown in fig. D.15 (left), where:

$$\left\{ \begin{array}{l} J'_{4,4} = J_{4,4} - D_{4,4}^3 - D_{4,4}^5, \\ J'_{4,2} = J_{4,2} - D_{4,2}^3, \\ J'_{4,6} = J_{4,6} - D_{4,6}^5, \\ J'_{2,4} = J_{2,4} - D_{2,4}^3, \\ J'_{2,2} = J_{2,2} - D_{2,2}^3, \\ J'_{6,4} = J_{6,4} - D_{6,4}^5, \\ J'_{6,6} = J_{6,6} - D_{6,6}^5, \\ R'_4 = R_4 - C_4^3 - C_4^5, \\ R'_2 = R_2 - C_2^3, \\ R'_6 = R_6 - C_6^5. \end{array} \right. \quad (\text{D.33})$$

Please note that  $J'_{4,4}$  and  $R'_4$  of node “R01” depend both on both child elements “R010” and “R011”. The elimination of the child elements can be done nonetheless independently. The information is provided to the upper level in form of Jacobian and residual updates, i.e. from element “R011”:

$$\left\{ \begin{array}{l} D_{4,4}^5 = J_{4,5} J'_{5,4} = J_{4,5} J_{5,5}^{-1} J_{5,4}, \\ D_{4,6}^5 = J_{4,5} J'_{5,6} = J_{4,5} J_{5,5}^{-1} J_{5,6}, \\ D_{6,4}^5 = J_{6,5} J'_{5,4} = J_{6,5} J_{5,5}^{-1} J_{5,4}, \\ D_{6,6}^5 = J_{6,5} J'_{5,6} = J_{6,5} J_{5,5}^{-1} J_{5,6}, \\ C_4^5 = J_{4,5} R'_5 = J_{4,5} J_{5,5}^{-1} R_5, \\ C_6^5 = J_{6,5} R'_5 = J_{6,5} J_{5,5}^{-1} R_5; \end{array} \right. \quad (\text{D.34})$$

and from element “R010”:

$$\left\{ \begin{array}{l} D_{4,4}^3 = J_{4,3} J'_{3,4} = J_{4,3} J_{3,3}^{-1} J_{3,4}, \\ D_{4,2}^3 = J_{4,3} J'_{3,2} = J_{4,3} J_{3,3}^{-1} J_{3,2}, \\ D_{2,4}^3 = J_{2,3} J'_{3,4} = J_{2,3} J_{3,3}^{-1} J_{3,4}, \\ D_{2,2}^3 = J_{2,3} J'_{3,2} = J_{2,3} J_{3,3}^{-1} J_{3,2}, \\ C_4^3 = J_{4,3} R'_3 = J_{4,3} J_{3,3}^{-1} R_3, \\ C_2^3 = J_{6,3} R'_3 = J_{6,3} J_{3,3}^{-1} R_3. \end{array} \right. \quad (\text{D.35})$$

The elimination of node “R01” is identical to the previous steps. The result is shown

in fig. D.15 (right), where:

$$\left\{ \begin{array}{l} J''_{4,2} = J'^{-1}_{4,4} J'_{4,2}, \\ J''_{4,6} = J'^{-1}_{4,4} J'_{4,6}, \\ J''_{2,2} = J'_{2,2} - J'_{2,4} J''_{4,2}, \\ J''_{2,6} = J'_{2,6} - J'_{2,4} J''_{4,6}, \\ J''_{6,2} = -J'_{6,4} J''_{4,2}, \\ J''_{6,6} = J'_{6,6} - J'_{6,4} J''_{4,6}, \\ R''_4 = J'^{-1}_{4,4} R_4, \\ R''_2 = R'_2 - J'_{2,4} R''_4, \\ R''_6 = R'_6 - J'_{7,4} R''_4. \end{array} \right. \quad (\text{D.36})$$

Thus, the following quantities are provided to the upper level “R0” from the node “R01”:

$$\left\{ \begin{array}{l} D^4_{2,2} = J'_{2,4} J''_{4,2} = (J_{2,4} - D^3_{2,4}) (J_{4,4} - D^3_{4,4} - D^5_{4,4})^{-1} (J_{4,2} - D^3_{4,2}), \\ D^4_{2,6} = J'_{2,4} J''_{4,6} = (J_{2,4} - D^3_{2,4}) (J_{4,4} - D^3_{4,4} - D^5_{4,4})^{-1} (J_{4,6} - D^5_{4,6}), \\ D^4_{6,2} = J'_{6,4} J''_{4,2} = (J_{6,4} - D^5_{6,4}) (J_{4,4} - D^3_{4,4} - D^5_{4,4})^{-1} (J_{4,2} - D^3_{4,2}), \\ D^4_{6,6} = J'_{6,4} J''_{4,6} = (J_{6,4} - D^5_{6,4}) (J_{4,4} - D^3_{4,4} - D^5_{4,4})^{-1} (J_{4,6} - D^5_{4,6}), \\ C^4_2 = J'_{2,4} R''_4 = (J_{2,4} - D^3_{2,4}) (J_{4,4} - D^3_{4,4} - D^5_{4,4})^{-1} (R_4 - C^3_4 - C^5_4), \\ C^4_6 = J'_{6,4} R''_4 = (J_{6,4} - D^5_{6,4}) (J_{4,4} - D^3_{4,4} - D^5_{4,4})^{-1} (R_4 - C^3_4 - C^5_4). \end{array} \right. \quad (\text{D.37})$$

After parallel elimination of “R00” the following is also submitted to the level of “R0”:

$$\left\{ \begin{array}{l} D^1_{0,0} = J_{0,1} J'_{1,0} = J_{0,1} J^{-1}_{1,1} J_{1,0}, \\ D^1_{0,2} = J_{0,1} J'_{1,2} = J_{0,1} J^{-1}_{1,1} J_{1,2}, \\ D^1_{2,0} = J_{2,1} J'_{1,0} = J_{2,1} J^{-1}_{1,1} J_{1,0}, \\ D^1_{2,2} = J_{2,1} J'_{1,2} = J_{2,1} J^{-1}_{1,1} J_{1,2}, \\ C^1_0 = J_{0,1} R'_1 = J_{0,1} J^{-1}_{1,1} R_1, \\ C^1_2 = J_{2,1} R'_1 = J_{2,1} J^{-1}_{1,1} R_1. \end{array} \right. \quad (\text{D.38})$$

The elimination process continues up the tree till the root node “R” ( $\mathbf{u}_6$ ) is eliminated. The linear system for root node looks then so:

$$\left( \begin{array}{ccc} J_{6,6} - D^2_{6,6} - D^8_{6,6} & -D^2_{6,0} & -D^8_{6,10} \\ -D^2_{0,6} & J_{0,0} - D^2_{0,0} & 0 \\ -D^8_{10,6} & 0 & J_{10,10} - D^8_{10,10} \end{array} \right) \left( \begin{array}{c} \Delta \mathbf{u}_6 \\ \Delta \mathbf{u}_0 \\ \Delta \mathbf{u}_{10} \end{array} \right) = \left( \begin{array}{c} R_6 - C^2_6 - C^8_6 \\ R_0 - C^2_0 \\ R_{10} - C^8_{10} \end{array} \right) \quad (\text{D.39})$$

with  $D$  and  $C$  propagated from the lower level, i.e. “R0” ( $\mathbf{u}_2$ ) and “R1” ( $\mathbf{u}_8$ ). Finally, eliminating the data corresponding to node “R” ( $\mathbf{u}_6$ ) the linear system for system boundaries is generated:

$$\left( \begin{array}{cc} J_{0,0} - D^6_{0,0} & -D^6_{0,10} \\ -D^6_{10,0} & J_{10,10} - D^6_{10,10} \end{array} \right) \left( \begin{array}{c} \Delta \mathbf{u}_0 \\ \Delta \mathbf{u}_{10} \end{array} \right) = \left( \begin{array}{c} R_0 - C^6_0 \\ R_{10} - C^6_{10} \end{array} \right). \quad (\text{D.40})$$

Resolving the system eq. (D.40) results in increment of one Newton iteration for boundary values  $\Delta \mathbf{u}_0$  and  $\Delta \mathbf{u}_{10}$ . Which in turn are propagated down the tree in order to get increments of other nodes and elements. The update of top node “R” is:

$$\Delta \mathbf{u}_6 = (J_{6,6} - D^2_{6,6} - D^8_{6,6})^{-1} (R_6 - C^2_6 - C^8_6 + D^2_{6,0} \Delta \mathbf{u}_0 + D^8_{6,10} \Delta \mathbf{u}_{10}). \quad (\text{D.41})$$

Please note that product of matrix inverse of  $(J_{6,6} - D_{6,6}^2 - D_{6,6}^8)$  with residual  $(R_6 - C_6^2 - C_6^8)$ ,  $D_{6,0}^2$  and  $D_{6,10}^8$  is already computed during upward elimination of the node.

The update of lower nodes is similar. Here, the update of previously discussed nodes  $R0$  ( $\Delta \mathbf{u}_2$ ),  $R01$  ( $\Delta \mathbf{u}_4$ ),  $R010$  ( $\Delta \mathbf{u}_3$ ) and  $R011$  ( $\Delta \mathbf{u}_5$ ) is only shown:

$$\begin{aligned}\Delta \mathbf{u}_2 &= (J_{2,2} - D_{2,2}^1 - D_{2,2}^4)^{-1} (R_2 - C_2^1 - C_2^4 + D_{2,0}^1 \Delta \mathbf{u}_0 + D_{2,6}^4 \Delta \mathbf{u}_6), \\ \Delta \mathbf{u}_1 &= (J_{1,1})^{-1} (R_1 - J_{1,0} \Delta \mathbf{u}_0 - J_{1,2} \Delta \mathbf{u}_2), \\ \Delta \mathbf{u}_4 &= (J_{4,4} - D_{4,4}^3 - D_{4,4}^5)^{-1} (R_4 - C_4^3 - C_4^5 + D_{4,2}^3 \Delta \mathbf{u}_2 + D_{4,6}^5 \Delta \mathbf{u}_6), \\ \Delta \mathbf{u}_3 &= (J_{3,3})^{-1} (R_3 - J_{3,2} \Delta \mathbf{u}_2 - J_{3,4} \Delta \mathbf{u}_4), \\ \Delta \mathbf{u}_5 &= (J_{5,5})^{-1} (R_5 - J_{5,4} \Delta \mathbf{u}_4 - J_{5,6} \Delta \mathbf{u}_6).\end{aligned}\tag{D.42}$$

The total solution process of the linear system corresponding spectral element method is displayed in fig. D.10. Starting from bottom level, the information is propagated up the tree (matrices  $C$  and  $D$ ) and after complete elimination of inner points, the update information about values increment (vectors  $\Delta \mathbf{u}_i$ ) is propagated down the tree. The process can be illustrated with a series of global matrices (see figs. D.16 through D.18). Firstly, the element points  $l = 1, 3, \dots, 9$  (fig. D.16) are eliminated, then the first level of nodes  $l = 4, 8$  (fig. D.17 (left)) is eliminated. After that the process follows to the node  $l = 2$  (fig. D.17 (right)), then last node  $l = 8$  can be processed (fig. D.18 (left)) and finally the system for global boundaries  $l = 0$  and  $l = 10$  can be resolved (fig. D.18 (right)). The process is repeated backwards propagating the increments of the boundaries  $\Delta \mathbf{u}^l$ .

Although global matrices are presented for explanation (fig. D.8 and fig. D.16), the method does not require a global storage. Each node (element) must contain only local information and must be aware only of its children (left and right). This allows the following advantages compared to classical Gauss elimination (see e.g. [QSS00]):

1. Independent elimination of nodes (elements). Most nodes (elements) are processed independently. It permits extensive parallelisation of process. Only the top most step, i.e. elimination of node "R" and of global boundaries must be performed in the main thread. In the latter case the matrix that is to be inverted is of size  $2n_v \times 2n_v$ , where  $n_v$  is number of state variables, like velocity, temperature, density and so on.
2. Partial Jacobian updates. Iterative solution of semi-linear system eq. (D.10) and (D.26) doesn't require an exact Jacobian. Mostly, the Jacobian is kept constant for several iterations and even time step. The independent elimination of nodes allows to update matrix-inverses (LU-Decomposition) only of a part of the system. The bottom-up part of the algorithm can be skipped for elements, where the change is marginal and only the nodes with significant change undergo expensive bottom-up elimination.
3. Hierarchical system allows to stop Newtonian iterations for a part of the system earlier. For example if a part of computational domain has experience fast change and the other only slow, the slow part will require much less Newtonian iterations to converge.

4. Dynamical linear system. The absence of global Jacobian allows to change the order within one element or split/join nodes without changing other parts of the system. It opens a pathway to dynamical grid and order adaptation.

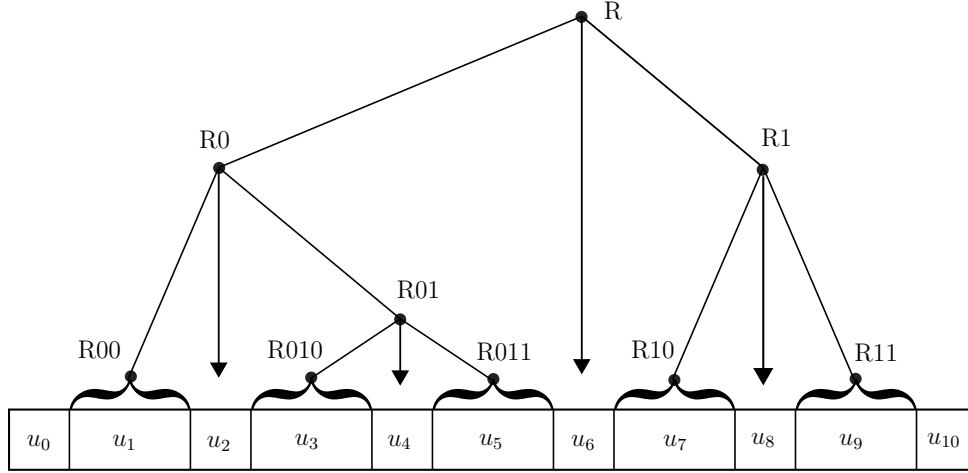


**Figure D.9.:** Information hierarchy (binary tree).

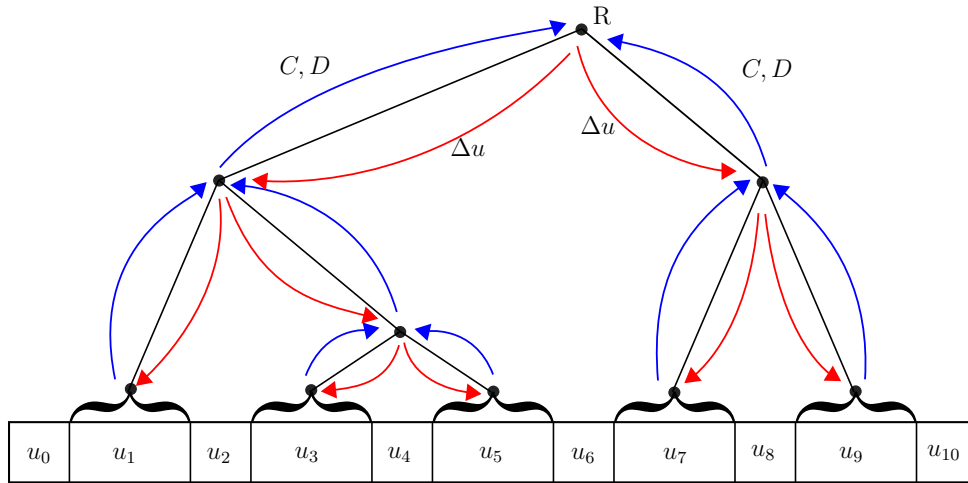


**Figure D.10.:** Information flow in binary tree.

### D.3. Implementation of adaptive pseudo spectral method

The general formulation adaptive pseudo spectral method (APSM), as described above, is applicable for variable time and space order within elements. For illustration reasons, the discussion is limited to second order Crank-Nicolson method (CNM) [QSS00], which allows to use spectral approximation only for space. A more general application with variable time orders is described in §3.3.

With CNM the general conservation equation in 1D, eq. (3.28), is discretised in time as:

$$\mathbf{f}_{t_{k+1}} - \mathbf{f}_{t_k} \approx \frac{\Delta t}{2} \left[ \mathbf{q}_{k+1} + \mathbf{q}_k - \frac{\partial}{\partial x} (\mathbf{f}_{x_{k+1}} + \mathbf{f}_{x_k}) \right], \quad (\text{D.43})$$





	$\Delta u_0$	$\Delta u_1$	$\Delta u_2$	$\Delta u_3$	$\Delta u_4$	$\Delta u_5$	$\Delta u_6$	$\Delta u_7$	$\Delta u_8$	$\Delta u_9$	$\Delta u_{10}$
$\Delta R_0$	$J'_{0,0}$		$J'_{0,1}$								
$\Delta R_1$	$J'_{1,0}$	$I$	$J'_{1,2}$								
$\Delta R_2$	$J'_{2,0}$		$J'_{2,2}$		$J'_{2,4}$						
$\Delta R_3$			$J'_{3,2}$	$I$	$J'_{3,4}$						
$\Delta R_4$			$J'_{4,2}$		$J'_{4,4}$		$J'_{4,6}$				
$\Delta R_5$					$J'_{5,4}$	$I$	$J'_{5,6}$				
$\Delta R_6$					$J'_{6,4}$		$J'_{6,6}$		$J'_{6,8}$		
$\Delta R_7$							$J'_{7,6}$	$I$	$J'_{7,8}$		
$\Delta R_8$							$J'_{8,6}$		$J'_{8,8}$		$J'_{8,10}$
$\Delta R_9$									$J'_{9,8}$	$I$	$J'_{9,10}$
$\Delta R_{10}$									$J'_{10,8}$		$J'_{10,10}$

**Figure D.16.:** Structure of global Jacobian before elimination. Red lines show the parts being eliminated.

	$\Delta u_0$	$\Delta u_2$	$\Delta u_4$	$\Delta u_6$	$\Delta u_8$	$\Delta u_{10}$
$\Delta R_0$	$J'_{0,0}$	$J'_{0,2}$				
$\Delta R_2$	$J'_{2,0}$	$J'_{2,2}$	$J'_{2,4}$			
$\Delta R_4$		$J'_{4,2}$	$J'_{4,4}$	$J'_{4,6}$		
$\Delta R_6$			$J'_{6,4}$	$J'_{6,6}$	$J'_{6,8}$	
$\Delta R_8$				$J'_{8,6}$	$J'_{8,8}$	$J'_{8,10}$
$\Delta R_{10}$					$J'_{10,8}$	$J'_{10,10}$

	$\Delta u_0$	$\Delta u_2$	$\Delta u_6$	$\Delta u_{10}$
$\Delta R_0$	$J''_{0,0}$	$J''_{0,2}$		
$\Delta R_2$	$J''_{2,0}$	$J''_{2,2}$	$J''_{2,6}$	
$\Delta R_6$		$J''_{6,2}$	$J''_{6,6}$	$J''_{6,10}$
$\Delta R_{10}$			$J''_{10,6}$	$J''_{10,10}$

**Figure D.17.:** Structure of global Jacobian after 1 (left) and 2 (right) step of elimination.

	$\Delta u_0$	$\Delta u_6$	$\Delta u_{10}$	
$\Delta R_0$	$J''_{0,0}$	$J'''_{0,6}$		
$\Delta R_6$	$J''_{6,0}$	$J''_{6,6}$	$J'''_{6,10}$	
$\Delta R_{10}$		$J'_{10,6}$	$J''_{10,10}$	

	$\Delta u_0$	$\Delta u_{10}$
$\Delta R_0$	$J''''_{0,0}$	$J''''_{0,10}$
$\Delta R_{10}$	$J''''_{10,0}$	$J''''_{10,10}$

**Figure D.18.:** Structure of global Jacobian after 3 (left) and 4 (right) step of elimination.

where subscript  $k$  indicates time step and

$$\begin{aligned} \mathbf{f}_{t_k} &= \mathbf{f}_t(t_k, x, \mathbf{u}_k, \frac{\partial}{\partial x} \mathbf{u}_k), \\ \mathbf{f}_{x_k} &= \mathbf{f}_x(t_k, x, \mathbf{u}_k, \frac{\partial}{\partial x} \mathbf{u}_k), \\ \mathbf{q}_k &= \mathbf{q}(t_k, x, \mathbf{u}_k, \frac{\partial}{\partial x} \mathbf{u}_k) \end{aligned} \quad (\text{D.44})$$

and

$$\mathbf{u}_k = \mathbf{u}(t_k, x). \quad (\text{D.45})$$

An approximation for time step  $k$  for the element  $l$ ,  $x \in [x_0^l, x_{N_p+1}^l]$  with a weighted sum basis functions is sought as

$$\tilde{\mathbf{U}}_k^l = \hat{\mathbf{U}}_k^l \Phi, \quad (\text{D.46})$$

where

$$\tilde{\mathbf{u}}_k^l = \left( \tilde{\mathbf{u}}(t_k, x_0^l), \tilde{\mathbf{u}}(t_k, x_1^l), \dots, \tilde{\mathbf{u}}(t_k, x_{N_p}^l) \right), \quad (\text{D.47})$$

is the solution approximation of state variables at each collocation point<sup>1</sup>, the matrix  $\hat{\mathbf{U}}_k^l$  describes weights of basis functions for each state variable and

$$\Phi = \begin{pmatrix} \varphi_0(x_0^l) & \varphi_0(x_1^l) & \cdots & \varphi_0(x_{N_p+1}^l) \\ \varphi_1(x_0^l) & \varphi_1(x_1^l) & \cdots & \varphi_1(x_{N_p+1}^l) \\ \vdots & \vdots & \ddots & \vdots \\ \varphi_{N_p+1}(x_0^l) & \varphi_{N_p+1}(x_1^l) & \cdots & \varphi_{N_p+1}(x_{N_p+1}^l) \end{pmatrix} \quad (\text{D.48})$$

is projector matrix, which transforms the solution from spectral to physical space of collocation points  $\mathbf{x}^l = (x_0^l, x_1^l, \dots, x_{N_p+1}^l)$ . Please note that the boundary points  $x_0^l = x^{l-1}$  and  $x_{N_p+1}^l = x^{l+1}$  belong to adjacent nodes  $l-1$  and  $l+1$ .

Typical basis function are well defined on a specific interval, e.g. Chebyshev polynomials and Legendre polynomials on  $[-1, +1]$  or Fourier series on  $[-\pi/2, +\pi/2]$ . Outside of the interval polynomials may swing up. In order to work inside of the well defined interval, a linear transformation (scaling) is introduced:

$$\xi = \frac{\Delta x^l}{\Delta \xi} (x - x_0^l) + \xi_0, \quad (\text{D.49})$$

<sup>1</sup>e.g. for state variables  $v, \rho, T$  (flow velocity, density and temperature) the solution approximation

matrix takes form: 
$$\tilde{\mathbf{U}}_k^l = \begin{pmatrix} v(t_k, x_0^l) & v(t_k, x_1^l) & \dots & v(t_k, x_{N_p+1}^l) \\ \rho(t_k, x_0^l) & \rho(t_k, x_1^l) & \dots & \rho(t_k, x_{N_p+1}^l) \\ T(t_k, x_0^l) & T(t_k, x_1^l) & \dots & T(t_k, x_{N_p+1}^l) \end{pmatrix}$$

where  $\Delta x^l = x_{N_p+1}^l - x_0^l$  is the physical length of the element  $l$  and  $\Delta \xi$  is fixed length of the interval of space of polynomial approximation, e.g.  $\Delta \xi = 2$  – for Chebyshev and Legendre polynomials, and  $\Delta \xi = \pi$  – for Fourier series. A proper definition of the projector matrix in local coordinates:

$$\Phi = \begin{pmatrix} \varphi_0(\xi_0) & \varphi_0(\xi_1) & \cdots & \varphi_0(\xi_{N_p+1}) \\ \varphi_1(\xi_0) & \varphi_1(\xi_1) & \cdots & \varphi_1(\xi_{N_p+1}) \\ \vdots & \vdots & \ddots & \vdots \\ \varphi_{N_p+1}(\xi_0) & \varphi_{N_p+1}(\xi_1) & \cdots & \varphi_{N_p+1}(\xi_{N_p+1}) \end{pmatrix} \quad (\text{D.50})$$

The derivative in physical space  $x$  and in virtual space  $\xi$  are related as:

$$\frac{\partial}{\partial x} f = \frac{\partial \xi}{\partial x} \frac{\partial}{\partial \xi} f. \quad (\text{D.51})$$

Due to the fact that the transformation is linear, it is valid:

$$\frac{\partial \xi}{\partial x} = \frac{\Delta \xi}{\Delta x^l}. \quad (\text{D.52})$$

This allows to define first derivative as a linear combination of function values at collocation points (compare eq. (D.13)):

$$\frac{\partial}{\partial x} (\tilde{U}_k^l) = \frac{\Delta \xi}{\Delta x^l} \tilde{U}_k^l \mathbf{H}, \quad (\text{D.53})$$

with

$$\mathbf{H} = \Phi^{-1} \frac{\partial}{\partial \xi} \Phi, \quad (\text{D.54})$$

and

$$\frac{\partial}{\partial \xi} \Phi = \begin{pmatrix} \frac{\partial}{\partial \xi} \varphi_0(\xi_0) & \frac{\partial}{\partial \xi} \varphi_0(\xi_1) & \cdots & \frac{\partial}{\partial \xi} \varphi_0(\xi_{N_p+1}) \\ \frac{\partial}{\partial \xi} \varphi_1(\xi_0) & \frac{\partial}{\partial \xi} \varphi_1(\xi_1) & \cdots & \frac{\partial}{\partial \xi} \varphi_1(\xi_{N_p+1}) \\ \vdots & \vdots & \ddots & \vdots \\ \frac{\partial}{\partial \xi} \varphi_{N_p+1}(\xi_0) & \frac{\partial}{\partial \xi} \varphi_{N_p+1}(\xi_1) & \cdots & \frac{\partial}{\partial \xi} \varphi_{N_p+1}(\xi_{N_p+1}) \end{pmatrix}. \quad (\text{D.55})$$

The set of optimal collocation points in  $\xi$  depend on polynomial type (Chebyshev, Legendre, Fourier) and the order of the series [Boy89]. It makes the matrix  $\mathbf{H}$  constant for given polynomial order and it can be computed beforehand and called from a database.

It is assumed additionally, that fluxes  $\mathbf{f}_x$  belong to the same polynomial space and thus, for derivative the same expression is valid:

$$\frac{\partial}{\partial x} (\tilde{\mathbf{F}}_{x_k}^l) = \frac{\Delta \xi}{\Delta x^l} \tilde{\mathbf{F}}_{x_k}^l \mathbf{H}, \quad (\text{D.56})$$

where

$$\tilde{\mathbf{F}}_{x_k, :; j}^l = \mathbf{f}_x(t_k, x_j^l, \tilde{U}_{k, :; j}^l, \frac{\partial}{\partial x} \tilde{U}_{k, :; j}^l), \quad j = 0, \dots, N_p + 1. \quad (\text{D.57})$$

Moreover, each spectral element is a subject of boundary conditions, which govern the evolution of nodes between elements:

$$\begin{cases} \frac{\partial}{\partial x} \mathbf{u}_k^{l+1}(x_0^{l+1}) = \frac{\partial}{\partial x} \mathbf{u}_k^{l-1}(x_{N_p-1}^{l-1}), & \forall l = 2, 4, \dots, (2N_x - 2), \\ \mathbf{f}_{0_{k+1}} - \mathbf{f}_{0_k} = \frac{1}{2} \Delta t (\mathbf{q}_{0_{k+1}} + \mathbf{q}_{0_k}), & l = 0, \\ \mathbf{f}_{\infty_{k+1}} - \mathbf{f}_{\infty_k} = \frac{1}{2} \Delta t (\mathbf{q}_{\infty_{k+1}} + \mathbf{q}_{\infty_k}), & l = (N_x - 1), \end{cases} \quad (\text{D.58})$$

here inner boundaries depend only on gradient of adjacent cells but outer boundary in most general case is described by an evolution function, which depends on the value and on the gradient of the state variable at the boundary:

$$\begin{aligned}\mathbf{f}_{0_k} &= \mathbf{f}_0 \left( t_k, \mathbf{u}_k(x_0), \frac{\partial}{\partial x} \mathbf{u}_k(x_0) \right), \\ \mathbf{q}_{0_k} &= \mathbf{q}_0 \left( t_k, \mathbf{u}_k(x_0), \frac{\partial}{\partial x} \mathbf{u}_k(x_0) \right), \\ \mathbf{f}_{\infty_k} &= \mathbf{f}_\infty \left( t_k, \mathbf{u}_k(x_\infty), \frac{\partial}{\partial x} \mathbf{u}_k(x_\infty) \right), \\ \mathbf{q}_{\infty_k} &= \mathbf{q}_\infty \left( t_k, \mathbf{u}_k(x_\infty), \frac{\partial}{\partial x} \mathbf{u}_k(x_\infty) \right).\end{aligned}\tag{D.59}$$

Now, all necessary building blocks are prepared for construction of APSM solution for one time step of given size  $\Delta t$  and for given spectral elements  $\mathbf{x}^l$  on the interval  $x \in [x_0, x_\infty]$ . Firstly, eq. (D.43) is rewritten for spectral approximation of point within element  $l$  and time step  $k + 1$ :

$$\begin{aligned}\tilde{\mathbf{f}}_{t_{k+1},i}^l - \tilde{\mathbf{f}}_{t_k,i}^l + \frac{\Delta t}{2} \left[ \frac{\Delta \xi}{\Delta x^l} \sum_{j=0}^{N_p+1} (\tilde{\mathbf{f}}_{x_{k+1},j}^l + \tilde{\mathbf{f}}_{x_{k,j}}^l) \mathbf{H}_{j,i} - \tilde{\mathbf{q}}_{k+1,i}^l - \tilde{\mathbf{q}}_{k,i}^l \right] &= \mathbf{R}_{k,i}^l, \\ \forall i = 1, \dots, N_p - 2, \\ \forall l = 1, 3, \dots, 2N_x - 1.\end{aligned}\tag{D.60}$$

Secondly, a discrete form of inner boundary conditions is formulated:

$$\begin{aligned}\frac{\Delta \xi}{\Delta x^{l+1}} \left( \sum_{j=1}^{N_p} \tilde{\mathbf{u}}_{k+1,j}^{l+1} \mathbf{H}_{j,0} + \tilde{\mathbf{u}}_{k+1}^l \mathbf{H}_{0,0} + \tilde{\mathbf{u}}_{k+1}^{l+2} \mathbf{H}_{N_p+1,0} \right) \\ - \frac{\Delta \xi}{\Delta x^{l-1}} \left( \sum_{j=1}^{N_p} \tilde{\mathbf{u}}_{k+1,j}^{l-1} \mathbf{H}_{j,N_p+1} + \tilde{\mathbf{u}}_{k+1}^{l-2} \mathbf{H}_{0,N_p+1} + \tilde{\mathbf{u}}_{k+1}^l \mathbf{H}_{N_p+1,N_p+1} \right) \\ = \mathbf{R}_k^l, \\ \forall l = 2, \dots, 2N_x - 2\end{aligned}\tag{D.61}$$

and for outer boundary conditions:

$$\tilde{\mathbf{f}}_{0_{k+1}} - \tilde{\mathbf{f}}_{0_k} - \frac{\Delta t}{2} [\tilde{\mathbf{q}}_{0_{k+1}} + \tilde{\mathbf{q}}_{0_k}] = \mathbf{R}_k^0,\tag{D.62}$$

$$\tilde{\mathbf{f}}_{\infty_{k+1}} - \tilde{\mathbf{f}}_{\infty_k} - \frac{\Delta t}{2} [\tilde{\mathbf{q}}_{\infty_{k+1}} + \tilde{\mathbf{q}}_{\infty_k}] = \mathbf{R}_k^{2N_x},\tag{D.63}$$

where

$$\begin{aligned}\tilde{\mathbf{f}}_{0_k} &= \mathbf{f}_{0_k} \left( t_k, \tilde{\mathbf{u}}_k^0, \left( \sum_{j=1}^{N_p} \tilde{\mathbf{u}}_{k,j}^1 \mathbf{H}_{j,0} + \tilde{\mathbf{u}}_k^0 \mathbf{H}_{0,0} + \tilde{\mathbf{u}}_k^2 \mathbf{H}_{N_p+1,0} \right) \right), \\ \tilde{\mathbf{q}}_{0_k} &= \mathbf{q}_{0_k} \left( t_k, \tilde{\mathbf{u}}_{x_{k,0}}^0, \sum_{j=0}^{N_p-1} \tilde{\mathbf{u}}_{x_{k,j}}^l \mathbf{H}_{j,0} \right), \\ \tilde{\mathbf{f}}_{\infty_k} &= \mathbf{f}_{\infty_k} \left( t_k, \tilde{\mathbf{u}}_{x_{k,0}}^{2N_x}, \sum_{j=0}^{N_p-1} \tilde{\mathbf{u}}_{x_{k,j}}^{2N_x} \mathbf{H}_{j,N_p-1} \right), \\ \tilde{\mathbf{q}}_{\infty_k} &= \mathbf{q}_{\infty_k} \left( t_k, \tilde{\mathbf{u}}_{x_k}^{2N_x}, \sum_{j=0}^{N_p-1} \tilde{\mathbf{u}}_{x_{k,j}}^{2N_x-1} \mathbf{H}_{j,N_p-1} \right).\end{aligned}\tag{D.64}$$

For Newton iterations a Jacobian of the residual is needed. The Jacobian of residual for element  $l = 1, 3, \dots, 2N_x - 1$  (compare figs. D.11 and D.11) has the following structure:

$$\left( \begin{array}{c|c|c|c} J_k^{l,l} & J_k^{l,l-1} & J_k^{l,l+1} & R_k^l \end{array} \right), \quad \forall l = 1, 3, \dots, 2N_x - 1,\tag{D.65}$$

here

$$\begin{aligned}
J_{k,i,j}^{l,l} &= \left( \frac{\partial \mathbf{f}_t}{\partial \mathbf{u}} \right)_{k,i} \delta_{i,j} + \frac{\Delta \xi}{\Delta x^l} \left( \frac{\partial \mathbf{f}_t}{\partial \left( \frac{\partial}{\partial x} \mathbf{u} \right)} \right)_{k,i} \mathbf{H}_{j+1,i+1} \\
&+ \frac{\Delta t}{2} \frac{\Delta \xi}{\Delta x^l} \left( \frac{\partial \mathbf{f}_x}{\partial \mathbf{u}} \right)_{k,j+1} \mathbf{H}_{j+1,i+1} \\
&+ \frac{\Delta t}{2} \left( \frac{\Delta \xi}{\Delta x^l} \right)^2 \sum_{m=1}^{N_p} \left( \frac{\partial \mathbf{f}_x}{\partial \left( \frac{\partial}{\partial x} \mathbf{u} \right)} \right)_{k,m} \mathbf{H}_{j+1,m} \mathbf{H}_{m,i+1} \\
&- \frac{\Delta t}{2} \left( \frac{\partial \mathbf{q}}{\partial \mathbf{u}} \right)_{k,i} \delta_{i,j} - \frac{\Delta t}{2} \frac{\Delta \xi}{\Delta x^l} \left( \frac{\partial \mathbf{q}}{\partial \left( \frac{\partial}{\partial x} \mathbf{u} \right)} \right)_{k,i} \mathbf{H}_{j+1,i+1}, \\
&\forall i = 0, 1, \dots, N_p - 1, \\
&\forall j = 0, 1, \dots, N_p - 1,
\end{aligned} \tag{D.66}$$

here  $J_{k,i,j}^{l,l}$  is a sub-matrix of size  $[N_v \times N_v]$ , where  $N_v$  is the number of state variables. The size of  $J^{l,l}$  is then  $[N_v N_p \times N_v N_p]$ , with  $N_p$  – number of points within element (the number of collocation points is equal  $N_p + 2$  and the element order –  $N_p + 1$ ). The dependency of element points on boundaries is described by:

$$\begin{aligned}
J_{k,i}^{l,l-1} &= \frac{\Delta \xi}{\Delta x^l} \left( \frac{\partial \mathbf{f}_t}{\partial \left( \frac{\partial}{\partial x} \mathbf{u} \right)} \right)_{k,i} \mathbf{H}_{0,i+1} + \frac{\Delta t}{2} \frac{\Delta \xi}{\Delta x^l} \left( \frac{\partial \mathbf{f}_x}{\partial \mathbf{u}} \right)_{k,0} \mathbf{H}_{0,i+1} \\
&+ \frac{\Delta t}{2} \left( \frac{\Delta \xi}{\Delta x^l} \right)^2 \sum_{m=1}^{N_p} \left( \frac{\partial \mathbf{f}_x}{\partial \left( \frac{\partial}{\partial x} \mathbf{u} \right)} \right)_{k,m} \mathbf{H}_{0,m} \mathbf{H}_{m,i+1}, \\
&- \frac{\Delta t}{2} \frac{\Delta \xi}{\Delta x^l} \left( \frac{\partial \mathbf{q}}{\partial \left( \frac{\partial}{\partial x} \mathbf{u} \right)} \right)_{k,i} \mathbf{H}_{0,i+1} \\
&\forall i = 0, 1, \dots, N_p - 1,
\end{aligned} \tag{D.67}$$

$$\begin{aligned}
J_{k,i}^{l,l+1} &= \frac{\Delta \xi}{\Delta x^l} \left( \frac{\partial \mathbf{f}_t}{\partial \left( \frac{\partial}{\partial x} \mathbf{u} \right)} \right)_{k,i} \mathbf{H}_{N_p+1,i+1} + \frac{\Delta t}{2} \frac{\Delta \xi}{\Delta x^l} \left( \frac{\partial \mathbf{f}_x}{\partial \mathbf{u}} \right)_{k,N_p+1} \mathbf{H}_{N_p+1,i+1} \\
&+ \frac{\Delta t}{2} \left( \frac{\Delta \xi}{\Delta x^l} \right)^2 \sum_{m=1}^{N_p} \left( \frac{\partial \mathbf{f}_x}{\partial \left( \frac{\partial}{\partial x} \mathbf{u} \right)} \right)_{k,m} \mathbf{H}_{N_p+1,m} \mathbf{H}_{m,i+1} \\
&+ \frac{\Delta t}{2} \frac{\Delta \xi}{\Delta x^l} \left( \frac{\partial \mathbf{q}}{\partial \left( \frac{\partial}{\partial x} \mathbf{u} \right)} \right)_{k,i} \mathbf{H}_{N_p+1,i+1}, \\
&\forall i = 0, 1, \dots, N_p - 1.
\end{aligned} \tag{D.68}$$

The size of partial Jacobians  $J_{k,i}^{l,l-1}$  and  $J_{k,i}^{l,l+1}$  is also  $[N_v \times N_v]$ . The size of blocks  $J_k^{l,l-1}$  and  $J_k^{l,l+1}$  is then  $[N_v N_p \times N_v]$ .

The structure of Jacobian for inner boundary nodes  $l = 2, 4, \dots, N_p - 2$  is:

$$\left( J_k^{l,l} \mid J_k^{l,l-2} \mid J_k^{l,l-1} \mid J_k^{l,l+1} \mid J_k^{l,l+2} \mid R_k^l \right), \quad \forall l = 2, 4, \dots, N_p - 2, \tag{D.69}$$

with

$$\left\{ \begin{array}{l} J_k^{l,l} = I \left( \frac{\Delta \xi}{\Delta x^{l+1}} \mathbf{H}_{0,0} - \frac{\Delta \xi}{\Delta x^{l-1}} \mathbf{H}_{N_p+1,N_p+1} \right), \\ J_k^{l,l-2} = -I \frac{\Delta \xi}{\Delta x^{l-1}} \mathbf{H}_{0,N_p+1}, \\ J_k^{l,l-1} = -I \frac{\Delta \xi}{\Delta x^{l-1}} \mathbf{H}_{j+1,N_p+1} \\ J_k^{l,l+1} = I \frac{\Delta \xi}{\Delta x^{l+1}} \mathbf{H}_{j+1,0}, \\ J_k^{l,l+2} = I \frac{\Delta \xi}{\Delta x^{l+1}} \mathbf{H}_{N_p+1,0}, \end{array} \right. \quad \forall j = 0, 1, \dots, N_p - 1, \tag{D.70}$$

here  $I$  is identity matrix of size  $[N_v \times N_v]$ . The size of blocks  $J^{l,l}$ ,  $J^{l,l-2}$  and  $J^{l,l+2}$  is  $[N_v \times N_v]$ , while the size of blocks  $J^{l,l-1}$  and  $J^{l,l+1}$  is  $[N_v \times N_v N_p]$ .

The Jacobian of the global left boundary has the following structure:

$$\left( J_k^{0,0} \mid J_k^{0,1} \mid J_k^{0,2} \mid R^0 \right), \quad (\text{D.71})$$

where

$$\left\{ \begin{array}{l} J_k^{0,0} = \left( \frac{\partial \mathbf{f}_0}{\partial \mathbf{u}} \right)_k + \frac{\Delta \xi}{\Delta x^1} \left( \frac{\partial \mathbf{f}_0}{\partial \left( \frac{\partial}{\partial x} \mathbf{u} \right)} \right)_k \mathbf{H}_{0,0} \\ \quad - \frac{\Delta t}{2} \left( \frac{\partial \mathbf{q}_0}{\partial \mathbf{u}} \right)_k - \frac{\Delta t}{2} \frac{\Delta \xi}{\Delta x^1} \left( \frac{\partial \mathbf{q}_0}{\partial \left( \frac{\partial}{\partial x} \mathbf{u} \right)} \right)_k \mathbf{H}_{0,0}, \\ J_{k,0,j}^{0,1} = \frac{\Delta \xi}{\Delta x^1} \left( \frac{\partial \mathbf{f}_0}{\partial \left( \frac{\partial}{\partial x} \mathbf{u} \right)} \right)_k \mathbf{H}_{j+1,0} - \frac{\Delta t}{2} \frac{\Delta \xi}{\Delta x^1} \left( \frac{\partial \mathbf{q}_0}{\partial \left( \frac{\partial}{\partial x} \mathbf{u} \right)} \right)_k \mathbf{H}_{j+1,0}, \\ \quad \forall j = 0, 1, \dots, N_p - 1, \\ J_k^{0,2} = \frac{\Delta \xi}{\Delta x^1} \left( \frac{\partial \mathbf{f}_0}{\partial \left( \frac{\partial}{\partial x} \mathbf{u} \right)} \right)_k \mathbf{H}_{N_p+1,0} - \frac{\Delta t}{2} \frac{\Delta \xi}{\Delta x^1} \left( \frac{\partial \mathbf{q}_0}{\partial \left( \frac{\partial}{\partial x} \mathbf{u} \right)} \right)_k \mathbf{H}_{N_p+1,0}. \end{array} \right. \quad (\text{D.72})$$

The size of blocks  $J_k^{0,0}$  and  $J_k^{0,2}$  is  $[N_v \times N_v]$  and of the block  $J_k^{0,1}$  is  $[N_v \times N_v N_p]$ .

The Jacobian of the global right boundary has the following structure:

$$\left( J_k^{2N_x, 2N_x} \mid J_k^{2N_x, 2N_x-1} \mid J_k^{2N_x, 2N_x-2} \mid R^{2N_x} \right), \quad (\text{D.73})$$

with

$$\left\{ \begin{array}{l} J_k^{2N_x, 2N_x} = \left( \frac{\partial \mathbf{f}_\infty}{\partial \mathbf{u}} \right)_k + \frac{\Delta \xi}{\Delta x^1} \left( \frac{\partial \mathbf{f}_\infty}{\partial \left( \frac{\partial}{\partial x} \mathbf{u} \right)} \right)_k \mathbf{H}_{0,0} \\ \quad - \frac{\Delta t}{2} \left( \frac{\partial \mathbf{q}_\infty}{\partial \mathbf{u}} \right)_k - \frac{\Delta t}{2} \frac{\Delta \xi}{\Delta x^1} \left( \frac{\partial \mathbf{q}_\infty}{\partial \left( \frac{\partial}{\partial x} \mathbf{u} \right)} \right)_k \mathbf{H}_{0,0}, \\ J_{k,0,j}^{2N_x, 2N_x-1} = \frac{\Delta \xi}{\Delta x^1} \left( \frac{\partial \mathbf{f}_\infty}{\partial \left( \frac{\partial}{\partial x} \mathbf{u} \right)} \right)_k \mathbf{H}_{j+1,0} - \frac{\Delta t}{2} \frac{\Delta \xi}{\Delta x^1} \left( \frac{\partial \mathbf{q}_\infty}{\partial \left( \frac{\partial}{\partial x} \mathbf{u} \right)} \right)_k \mathbf{H}_{j+1,0}, \\ \quad \forall j = 0, 1, \dots, N_p - 1, \\ J_k^{2N_x, 2N_x-2} = \frac{\Delta \xi}{\Delta x^1} \left( \frac{\partial \mathbf{f}_\infty}{\partial \left( \frac{\partial}{\partial x} \mathbf{u} \right)} \right)_k \mathbf{H}_{N_p+1,0} - \frac{\Delta t}{2} \frac{\Delta \xi}{\Delta x^1} \left( \frac{\partial \mathbf{q}_\infty}{\partial \left( \frac{\partial}{\partial x} \mathbf{u} \right)} \right)_k \mathbf{H}_{N_p+1,0}. \end{array} \right. \quad (\text{D.74})$$

The size of blocks  $J_k^{2N_x, 2N_x}$  and  $J_k^{2N_x, 2N_x-2}$  is  $[N_v \times N_v]$  and of the block  $J_k^{2N_x, 2N_x-1}$  is  $[N_v \times N_v N_p]$ .

The discrete approximation is always created with binary tree by splitting required elements and thus, creating new inner boundaries. The solution of the linear system of Newton iteration starts from bottom of the tree by eliminating the elements (compare §D.2). As it can be seen from equations (D.70), (D.72) and (D.74), a solution in one element depends from adjacent elements only through gradients. For this reason, element  $l$  receives dependency of left  $l-1$  and right  $l+1$  boundaries from the gradient at the boundary with the element:

$$M_a^l = \begin{cases} \left( \frac{\partial \mathbf{f}_0}{\partial \left( \frac{\partial}{\partial x} \mathbf{u} \right)} \right)_k - \frac{\Delta t}{2} \left( \frac{\partial \mathbf{q}_0}{\partial \left( \frac{\partial}{\partial x} \mathbf{u} \right)} \right)_k, & \forall l = 1 \\ -I, & \forall l = 3, 5, \dots, 2N_x - 1 \end{cases} \quad (\text{D.75})$$

and

$$M_b^l = \begin{cases} \left( \frac{\partial \mathbf{f}_\infty}{\partial \left( \frac{\partial}{\partial x} \mathbf{u} \right)} \right)_k - \frac{\Delta t}{2} \left( \frac{\partial \mathbf{q}_\infty}{\partial \left( \frac{\partial}{\partial x} \mathbf{u} \right)} \right)_k, & \forall l = 2N_x - 1, \\ I, & \forall l = 1, 3, \dots, 2N_x - 3. \end{cases} \quad (\text{D.76})$$

Now, only elements  $l = 1, 3, \dots, 2N_x - 2$  are considered. The linear system for them with boundaries  $l - 1$  and  $l + 1$  looks so:

	$\Delta \mathbf{u}^l$	$\Delta \mathbf{u}^{l-1}$	$\Delta \mathbf{u}^{l+1}$	$\Delta \mathbf{u}^{l-3}$	$\Delta \mathbf{u}^{l-2}$	$\Delta \mathbf{u}^{l+2}$	$\Delta \mathbf{u}^{l+3}$	$R$
$\Delta R_k^l$	$J_k^{l,l}$	$J_k^{l,l-1}$	$J_k^{l,l+1}$	0	0	0	0	$R_k^l$
$\Delta R_k^{l-1}$	$J_k^{l-1,l}$	$J_k^{l-1,l-1}$	$J_k^{l-1,l+1}$	$J^{l-1,l-3}$	$J^{l-1,l-2}$	0	0	$R_k^{l-1}$
$\Delta R_k^{l+1}$	$J^{l+1,l}$	$J^{l+1,l-1}$	$J^{l+1,l+1}$	0	0	$J^{l+1,l+2}$	$J^{l+1,l+3}$	$R_k^{l+1}$

$\forall l = 1, 3, \dots, N_p - 1.$

(D.77)

In order to eliminate the element  $l = 1, 3, \dots, 2N_x - 1$ ,  $J_k^{l,l}$  is firstly reduced, compare eqs. (D.32) and (D.33):

	$\Delta \mathbf{u}^l$	$\Delta \mathbf{u}^{l-1}$	$\Delta \mathbf{u}^{l+1}$	$\Delta \mathbf{u}^{l-3}$	$\Delta \mathbf{u}^{l-2}$	$\Delta \mathbf{u}^{l+2}$	$\Delta \mathbf{u}^{l+3}$	$R$
$\Delta R_k^l$	$I$	$B_a^l$	$B_b^l$	0	0	0	0	$A^l$

$\forall l = 1, 3, \dots, N_p - 1,$

(D.78)

where  $I$  is identity matrix of size  $[N_v N_p \times N_v N_p]$ , 0 are zeros matrices of size  $[N_v N_p \times N_v N_p]$  and  $[N_v N_p \times N_v]$  and

$$\begin{cases} B_a^l = \left( J_k^{l,l} \right)^{-1} J_k^{l,l-1}, \\ B_b^l = \left( J_k^{l,l} \right)^{-1} J_k^{l,l+1}, \\ A^l = \left( J_k^{l,l} \right)^{-1} R_k^l. \end{cases} \quad (\text{D.79})$$

The structure eq. (D.78) can be used to reconstruct increment of inner points  $\Delta \mathbf{u}^l$  from increment of boundary points  $\Delta \mathbf{u}^{l-1}$  and  $\Delta \mathbf{u}^{l+1}$  during Newtonian iterations. Then, the part of Jacobian  $J^{l-1,l}$  of the left element boundary and  $J^{l+1,l}$  of the right element boundary are constructed:

$$\begin{cases} J_{k,0,j}^{l-1,l} = \frac{\Delta \xi}{\Delta x^l} M_a^l H_{j+1,0}, & \forall j = 0, 1, \dots, N_p - 1, \\ J_{k,0,j}^{l+1,l} = \frac{\Delta \xi}{\Delta x^l} M_b^l H_{j+1,N_p+1}, & \forall j = 0, 1, \dots, N_p - 1. \end{cases} \quad (\text{D.80})$$

The latter must be zero after the complete elimination of the element  $l$ . The following identities as a part of blocks  $J^{l-1,l-1}$ ,  $J^{l-1,l+1}$  and  $R^{l-1}$  are constructed:

$$\begin{cases} D_{aa}^l = \frac{\Delta \xi}{\Delta x^l} H_{0,0} M_a^l - J_k^{l-1,l} B_a^l, \\ D_{ab}^l = \frac{\Delta \xi}{\Delta x^l} H_{N_p+1,0} M_a^l - J_k^{l-1,l} B_b^l, \\ C_a^l = -J_k^{l-1,l} A^l, \\ \forall l = 1, 3, \dots, 2N_x - 1. \end{cases} \quad (\text{D.81})$$

Similarly, the parts of blocks  $J^{l+1,l-1}$ ,  $J^{l+1,l+1}$  and  $R^{l+1}$  are defined:

$$\begin{cases} D_{ba}^l = \frac{\Delta \xi}{\Delta x^l} H_{0,N_p+1} M_b^l - J_k^{l+1,l} B_a^l, \\ D_{bb}^l = \frac{\Delta \xi}{\Delta x^l} H_{N_p+1,N_p+1} M_b^l - J_k^{l+1,l} B_b^l, \\ C_b^l = -J_k^{l+1,l} A^l, \\ \forall l = 1, 3, \dots, 2N_x - 1. \end{cases} \quad (\text{D.82})$$

Now, elements  $l = 1, 3, \dots, 2N_x - 1$  can be completely eliminated. The new linear system for boundary nodes  $l = 0, 2, \dots, 2N_x$  without elements  $l = 1, 3, \dots, 2N_x - 1$  looks as follows:

$$\begin{array}{c|c|c|c} \Delta \mathbf{u}^0 & \Delta \mathbf{u}^2 & \Delta \mathbf{u}^4 & R \\ \hline \left( \frac{\partial \mathbf{f}_0}{\partial \mathbf{u}} \right)_k - \frac{\Delta t}{2} \left( \frac{\partial \mathbf{q}_0}{\partial \mathbf{u}} \right)_k + D_{aa}^1 & D_{ab}^1 & 0 & R_k^0 + C_a^1 \\ \hline D_{ba}^1 & D_{aa}^3 + D_{bb}^1 & D_{ab}^3 & R_k^2 + C_b^1 + C_a^3 \end{array} \quad (\text{D.83})$$

$$\begin{array}{c|c|c|c|c|c} \Delta \mathbf{u}^l & \Delta \mathbf{u}^{l-2} & \Delta \mathbf{u}^{l+2} & \Delta \mathbf{u}^{l-4} & \Delta \mathbf{u}^{l+4} & R \\ \hline D_{aa}^{l+1} + D_{bb}^{l-1} & D_{ba}^{l-1} & D_{ab}^{l+1} & 0 & 0 & R_k^l + C_b^{l-1} + C_a^{l+1} \\ \hline D_{ab}^{l-1} & D_{aa}^{l-1} + D_{bb}^{l-3} & 0 & D_{ba}^{l-3} & 0 & R_k^{l-2} + C_b^{l-3} + C_a^{l-1} \\ \hline D_{ba}^{l+1} & 0 & D_{aa}^{l+3} + D_{bb}^{l+1} & 0 & D_{ab}^{l+3} & R_k^{l+2} + C_b^{l+1} + C_a^{l+3} \end{array} \quad \forall l = 2, 4, \dots, N_p - 2, \quad (\text{D.84})$$

$$\begin{array}{c|c|c|c} \Delta \mathbf{u}^{2N_x} & \Delta \mathbf{u}^{2N_x-2} & \Delta \mathbf{u}^{2N_x-4} & R \\ \hline \left( \frac{\partial \mathbf{f}_\infty}{\partial \mathbf{u}} \right)_k - \frac{\Delta t}{2} \left( \frac{\partial \mathbf{q}_\infty}{\partial \mathbf{u}} \right)_k + D_{bb}^{2N_x-1} & D_{ba}^{2N_x-1} & 0 & R_k^{2N_x} + C_b^{2N_x-1} \\ \hline D_{ab}^{2N_x-1} & D_{aa}^{2N_x-1} + D_{bb}^{2N_x-3} & D_{ba}^{2N_x-3} & R_k^{2N_x-2} + C_b^{2N_x-3} + C_a^{2N_x-1} \end{array} \quad (\text{D.85})$$

Now the next layer in binary tree must be eliminated, e.g. every second node  $l = 2, 6, 10, \dots, 2N_x - 2$ . The structure of these nodes after elimination looks then so:

$$\begin{array}{c|c|c|c|c|c|c} & \Delta \mathbf{u}^l & \Delta \mathbf{u}^{l-2} & \Delta \mathbf{u}^{l+2} & \Delta \mathbf{u}^{l-4} & \Delta \mathbf{u}^{l+4} & R \\ \hline \Delta R_k^l & I & B_a^l & B_b^l & 0 & 0 & A^l \end{array} \quad \forall l = 2, 6, 10, \dots, 2N_x - 2, \quad (\text{D.86})$$

here  $I$  is identity matrix and  $0$  is zero matrix. Both are of size  $[N_v \times N_v]$ . This part is required for reconstruction of inner points:

$$\begin{cases} B_a^l = \left( D_{aa}^{l+1} + D_{bb}^{l-1} \right)^{-1} D_{ba}^{l-1}, \\ B_b^l = \left( D_{aa}^{l+1} + D_{bb}^{l-1} \right)^{-1} D_{ab}^{l+1}, \\ A^l = \left( D_{aa}^{l+1} + D_{bb}^{l-1} \right)^{-1} \left( R_k^l + C_b^{l-1} + C_a^{l+1} \right), \end{cases} \quad (\text{D.87})$$

and the following data is submitted to the upper level:

$$\begin{cases} D_{aa}^l = D_{aa}^{l-1} - D_{ab}^{l-1} B_a^l, \\ D_{ab}^l = -D_{ab}^{l-1} B_b^l, \\ C_a^l = R_k^{l-2} + C_a^{l-1} - D_{ab}^{l-1} A^l, \\ D_{ba}^l = -D_{ba}^{l+1} B_a^l, \\ D_{bb}^l = D_{bb}^{l+1} - D_{ba}^{l+1} B_b^l, \\ C_b^l = C_b^{l+1} - D_{ba}^{l+1} A^l. \end{cases} \quad (\text{D.88})$$

It is to see from the expression (D.88), that no information is required from adjacent nodes  $l - 2$ ,  $l + 2$  any more. Only the information received from child elements  $l - 1$  and  $l + 1$  is used for further calculation. The linear system of the level above  $l = 0, 4, 8, \dots, 2N_x$  looks now as:

$$\begin{array}{c|c|c|c} \Delta \mathbf{u}^0 & \Delta \mathbf{u}^4 & \Delta \mathbf{u}^8 & R \\ \hline \left( \frac{\partial \mathbf{f}_0}{\partial \mathbf{u}} \right)_k - \frac{\Delta t}{2} \left( \frac{\partial \mathbf{q}_0}{\partial \mathbf{u}} \right)_k + D_{aa}^2 & D_{ab}^2 & 0 & R_k^0 + C_a^2 \\ \hline D_{ba}^2 & D_{aa}^6 + D_{bb}^2 & D_{ab}^6 & R_k^4 + C_b^2 + C_a^6 \end{array} \quad (\text{D.89})$$

$$\begin{array}{c|c|c|c|c|c} \Delta \mathbf{u}^l & \Delta \mathbf{u}^{l-4} & \Delta \mathbf{u}^{l+4} & \Delta \mathbf{u}^{l-8} & \Delta \mathbf{u}^{l+8} & R \\ \hline D_{aa}^{l+2} + D_{bb}^{l-2} & D_{ba}^{l-2} & D_{ab}^{l+2} & 0 & 0 & R_k^l + C_b^{l-2} + C_a^{l+2} \\ \hline D_{ab}^{l-2} & D_{aa}^{l-2} + D_{bb}^{l-6} & 0 & D_{ba}^{l-6} & 0 & R_k^{l-4} + C_b^{l-6} + C_a^{l-2} \\ \hline D_{ba}^{l+2} & 0 & D_{aa}^{l+6} + D_{bb}^{l+2} & 0 & D_{ab}^{l+6} & R_k^{l+4} + C_b^{l+2} + C_a^{l+6} \end{array} \quad \forall l = 4, 12, 20, \dots, 2N_x - 4, \quad (\text{D.90})$$

$$\begin{array}{c|c|c|c} \Delta \mathbf{u}^{2N_x} & \Delta \mathbf{u}^{2N_x-4} & \Delta \mathbf{u}^{2N_x-8} & R \\ \hline \left( \frac{\partial \mathbf{f}_\infty}{\partial \mathbf{u}} \right)_k - \frac{\Delta t}{2} \left( \frac{\partial \mathbf{q}_\infty}{\partial \mathbf{u}} \right)_k + D_{bb}^{2N_x-2} & D_{ba}^{2N_x-2} & 0 & R_k^{2N_x} + C_b^{2N_x-2} \\ \hline D_{ab}^{2N_x-2} & D_{aa}^{2N_x-2} + D_{bb}^{2N_x-6} & D_{ba}^{2N_x-6} & R_k^{2N_x-4} + C_b^{2N_x-6} + C_a^{2N_x-2} \end{array} \quad (\text{D.91})$$

This process can be further continued by eliminating nodes  $l = 4, 12, 20, \dots, (2N_x - 4)$ , then nodes  $l = 8, 16, \dots, (2N_x - 8)$  and so on, till the system of only 2 nodes  $l = 1, 2N_x$  is achieved:

$$\begin{array}{c|c|c} \Delta \mathbf{u}^0 & \Delta \mathbf{u}^{2N_x} & R \\ \hline \left( \frac{\partial \mathbf{f}_0}{\partial \mathbf{u}} \right)_k - \frac{\Delta t}{2} \left( \frac{\partial \mathbf{q}_0}{\partial \mathbf{u}} \right)_k + D_{aa}^{N_x} & D_{ab}^{N_x} & R_k^0 + C_a^{N_x} \\ \hline D_{ba}^{N_x} & \left( \frac{\partial \mathbf{f}_\infty}{\partial \mathbf{u}} \right)_k - \frac{\Delta t}{2} \left( \frac{\partial \mathbf{q}_\infty}{\partial \mathbf{u}} \right)_k + D_{bb}^{N_x} & R_k^{2N_x} + C_b^{N_x} \end{array} \quad (\text{D.92})$$

By solving the linear system eq. (D.92), an increment of values of state variables  $\Delta \mathbf{u}^0$  and  $\Delta \mathbf{u}^{2N_x}$  at the global boundaries during one Newtonian iteration is computed. The latter is then propagated down the tree (compare fig. D.10).

$$\begin{aligned} \Delta \mathbf{u}^{N_x} &= A^{N_x} - B_a^{N_x} \Delta \mathbf{u}^0 - B_b^{N_x} \Delta \mathbf{u}^{2N_x} \\ &\vdots \\ \Delta \mathbf{u}^l &= A^l - B_a^l \Delta \mathbf{u}^{l-4} - B_b^l \Delta \mathbf{u}^{l+4} \quad \forall l = 4, 12, 20, \dots, N_p - 4 \\ \Delta \mathbf{u}^l &= A^l - B_a^l \Delta \mathbf{u}^{l-2} - B_b^l \Delta \mathbf{u}^{l+2} \quad \forall l = 2, 6, 10, \dots, N_p - 2 \\ \Delta \mathbf{u}^l &= A^l - B_a^l \Delta \mathbf{u}^{l-1} - B_b^l \Delta \mathbf{u}^{l+1} \quad \forall l = 1, 3, 5, \dots, N_p - 1. \end{aligned} \quad (\text{D.93})$$

This process is repeated till the relative increment of Newtonian iteration for current time step is small:

$$\frac{\|\Delta \mathbf{u}^l\|_2}{\|\mathbf{u}^l\|_2} \leq \varepsilon, \quad \forall l = 0, 1, \dots, 2N_x. \quad (\text{D.94})$$

It is worth to mention that the iterations can be stopped in one part of the system earlier as in the other, as soon as the criteria eq. (D.94) is reached locally. The value  $\varepsilon = 10^{-9}$  was used in computations.

#### D.4. Grid adaptation

The proposed adaptive pseudo spectral method (APSM) allows two types of adaptation:

- p-Refinement: Increase order of polynomial within one or several elements,
- r-Refinement: Increase number of elements by splitting and thus, increasing the depth of the binary tree.

The first method is advantageous as during increase of the order almost no information is being lost and during the decrease of the order the loss of the information can be controlled. Recapitulate that an approximation of vector function  $\mathbf{u}$  of order  $N$  on the interval  $x \in [x_0^l, x_N^l]$  is a weighted sum of  $N + 1$  basis functions. This can be represented as matrix product:

$$\tilde{\mathbf{U}}_M^l = \hat{\mathbf{U}}_N^l \Phi_{N,M}, \quad (\text{D.95})$$

here  $\tilde{\mathbf{U}}_M^l$  is the approximation of  $\mathbf{u}$  on  $M + 1$  collocation points,  $\hat{\mathbf{U}}^l$  represent corresponding  $N + 1$  spectral coefficients and  $\Phi_{N,M}$  is matrix of size  $[(N + 1) \times (M + 1)]$ :

$$\Phi_{N,M} = \begin{pmatrix} \varphi_0(x_0^l) & \varphi_0(x_1^l) & \cdots & \varphi_0(x_M^l) \\ \varphi_1(x_0^l) & \varphi_1(x_1^l) & \cdots & \varphi_1(x_M^l) \\ \vdots & \vdots & \ddots & \vdots \\ \varphi_N(x_0^l) & \varphi_N(x_1^l) & \cdots & \varphi_N(x_M^l) \end{pmatrix}. \quad (\text{D.96})$$

In order to avoid uncertainties  $N = M$  is used in calculations. Then the spectral coefficients can be computed:

$$\hat{\mathbf{U}}_M^l = \tilde{\mathbf{U}}_M^l \Phi_{M,M}^{-1}. \quad (\text{D.97})$$

The polynomial order can be changed by simply padding with zero(s):

$$\hat{\mathbf{U}}_{M+1}^l = (\hat{\mathbf{u}}_0, \hat{\mathbf{u}}_1, \dots, \hat{\mathbf{u}}_M, \mathbf{0}), \quad (\text{D.98})$$

here the order is increased by one. Then the solution of the increased order  $K > M$  is:

$$\tilde{\mathbf{U}}_K^l = \hat{\mathbf{U}}_K^l \Phi_{K,K} = \hat{\mathbf{U}}_M^l \Phi_{M,K}, \quad (\text{D.99})$$

with  $\Phi_{M,K}$  is derived from  $\Phi_{K,K}$  by removing the lines corresponding to padded zeros in  $\hat{\mathbf{U}}_K^l$ , e.g. for  $K = M + 1$

$$\Phi_{M,M+1} = \begin{pmatrix} \varphi_0(x_0^l) & \varphi_0(x_1^l) & \cdots & \varphi_0(x_{M+1}^l) \\ \varphi_1(x_0^l) & \varphi_1(x_1^l) & \cdots & \varphi_1(x_{M+1}^l) \\ \vdots & \vdots & \ddots & \vdots \\ \varphi_M(x_0^l) & \varphi_M(x_1^l) & \cdots & \varphi_M(x_{M+1}^l) \end{pmatrix}. \quad (\text{D.100})$$

Here  $\{x_0^l, \dots, x_M^l\}$  and  $\{x_0^l, \dots, x_K^l\}$  are corresponding Gauss-Lobatto points for order of polynomials  $M$  and  $K$  respectively. The function values on the new optimal set of points, e.g.  $K = M + 1$ , are:

$$\tilde{\mathbf{U}}_K^l = \tilde{\mathbf{U}}_M^l T_{M,K}, \quad (\text{D.101})$$

where

$$T_{M,K} = \Phi_{M,M}^{-1} \Phi_{M,K} \quad (\text{D.102})$$

is the transformation matrix from order  $M$  to order  $K$ . This matrix allows to project a solution from collocation points, corresponding to order  $M$ , to collocation points corresponding to increased order  $K$ . As the collocation points are predefined, transformation matrices are constant and can be computed beforehand.

Although, as discussed in the previous section, the error of the order increase is limited to interpolation error

$$E_I(M) \approx \hat{\mathbf{u}}_M^l. \quad (\text{D.103})$$

However practically the results are identical.

Truncating the series in the similar fashion

$$\hat{\mathbf{U}}_{M-1}^l = (\hat{\mathbf{u}}_0, \hat{\mathbf{u}}_1, \dots, \hat{\mathbf{u}}_{M-1}, 0) \quad (\text{D.104})$$

produces undesired results. Consider for example fig. D.19. Although the approximation with truncated order  $O(4)$  compared to initial order  $O(5)$  is similar, the gradient at both boundaries has changed the sign. This makes the boundary conditions eq. (D.24) not consistent anymore. As polynomial degree increases, so does the tendency of this polynomial to oscillate near endpoints [Boy89]. It is called Runge phenomenon [Boy89]. In fig. D.20 it can be seen that, although a better approximation of the Runge function (black line) with polynomial of order 14 (red line) as with polynomial of order 6 (blue line) is achieved, the oscillations are much stronger for  $O(14)$  near the ends of the interval.

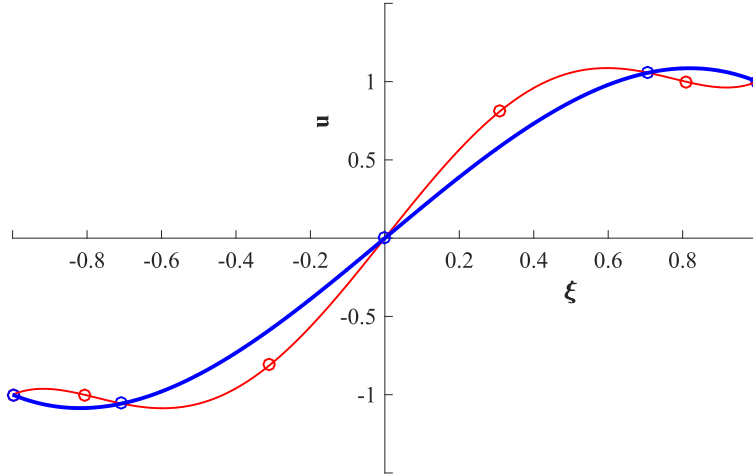


**Figure D.19.:** Solution approximation after order decrease through truncation. Red line shows the initial approximation  $O(5)$  with red points showing the collocation points, blue line shows the decreased order  $O(4)$ .

The inconsistency of inner boundary conditions eq. (D.24) can be avoided by imposing values and gradients at the boundaries during reinterpolation (order reduction):

$$\left\{ \begin{array}{l} \tilde{\mathbf{u}}_K^l(x_0^l) = \tilde{\mathbf{u}}_M^l(x_0^l), \\ \tilde{\mathbf{u}}_K^l(x_K^l) = \tilde{\mathbf{u}}_M^l(x_M^l), \\ \frac{\partial}{\partial x} \tilde{\mathbf{u}}_K^l(x_0^l) = \frac{\partial}{\partial x} \tilde{\mathbf{u}}_M^l(x_0^l), \\ \frac{\partial}{\partial x} \tilde{\mathbf{u}}_K^l(x_K^l) = \frac{\partial}{\partial x} \tilde{\mathbf{u}}_M^l(x_M^l) \end{array} \right. \quad (\text{D.105})$$

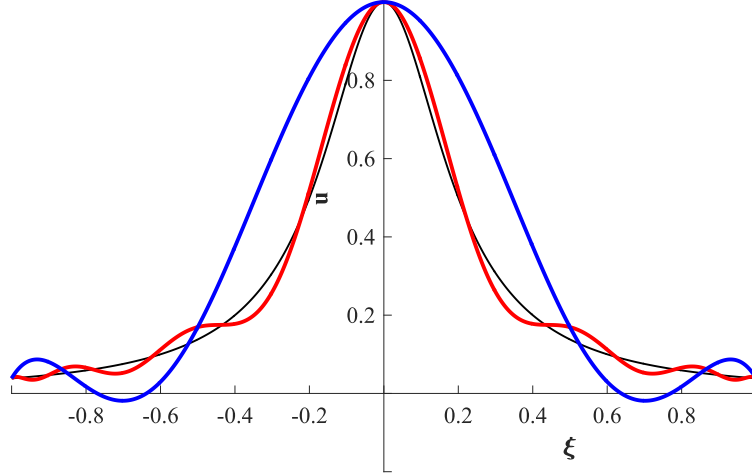


**Figure D.20.:** Approximation of  $f(x) = 1/(1 + (x/5)^2)$  (black line) with order 6 (blue line) and with order 14 (red line).

with  $\tilde{\mathbf{u}}_K^l$  is an approximation of order  $O(K)$  and  $\tilde{\mathbf{u}}_M^l$  is an approximation of order  $O(M)$  for  $K < M$ . Four boundary condition imply that minimal polynomial order that can fulfil them is  $O(3)$ . Boundary conditions, eq. (D.105), reduce the number of unknown degrees of freedom for inner boundaries to  $K - 3$ . The values at the boundaries and on  $K - 3$  inner points can be calculated by imposing equality of approximations on  $K - 3$  collocation points. Remember that (see §D.3):

$$H_M = \Phi_{M,M}^{-1} \frac{\partial}{\partial x} \Phi_{M,M}. \quad (\text{D.106})$$

Then, the following linear system for  $K + 1$  collocation points can be formulated:

$$\begin{cases} \tilde{\mathbf{U}}_K H_{K_0} = \tilde{\mathbf{U}}_M H_{M_0}, \\ \tilde{\mathbf{U}}_K T_{K,K-2} = \tilde{\mathbf{U}}_M T_{M,K-2}, \\ \tilde{\mathbf{U}}_K H_{K_{K+1}} = \tilde{\mathbf{U}}_M H_{M_{M+1}} \end{cases} \quad (\text{D.107})$$

where  $H_{K_i}$  means the  $i$ -th column of the matrix  $H_K$ . The first and the last equation impose equality of gradients and the middle one impose equality of polynomials on  $K - 1$  points, including boundary points. Practically, best results achieved using Gauss-Lobatto points for polynomial of order  $O(K - 2)$ . Then the new transformation matrix  $P_{M,K}$  for order reduction from  $M$  to  $K$ :

$$\tilde{\mathbf{U}}_K = \tilde{\mathbf{U}}_M P_{M,K}, \quad (\text{D.108})$$

is

$$P_{M,K} = \left( H_{M_0} \mid T_{M,K-2} \mid H_{M_{M+1}} \right) \left( H_{K_0} \mid T_{K,K-2} \mid H_{K_{K+1}} \right)^{-1}. \quad (\text{D.109})$$

The result of order reduction with fixed gradients is shown in fig. D.21. The boundary values and gradients are exact but a stronger deviation is seen in the middle of the domain. Although the polynomial order is reduced by 1 (from 5 to 4), 2 orders are lost for fixing the boundary gradients, leaving just 2 orders for inner points. In other words by reducing the order by 1 with fixed gradients, the order for inner points is

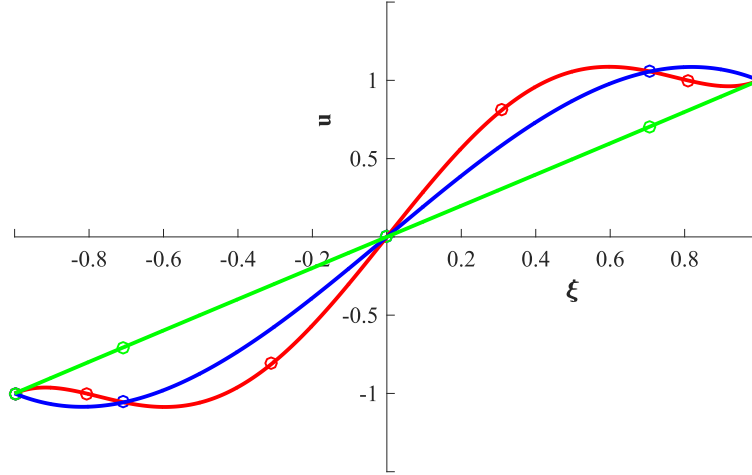


**Figure D.21.:** Solution approximation after order decrease through interpolation with fixed gradients. Red line shows the initial approximation  $O(5)$  with red points showing the collocation points, blue line shows the decreased order through truncation  $O(4)$  and green line – reinterpolation with fixed boundary gradients.

reduced by 3. However, this method is still preferable to simple truncation, as it does not provide distortion to the rest of computational domain (neighbour elements). As the collocation points are predefined, transformation matrices  $H_{M,K}$  and  $P_{M,K}$  are constant and can be computed beforehand. It is advisable to increase or to decrease the order only by 1 only, due to the minimisation of disturbances in the solution. As discussed in the previous section, the error of the order increase is limited to interpolation error:

$$E_I(M) \approx \hat{\mathbf{u}}_M^l. \quad (\text{D.110})$$

The error of order reduction is then:

$$E_T(M) \approx \hat{\mathbf{u}}_{M-3}^l. \quad (\text{D.111})$$

The procedure of order increase/decrease is in itself efficient (matrix-vector multiplication) and provide little disturbance to the solution, if the trailing coefficient is small. However, the solution of discretised PDE with high orders requires more CPU power because an LU-Decomposition of dense matrix of size  $[N_v(M-1) \times N_v(M-1)]$  is require for each element. This procedure is of computational order  $O((N_v(M-1))^3)$  [QSS00]. Thus infinite increase of polynomial order is not practical, within the proposed scheme.

Distributed data storage (within nodes and elements) and processing in binary tree permits a structured straightforward unification and splitting of elements without any distortions in the rest of the domain.

As next, imagine a splitting of an element  $l$ , which produces 2 children  $l-1$  and  $l+1$ . The numeration  $\{l-1, l, l+1\}$  is in the new resulted system after splitting, where the parent element becomes the node  $l$  (consider e.g. node “RO01” in fig. D.9). Each element is split up exactly in the middle, by keeping the order for all 3 elements

$O(M)$ :

$$\begin{cases} x_0^{l-1} = x_0^l, \\ x_M^{l-1} = x_0^{l+1} = \frac{1}{2}(x_0^l + x_M^l), \\ x_M^{l+1} = x_M^l. \end{cases} \quad (\text{D.112})$$

Surely a split with an unequal width of child elements can be advantageous but it requires a further investigation. Additionally, unequal split results in variable transformation matrices which cannot be precomputed and thus providing an additional overhead.

If the approximation order is preserved, then the splitting doesn't distort the solution. It comes from the fact that scaling and shifting of the coordinate system does not change the polynomial order:

$$\begin{cases} \xi^0 = \frac{1}{2}(\xi^{-1} - 1), \\ \xi^0 = \frac{1}{2}(\xi^{+1} + 1). \end{cases} \quad (\text{D.113})$$

Introducing coordinate transformation for sub-elements (eq. (D.113)) and using the definition of Chebyshev polynomials, it is possible to calculate the coefficients for splits directly. However, it is more straightforward to use interpolation, which results in a linear operation. Firstly, a projection matrix of  $N$  spectral coefficients in parent element ( $\xi^0$ ) to  $M$  collocation points in the *left* child element is defined:

$$\Phi_{N,M}^{l-1} = \begin{pmatrix} \varphi_0\left(\frac{1}{2}(\xi_0^{-1} - 1)\right) & \varphi_0\left(\frac{1}{2}(\xi_1^{-1} - 1)\right) & \cdots & \varphi_0\left(\frac{1}{2}(\xi_M^{-1} - 1)\right) \\ \varphi_1\left(\frac{1}{2}(\xi_0^{-1} - 1)\right) & \varphi_1\left(\frac{1}{2}(\xi_1^{-1} - 1)\right) & \cdots & \varphi_1\left(\frac{1}{2}(\xi_M^{-1} - 1)\right) \\ \vdots & \vdots & \ddots & \vdots \\ \varphi_N\left(\frac{1}{2}(\xi_0^{-1} - 1)\right) & \varphi_N\left(\frac{1}{2}(\xi_1^{-1} - 1)\right) & \cdots & \varphi_N\left(\frac{1}{2}(\xi_M^{-1} - 1)\right) \end{pmatrix} \quad (\text{D.114})$$

and similarly – the projection matrix for the *right* child element:

$$\Phi_{N,M}^{l+1} = \begin{pmatrix} \varphi_0\left(\frac{1}{2}(\xi_0^{-1} + 1)\right) & \varphi_0\left(\frac{1}{2}(\xi_1^{-1} + 1)\right) & \cdots & \varphi_0\left(\frac{1}{2}(\xi_M^{-1} + 1)\right) \\ \varphi_1\left(\frac{1}{2}(\xi_0^{-1} + 1)\right) & \varphi_1\left(\frac{1}{2}(\xi_1^{-1} + 1)\right) & \cdots & \varphi_1\left(\frac{1}{2}(\xi_M^{-1} + 1)\right) \\ \vdots & \vdots & \ddots & \vdots \\ \varphi_N\left(\frac{1}{2}(\xi_0^{-1} + 1)\right) & \varphi_N\left(\frac{1}{2}(\xi_1^{-1} + 1)\right) & \cdots & \varphi_N\left(\frac{1}{2}(\xi_M^{-1} + 1)\right) \end{pmatrix}. \quad (\text{D.115})$$

Then linear projector from values on parent collocation points ( $\xi^0$ ) to collocation points of child elements ( $\xi^{l-1}$ ,  $\xi^{l+1}$ ):

$$\begin{cases} S_N^{-1} = (\Phi_{N,N})^{-1} \Phi_{N,N}^{l-1}, \\ S_N^{+1} = (\Phi_{N,N})^{-1} \Phi_{N,N}^{l+1}. \end{cases} \quad (\text{D.116})$$

Similar to the element order reduction, the union of elements leads to an information loss, which is particularly pronounced near the boundaries. Consider fig. D.22, two elements “green” and “blue” are united. With simple reinterpolation (red dotted line), a relatively good fit is acquired, but as in the case of the order reduction, the gradients at boundaries deviate strongly. With fixed gradients (smooth) at the boundaries, a worse approximation within the volume is achieved because 2 orders are lost for gradients.

Assume that the left element ( $l - 1$ ) with order  $M$  and the right element with order ( $l + 1$ ) are united to element ( $l$ ) with order  $K$ . In order to minimise the distortion of

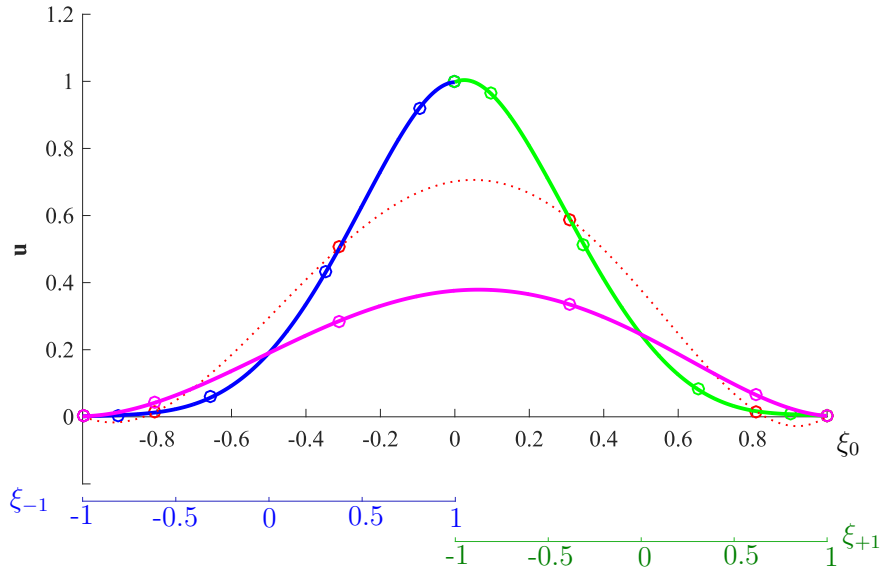


**Figure D.22.:** Solution approximation before and after element union with  $O(5)$ . Red line shows the approximation after union with, blue dotted line shows initial data of the left child element and green dotted line – initial right child. Circles show collocation points.

the rest of the system, 1 order is lost for the smoothness (equality of gradients) at the boundaries:

$$\begin{cases} \tilde{\mathbf{u}}_M^{l-1}(x_0^{l-1}) = \tilde{\mathbf{u}}_M^l(x_0^l), \\ \tilde{\mathbf{u}}_M^{l+1}(x_M^{l+1}) = \tilde{\mathbf{u}}_M^l(x_M^l), \\ \frac{\partial}{\partial x} \tilde{\mathbf{u}}_M^{l-1}(x_0^{l-1}) = \frac{\partial}{\partial x} \tilde{\mathbf{u}}_M^l(x_0^l), \\ \frac{\partial}{\partial x} \tilde{\mathbf{u}}_M^{l+1}(x_M^{l+1}) = \frac{\partial}{\partial x} \tilde{\mathbf{u}}_M^l(x_M^l), \end{cases} \quad (\text{D.117})$$

here again, the elements  $l-1$  and  $l+1$  are united to element  $l$ .

By imposing additionally gradients at the boundaries, the degrees of freedom are reduced by two. Then,  $K-2$  Gauss-Lobatto collocation points for reinterpolation are introduced, e.g.  $\xi \in [-1, +1]$

$$\boldsymbol{\xi}^{K-2} = (\xi_0^{K-2}, \xi_1^{K-2}, \dots, \xi_{K-2}^{K-2}), \quad (\text{D.118})$$

which can be mapped to the coordinate system of left child element  $l-1$  (see fig. D.22)

$$\xi^{l-1} = 2\xi^l + 1, \quad (\text{D.119})$$

and the mapping the coordinates system of the right child element  $l+1$  is

$$\xi^{l+1} = 2\xi^l - 1. \quad (\text{D.120})$$

The left half of the interpolation points is mapped from the left element  $l-1$  and the right half from the right element  $l+1$ :

$$\begin{aligned} \boldsymbol{\xi}_{l-1}^M &\rightarrow (\xi_0^{K-2}, \xi_1^{K-2}, \dots, \xi_k^{K-2}), \\ \boldsymbol{\xi}_{l+1}^M &\rightarrow (\xi_{k+1}^{K-2}, \xi_{k+2}^{K-2}, \dots, \xi_{K-2}^{K-2}), \end{aligned} \quad (\text{D.121})$$

where

$$k = \left\lfloor \frac{K-2}{2} \right\rfloor. \quad (\text{D.122})$$

This corresponds to the linear operation:

$$\begin{cases} \tilde{U}^l A = \tilde{U}^{l-1} C, \\ \tilde{U}^l B = \tilde{U}^{l+1} D, \end{cases} \quad (\text{D.123})$$

where

$$A = (\Phi_{K,K})^{-1} \begin{pmatrix} \varphi_0(\xi_0^{K-2}) & \varphi_0(\xi_1^{K-2}) & \cdots & \varphi_0(\xi_k^{K-2}) \\ \varphi_1(\xi_0^{K-2}) & \varphi_1(\xi_1^{K-2}) & \cdots & \varphi_1(\xi_k^{K-2}) \\ \vdots & \vdots & \ddots & \vdots \\ \varphi_K(\xi_0^{K-2}) & \varphi_K(\xi_1^{K-2}) & \cdots & \varphi_K(\xi_k^{K-2}) \end{pmatrix}, \quad (\text{D.124})$$

$$B = (\Phi_{K,K})^{-1} \begin{pmatrix} \varphi_0(\xi_{k+1}^{K-2}) & \varphi_0(\xi_{k+2}^{K-2}) & \cdots & \varphi_0(\xi_{K-2}^{K-2}) \\ \varphi_1(\xi_{k+1}^{K-2}) & \varphi_1(\xi_{k+2}^{K-2}) & \cdots & \varphi_1(\xi_{K-2}^{K-2}) \\ \vdots & \vdots & \ddots & \vdots \\ \varphi_K(\xi_{k+1}^{K-2}) & \varphi_K(\xi_{k+2}^{K-2}) & \cdots & \varphi_K(\xi_{K-2}^{K-2}) \end{pmatrix}, \quad (\text{D.125})$$

$$C = (\Phi_{M,M})^{-1} \begin{pmatrix} \varphi_0(2\xi_0^{K-2} + 1) & \varphi_0(2\xi_1^{K-2} + 1) & \cdots & \varphi_0(2\xi_k^{K-2} + 1) \\ \varphi_1(2\xi_0^{K-2} + 1) & \varphi_1(2\xi_1^{K-2} + 1) & \cdots & \varphi_1(2\xi_k^{K-2} + 1) \\ \vdots & \vdots & \ddots & \vdots \\ \varphi_M(2\xi_0^{K-2} + 1) & \varphi_M(2\xi_1^{K-2} + 1) & \cdots & \varphi_M(2\xi_k^{K-2} + 1) \end{pmatrix}, \quad (\text{D.126})$$

$$D = (\Phi_{N,N})^{-1} \begin{pmatrix} \varphi_0(2\xi_{k+1}^{K-2} + 1) & \varphi_0(2\xi_{k+2}^{K-2} + 1) & \cdots & \varphi_0(2\xi_{K-2}^{K-2} + 1) \\ \varphi_1(2\xi_{k+1}^{K-2} + 1) & \varphi_1(2\xi_{k+2}^{K-2} + 1) & \cdots & \varphi_1(2\xi_{K-2}^{K-2} + 1) \\ \vdots & \vdots & \ddots & \vdots \\ \varphi_N(2\xi_{k+1}^{K-2} + 1) & \varphi_N(2\xi_{k+2}^{K-2} + 1) & \cdots & \varphi_N(2\xi_{K-2}^{K-2} + 1) \end{pmatrix}. \quad (\text{D.127})$$

The boundary gradients can be preserved with:

$$\begin{cases} \tilde{U}^l \mathbf{h}_0^K = 2\tilde{U}^{l-1} \mathbf{h}_0^M, \\ \tilde{U}^l \mathbf{h}_K^K = 2\tilde{U}^{l+1} \mathbf{h}_N^N, \end{cases}, \quad (\text{D.128})$$

where

$$\mathbf{h}_0^K = (\Phi_{K,K})^{-1} \begin{pmatrix} \frac{\partial}{\partial \xi} \varphi_0(\xi_0^K) \\ \frac{\partial}{\partial \xi} \varphi_1(\xi_0^K) \\ \vdots \\ \frac{\partial}{\partial \xi} \varphi_K(\xi_0^K) \end{pmatrix}, \quad (\text{D.129})$$

$$\mathbf{h}_K^K = (\Phi_{K,K})^{-1} \begin{pmatrix} \frac{\partial}{\partial \xi} \varphi_0(\xi_K^K) \\ \frac{\partial}{\partial \xi} \varphi_1(\xi_K^K) \\ \vdots \\ \frac{\partial}{\partial \xi} \varphi_K(\xi_K^K) \end{pmatrix}. \quad (\text{D.130})$$

Here, the factor 2 comes from the interval scaling, see eq. (D.119), eq. (D.120) and refer to fig. D.22:

$$\begin{cases} d\xi^{l-1} = 2d\xi^l, \\ d\xi^{l+1} = 2d\xi^l. \end{cases} \quad (\text{D.131})$$

Now, a linear system for  $K$  collocation points in the parent element after union can be constructed:

$$\tilde{U}^l \begin{pmatrix} \mathbf{h}_0^K & A & B & \mathbf{h}_K^K \end{pmatrix} = \begin{pmatrix} \tilde{U}^{l-1} & \tilde{U}^{l+1} \end{pmatrix} \begin{pmatrix} 2\mathbf{h}_0^M & C & 0 & 0 \\ 0 & 0 & D & 2\mathbf{h}_N^N \end{pmatrix}. \quad (\text{D.132})$$

Then the solution on  $K$  collocation points:

$$\tilde{\mathbf{U}}^l = \left( \tilde{\mathbf{U}}^{l-1} \quad \tilde{\mathbf{U}}^{l+1} \right) \mathbf{Q}, \quad (\text{D.133})$$

with

$$\mathbf{Q} = \begin{pmatrix} 2\mathbf{h}_0^M & C & 0 & 0 \\ 0 & 0 & D & 2\mathbf{h}_N^N \end{pmatrix} \left( \mathbf{h}_0^K \quad A \quad B \quad \mathbf{h}_K^K \right)^{-1}, \quad (\text{D.134})$$

which is constant for given  $M$ ,  $N$  and  $K$ . However, it more practical to treat child elements separately, thus:

$$\tilde{\mathbf{U}}^l = \tilde{\mathbf{U}}^{l-1} \mathbf{Q}_{M,K}^a + \tilde{\mathbf{U}}^{l+1} \mathbf{Q}_{N,K}^b, \quad (\text{D.135})$$

where  $\mathbf{Q}_{M,K}^a$  and  $\mathbf{Q}_{N,K}^b$  are upper (rows 0 to  $M$ ) and lower parts (rows  $M + 1$  to  $M + N$ ) of the matrix  $\mathbf{Q}$  respectively:

$$\begin{pmatrix} \mathbf{Q}_{M,K}^a \\ \mathbf{Q}_{N,K}^b \end{pmatrix} = \mathbf{Q}. \quad (\text{D.136})$$



# List of Figures

2.1.	Change of an extensive quantity in control volume (in 2D) . . . . .	6
3.1.	Aliasing effect. Black line - original signal, red line - bad sampled signal on 4 collocation points. . . . .	26
3.2.	Spectral approximation of discontinuity (left) and the corresponding spectral coefficients (right) . . . . .	26
3.3.	Algorithm of incremental method . . . . .	30
3.4.	Algorithm of modified Newton method . . . . .	31
3.5.	Information flow in binary tree for APSM. . . . .	37
3.6.	Structure of the global Jacobian for APSM and its factorisation. Blocks shown in grey remains unchanged, red blocks are eliminated, modified blue blocks are propagated to the upper level, modified green blocks are used to reconstruct the solution from local boundary values. . . . .	38
3.7.	Gauss-Lobatto collocation points . . . . .	40
3.8.	Converging series with zero even coefficients. . . . .	41
3.9.	Solution approximation after order increase. Red line shows the initial approximation $O(5)$ with red points showing the collocation points, blue dotted line shows the increased order $O(6)$ with $a_6 = 0$ . . . . .	42
3.10.	Solution approximation after order decrease through interpolation with fixed gradients. Red line shows the initial approximation $O(5)$ with red points showing the collocation points, blue line shows the decreased order through truncation $O(4)$ and green line - reinterpolation with fixed boundary gradients. . . . .	42
3.11.	Solution approximation before and after element split with $O(5)$ . Red line shows the initial approximation, blue dotted line shows left child element with and green dotted line – right child. Circles show collocation points. . . . .	44
3.12.	Solution approximation before and after element union with $O(5)$ . Red line shows the approximation after union with, blue dotted line shows initial data of the left child element and green dotted line – initial right child. Circles show collocation points. . . . .	44
3.13.	Grid adaptation Algorithm. . . . .	46
4.1.	Six illustrative GRBFs $\varphi_i(E)$ (solid lines) with $\Delta E = 2000 \text{ cm}^{-1}$ and $\Sigma = 2402 \text{ cm}^{-1}$ from eq. (4.13), sum of the six GRBFs, $S(E)$ (dashed line), and a test function $I_j(E)$ for $j = 2$ (dotted line) [KYB <sup>+</sup> 18]. . . . .	53
4.2.	Schematic potential energy diagram, including zero-point energy, relative to 25DMF2H (adapted from [FSO13]). . . . .	56
4.3.	Temperature dependence of the rate constant (left) and Pressure dependence of the rate constant (right). . . . .	58

4.4.	Relative error of pressure dependence of the rate constant . . . . .	59
4.5.	Calculated time-dependent rate constants. . . . .	59
4.6.	Relative error of calculated time-dependent rate constants. . . . .	59
4.7.	Dependence of the relative error on the linear size. System for thermal (solid lines) and chemical (dashed lines) activation conditions, with CDM (blue), fixed SM (red) and adaptive SM (green) at $T = 1100$ K, $p = 1$ bar, $E_{max} = 52318 \text{ cm}^{-1}$ , reference method: CDM with $N = 5238$ . . . . .	60
4.8.	Relative computation times for a given method necessary to obtain rate constants with given relative errors. System for thermal (solid lines) and chemical (dashed lines) activation conditions, with CDM (blue), fixed SM (red) and adaptive SM (green) at $T = 1100$ K, $p = 1$ bar, $E_{max} = 52318 \text{ cm}^{-1}$ , reference method: CDM with $N = 5238$ . . . . .	61
4.9.	Time dependence of the total population. . . . .	62
4.10.	Schematic potential energy diagram, including zero-point energy, relative to Propyne. . . . .	65
4.11.	Example of allene to propyne isomerisation at $T = 1400$ K and $P = 0.5$ bar. Colour intensity represent time evolution. . . . .	66
4.12.	Summary of reaction rates of allene isomerisation. . . . .	67
4.13.	Rate constant comparison for $T = 1200$ K and $P = 0.5$ bar: Time dependent vs. asymptotic rate constant (left); evolution of concentration with time dependent vs. fixed asymptotic rate constant (right). Red corresponds to allene ( $k_{p \leftarrow a}$ and $[a\text{-C}_3\text{H}_4]$ ), blue – propyne ( $k_{a \leftarrow p}$ and $[p\text{-C}_3\text{H}_4]$ ). Solid lines represent time dependent values of rate constants, dashed line – fixed asymptotic rate constants. . . . .	68
4.14.	Relative error for rate constants at different temperatures: concentration of allene (left); concentration of propyne (right). . . . .	68
4.15.	Resolution test for computation of rate constant $k_{p \leftarrow a}$ : relative error over time for $T = 1200$ K and $P = 1$ bar (left); dependence of relative error on temperature. All data is in relation to $N_{BF} = 200$ . Dotted line shows maximum of error, solid line asymptotic error. . . . .	68
5.1.	Pressure and temperature dependence of ignition delay computed with Warnatz (left) and Keromnes (right) mechanisms for stoichiometric mixture of hydrogen with air. Solid lines correspond to computations with Phlogia, dotted lines – HOMREA, dashed line – CHEMKIN. Blue colour represents pressure 1 bar, green – 10 bar and red – 50 bar. . . . .	73
5.2.	Equivalence ration and temperature dependence of ignition delay computed with Warnatz (left) and Keromnes (right) mechanisms for pressure 10 bar (left). Red represents $\Phi = 0.2$ , green – $\Phi = 1$ and blue – $\Phi = 5$ . Solid lines correspond to computations with Phlogia, dotted lines – HOMREA and dashed lines – CHEMKIN. . . . .	74
5.3.	Comparison of ignition delay time computed with Warnatz (dashed lines), Keromnes (dotted lines) and ELTE (solid lines) mechanisms: On the left – Temperature dependence for pressure 1 (blue), 4 (green) and 16 bar (red); On the right – Equivalence ratio dependence for temperature 900 (blue), 1100 (green) and 1300 K (red). Circles are experimental results of J. Herzler and C. Naumann [HN09]; Crosses represent experimental data of Y. Zhang et. al. [ZHW <sup>+</sup> 12]. Mixture composition $X_{\text{H}_2} = 0.035$ , $X_{\text{O}_2} = 0.035$ and $X_{\text{Ar}} = 0.932$ . . . . .	74

5.4.	Pressure wave propagation after ignition shown on profiles of temperature (left) and pressure (right) for $t \in [0, 10^{-5}]$ . . . . .	76
5.5.	Stationary profiles of hydrogen-oxygen flame for species: Mole fraction of $H_2$ (top-left), mole fraction of $H_2O$ (top-right), mole fraction of $OH$ (bottom-left) and mole fraction of $HO_2$ (bottom-right). Solid line correspond to Phlogia results and dotted line – INSFLA. . . . .	77
5.6.	Stationary profiles of hydrogen-oxygen flame for temperature (left) and pressure (right). Solid line corresponds to Phlogia results and dotted line – INSFLA. Blue colour represents $RTOL=10^{-4}$ , red – $RTOL=10^{-3}$ . . . . .	77
5.7.	Relative amplitude of numerical oscillations (left) and relative error for pressure (right). . . . .	78
5.8.	Comparison of computed laminar burning velocities with experimental measurements, adopted from [BKKY] . . . . .	80
5.9.	Laminar burning velocities vs. experiment type, adopted from [BKKY].	81
5.10.	Geometrical configuration of narrow duct: half-open (left) and closed (right). Red point indicates the hot spot position. . . . .	83
5.11.	Comparison of stationary tulip flame with heat release rate and flow lines. Upper half results attained in [MR04], lower half – this work. . . . .	86
5.12.	Stages of tulip flame formation. Left half schlieren images adapted from [XMSM12], right half are computational schlieren images (this work). . . . .	86
5.13.	Flame position (top), flame velocity (middle) and sequence of flame front contours (bottom). . . . .	87
5.14.	Comparison of flame tip velocities for different width/length ratios. . . . .	88
5.15.	Comparison of flame tip inversion times for different width/length ratios. Zero corresponds to plane flame. . . . .	89
5.16.	Comparison of quasi-stationary tulip configurations for different width/length ratios. . . . .	89
5.17.	Flame development in closed duct $10 \times 100$ mm. Solid black line shows flame front, colour codes the pressure, cyan arrows represent velocity field. . . . .	91
5.18.	Vorticity of quasi-stationary tulip flame: vorticity with overlapped velocity field $\omega$ (left), vorticity generation $\partial\omega/\partial t$ (right). Black arrows represent local velocity vector, grey line corresponds to flame position. . . . .	92
5.19.	Vorticity of forming secondary tulip flame: vorticity with overlapped velocity field $\omega$ (left), vorticity generation $\partial\omega/\partial t$ (right), initiation of the secondary tulip (top), later stages of secondary tulip (bottom). Black arrows represent local velocity vector, grey line corresponds to flame position. . . . .	93
5.20.	Development of finger flame in thermochemical state space in projection to $H_2O$ , $H_2$ , $OH$ (left) and to $H$ , $O$ , $OH$ (right). . . . .	94
5.21.	Development of plane flame in thermochemical state space in projection to $H_2O$ , $H_2$ , $OH$ (left) and to $H$ , $O$ , $OH$ (right). . . . .	94
5.22.	Development of tulip flame in thermochemical state space in projection to $H_2O$ , $H_2$ , $OH$ (left) and to $H$ , $O$ , $OH$ (right). . . . .	94
5.23.	Development of secondary tulip and quasi-steady tulip flame in thermochemical state space in projection to $H_2O$ , $H_2$ , $OH$ (left) and to $H$ , $O$ , $OH$ (right). . . . .	95

5.24. Stages of flame development in half-open channel. On the left schlieren images of experimental observations [XWH <sup>+</sup> 11]; On the right are computational schlieren images (this work). . . . .	95
5.25. Flame position (top), flame velocity (middle) and sequence of flame front contours (bottom). . . . .	97
5.26. Comparison of turbulent flame tip velocities for different width/length ratios. . . . .	97
5.27. Flame development in half open duct 10 × 100 mm. Solid black line shows flame front, colour codes the pressure, cyan arrows represent velocity field. . . . .	98
5.28. Development of finger flame of half open duct in thermochemical state space in projection to H <sub>2</sub> O, H <sub>2</sub> , OH (left) and to H, O, OH (right). .	100
5.29. Last stages of finger flame of half open duct in thermochemical state space, in projection to H <sub>2</sub> O, H <sub>2</sub> , OH (left) and to H, O, OH (right). .	100
5.30. Development of turbulent flame of half open duct in thermochemical state space in projection to H <sub>2</sub> O, H <sub>2</sub> , OH (left) and to H, O, OH. . .	100
5.31. Schematic of experimental setup of micro scale combustor, adapted from [NTT <sup>+</sup> 16]. . . . .	101
5.32. Modelling configuration of micro flow channel. . . . .	102
5.33. Integral camera image: camera view through cylinder (left), projection of rotated layers to horizontal plane (right). . . . .	106
5.34. Chemiluminescence in micro flow reactor for various fuel composition. In each frame, the upper half corresponds to experimental results [NTT <sup>+</sup> 16], the lower half – numerical energy release rate (this work) .	107
5.35. Comparison of computed flame position with experimental measurements, adopted from [NTT <sup>+</sup> 16]. . . . .	107
5.36. Weak flame stationary profiles in 2D for volume ratios of CO=50 % and H <sub>2</sub> =50 % ifn fuel. . . . .	108
5.37. Projection of thermochemical state of stationary flame for various CO to H <sub>2</sub> ratios: blue – 10 %, red – 25 %, orange – 50 %, violet – 75 %, green – 90 % CO. . . . .	108
5.38. Species profiles for various CO to H <sub>2</sub> ratios: blue – 10 %, red – 25 %, orange – 50 %, violet – 75 %, green – 90 % CO. Dashed lines correspond to reaction products CO <sub>2</sub> and H <sub>2</sub> O. . . . .	110
6.1. Width of the initiation hot spot $l$ mm vs. folding factor $\Sigma$ . . . . .	113
6.2. Flame speed as a function of $\Sigma$ : red solid line – actual flame front speed, blue solid line – quasi stationary ignition shock wave speed, dotted line – extrapolated from laminar flame speed with $\Sigma = 1$ , dashed line – shock wave speed for $\Sigma = 1$ . . . . .	114
6.3. Flame and shock for $\Sigma = 6.0$ . On the Left: Position of the flame front (red) and the ignition shock wave (red); On the right Velocity of the flame front (red) and the velocity of the ignition shock wave (blue). .	115
6.4. Flame and shock for $\Sigma = 6.25$ . On the Left: Position of the flame front (red) and the ignition shock wave (red); On the right Velocity of the flame front (red) and the velocity of the ignition shock wave (blue).115	

6.5.	Comparison of critical velocities for $\Sigma = 5.75$ (left) and $\Sigma = 6.25$ (right). Solid line – flame speed, dashed line – sound velocity at the position of maximal pressure, dotted line – sound velocity in the products. . . . .	116
6.6.	On the left: evolution of pressure profile for $\Sigma = 6.25$ before and at the DDT. On the right: zoom of the pressure profile for $\Sigma = 6.25$ at the DDT: solid line $t=3.12378 \mu s$ , dotted line $t=3.12373 \mu s$ , dashed line $t=3.12382 \mu s$ . . . . .	116
6.7.	The radical profile of $H_2O_2$ specific mole numbers with the folding factor $\Sigma = 5.75$ (left) and $\Sigma = 6.25$ (right) over several instances of time.	117
6.8.	3D projections of the profiles during ignition and deflagration stages of specific mole numbers of $H_2$ , $H_2O$ and $OH$ for $\Sigma = 5.75$ (top) and for $\Sigma = 6.25$ (bottom). Solid line indicate stationary deflagration. Grey lines represent corresponding 2D projections. . . . .	119
6.9.	Sigma dependence of stationary deflagration profiles in projection to specific mole numbers of $H_2$ , $H_2O$ , $OH$ (top) and $H$ , $O$ , $OH$ (bottom). Grey lines represent corresponding 2D projections. . . . .	120
6.10.	3D projections of the profiles during transition of specific mole numbers of $H_2$ , $H_2O$ , $OH$ (top) and $H$ , $O$ , $OH$ (bottom). Blue lines correspond to deflagration regime, dashed red lines – transition phase and solid red line – detonation. Grey lines represent corresponding 2D projections.	121
6.11.	Comparison of critical velocities of free flame depending on $\Sigma$ . On the left: deflagration regimes, on the right: regimes including transition. Velocity of flame front (red), velocity of burned gases (blue), speed of sound in products (dashed), extrapolated flame speed (dotted). . . . .	123
6.12.	Dependance of thermodynamic properties on $\Sigma$ : pressure (left) and temperature (right) . . . . .	123
6.13.	Dependance of intermediate species profiles on $\Sigma$ : $OH$ (left) and $H_2O_2$ (right). . . . .	124
6.14.	3D projections of stationary profiles for different $\Sigma$ of specific mole numbers of $H_2$ , $H_2O$ , $OH$ (top) and $H$ , $O$ , $OH$ (bottom). Black lines show state $\Sigma = 8.4$ . Grey lines represent corresponding 2D projections.	125
6.15.	3D projections during DDT of a free flame for specific mole numbers of $H_2$ , $H_2O$ , $OH$ (top) and $H$ , $O$ , $OH$ (bottom). Solid blue lines show initial stationary deflagration mode and solid red line – the final detonation regime. Grey lines represent corresponding 2D projections.	126
A.1.	General orthogonal coordinates. . . . .	131
B.2.	Static 1D coordinate transformation. . . . .	137
B.3.	Dynamic 1D coordinate transformation. . . . .	138
B.4.	Static 2D coordinate transformation. . . . .	139
C.5.	ODE Solver performance for Semenov's Explosion . . . . .	147
C.6.	ODE Solver performance for Reaction of Robertson . . . . .	148
C.7.	ODE Solver performance for HIRES . . . . .	149
D.8.	Structure of the Jacobian of the global spectral element system. . . . .	154
D.9.	Information hierarchy (binary tree). . . . .	158
D.10.	Information flow in binary tree. . . . .	158
D.11.	Data structure for element R010 before elimination. . . . .	159
D.12.	Data structure for element R010 after elimination. . . . .	159

D.13.	Data structure for element R011 before elimination. . . . .	159
D.14.	Data structure for element R011 after elimination. . . . .	160
D.15.	Data structure for node R01 before elimination (left) and after elimination (right). . . . .	160
D.16.	Structure of global Jacobian before elimination. Red lines show the parts being eliminated. . . . .	161
D.17.	Structure of global Jacobian after 1 (left) and 2 (right) step of elimination.	161
D.18.	Structure of global Jacobian after 3 (left) and 4 (right) step of elimination.	162
D.19.	Solution approximation after order decrease through truncation. Red line shows the initial approximation $O(5)$ with red points showing the collocation points, blue line shows the decreased order $O(4)$ . . . . .	171
D.20.	Approximation of $f(x) = 1/(1 + (x/5)^2)$ (black line) with order 6 (blue line) and with order 14 (red line). . . . .	172
D.21.	Solution approximation after order decrease through interpolation with fixed gradients. Red line shows the initial approximation $O(5)$ with red points showing the collocation points, blue line shows the decreased order through truncation $O(4)$ and green line – reinterpolation with fixed boundary gradients. . . . .	173
D.22.	Solution approximation before and after element union with $O(5)$ . Red line shows the approximation after union with, blue dotted line shows initial data of the left child element and green dotted line – initial right child. Circles show collocation points. . . . .	175

# List of Tables

2.1. Coefficients for fits of $\Omega^{(1,1)*}$ and $\Omega^{(2,2)*}$ . . . . .	14
5.1. Resolution test with APSM in unconfined settings for stoichiometric conditions. . . . .	81
5.2. Duct configurations used in study. . . . .	83
5.3. Micro flow channel configurations used in study. . . . .	105
6.1. Effect of tolerances on solution of DDT. . . . .	116
A.1. Spherical and Cylindrical coordinate transformations. . . . .	136



# Bibliography

- [ADP06] Atkins, P. W. und Julio De Paula: *Atkins Physical chemistry*. Oxford University Press, Oxford, 8. ed. Auflage, 2006, ISBN 978-0-19-870072-2.
- [AHF98] Aung, K. T., M. I. Hassan und G. M. Faeth: *Effects of pressure and nitrogen dilution on flame/stretch interactions of laminar premixed H<sub>2</sub>/O<sub>2</sub>/N<sub>2</sub> flames*. *Combustion and flame*, 112(1-2):1–15, 1998.
- [BBH89] Brown, Peter N, George D Byrne und Alan C Hindmarsh: *VODE: A variable-coefficient ODE solver*. *SIAM journal on scientific and statistical computing*, 10(5):1038–1051, 1989.
- [BCJD09] Burke, Michael P., Zheng Chen, Yiguang Ju und Frederick L. Dryer: *Effect of cylindrical confinement on the determination of laminar flame speeds using outwardly propagating flames*. *Combustion and Flame*, 156(4):771–779, 2009.
- [BGG<sup>+</sup>04] Bykov, Viatcheslav, Igor Goldfarb, Vladimir Gol'dshtein, Leonid Kagan und Gregory Sivashinsky: *Effects of hydraulic resistance and heat losses on detonability and flammability limits*. *Combustion Theory and Modelling*, 8(2):413–424, 2004.
- [BHB04] Burrage, P. M., R. Herdiana und K. Burrage: *Adaptive stepsize based on control theory for stochastic differential equations*. *Journal of Computational and Applied Mathematics*, 170(2):317 – 336, 2004.
- [BKKY] Bykov, Viatcheslav., Aleksey Kiverin, Andrey Koksharov und Ivan Yakovenko: *Analysis of transient combustion with the use of contemporary CFD techniques*. *Computers and Fluids*. In review.
- [BM87] Bayliss, A. und B. J. Matkowsky: *Fronts, relaxation oscillations, and period doubling in solid fuel combustion*. *Journal of Computational Physics*, 71(1):147–168, 1987.
- [Boy89] Boyd, John P.: *Chebyshev & Fourier Spectral Methods*. Lecture notes in engineering. Springer, Berlin, 1989, ISBN 3-540-51487-2.
- [Bro67] Broyden, C. G.: *Quasi-Newton Methods and their Application to Function Minimisation*. *Mathematics of Computation*, 21(99):pp. 368–381, 1967.
- [BS00] Brailovskya, I. und G. Sivashinsky: *Hydraulic resistance and multiplicity of detonation regimes*. *Combustion and flame*, 122(1):130–138, 2000.

- [BSL07] Bird, Robert Byron, Warren E. Stewart und Edwin N. Lightfoot: *Transport phenomena*. Wiley, New York, revised 2. ed. Auflage, 2007, ISBN 978-0-470-11539-8.
- [BVAL12] Bychkov, Vitaly, Damir Valiev, V'yacheslav Akkerman und Chung K Law: *Gas compression moderates flame acceleration in deflagration-to-detonation transition*. Combustion Science and Technology, 184(7-8):1066–1079, 2012.
- [BVE08] Bychkov, Vitaly, Damir Valiev und Lars Erik Eriksson: *Physical mechanism of ultrafast flame acceleration*. Physical review letters, 101(16):164501, 2008.
- [CH96] Clavin, Paul und Longting He: *Acoustic effects in the nonlinear oscillations of planar detonations*. Physical Review E, 53(5):4778, 1996.
- [Cla00] Clavin, Paul: *Dynamics of combustion fronts in premixed gases: from flames to detonations*. Proceedings of the Combustion Institute, 28(1):569–585, 2000.
- [CM00] Chorin, Alexandre Joel und Jerrold E. Marsden: *A mathematical introduction to fluid mechanics*. Texts in applied mathematics. Springer, New York, 3. ed., corr. 4. print. Auflage, 2000, ISBN 3-540-97918-2.
- [CS96] Clanet, Christophe und Geoffrey Searby: *On the “tulip flame” phenomenon*. Combustion and flame, 105(1-2):225–238, 1996.
- [Dah05] Dahoe, A. E.: *Laminar burning velocities of hydrogen–air mixtures from closed vessel gas explosions*. Journal of Loss Prevention in the Process Industries, 18(3):152–166, 2005.
- [DDHR99] Damm, Matthias, Frank Deckert, Horst Hippler und Gunda Rink: *Specific rate constants for the fragmentation of vibrationally excited benzyl radicals*. Phys. Chem. Chem. Phys., 1(1):81–90, 1999.
- [DES82] Dembo, R., S. Eisenstat und T. Steihaug: *Inexact Newton Methods*. SIAM Journal on Numerical Analysis, 19(2):400–408, 1982.
- [DHT81] Delfour, M., W. Hager und F. Trochu: *Discontinuous Galerkin methods for ordinary differential equations*. Mathematics of Computation, 36(154):455–473, 1981.
- [DJ89] Deshaies, B. und G. Joulin: *Flame-speed sensitivity to temperature changes and the deflagration-to-detonation transition*. Combustion and flame, 77(2):201–212, 1989.
- [DLW99] Davis, Scott G., Chung K. Law und Hai Wang: *Propyne pyrolysis in a flow reactor: An experimental, RRKM, and detailed kinetic modeling study*. The Journal of Physical Chemistry, 103(30):5889–5899, 1999.
- [DM77] Dennis, J. E. Jr. und Jorge J. Moré: *Quasi-Newton Methods, Motivation and Theory*. SIAM Journal on Scientific Computing, 19(1):46 – 89, 1977.

- [DR09] Dunn-Rankin, Derek: *Deflagrations in Closed Tubes*. Combustion Phenomena: Selected Mechanisms of Flame Formation, Propagation and Extinction, Seite 93, 2009.
- [DRBS88] Dunn-Rankin, D., P. K. Barr und R. F. Sawyer: *Numerical and experimental study of “tulip” flame formation in a closed vessel*. In: *Symposium (International) on Combustion*, Band 21, Seiten 1291–1301. Elsevier, 1988.
- [DRS98] Dunn-Rankin, D. und R. F. Sawyer: *Tulip flames: changes in shape of premixed flames propagating in closed tubes*. *Experiments in fluids*, 24(2):130–140, 1998.
- [DSTW91] Dowdy, David R., David B. Smith, Simon C. Taylor und Alan Williams: *The use of expanding spherical flames to determine burning velocities and stretch effects in hydrogen/air mixtures*. *Symposium (International) on Combustion*, 23(1):325–332, 1991.
- [DT02] Driscoll, Tobin A und Lloyd N Trefethen: *Schwarz-christoffel mapping*, Band 8. Cambridge University Press, 2002.
- [EJL04] Eriksson, Kenneth, Claes Johnson und Anders Logg: *Explicit Time-Stepping for Stiff ODEs*. *SIAM Journal on Scientific Computing*, 25(4):1142 – 1157, 2004.
- [EL91] Egolfopoulos, F. N. und C. K. Law: *An experimental and computational study of the burning rates of ultra-lean to moderately-rich H<sub>2</sub>/O<sub>2</sub>/N<sub>2</sub> laminar flames with pressure variations*. *Symposium (International) on Combustion*, 23(1):333–340, 1991.
- [Ell28] Ellis, O.C. de C.: *Flame movement in gaseous explosive mixtures*. *Fuel in Science and Practice*, 7, 1928.
- [FK63] Freiwald, H. und H. W. Koch: *Spherical detonations of acetylene-oxygen-nitrogen mixtures as a function of nature and strength of initiation*. In: *Symposium (International) on Combustion*, Band 9, Seiten 275–281. Elsevier, 1963.
- [For03] Forst, Wendell: *Unimolecular reactions: a concise introduction*. Cambridge University Press, 2003, ISBN 978-0521821902.
- [FSO13] Friese, Philipp, John M Simmie und Matthias Olzmann: *The reaction of 2,5-dimethylfuran with hydrogen atoms—An experimental and theoretical study*. *Proceedings of the Combustion Institute*, 34(1):233–239, 2013.
- [GAB14] García-Armingol, Tatiana und Javier Ballester: *Flame chemiluminescence in premixed combustion of hydrogen-enriched fuels*. *International Journal of Hydrogen Energy*, 39(21):11299–11307, 2014.
- [GBS92] Gonzalez, M., R. Borghi und A. Saouab: *Interaction of a flame front with its self-generated flow in an enclosure: The “tulip flame” phenomenon*. *Combustion and flame*, 88(2):201–220, 1992.

- [GFB<sup>+</sup>11] Giri, Binod R., Ravi X. Fernandes, Tobias Bentz, Horst Hippler und Matthias Olzmann: *High-temperature kinetics of propyne and allene: Decomposition vs. isomerization*. Proceedings of the Combustion Institute, 33(1):267–272, 2011.
- [GIS88] Gostintsev, Yu. A., A. G. Istratov und Yu. V. Shulenin: *Self-similar propagation of a free turbulent flame in mixed gas mixtures*. Combustion, Explosion and Shock Waves, 24(5):563–569, 1988.
- [GJ72] Günther, R. und G. Janisch: *Measurements of burning velocity in a flat flame front*. Combustion and Flame, 19(1):49–53, 1972.
- [Gla41] Glasstone, Samuel: *Statistical treatment of reaction rates*. The theory of rate processes, 1941.
- [GLT83] Gilbert, R. G., K. Luther und J. Troe: *Theory of Thermal Unimolecular Reactions in the Fall-off Range. II. Weak Collision Rate Constants*. Berichte der Bunsengesellschaft für physikalische Chemie, 87(2):169–177, 1983.
- [Gri10] Griffiths, David F.: *Numerical Methods for Ordinary Differential Equations : Initial Value Problems*. Springer, London, 2010, ISBN 978-0-85729-147-9.
- [GS90] Gilbert, Robert G. und Sean C. Smith: *Theory of unimolecular and recombination reactions*. Physical Chemistry Texts. Blackwell Science Ltd, 1990, ISBN 978-0632027491.
- [Gus88] Gustafsson, Kjell: *API stepsize control for the numerical solution of ordinary differential equations*. BIT Numerical Mathematics, 28(2):279 – 287, 1988.
- [GYC81] Garcia-Ybarra, L. T. und P. Clavin: *Cross-Transport Effects in Nonadiabatic Premixed Flames*. Combustion in Reactive Systems, Seiten 463–481, 1981.
- [GZKK13] Goloviznin, V. M., M. A. Zaitsev, S. A. Karabasov und I. A. Korotkin: *New Computational Fluid Dynamics Algorithms for Multiprocessor Computers (in Russian)*. MSU Publishing, Moscow, Russia, 2013, ISBN 978-5-211-06426-3.
- [Hai10] Hairer, Ernst: *Solving Ordinary Differential Equations II : Stiff and Differential-Algebraic Problems*. Springer, Berlin, Heidelberg, 2010, ISBN 978-3-642-05221-7.
- [Har87] Harten, Ami: *On the nonlinearity of modern shock-capturing schemes*. In: *Wave Motion: Theory, Modelling, and Computation*, Seiten 147–201. Springer, 1987.
- [HCB54] Hirschfelder, Joseph O., Charles F. Curtiss und Robert Byron Bird: *Molecular theory of gases and liquids*. Structure of matter series. Wiley, New York, 1954.

- [He96] He, Longting: *Theoretical determination of the critical conditions for the direct initiation of detonations in hydrogen-oxygen mixtures*. Combustion and Flame, 104(4):401–418, 1996.
- [Her66] Herzberg, Gerhard: *Molecular spectra and molecular structure. Vol. 3: Electronic spectra and electronic structure of polyatomic molecules*. New York: Van Nostrand, Reinhold, 1966, 1966.
- [Hin29] Hinshelwood, Cyril Norman: *Kinetics of chemical change in gaseous systems*. Oxford University Press, Oxford, 1929.
- [HN09] Herzler, J. und C. Naumann: *Shock-tube study of the ignition of methane/ethane/hydrogen mixtures with hydrogen contents from 0% to 100% at different pressures*. Proceedings of the Combustion Institute, 32(1):213 – 220, 2009.
- [HNM<sup>+</sup>89] Hidaka, Yoshiaki, Takuji Nakamura, Aya Miyauchi, Toshihiko Shiraishi und Hiroyuki Kawano: *Thermal decomposition of propyne and allene in shock waves*. International Journal of Chemical Kinetics, 21(8):643–666, 1989.
- [HPR96] Holbrook, Kenneth A., Michael J. Pilling und Struan H. Robertson: *Unimolecular reactions*. Wiley, Chichester, 2. ed. Auflage, 1996, ISBN 0-471-92268-4.
- [Hul72] Hulme, Bernie L.: *One-step piecewise polynomial Galerkin methods for initial value problems*. Mathematics of Computation, 26:415–426, 1972.
- [IKL11] Ivanov, M. F., A. D. Kiverin und M. A. Liberman: *Hydrogen-oxygen flame acceleration and transition to detonation in channels with no-slip walls for a detailed chemical reaction model*. Physical Review E, 83(5):056313, 2011.
- [JLW78] Jones, A. R., S. A. Lloyd und Felix Jiri Weinberg: *Combustion in heat exchangers*. Proc. R. Soc. Lond., 360(1700):97–115, 1978.
- [Joh05] Johnson, Richard W.: *A B-spline collocation method for solving the incompressible Navier–Stokes equations using an ad hoc method: The boundary residual method*. Computers & fluids, 34(1):121–149, 2005.
- [Kai03] Kailasanath, K.: *Recent developments in the research on pulse detonation engines*. AIAA journal, 41(2):145–159, 2003.
- [KBKS18] Koksharov, Andrey, Viatcheslav Bykov, Leonid Kagan und Gregory Sivashinsky: *Deflagration-to-detonation transition in an unconfined space*. Combustion and Flame, 195:163–169, 2018. Special Commemorative Issue: Professor Chung King (Ed) Law 70th Birthday.
- [KCG03] Kee, Robert J., Michael Elliott Coltrin und Peter Glarborg: *Chemically reacting flow : theory and practice*. Wiley Interscience, Hoboken, NJ, 2003, ISBN 978-0-471-26179-7.

- [KF01] Kwon, O. C. und G. M. Faeth: *Flame/stretch interactions of premixed hydrogen-fueled flames: Measurements and predictions*. Combustion and Flame, 124(4):590–610, 2001.
- [KG09] Karabasov, S. A. und V. M. Goloviznin: *Compact Accurately Boundary-Adjusting high-REsolution Technique for fluid dynamics*. Journal of Computational Physics, 228(19):7426–7451, 2009.
- [KK68] Korn, Granino Arthur und Theresa M. Korn: *Mathematical handbook for scientists and engineers : definitions, theorems, and formulas for reference and review*. McGraw-Hill handbook. McGraw-Hill, New York, 2., enl. and rev. ed. Auflage, 1968, ISBN 0-07-035370-0.
- [KKGJ12] Kuznetsov, M., S. Kobelt, J. Grune und T. Jordan: *Flammability limits and laminar flame speed of hydrogen-air mixtures at sub-atmospheric pressures*. International Journal of Hydrogen Energy, 37(22):17580–17588, 2012.
- [KKIL13] Kiverin, Alexey D., David R. Kassoy, Mikhail F. Ivanov und Michael A. Liberman: *Mechanisms of ignition by transient energy deposition: Regimes of combustion wave propagation*. Physical Review, 87(3):033015, 2013.
- [KKM94] Kiefer, J. H., S. S. Kumaran und P. S. Mudipalli: *The mutual isomerization of allene and propyne*. Chemical physics letters, 224(1-2):51–55, 1994.
- [KLAM17] Kuznetsov, M., A. Lelyakin, V. Alekseev und I. Matsukov: *Detonation Transition in Relatively Short Tubes*. In: *30th International Symposium on Shock Waves 1*, Seiten 481–485. Springer, 2017.
- [KLM10] Kuznetsov, M., M. Liberman und I. Matsukov: *Experimental study of the preheat zone formation and deflagration to detonation transition*. Combustion Science and Technology, 182(11-12):1628–1644, 2010.
- [KLW97] Karpov, Vladimir P., Andrei N. Lipatnikov und Piotr Wolanski: *Finding the markstein number using the measurements of expanding spherical laminar flames*. Combustion and Flame, 109(3):436–448, 1997.
- [KMH<sup>+</sup>13] Kéromnès, Alan, Wayne K. Metcalfe, Karl A. Heufer, Nicola Donohoe, Apurba K. Das, Chih Jen Sung, Jürgen Herzler, Clemens Naumann, Peter Griebel, Olivier Mathieu, Michael C. Krejci, Eric L. Petersen, William J. Pitz und Henry J. Curran: *An experimental and detailed chemical kinetic modeling study of hydrogen and syngas mixture oxidation at elevated pressures*. Combustion and Flame, 160(6):995 – 1011, 2013.
- [KMS<sup>+</sup>97] Kiefer, J. H., P. S. Mudipalli, S. S. Sidhu, R. D. Kern, B. S. Jursic, K. Xie und H. Chen: *Unimolecular dissociation in allene and propyne: the effect of isomerization on the low-pressure rate*. The Journal of Physical Chemistry, 101(22):4057–4071, 1997.

- [KMV<sup>+</sup>12] Krejci, M. C., O. Mathieu, A. J. Vissotski, S. Ravi, T. G. Sikes, E. L. Petersen, A. Keromnes, W. Metcalfe und H. J. Curran: *Laminar Flame Speed and Ignition Delay Time Data for the Kinetic Modeling of Hydrogen and Syngas Fuel Blends*. Volume 2: Combustion, Fuels and Emissions, Parts A and B, 2(PARTS A AND B):931, 2012.
- [KNL10] Kamenskihs, Vsevolods, Hoi Dick Ng und John HS Lee: *Measurement of critical energy for direct initiation of spherical detonations in stoichiometric high-pressure H<sub>2</sub>-O<sub>2</sub> mixtures*. Combustion and Flame, 157(9):1795–1799, 2010.
- [KNT<sup>+</sup>14] Kamada, Taiki, Hisashi Nakamura, Takuya Tezuka, Susumu Hasegawa und Kaoru Maruta: *Study on combustion and ignition characteristics of natural gas components in a micro flow reactor with a controlled temperature profile*. Combustion and Flame, 161(1):37–48, 2014.
- [KNT<sup>+</sup>15] Kizaki, Yuta, Hisashi Nakamura, Takuya Tezuka, Susumu Hasegawa und Kaoru Maruta: *Effect of radical quenching on CH<sub>4</sub>/air flames in a micro flow reactor with a controlled temperature profile*. Proceedings of the Combustion Institute, 35(3):3389–3396, 2015.
- [KOBGL88] Karni, M., I. Oref, S. Barzilai-Gilboa und A. Lifshitz: *Isomerization of cyclopropene to allene and propyne at elevated temperatures: experimental, ab initio, and model calculations*. The Journal of Physical Chemistry, 92(24):6924–6929, 1988.
- [KOW97] Khokhlov, Alexei M, Elaine S Oran und J Craig Wheeler: *A theory of deflagration-to-detonation transition in unconfined flames*. Combustion and Flame, 108(4):503–517, 1997.
- [KRB<sup>+</sup>11] Kuznetsov, M., R. Redlinger, W. Breitung, J. Grune, A. Friedrich und N. Ichikawa: *Laminar burning velocities of hydrogen-oxygen-steam mixtures at elevated temperatures and pressures*. Proceedings of the Combustion Institute, 33(1):895–903, 2011.
- [KS03] Kagan, Leonid und Gregory Sivashinsky: *The transition from deflagration to detonation in thin channels*. Combustion and Flame, 134(4):389–397, 2003.
- [KS16] Kagan, Leonid und Gregory Sivashinsky: *Deflagration-to-detonation transition in narrow channels: hydraulic resistance versus flame folding*. Combustion Theory and Modelling, 20(5):798–811, 2016.
- [KS17a] Kagan, Leonid und Gregory Sivashinsky: *Parametric transition from deflagration to detonation: Runaway of fast flames*. Proceedings of the Combustion Institute, 36(2):2709–2715, 2017.
- [KS17b] Kagan, Leonid und Gregory Sivashinsky: *Transition to detonation of an expanding spherical flame*. Combustion and Flame, 175:307–311, 2017.

- [KYB<sup>+</sup>15] Koksharov, Andrey, Chunkan Yu, Viatcheslav Bykov, Ulrich Maas, Mark Pfeifle und Matthias Olzmann: *Quasi spectral method for the calculation of rate constants for reactions with unimolecular steps*. In: *Proceedings of the European Combustion Meeting*, 2015.
- [KYB<sup>+</sup>18] Koksharov, Andrey, Chunkan Yu, Viatcheslav Bykov, Ulrich Maas, Mark Pfeifle und Matthias Olzmann: *Quasi-Spectral Method for the Solution of the Master Equation for Unimolecular Reaction Systems*. *International Journal of Chemical Kinetics*, 50(5):357–369, 2018.
- [KYI16] Kiverin, A. D., I. S. Yakovenko und M. F. Ivanov: *On the structure and stability of supersonic hydrogen flames in channels*. *International Journal of Hydrogen Energy*, 41(47):22465–22478, 2016.
- [LDCP03] Lamoureux, N., N. Djebaili-Chaumeix und C. E. Paillard: *Laminar flame velocity determination for H<sub>2</sub>–air–He–CO<sub>2</sub> mixtures using the spherical bomb method*. *Experimental Thermal and Fluid Science*, 27(4):385–393, 2003.
- [Lee77] Lee, John H. S.: *Initiation of gaseous detonation*. *Annual Review of Physical Chemistry*, 28(1):75–104, 1977.
- [Lee08] Lee, John H. S.: *The detonation phenomenon*, Band 2. Cambridge University Press Cambridge, 2008, ISBN 9780521897235.
- [LFB75] Lifshitz, Assa, Michael Frenklach und Alexander Burcat: *Structural isomerization allene. dblarw. propyne. Studies with a single pulse shock tube*. *The Journal of Physical Chemistry*, 79(12):1148–1152, 1975.
- [LI14] Lv, Yu und Matthias Ihme: *Discontinuous Galerkin method for multicomponent chemically reacting flows and combustion*. *Journal of Computational Physics*, 270:105–137, 2014.
- [LKP<sup>+</sup>17] Leitner, Walter, Jürgen Klankermayer, Stefan Pischinger, Heinz Pitsch und Katharina Kohse-Höinghaus: *Advanced biofuels and beyond: chemistry solutions for propulsion and production*. *Angewandte Chemie International Edition*, 56(20):5412–5452, 2017.
- [LM83] Liu, D. D. S. und R. MacFarlane: *Laminar burning velocities of hydrogen-air and hydrogen-air steam flames*. *Combustion and Flame*, 49(1-3):59–71, 1983.
- [Log98] Logg, Anders: *Multi-Adaptive Error Control for ODEs*. Technischer Bericht, Chalmers University of Technology, 1998.
- [Log03] Logg, Anders: *Multi-Adaptive Galerkin Methods for ODEs I*. *SIAM Journal on Scientific Computing*, 24(6):1879 – 1902, 2003.
- [Log04a] Logg, Anders: *Multi-Adaptive Galerkin Methods for ODEs II: implementation and Applications*. *SIAM Journal on Scientific Computing*, 25(4):1119 – 1141, 2004.

- [Log04b] Logg, Anders: *Multiadaptive Galerkin Methods for ODEs III: A Priori Error Estimates*. SIAM Journal on Scientific Computing, 43(6):2024 – 2646, 2004.
- [Maa88] Maas, Ulrich: *Mathematische Modellierung instationärer Verbrennungsprozesse unter Verwendung detaillierter Reaktionsmechanismen*. Dissertation, Universität Heidelberg, 1988.
- [MB97] Minion, Michael L. und David L. Brown: *Performance of under-resolved two-dimensional incompressible flow simulations, II*. Journal of Computational Physics, 138(2):734–765, 1997.
- [MJCL98] Mebel, A. M., W. M. Jackson, A. H. H. Chang und S. H. Lin: *Photodissociation Dynamics of Propyne and Allene: A View from ab Initio Calculations of the C<sub>3</sub>H<sub>n</sub> (n= 1-4) Species and the Isomerization Mechanism for C<sub>3</sub>H<sub>2</sub>*. Journal of the American Chemical Society, 120(23):5751–5763, 1998.
- [MK03] Miller, James A und Stephen J Klippenstein: *From the multiple-well master equation to phenomenological rate coefficients: Reactions on a C<sub>3</sub>H<sub>4</sub> potential energy surface*. The Journal of Physical Chemistry, 107(15):2680–2692, 2003.
- [MK06] Miller, James A. und Stephen J. Klippenstein: *Master equation methods in gas phase chemical kinetics*. The Journal of Physical Chemistry, 110(36):10528–10544, 2006.
- [MKK<sup>+</sup>05] Maruta, Kaoru, Takuya Kataoka, Nam Il Kim, Sergey Minaev und Roman Fursenko: *Characteristics of combustion in a narrow channel with a temperature gradient*. Proceedings of the Combustion Institute, 30(2):2429–2436, 2005.
- [ML85] Mallard und Le Chatelier: *Recherches sur la combustion des mélanges gazeux explosifs*. J. Phys. Theor. Appl., 4(1):59 – 84, 1885.
- [MM61] Monchick, Louis und E. A. Mason: *Transport properties of polar gases*. The Journal of Chemical Physics, 35(5):1676–1697, 1961.
- [MPO<sup>+</sup>04] Maruta, K., J. K. Parc, K. C. Oh, T. Fujimori, S. S. Minaev und R. V. Fursenko: *Characteristics of microscale combustion in a narrow heated channel*. Combustion, Explosion and Shock Waves, 40(5):516–523, 2004.
- [MR04] Michaelis, B. und B. Rogg: *FEM-simulation of laminar flame propagation. I: Two-dimensional flames*. Journal of computational physics, 196(2):417–447, 2004.
- [MW88] Maas, U. und J. Warnatz: *Ignition processes in hydrogen-oxygen mixtures*. Combustion and Flame, 74(1):53–69, 1988.
- [Net12] Nettleton, Michael A.: *Gaseous detonations: their nature, effects and control*. Springer Science & Business Media, London, New York, 2012, ISBN 978-94-010-7915-0.

- [NFGLC93] N’konga, B., G. Fernandez, H. Guillard und B. Larrouturou Cermics: *Numerical investigations of the tulip flame instability—comparisons with experimental results*. Combustion science and technology, 87(1-6):69–89, 1993.
- [NS07] Nori, Venkata und Jerry Seitzman: *Chemiluminescence measurements and modeling in syngas, methane and jet-A fueled combustors*. In: *45th AIAA Aerospace Sciences Meeting and Exhibit*, Seite 466, 2007.
- [NTT<sup>+</sup>16] Nakamura, Hisashi, Hiroki Takahashi, Takuya Tezuka, Susumu Hasegawa, Kaoru Maruta und Kazuki Abe: *Effects of CO-to-H<sub>2</sub> ratio and diluents on ignition properties of syngas examined by weak flames in a micro flow reactor with a controlled temperature profile*. Combustion and Flame, 172:94–104, 2016.
- [OB05] Oran, Elaine S und Jay P Boris: *Numerical simulation of reactive flow*. Cambridge University Press, Cambridge, 2005, ISBN 0-521-02236-3.
- [OG07] Oran, Elaine S. und Vadim N. Gamezo: *Origins of the deflagration-to-detonation transition in gas-phase combustion*. Combustion and Flame, 148(1):4–47, 2007.
- [Olz13] Olzmann, M.: *Statistical Rate Theory in Combustion: An Operational Approach*. In: Battin-Leclerc, F., J.M. Simmie und E. Blurock (Herausgeber): *Cleaner Combustion: Developing Detailed Chemical Kinetic Models*, Seiten 549–576. Springer: London, UK, London, 2013, ISBN 978-1-4471-5306-1.
- [PBO10] Pareja, Jhon, Hugo J. Burbano und Yasuhiro Ogami: *Measurements of the laminar burning velocity of hydrogen–air premixed flames*. International Journal of Hydrogen Energy, 35(4):1812–1818, 2010.
- [PCT95] Poinot, Thierry, Sébastien Candel und Arnaud Trouvé: *Applications of direct numerical simulation to premixed turbulent combustion*. Progress in Energy and Combustion Science, 21(6):531–576, 1995.
- [PF77] Penner, Alvin P. und Wendell Forst: *Analytic solution of relaxation in a system with exponential transition probabilities*. J. Chem. Phys., 67(11):5296–5307, 1977.
- [PFM<sup>+</sup>08] Pizza, Gianmarco, Christos E Frouzakis, John Mantzaras, Ananias G Tomboulides und Konstantinos Boulouchos: *Dynamics of premixed hydrogen/air flames in microchannels*. Combustion and Flame, 152(3):433–450, 2008.
- [PFM<sup>+</sup>10] Pizza, Gianmarco, Cristos E. Frouzakis, John Mantzaras, Ananias G. Tomboulides und Konstantinos Boulouchos: *Three-dimensional simulations of premixed hydrogen/air flames in microtubes*. Journal of Fluid Mechanics, 658:463–491, 2010.
- [PL92] Poinot, T.J und S.K Lele: *Boundary conditions for direct simulations of compressible viscous flows*. Journal of Computational Physics, 101(1):104 – 129, 1992.

- [PLS69] Palm-Leis, Ahto und Roger A. Strehlow: *On the propagation of turbulent flames*. Combustion and flame, 13(2):111–129, 1969.
- [PMF<sup>+</sup>09] Pizza, Gianmarco, John Mantzaras, Christos E. Frouzakis, Ananias G. Tomboulides und Konstantinos Boulouchos: *Suppression of combustion instabilities of premixed hydrogen/air flames in microchannels using heterogeneous reactions*. Proceedings of the Combustion Institute, 32(2):3051–3058, 2009.
- [QKN00] Qin, Xiao, Hideaki Kobayashi und Takashi Niioka: *Laminar burning velocity of hydrogen–air premixed flames at elevated pressure*. Experimental Thermal and Fluid Science, 21(1-3):58–63, 2000.
- [QSS00] Quarteroni, Alfio, Riccardo Sacco und Fausto Saleri: *Numerical mathematics*. Texts in applied mathematics. Springer, New York, 2000, ISBN 0-387-98959-5.
- [QT77] Quack, M. und J. Troe: *Unimolecular reactions and energy transfer of highly excited molecules*. In: Ashmore, P. G. und R. J. Donovan (Herausgeber): *Gas Kinetics and Energy Transfer: Volume 2*, Band 2, Seiten 175–238. The Royal Society of Chemistry, 1977, ISBN 978-0-85186-766-3.
- [RH93] Radhakrishnan, Krishnan und Alan C Hindmarsh: *Description and use of LSODE, the Livermore solver for ordinary differential equations*. National Aeronautics and Space Administration, Office of Management, Scientific and Technical Information Program, 1993.
- [Rin97] Rink, Gunda: *Mastergleichungsanalyse der stoßinduzierten Energieübertragung in vielatomigen Molekülen*. Dissertation, Universität Karlsruhe, 1997.
- [RO88] Rotman, D. A. und A. K. Oppenheim: *Aerothermodynamic properties of stretched flames in enclosures*. In: *Symposium (International) on Combustion*, Band 21, Seiten 1303–1312. Elsevier, 1988.
- [Rob66] Robertson, H. H.: *The solution of a set of reaction rate equations*. Numerical analysis: an introduction, Seiten 178–182, 1966.
- [Sch75] Schäfer, E.: *A new approach to explain the “high irradiance responses” of photomorphogenesis on the basis of phytochrome*. Journal of Mathematical Biology, 2(1):41–56, 1975.
- [Sem28] Semenov, N.: *Zur Theorie des Verbrennungsprozesses*. Zeitschrift für Physik, 48:571–582, 1928.
- [Sha49] Shannon, Claude Elwood: *Communication in the presence of noise*. Proceedings of the IRE, 37(1):10–21, 1949.
- [Sha70] Shanno, D. F.: *Conditioning of quasi-Newton methods for function minimization*. Mathematics of Computation, 24:647–656, 1970.

- [Shi72] Shimanouchi, Takehiko: *Tables of molecular vibrational frequencies. Consolidated volume I*, Band 39. U.S. Government Printing Office, 1972.
- [SHN<sup>+</sup>13] Suzuki, Satoshi, Mikito Hori, Hisashi Nakamura, Takuya Tezuka, Susumu Hasegawa und Kaoru Maruta: *Study on cetane number dependence of diesel surrogates/air weak flames in a micro flow reactor with a controlled temperature profile*. Proceedings of the Combustion Institute, 34(2):3411–3417, 2013.
- [SP17] Shen, Hua und Matteo Parsani: *The role of multidimensional instabilities in direct initiation of gaseous detonations in free space*. Journal of Fluid Mechanics, 813, 2017.
- [SR97] Shampine, L. und M. Reichelt: *The MATLAB ODE Suite*. SIAM Journal on Scientific Computing, 18(1):1 – 22, 1997.
- [sve] *Estimated viscosities and thermal conductivities of gases at high temperatures*. NASA technical report. TR R-132.
- [SW14] Sánchez, Antonio L. und Forman A. Williams: *Recent advances in understanding of flammability characteristics of hydrogen*. Progress in Energy and Combustion Science, 41(1):1–55, 2014.
- [Tad90] Tadmor, Eitan: *Shock capturing by the spectral viscosity method*. Computer Methods in Applied Mechanics and Engineering, 80(1):197 – 208, 1990.
- [TGK96] Truhlar, Donald G., Bruce C. Garrett und Stephen J. Klippenstein: *Current status of transition-state theory*. The Journal of physical chemistry, 100(31):12771–12800, 1996.
- [TZL00] Tse, S. D., D. L. Zhu und C. K. Law: *Morphology and burning rates of expanding spherical flames in H<sub>2</sub>/O<sub>2</sub>/inert mixtures up to 60 atmospheres*. Proceedings of the Combustion Institute, 28(2):1793–1800, 2000.
- [VBA<sup>+</sup>10] Valiev, Damir, Vitaly Bychkov, V'yacheslav Akkerman, Chung K Law und Lars Erik Eriksson: *Flame acceleration in channels with obstacles in the deflagration-to-detonation transition*. Combustion and Flame, 157(5):1012–1021, 2010.
- [VEL94] Vagelopoulos, C. M., F. N. Egolfopoulos und C. K. Law: *Further considerations on the determination of laminar flame speeds with the counterflow twin-flame technique*. Symposium (International) on Combustion, 25(1):1341–1347, 1994.
- [VNO<sup>+</sup>15] Varga, T., T. Nagy, C. Olm, I.Gy. Zsély, R. Pálvölgyi, É. Valkó, G. Vincze, M. Cserhádi, H.J. Curran und T. Turányi: *Optimization of a hydrogen combustion mechanism using both direct and indirect measurements*. Proceedings of the Combustion Institute, 35(1):589 – 596, 2015.

- [VWLS05] Verhelst, S., R. Woolley, M. Lawes und R. Sierens: *Laminar and unstable burning velocities and Markstein lengths of hydrogen-air mixtures at engine-like conditions*. Proceedings of the Combustion Institute, 30(1):209–215, 2005.
- [Wil88] Williams, Forman A.: *Combustion theory: the fundamental theory of chemically reacting flow systems*. Combustion science and engineering series. Addison Wesley, Redwood City, Calif., 2. ed., repr. with corr. Auflage, 1988, ISBN 0-8053-9801-5.
- [WK87] Wu, CH und RD Kern: *Shock-tube study of allene pyrolysis*. Journal of Physical Chemistry, 91(24):6291–6296, 1987.
- [WL85] Wu, C. K. und C. Kl. Law: *On the determination of laminar flame speeds from stretched flames*. In: *Symposium (International) on Combustion*, Band 20, Seiten 1941–1949. Elsevier, 1985.
- [WLC<sup>+</sup>15] Wu, Fujia, Wenkai Liang, Zheng Chen, Yiguang Ju und Chung K. Law: *Uncertainty in stretch extrapolation of laminar flame speed from expanding spherical flames*. Proceedings of the Combustion Institute, 35(1):663–670, 2015.
- [WMD06] Warnatz, Jürgen, Ulrich Maas und Robert W. Dibble: *Combustion: physical and chemical fundamentals, modelling and simulation, experiments, pollutant formation*. Springer, Berlin, 4. Auflage, 2006, ISBN 978-3-540-25992-3.
- [WZSN12] Wang, Cheng, Xiangxiong Zhang, Chi Wang Shu und Jianguo Ning: *Robust high order discontinuous Galerkin schemes for two-dimensional gaseous detonations*. Journal of Computational Physics, 231(2):653–665, 2012.
- [XHO15] Xiao, Huahua, Ryan W Houim und Elaine S. Oran: *Formation and evolution of distorted tulip flames*. Combustion and Flame, 162(11):4084–4101, 2015.
- [XHO17] Xiao, Huahua, Ryan W. Houim und Elaine S. Oran: *Effects of pressure waves on the stability of flames propagating in tubes*. Proceedings of the Combustion Institute, 36(1):1577–1583, 2017.
- [XMSM12] Xiao, Huahua, Dmitriy Makarov, Jinhua Sun und Vladimir Molkov: *Experimental and numerical investigation of premixed flame propagation with distorted tulip shape in a closed duct*. Combustion and Flame, 159(4):1523–1538, 2012.
- [XWH<sup>+</sup>11] Xiao, Huahua, Qingsong Wang, Xuechao He, Jinhua Sun und Xiaobo Shen: *Experimental study on the behaviors and shape changes of premixed hydrogen-air flames propagating in horizontal duct*. international journal of hydrogen energy, 36(10):6325–6336, 2011.
- [YS07] Yee, Helen C und Björn Sjögreen: *Development of low dissipative high order filter schemes for multiscale Navier–Stokes/MHD systems*. Journal of Computational Physics, 225(1):910–934, 2007.

- [Zel48] Zeldovich, Yakov B.: *Theory of flame propagation*. Zhurnal Fizicheskoi Khimii (USSR), 22:27–49, 1948.
- [ZHW<sup>+</sup>12] Zhang, Yingjia, Zuohua Huang, Liangjie Wei, Jiayang Zhang und Chung K. Law: *Experimental and modeling study on ignition delays of lean mixtures of methane, hydrogen, oxygen, and argon at elevated pressures*. Combustion and Flame, 159(3):918 – 931, 2012.
- [ZLMS70] Zeldovich, Ya. B., V. B. Librovich, G. M. Makhviladze und G. Ii. Sivashinsky: *On the development of detonation in a non-uniformly preheated gas*. Astronautica Acta, 15(5-6):313–321, 1970.
- [ZR47] Zeldovich, Yakov B. und A. I. Rozlovskii: *On the onset of unstable normal burning: transition of a spherical flame to detonation*. Dokl. Akad. Nauk SSSR, 57:365–368, 1947.
- [ZWX<sup>+</sup>12] Zhen, Xudong, Yang Wang, Shuaiqing Xu, Yongsheng Zhu, Chengjun Tao, Tao Xu und Mingzhi Song: *The engine knock analysis—an overview*. Applied Energy, 92:628–636, 2012.